INVESTIGATION INTO THE CONTRIBUTION OF THE MC-DC PROCESS ON MICROSTRUCTURAL EVOLUTION OF DIRECT CHILL CAST ROUND INGOTS OF 6XXX SERIES ALUMINIUM ALLOYS WITH AN AIM TO REDUCE HOMOGENISATION

A thesis submitted for the degree of Doctor of Philosophy

by

Simon John Jones

Brunel Centre for Advanced Solidification Technology, Brunel University

30th November 2014

ACKNOWLEDGMENTS

I would like to express my sincerest and deepest thanks to Professor Zhongyun Fan for the opportunity of my PhD and the continued mentorship during my studies and continuing into my life as a research engineer. Your insight and passion of this subject have been invaluable.

Thank you also to my committee members, Professor Koulis Pericleous, Dr. Brian McKay and Dr. Hari-Babu Nadendla, for serving on my committee. Good discussions were had during my defense for an enjoyable experience. Your kind and well directed comments are very appreciated and I thank you all for the time you took.

A special thank you goes to Dr. Hu-Tian Li without who's help and guidance during my thesis writing and infinite patience during failed experiments I would have not been able to complete. You have a calming and reassuring presence that made working with you a joy. I look forward to continuing to work with you in the future.

My deepest gratitude goes to Sapa, specifically my colleagues and friends at Sapa Technology. Thank you so much for the opportunity and the support to complete this body of work and gain my PhD. I have been gifted to have this time to focus on this subject and look forward to using the skills and knowledge I have gained into good use for Sapa. I would especially like to thank Kristina for your constant support and connection back to ST, at times it felt like a lifeline. Stanislaw, thank you so much for the time spent on the SEM together and discussions that followed. And Jan, thank you sincerely for this opportunity. I enjoyed working on this with you, Stanislaw and Kristina, provoking much discussion and interest and excitement for the future.

Without the support of my family and friends this simply would not have been possible. During the years of my PhD there have been many ups and downs that you Hannah were able to shield me from at great cost to yourself. Thank you for giving me the chance to focus when I needed it the most. Building that Lego Death Star one layer a week did more to soothe my mind than you can imagine. Those evenings in London are some I treasure the most in my life.

Jim, thank you for letting me camp out at your house for weeks on end, sat at your dining room table to write and combine this work. Thank you Tim for your support when my IT skills failed me and frustration began to kick in.

To my beloved wife who I met and married during my PhD. You have been with me through it all, moved countries twice, house three times, suffered the late nights and "Sunday silences" when I could think of nothing but the coming week and pursuit of result. You are the rock I have built my life upon and I am so very grateful for your love and support.

Thank you all for your sacrifice and support, this work is dedicated to you

Simon

ABSTRACT

Aluminium applications can be found in the vast majority of industries – particularly the automotive, aerospace and building sectors. Light weight, good corrosion resistance, high strength with good machining and weldability has led 6xxx series alloy to be the most widely used for extrusion products. Semi-continuous direct-chill (DC) casting is a well established process and the most widely used in the production of wrought aluminium extrusion billets. The techniques have continuously evolved since its invention in the 1930s. To ensure high productivity and a quality billet by DC casting, grain refiners are added during casting prior to solidification. It is efficient, cost effective and considered optimized in modern production techniques. However, some problems still persist, for example, macrosegregation, centerline cracking, porosity, hot tearing, etc. For surface finish critical products, particles in added grain refiners may cause surface defects during downstream processing. Additions of grain refiners are also not desirable for recycling of the end use products.

As a novel DC casting technology, the melt conditioned DC casting (MC-DC) technology is developed to achieve uniform fine equiaxed grains without deliberate additions of grain refiners. The MC-DC process is implemented by submerging a rotor-stator high shear device into the mould assembly of a conventional hot-top vertical DC caster. In this work, the fundamentals of MC-DC process has been investigated by studying the flow patterns in the sump using computer modelling in combination with thermal field measurement and delineation of the sump profile. Followed is the microstructural evolution of the MC-DC castings. Then the formation of Fe-bearing intermetallics which are critical to the arrangement of homogenisation treatment are presented. The grain refining mechanism by MC-DC is due to enhanced heterogeneous nucleation on dispersed oxides and grain fragments by intensive melt shearing, in combination with dendrite fragmentation and transportation in a uniform temperature and solute field. By optimising MC-DC parameters, alleviation of macrosegregation can be achieved even compared with DC-GR castings. Another finding is the correlation between grain structure and the distribution of the Fe-intermetallic particles. It has been demonstrated that equiaxed dendritic grains with fine secondary dendritic arm spacings achieved in MC-DC are preferred rather than finer granular grains in grain refined material. MC-DC also promotes the formation of α- Fe-bearing intermetallics. All these offer the potential for

the reduction of homogenisation practices currently required as part of the DC process.

TABLE OF CONTENTS

Chapter 1 - Introduction 1

Chapter 2 - Literature Review 3

2.1 Structure formation in as-cast DC castings 6

2.2 Refinement of as cast structure 12

2.3 macrosegregation, Grain structure and DC casting process parameters 27

Chapter 3 - Experimental Procedure 31

3.1 The Shearing device 32

3.2 Static Mould Experiment 32

3.3 MC-DC casting at BCAST lab 37

3.4 MC-DC Casting at Oxford Begbroke Science Park 40

Chapter 4 – Results-process development 53

4.1 Process Development 53

Chapter 4.2 – results - Microstructure Evolution 89

4.3 results-formation of Fe-bearing Intermetallics 141

Chapter 5 - Discussion 199

5.1 microstructures of dc casting with and without grain refiner 199

5.2 Microstructural evolution through melt conditioning 202

5.3 Columnar to equiaxed transition (CET) in Mc-dc casting 214

5.4 refinement of grain structure and intermetallics in mc-dc casting 216

5.5 Potential to reduce homogenisation treatment due to refined intermetallics 217

5.6 alleviated macrosegregation in mc-dc casting 218

5.6 Tool Perfomrance During mc-dc casting 219

Chapter 6 - Conclusions 222

Future work 225

Bibliography 226

Appdendix 1 - intermetallics formed in DC castings at BCAST Pilot 231

Appdendix 2 – Flow Pattern Assembly Diagrams 258

TABLE OF FIGURES

Figure 2.1 Cross section of a Hot-top DC casting ……4

Figure 2.2 Schematic representation of the transition region formed in direct chill (DC) casting…7

Figure 2.3 Schematic of the shearing device stator……24

Figure 2.4 Diagram of the MC-DC process……..25

Figure 2.5 Sketch illustrates the solidification mechanism of MC-DC process……...26

Figure 2.6 A typical pattern of macrosegregation……27

Figure 3.1 Schematic of the static mould experiment apparatus……..34

Figure 3.2 Thermocalc phase diagram for 6060……42

Figure 3.3 Schematic of the MC-DC process at Oxford Begbroke……...42

Figure 3.4 Thermocalc phase diagram for 6063……..50

Figure 3.5 Schematic of Oxford Begbroke DC casting unit……45

Figure 3.5 Schematic of a cast log and billet slices positions……49

Figure 3.6 Schematic of the billet slice sectioned for analysis……..50

Figure 4.1 SolidWork flow patterns for MC-DC-P1 billet……57

Figure 4.2 SolidWorks flow patterns for MC-DC-P2 billet……..59

Figure 4.3 SolidWorks flow patterns for MC-DC-P3 billet……..60

Figure 4.4 Billet slice taken from the MC-DC-P2 billet sheared at 4500 rpm……62

Figure 4.5 Macrographs of 206 mm billet vertical cross-section……70-66

Figure 4.6 Temperature profiles of MC-DC billets cast in 8” diameter mould……75

Figure 4.7 OES measurement of DC-GR billet ……84

Figure 4.8 OES measurement of MD-DC-P2 billet at 4500 and 6400 rpm…..……86

Figure 4.9 OES measurement of MC-DC-P3 billet at 3000, 4500 and 6400 rpm..……89

Figure 4.10 OES measurement of MC-DC-P2-GR billet at 4500 and 6400 rpm……..92

Figure 4.11 Macro etched sample showing static mould solidified billet after shearing..……90

Figure 4.12 Micrographs of static mould microstructure……...92

Figure 4.13 BCAST pilot scale billet macro image……...97

Figure 4.14 BCAST.pilot scale billet grain structure images……101

Figure 4.15 BCAST pilot scale billet average grain sizes……..102

Figure 4.16 BCAST pilot scale average P* value……..103

Figure 4.17 BCAST pilot scale billet microstructure images that correspond to the P* values……105

Figure 4.18 Macro-etched vertical cross-section of the DC-GR billet……..108

Figure 4.19 Microstructure of DC-GR billet cast at Oxford Begbroke……..108

Figure 4.20 Average grain size of DC-GR billet cast at Oxford Begbroke……..109

Figure 4.21 Macro images of the MC-DC-P2 billet cross section……115-113

Figure 4.22 Grain structure mosaics from the MC-DC-P2 and P3 billet……121

Figure 4.23 Grain structure mosaics from the MC-DC-P2-GR billet...……127
Figure 4.24 Average grain size graphs for the MC-DC billets ……..125
Figure 4.25 Micrographs obtained from the shell zone and surface region of the MC-DC billets…132
Figure 4.26 Micrographs of MC-DC-P2 coarse grain structures……...134
Figure 4.27 Micrographs of the MC-DC-P2 & P3 at mid-radius of the billet……136
Figure 4.28 Micrographs of the MC-DC-P2 & P3 billet centre after shearing..…….....138
Figure 4.29 Micrographs obtained from the MC-DC-P2 billet sheared at 4500 rpm…….....140
Figure 4.30 Micrographs obtained from the MC-DC-GR-P2 billet sheared at 6400 rpm…….....140
Figure 4.31 P* measurement values of the MC-DC 8" billets from the surface to the billet centre.131
Figure 4.32 Micrographs of the intermetallics formed in the static mould ……..140
Figure 4.33 Graphs of the average particle size in the four static mould zones……143
Figure 4.34 SEM (BSE) images of static mould billet intermetallics Zone 1.……147
Figure 4.35 Intermetallic ratio graphs from static mould billet Zone 1.....……147
Figure 4.36 SEM (BSE) images of static mould billet intermetallics Zone 2.....149
Figure 4.37 Intermetallic ratio graphs from static mould billet Zone 2……...150
Figure 4.38 SEM (BSE) images of static mould billet intermetallics Zone 3……..151
Figure 4.39 Intermetallic ratio graphs from static mould billet Zone 3……..151
Figure 4.40 SEM (BSE) images of static mould billet intermetallics Zone 4……..…153
Figure 4.41 Intermetallic ratio graphs from static mould billet Zone 4……..153
Figure 4.42 As-cast microstructure of DC-GR billet……155
Figure 4.43 Average particle measurements DC-GR billet……156
Figure 4.44 SEM (BSE) images of intermetallic particles from the DC-GR as-cast billet……157
Figure 4.45 Intermetallic ratio graphs from DC-GR billet……158
Figure 4.46 MC-DC-GR-P2 billet sheared at 4500 rpm intermetallic images……160
Figure 4.47 Average particle measurements MC-DC-GR-P2 billet……..161
Figure 4.48 SEM (BSE) images of MC-DC-GR-P2 4500 rpm intermetallics……..163
Figure 4.49 Intermetallic ratio graphs from MC-DC-GR-P2 billet sheared at 4500 rpm……164
Figure 4.50 MC-DC-GR-P2 6400 rpm intermetallic images……..166
Figure 4.51 Average particle measurements MC-DC-GR-P2 6400 rpm billet……167
Figure 4.52 SEM (BSE) images of MC-DC-GR-P2 6400 rpm intermetallics……..169
Figure 4.53 Intermetallic ratio graphs MC-DC-GR-P2-6400 rpm……..170
Figure 4.54 MC-DC-P2 billet intermetallic images……...172
Figure 4.55 MC-DC-P2 CGC billet intermetallic images……173
Figure 4.56 MC-DC-P2 billet centre intermetallic images……..174
Figure 4.57 Intermetallic ratio graphs MC-DC-P2 4500 rpm……176
Figure 4.58 Intermetallic ratio graphs MC-DC-P2 6400 rpm……176
Figure 4.59 SEM images of MC-DC-P2 4500 rpm intermetallics……..178
Figure 4.60 SEM images of MC-DC-P2 6400 rpm intermetallics……..178
Figure 4.61 SEM images of MC-DC-P2 billet centre intermetallics……..180
Figure 4.62 Particle measurement graphs MC-DC-P2 4500 rpm……181

Figure 4.63 Particle measurement graphs MC-DC-P2 6400 rpm……182
Figure 4.64 MC-DC-P3 4500 rpm billet intermetallic images……183
Figure 4.65 MC-DC-P3 6400 rpm billet intermetallic images……184
Figure 4.66 Particle measurement graphs MC-DC-P3 4500 rpm……187
Figure 4.67 Particle measurement graphs MC-DC-P3 6400 rpm……187
Figure 4.68 SEM images of MC-DC-P3 4500 rpm intermetallics……189
Figure 4.69 Particle measurement graphs MC-DC-P3 4500 rpm……191
Figure 4.70 SEM images of MC-DC-P3 6400 rpm intermetallics……192
Figure 4.71 Particle measurement graphs MC-DC-P3 6400 rpm……194

CHAPTER 1 - INTRODUCTION

Aluminium applications can be found in the vast majority of industries - particularly the automotive, aerospace and building sectors. Light weight, good corrosion resistance, high strengths with good machining and weldability has led the 6xxx alloy series to be the most widely used for extrusion products. Semi-continuous direct-chill (DC) casting is a well-established process and the most common method used in the production of wrought aluminium extrusion billets (Eskin D. G., 2008) (Grandfield, Eskin, & Bainbridge, 2013). The techniques and equipment used in the production process have continuously evolved since its conception in the 1930s.

Even though the DC process has been developed over the last 90 years, defects are still inherent in the process. Examples of the defects are centerline cracking, non-uniform grain structures, hot tearing, macrosegregation (non-uniform distribution of elements across the casting), porosity and inclusions. Optimization of DC casting in relation to defect suppression, productivity and economic performance is continuous within the industry as it attempts to keep pace with the ever increasing innovation and utilization of extruded aluminium products. To this end various methods of melt treatment have been studied from parameter adjustment (casting speed, melt temperatures), chemical inoculation (grain refiner additions) and forced convection (ultrasonic cavitation, electromagnetic stirring and mechanical stirring, etc.). The most efficient and economical method is inoculation (grain refinement) which treats the melt during casting. Grain refiner enables faster casting speeds as it promotes nucleation and development of fine equiaxed grains, which prevent the billet from cracking. In some instances a combination of methods is employed, but this is rare.

Additional to the defects that are described above, iron (Fe) bearing intermetallic phases form during solidification. Refinement of these constituent phases is critical to achieving properties and acceptable quality of the extruded profiles after down-stream processing. The alloy system that is cast in this work is AA6060 of the 6xxx series. It is a magnesium – silicon (Mg-Si) based alloy but as with all commercial alloys, Fe is present in the material as an impurity. There are no known economical methods of removing the iron from aluminium and during solidification Fe segregates

out to the grain boundaries due to its low solid solubility. It combines with the other elements – Mg, Si and Mn – to form various intermetallic phases, the most dominant of which are the alpha phases α-Al_8Fe_2Si and α-$Al_{15}(FeMn)Si_3$ and the beta phase β-Al_5FeSi. Beta Fe-bearing intermetallic phase is universally considered to be detrimental to the extrusion process and mechanical properties of the finished product. The formation of the different phases depends on the element concentration and cooling rate during solidification. A thermal treatment process known as homogenisation is applied to the as-cast billet to transform the β-Al_5FeSi particles into the α-Al_8Fe_2Si phase. Homogenisation is an extremely costly process that requires heating the billet up to 585 ºC and holding it at this temperature for 2 hrs or longer (soak time) depending on the volume of beta phase to transform and the alloy composition.

The aim of this present research therefore, is to investigate the effect melt conditioning (MC) has on the microstructure of a DC cast billet, on the one hand, understanding the flow patterns modified by intensive melt shearing in the sump by computer modelling, measurement of temperature field in the sump, and delineation of the sump profile by pouring into liquid zinc; on the other hand, characterizing grain structure evolution, grain size, macrosegregation and constituent phase formation with the goal to reduce or eliminate homogenisation. One of the main aims of the present work is the successful integration of melt conditioning into the direct chill process, creating the MC-DC process. So the investigations will attempt to determine whether:

1) shearing and DC casting can be integrated together,
2) the process can be up-scaled to industrial sized castings,
3) the intermetallics that formed are of a type or size that leads to the reduction or elimination of homogenisation at the industrial scale,
4) an equiaxed and uniform grain size is achievable without grain refiner,
5) Irreversible defects such as porosity, macrosegregation, cracking and inclusions are alleviated or removed by the MC-DC process.

CHAPTER 2 - LITERATURE REVIEW

Direct chill (DC) casting is the most common method of producing wrought aluminium (Al) extrusion billet. The technology as we know was conceived in the 1930s almost simultaneously in Germany and America (Emley, 1976) (Grandfield & McGlade, 1996) (Nadella, Eskin, Du, & Katgerman, 2008) (Eskin D. G., 2008). The basic process has remained the same even though the technology has of course evolved over the years. Melt enters the water cooled mould from the top where it begins to solidify against the starting head and mould walls (primary cooling) which forms the base and shell respectively. Inside this shell a semi-solid/ liquid mix is contained. Further cooling of the billet occurs by jets of water impinging directly onto its surface (secondary cooling), as it is being drawn out of the mould. Secondary cooling extracts the majority of the heat from the melt inside the billet before it is immersed into water within the casting pit. The starting head is lowered into the pit at a constant speed with a constant melt level maintained above the mould. This ensures that during steady-state casting, the semi-solid regions within the sump and the sump itself remains constant throughout.

Modern casting systems still use these principles but new mould designs and feeding stock have been introduced across the industry. In the ‘70s the “hot-top” was introduced and quickly became the system of choice for the industry (Eskin, Zuidema Jr, Savran, & Katgerman, 2004). A schematic of the components that constitute a typical Hot-top DC casting unit is shown in Figure 2.1. In this system, a reservoir of liquid melt is insulated within the mould by refractory material. It consists of two refractory sections; the table refractory and melt inlet above the mold; the transition plate (T-plate) which seals against the graphite ring of the mould and then against the underside of the table refractory. This essentially includes the refractory material as part of the mould design, retaining a constant volume of isolated melt within the mould regardless of level on the table. The Hot-Top setup therefore offers a far more manageable system providing a much wider range of cast rates, flatter sump shape, less inverse segregation and overall greater productivity (Emley, 1976).

There are number of stages before and after casting that the metal must go through before it can be sent to the customer and extruded. The following is a basic overview

of the process with critical stages looked at in more detail at a later stage in this chapter.

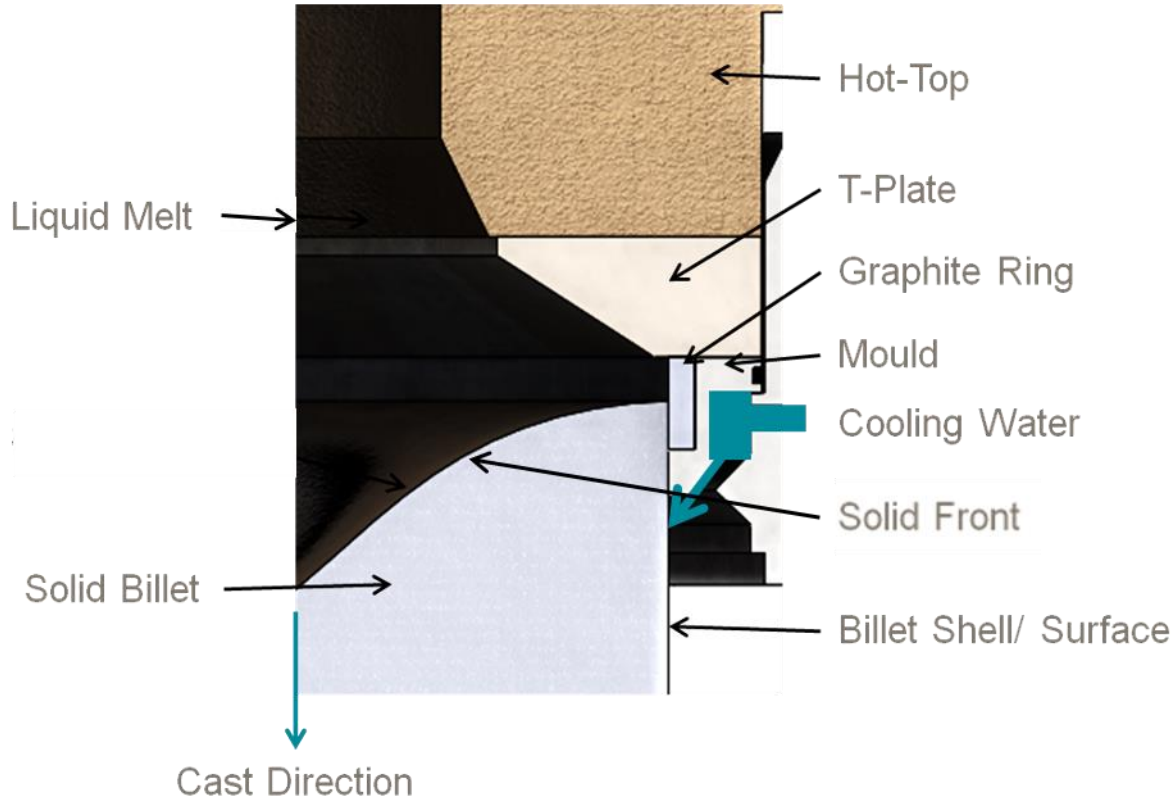

Figure 2.1 Cross section of a Hot-top DC casting unit showing the specific componets of the system

First stage of the process is the melting or remelting of material to create the molten bath of liquid aluminium. Typically, aluminium scrap of a similar composition to that of the planned cast material is loaded into a furnace. This is known as a charge and contains both pure material and scrap such as extruded sections and production cut-offs, butt-ends and external material supplies. If the scrap is of good quality and of a sufficient quantity, prime aluminium ingots should not be required in the charge. When the charge is fully molten, the composition is checked by optical emission spectroscopy (OES) using standard methods. The amount of hardeners (element additions) needed to achieve the correct specifications are calculated and added to the melt in the furnace. From here the melt is then transferred to a holding furnace along a series of ceramic refractory lined launders. The holding furnace, not surprisingly, holds the melt at the set pouring temperature before casting. Here the

melt composition is checked again and amended if needed. With the target specification correct and the melt at casting temperature – typically 720 ºC ± 5 ºC for 6xxx alloys – the melt is transferred to the casting table via a similar launder system. Before it enters the casting table, the melt would pass through a degassing process. This is where the melt flows through a baffled box containing spinning graphite rotors that introduces argon gas to the melt. The spinning rotors produce bubbles that extract hydrogen from the melt by allowing hydrogen to diffuse into the bubbles and rise to the surface. As these bubbles rise to the surface, they collect any oxide particles that might be present in the melt. This process thus reduces the chance of porosity and inclusions by removing any hydrogen and oxide dirt from the melt, respectively. Before the melt enters the casting table it will pass through a filtration system designed to catch what the degasser does not remove. Filtration systems consist of either a ceramic foam filter (CFF) or a ceramic glass filter net arrangement.

A typical casting table contains multiple strands each of the same diameter. Additional to the components of the mould package shown in Figure 2.1 is a starting head. The starting head provides a solid ingot butt at the start of a cast and supports the log there after. At the start the head is positioned inside the mould level with the bottom edge of the graphite ring, sealing the mould and forming the solidified butt of the billet. The starting heads are mounted on a fixed platen ensuring each head is drawn down at the same rate and level. The platen is lowered into a pit that is filled with water to approximately a few metres below the casting table, depending on alloy and casting system used. As the melt fills the sealed mould, the shell forms which contains the semi-solid/ liquid mix. When each mould is filled, a hold time is applied to ensure a good shell and butt form before the cast is released and the starting head begins to descend, drawing the solidifying billet down and out of the mould. As the billet exits the mould, the secondary cooling water impinges the surface increasing the cooling rate and driving the solidification across the billet. This is further intensified as the billets are submerged into the water.

After the cast is complete, the water is drained and the logs lifted from the pit and laid down for inspection. Ultra-sonic crack inspection is usually carried out now especially if the billets are intended for the production of safety critical extrusions e.g. aeronautical or automotive profiles. Cracking can occur if titanium concentrations are low (<0.2 wt%), grain refinement either stopped during the cast or was insufficient or

the casting parameters were unsound for the alloy cast. Crack free logs will then be transported for homogenisation in either batch or continuous processing ovens. This is a heat treatment stage designed to anneal the billet prior to extrusion by refining iron (Fe) bearing second phase particles and low temperature melting eutectics that congregate at the grain boundaries. The logs are heated rapidly to a set point where they are held for a number of hours depending on alloy and then rapidly cooled to ensure the solute elements do not come out of solid solution and re-coarsen. This is the final stage in the process and the logs will be sent to the extrusion plants for processing.

2.1 STRUCTURE FORMATION IN AS-CAST DC CASTINGS

The structure achieved is decided by the sump and the thermal conditions across it. The process variables, particularly the casting speed has a large influence upon the sump profile (Eskin D. G., 2008) (Eskin, Zuidema Jr, Savran, & Katgerman, 2004). An increase in casting speed is followed by an increase in the sump depth and subsequent increase in mushy zone thickness (Eskin, Zuidema Jr, Savran, & Katgerman, 2004) (Eskin D. G., 2008) (Nadella, Eskin, Du, & Katgerman, 2008). The mushy zone of the sump is a region of solid and liquid between the solidus and liquidus isotherms; effectively an intermediate zone between the fully liquid pool above it and the solid billet below (Figure 2.2). The mushy zone can be separated into two parts also, the mushy and the slurry above which consists of a semi-solid mix but the volume fraction of solid is less than in the mushy zone. Nadella *et al* describe the slurry and mushy zones together as the transition region from the fully liquid to the fully solid. The transition region is contained within the liquidus and solidus isotherms, with the mushy and slurry zones further separated by what they termed the coherency isotherm; solid grains (usually dendrites) are beginning to come into contact with each other, forming a macroscopically coherent network (Arnberg, Ba¨ckerud, & Chai, 1996) (Nadella, Eskin, Du, & Katgerman, 2008).

Due to the nature of DC casting and the difference in heat extraction across the billet radius – cooling rate at the surface can be as large as 10 Ks^{-1} but in the centre it can be as low as 0.4 Ks^{-1} - solidification varies considerably along the billet cross section

(Chu, 2002). During a cast, the liquid metal solidifies against the wall of the mould due to primary cooling. Between this initial contact and the base of the mould, the billet shell shrinks away from the mould wall. An air gap now forms between the mould and shell which causes a reduction in the amount of heat extracted by the mould before the secondary cooling water can take effect. It is at this point where the air gap forms that the risk of surface tears and bleedouts (liquid melt running out of the billet due to opening in the shell) is greatest, as the subsurface layer forms under reduced cooling, having the potential to remelt through the surface. In contrast to this, the next layer to solidify does so under the highest cooling conditions as the secondary cooling water impinges the surface. From this point on, the cooling rate decreases towards the centre resulting in a non-uniform transition region in the sump, that becomes deeper at the centre.

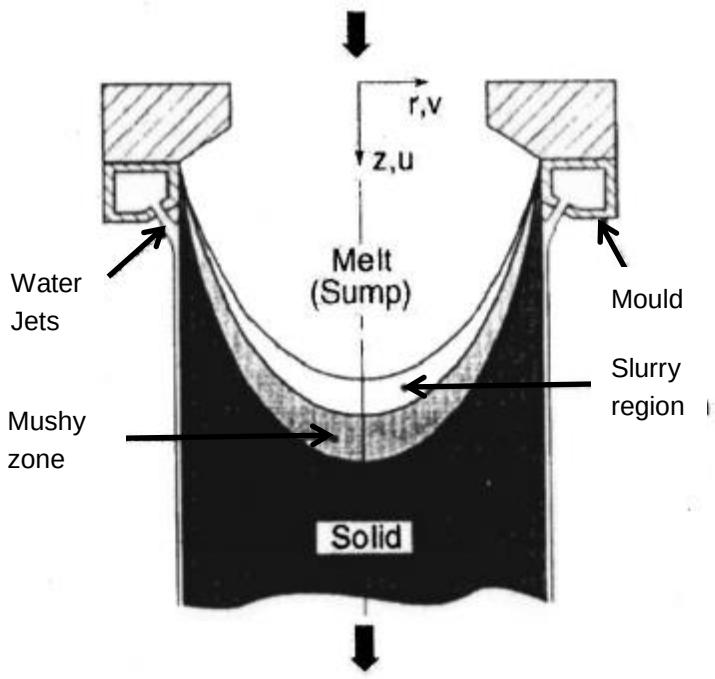

Figure 2.2 Schematic representation of the transition region formed in direct chill (DC) casting (Vreeman, Schloz, & Krane, 2002).

The sequence of structures that forms as a result of the cooling rate variations have good agreement with multiple alloy systems, with the common understanding that depending on alloying element content, nucleant potency and heat extraction, metal that is cooled rapidly forms equiaxed grains and those cooled slowly form as

columnar crystals (Chalmers, Principles of Solidification, 1964). Typically un-grain refined castings develop with structures consisting of both equiaxed and columnar growth. In DC castings, the shell forms as an equiaxed zone due to the high rate of heat extraction and subsequent copious nucleation events. Following on from this is a zone of coarse grain growth consisting of cellular-dendritic grains that solidified in the air gap between the primary and secondary cooling zones. These grains grow inwards towards the centre and melt flows present in the mould perpendicular to the mould wall at preferred growth orientations of <100> (Chalmers, Principles of Solidification, 1964). Growth competition occurs between the crystals that nucleate in this zone with the least favorably orientated grains being suppressed, resulting in fewer grains and bands of coarse structure develop. The columnar zone may very well originate from crystals that formed as a result of the primary cooling at the mould wall and survived due to their favorable orientation.

The structure of the third region is either equiaxed dendritic, a continuation of the columnar dendritic or twinned columnar known as feather grains. Which one is present in a casting depends on the type of casting, alloy and cooling rates. In castings, Chalmers states that it is typically an equiaxed structure that forms due to nucleation of crystals in a constitutionally undercooled region, because of the rejected solute layer ahead of the columnar band (Winegard & Chalmers, 1954). The growth of the equiaxed grains is sufficient to block the columnar growth. Chalmers also suggested that the nuclei for the equiaxed grains originate at the shell or “chill zone” of the melt at the mould wall (Chalmers, 1963). The crystals are then transported to the central region of the billet by convection inhibiting the growth of the columnar grains. Jackson *et al* found that the origin of the equiaxed zone in castings was the partial remelting of dendrites due to growth fluctuations caused by natural thermal-solutal convection or forced thermal-solutal convection generated by stirring the liquid (Jackson, Hunt, Uhlmann, & Seward III, 1966). For these new crystals to survive and grow they must find their way to the billet centre as soon as possible which in turn needs to be constitutionally supercooled for the equiaxed region to develop. This is known as the columnar to equiaxed transition (CET) (Hunt, 1984). As suggested by many previous studies, the CET, caused by the competition between columnar and equiaxed growth, is primarily dictated by such casting parameters as the alloy composition, pouring temperature, nuclei number density present in the

melt, cooling capacity at the melt/mould interface, and convection (Wang & Beckermann, 1994). Qualitatively, it can be anticipated that the CET occurs easily when an alloy has a higher solute level, lower pouring temperature, smaller thermal gradient, higher nuclei number density present in the melt, and more vigorous melt convection (Wang & Beckermann, 1994). Hunt first developed an analytical model by considering steady-state columnar and equiaxed growth and Hunt's model is widely considered an accurate mechanism for the CET in castings. The model qualitatively reveals the influences of alloy composition, nuclei density, and cooling rate/thermal gradient on the CET (Hunt, 1984).

For small specimens of almost uniform temperature, experimental observations indicate that nucleation and growth of the equiaxed grains ahead of the columnar front are the most important mechanisms for causing the CET (Brown & Spittle, 1989) (Wang & Beckermann, 1994). For large sized castings, the temperature field significantly affects the competitive columnar and equiaxed solidification, since columnar growth is constrained by the movement of the isotherms, and equiaxed growth ahead of the columnar front in turn alters the temperature field through the release of latent heat. For example, in continuous casting such as DC casting, large temperature gradients can be present within the central region of the sump which typically leads to a coarsening of the structure compared with mould castings (high pressure die casting, permanent mould casting, sand casting, investment casting,…). Thermal gradients that develop as a consequence of the secondary cooling effects reducing from the surface towards the centre can see the generation of columnar or feather grains dominate the central structure. This thermal gradient also results in melt/slurry movement (thermal solutal convection) and Nadella et al [4] showed that flows of varying types are present in the sump of DC casting (Nadella, Eskin, Du, & Katgerman, 2008). They range from thermal-solutal convection due to associated gradient; gravity, buoyancy and transportation mechanisms due to melt in-flow; solidification shrinkage during solidification. In turn, different movement mechanisms alter the thermal profile in the sump and therefore influence the formation of grain structures. These flows add further to the complications of CET during DC casting. This will be discussed in a later section concerning the mechanisms of macrosegregation.

It is well accepted that feather grains grow along thermal gradients in melts with strong flows, low solute concentration and dominate the growth competition consuming grains of different orientation (Henry, Jarry, & Rappaz, 1998) (Henry, Gruen, & Rappaz, 2004) (Turchin, Zuijderuiyk, Pool, Eskin, & Katgerman, 2007) (Henry, Minghetti, & Rappaz, 1998). Due to the nature of DC casting, gradients exist between the centre of the billet and the surface. These cause buoyancy differences between the cooler more dense liquid near the chill zones and the less dense hotter melt at the centre. As the heavier liquid falls it creates flow along the solidification front towards the centre, carrying solute and crystal fragments with it. This is thermo-solutal convection (Eskin D. G., 2008) (Nadella, Eskin, Du, & Katgerman, 2008). The crystal fragments are carried beyond the columnar bands where they settle at the solid front and grow when their <110> orientation is closely aligned to the thermal gradient (Henry, Jarry, & Rappaz, 1998) (Henry, Gruen, & Rappaz, 2004). Forced convection through melt stirring is known to eliminate feather grain growth as is process parameter adjustment (reduction of secondary cooling water).

There are a number of reasons why the control of grain size and type is important in DC casting alloys (McCartney, 1989). First, reduced mechanical properties have been noted in plate products for structural applications when a uniform as cast grain structure is not achieved. In particular, feather grains have been reported to reduce fabricability, yield strength, and tensile elongation to failure due to their anisotropic nature. Second, a coarse grained structure may result in a variety of surface defects in alloys used in rolled or extruded form for architectural applications. Third, it is generally conceived that hot cracking in the shell zone of a DC ingot is more severe if the grain structure is not equiaxed, an equiaxed structure generally allows a higher casting rate to be achieved before hot cracking is encountered. In practice, the most common method of control of grain size and type is inoculation which is covered in the following section (McCartney, 1989).

2.1.1 CONTROL OF THE CAST STRUCTURE THROUGH PROCESS PARAMETERS

The key parameters that have the most influence on the structure of castings are casting speed, melt temperature and water flow rates (Emley, 1976). Casting speed is the rate at which the billet is withdrawn from the mould down into the pit. Water flow rate affects the cooling rate of the billet by controlling the rate of heat extraction. What needs to be understood is how the two variables interact with the sump profile within the solidifying billet and therefore the structure.

Increasing the casting speed increases the depth of the liquid pool, the distance between the liquidus and solidus isotherms and the mushy zone (specifically at the periphery of the billet and centre) (Nadella, Eskin, Du, & Katgerman, 2008). The solidification rate is directly related to the sump shape and depends on the casting speed by the following:

$$V_{sol} = V_{cast}\cos\varphi$$

where V_{sol} is the velocity of the solidification front, V_{cast} is the casting speed, φ is the angle between the billet axis and the normal to the solidification front (Eskin, Zuidema Jr, Savran, & Katgerman, 2004). The solidification rate is at its fastest in the centre and at the billet periphery. Eskin et al found that increases in casting speed refined the grain structure and reduced porosity, with the central region of the billet experiencing the biggest reductions (Eskin, Zuidema Jr, Savran, & Katgerman, 2004).

It was found that water flow rate fluctuations had far less of an impact on the structure (Eskin, Zuidema Jr, Savran, & Katgerman, 2004). It is generally accepted that an increase in the cooling rate results in finer grain size and a reduction in the secondary dendrite arm spacing (SDAS) (Mulazimoglu, Zaluska, Guzleski, & Paray, 1996) (Verma, Kumar, Grant, & O'Reilly, 2013). However, increasing the water flow rates has marginal effect upon the sump depth especially nearer the centre of the billet as the cooling rate decreases with distance from the surface. Structure refinement is experienced by an increased water flow rate but the results are not as strong as those associated with casting speed increase. This is especially true at high casting speeds when the effect of increased water flow is negligible (Eskin, Zuidema Jr, Savran, & Katgerman, 2004).

Melt temperature is a critical parameter to the soundness of a casting. Increasing the melt temperature raises the risk of bleed-outs through the surface as it increases the size of the liquid pool, deepening the sump and moving the liquidus isotherm downwards along the centerline. At the periphery the solidus isotherm is the one to react as it shifts downwards with an increase in the melt temperature. This moves the mushy zone lower in the mould with the possibility it could slip below the chill face of the mould, especially if the casting speed is maintained or increased, resulting in remelting of the surface and a bleed-out. Eskin *et al* found that increasing the melt temperature resulted in a general coarsening of the grain structure with increased size and SDAS (Eskin, Savran, & Katgerman, 2005). The effects were particularly acute in the centre and if the casting speed was decreased. Reduction of cooling rate and grain growth was attributed to this result. The raising of the melt temperature also reduces the amount of nuclei that survive and therefore the rate of nucleation.

2.2 REFINEMENT OF AS CAST STRUCTURE

2.2.1 GRAIN REFINEMENT THROUGH INOCULATION ADDITIONS

It is generally accepted that mechanical properties, surface appearance of anodized sections and decorative applications, uniform second phase distribution and subsequent machining benefit from a fine and homogeneous equiaxed grain structure (Maxwell & Hellawell, 1975) (Murty, Kori, & Chackraborty, 2002). The most efficient and cost effective method of ensuring a fine equiaxed grain structure is through inoculation, commonly referred to as grain refiner additions (Murty, Kori, & Chackraborty, 2002). Grain refinement of Al alloys also facilitates the casting process, reduces cast defects and, therefore, offers improved casting quality (Sigworth, 2008). It is typically an in-line treatment where aluminium rod is fed into the melt stream before it reaches the casting table, ensuring an even distribution of particles throughout the melt. The most widely used grain refiner for Al-alloys is the Al-5Ti-1B (all compositions are in wt.% unless otherwise specified) master alloy, which contains both the Al3Ti intermetallic compound and TiB2 particles in an aluminium matrix. The Al-5Ti-1B master alloy contains 2.8% excess Ti over the stoichiometric ratio of TiB_2 (i.e., Ti: B =2.2:1 in wt.%). The Al-5Ti-1B master alloy is

very effective for the grain refinement of most Al alloys with a nucleation undercooling of usually less than 1K (Murty, Kori, & Chackraborty, 2002). Since the introduction of Al-Ti-B based grain refiners over 60 years ago (Cibula, 1949) (Cibula, 1951), tremendous efforts have been made to understand the mechanism of grain refinement, which has been the subject of a number of review papers (McCartney, 1989) (Murty, Kori, & Chackraborty, 2002) (Quested, 2004). However, until now, there has been no consensus on the exact mechanism for grain refinement involving the addition of Al-Ti-B based grain refiners (Quested, 2004).

In the 1950's, the carbide-boride particle theory was first proposed by Cibula (Cibula, 1949) (Cibula, 1951). This theory proposed that insoluble TiB_2 particles in the melt acted as the heterogeneous nucleation sites. However, Mohanty *et al* observed that the borides are pushed to grain boundaries, and no grain refinement was observed in the absence of Ti solute (Mohanty & Gruzleski, 1995). This contradicted the carbide-boride particle theory. Similarly, AlB_2 particles (less stable than TiB_2 particles in the Al melt) do not act as heterogeneous nucleation sites (Jones & Pearson, 1976).

Parallel to the carbide-boride particle theory is the peritectic theory proposed by Crossley and Mondolfo (Crossley & Mondolfo, 1951) in the early 1950's. This theory conjectured that Al_3Ti, not TiB_2, nucleated □-Al via the peritectic reaction. There were experimental observations that appeared to support the peritectic theory. For example, Marcantonio and Mondolfo (Marcantonio & Mondolfo, 1970) and Maxwell and Hellawell (Maxwell & Hellawell, 1975) showed that the nucleation of □-Al required a smaller undercooling in the presence of Al3Ti compared with TiB2, indicating that Al3Ti is a more potent nucleant than TiB2. Davies et al observed Al3Ti at the centres of the grains and suggested that Al3Ti may be the nucleant (Davies, Dennis, & Hellawell, 1970). However, during the grain refinement of Al-alloys using Al-Ti-B master alloys, the amount of free Ti added to the melt via the master alloy is usually less than 0.01%, which is much lower than the Ti level required for peritectic reaction (0.15%). Therefore, Al_3Ti is not thermodynamically stable for the hypoperitectic case. For example, Johnsson indicated that the aluminides probably take less than 1 minute, but definitely less than 5 minutes to dissolve at a holding temperature of 775 ^{o}C (Johnsson, 1993). Jones and Pearson suggested that all aluminides dissolved in molten Al in less than 30 seconds (Jones & Pearson, 1976). Although the dissolution time depends on both the holding temperature and the size

of the Al_3Ti particles, the resulting consensus is that Al_3Ti dissolves rapidly above the Al liquidus and, hence, the peritectic reaction is not thermodynamically feasible.

For Al_3Ti to be responsible for grain refinement during solidification of hypoperitectic alloys, other factors have to be operational. Vader *et al* and Backerud *et al* proposed the peritectic hulk theory in the early 1990's (Vader, Noordegraaf, & van Wiggen, 1991) (Backerud, Gustafson, & Johnsson, 1991). This theory recognized that Al_3Ti is a more potent nucleant than the TiB_2 and attempted to explain how the borides increase the stability of aluminides. It was suggested that the borides form a shell around the aluminides, and slow down dissolution of the aluminides. The aluminides eventually dissolve and leave a cell of liquid with approximately the peritectic composition. The peritectic reaction can then take place to form the □-Al. In addition, Marcantonio and Mondolfo suggested that boron additions could change the phase diagram considerably, so that Al_3Ti could be stable even at lower concentration (Marcantonio & Mondolfo, 1971). However, a number of researchers investigated the Al-rich corner of the Al-Ti-B phase diagram and showed that boron had virtually no effect on the Al-Ti phase diagram (Jones & Pearson, 1976) (Sigworth, 1984). Therefore, the nucleation process cannot be explained purely based on theories which attempt to modify the conditions for the peritectic reaction to occur.

Both TiB_2 and Al_3Ti have been observed within individual Al grains (Mohanty & Gruzleski, 1995). It has been generally recognized that both can act as nucleation sites for Al (Kumar, Murty, & Chakraborty, 2010), although Al_3Ti is more potent than TiB_2. It is also known that incorporating a small amount of excess Ti (less than 0.15%) in the melt can cause a drastic reduction of grain size compared with the grain refining using solely TiB_2 (Quested, 2004) (Cibula, 1949) (Cibula, 1951). Subsequently, the necessity for both TiB_2 and the small amount of excess Ti has led to other theoretical developments.

The hypernucleation theory was proposed by Jones (Jones G. , 1987), who suggested that Ti atoms in the melt segregated to the melt/TiB_2 interface and, subsequently, promoted the formation of a pseudo-crystal with a structure similar to that of □-Al phase. This pseudo-crystal would be stable at temperatures above Al liquidus and could grow at temperatures below the liquidus, thus requiring little or no nucleation undercooling. Since this theory was proposed, the stability of the pseudo-

crystal above the Al liquidus has become the main focus of debate because it appears to violate the principles of thermodynamics. However, the recent HRTEM study of liquid Xe/□-Al (Donnelly, et al., 2002) and liquid Al/□-Al_2O_3 (Oh, Kauffmann, Scheu, Kaplan, & Rühle, 2005) interfaces and molecular dynamic simulation (Men & Fan, 2014) have shown that there is considerable atomic ordering at the liquid/substrate interface, providing both experimental and theoretical support for the existence of pseudo-crystals at the liquid/substrate interface.

The duplex nucleation theory was proposed by Mohanty and Gruzleski (Mohanty & Gruzleski, 1995), who suggested that Ti segregation to the melt/TiB_2 interface can reach such a level that the formation of Al_3Ti would be favoured, implying that the Ti content in the melt close to the interface would exceed 0.15% to allow the peritectic reaction to take place. However, this concept was dismissed by Sigworth (Sigworth, 1996) based on thermodynamic argument. In order to verify the duplex nucleation theory, Schumacher et al (Schumacher, et al., 1998) (Schumacher & Greer, 1994) used a melt spinning technique to produce amorphous Al85Y8Ni5Co2 alloy ribbons containing TiB_2 particles. They observed that a thin crystalline phase of 3 nm thickness with a lattice spacing close to that of Al_3Ti phase existed between TiB_2 and the amorphous Al. However, it was difficult to precisely identify the Al_3Ti phase. It is possible that the observed 3 nm crystal layer on the TiB_2 surface is □-Al formed in the solid state since the amorphous Al85Y8Ni5Co2 alloy is highly metastable and crystallization may take place in the solid state.

The solute theory suggested that both the nucleating particles and the solute elements in the alloy melt were important factors affecting grain refinement (Johnsson, Backrud, & Sigworth, 1993). The effect of solute elements on heterogeneous nucleation was taken into account through their effect on growth restriction to allow more nucleating substrates to be active before recalescence (Easton & StJohn, 1999). Easton and StJohn proposed a semi-empirical model based on the constitutional undercooling theory (Easton & StJohn, 1999) (Easton & StJohn, 2001). Their analysis showed that grain size can be related closely to the growth restriction factor. In such an approach, the grain refinement due to the increased solute contents was explained by the increased nucleation events through delayed recalescence (Easton & StJohn, 2001) (Men & Fan, 2011). Further development along this direction has seen a more analytical approach to the solute

effect (Easton & StJohn, 2005) (Qian, Cao, Easton, McDonald, & StJohn, 2010) and the postulation of the interdependence theory by StJohn et al (StJohn, Qian, Easton, & Cao, 2011). They proposed that grain formation was the result of repeated cycles of growth and nucleation events moving towards the thermal centre of the casting. However, it is likely that the solute theory and its extension may have over-estimated the effect of solute on grain refinement. Recently, Du and Li (Du & Li, 2014) extended the Kampmann–Wagner numerical model (Wagner & Kampmann, 1991) for solid state precipitation to predict grain size in solidified multicomponent alloys. Their simulation results showed that the solute suppressed nucleation (SSN) effect has a negligible influence on the nucleation behaviour and the final grain size during isothermal melt solidification.

Most recently, Fan and co-workers present experimental evidence for the existence of an atomic monolayer of (112) Al_3Ti 2-dimensional compound (2DC) on the (0001) TiB2 surface of commercial Al-Ti-B based grain refiners (Fan, et al., 2015). They demonstrate experimentally that the Al_3Ti 2DC forms at the liquid Al/TiB_2 interface in concentrated Al-Ti solutions, but dissolves in dilute Al-Ti solutions, although the kinetics of both formation and dissolution of Al_3Ti 2DC are relatively sluggish. The effective grain refinement of Al-5Ti-1B grain refiner can be attributed to the enhanced potency of TiB_2 particles with the Al_3Ti 2DC monolayer in place and adequate free Ti solute in the melt after grain refiner addition to achieve the columnar-to-equiaxed transition.

2.2.2 GRAIN REFINEMENT THROUGH PHYSICAL FIELDS IMPOSED

As stated in previous section, Al-Ti-B master alloys as grain refiners are commonly added to melts for the DC casting production of wrought aluminium alloys. However, only 1% of the added TiB_2 particles successfully nucleate aluminium grains and this low efficiency is undesirable not only for its immediate cost implications, but also because refiner particles (TiB_2) may themselves be detrimental in the final microstructures (Greer, 2003) particularly for products intended for extrusion, deep drawing, or high performance structural applications, in particular, for those surface finish critical products.

Alternatively, another mechanism responsible for the grain refinement can be the enhanced nucleation upon the fragments of crystals inherent to cast structures. These crystal fragments are of the base material themselves and as such have a perfect lattice match resulting in low energy requirements for nucleation. Fragmentation occurs by growth fluctuations resulting from convection (thermal-solutal) or forced flows induced by mechanical means (Nadella, Eskin, Du, & Katgerman, 2008) (Hellwell, Liu, & Lu, 1997) (Paradies, Smith, & Glicksman, 1997) (Eskin G. I., 1994). Thermal-solutal convection occurs because of density differences arising from temperature and composition inhomogeneity. Cooler liquid at the periphery of the mould is denser than at the centre so it sinks forcing liquid in the centre to rise (Nadella, Eskin, Du, & Katgerman, 2008). Solute concentrations rise upon freezing creating density differences due to compositional increases. These are naturally occurring forces and have been covered previously regarding solidification in DC casting. Natural convection is seen as the mechanism for transportation of solute and crystals fragments ahead of the columnar front, providing the constitutionally undercooled zone and nuclei for equiaxed growth respectively. Unfortunately, the typical process parameter settings do not contribute to the fragmenting of the dendrites sufficiently to induce a fully fine equiaxed grain structure without grain refiner additions. Either coarse columnar dendritic grains or feather grains are the natural outcome in this situation.

However, forced convection has been known to augment the thermal-solutal convective flows and subsequent fragmentation. Emley states that feather grains can be stopped by grain refiner additions or by stirring of the melt (Emley, 1976). The mechanism that is most widely accepted is the variation in thermal-solutal concentrations at the interface, which causes remelting of the dendrite arms at the neck due to growth fluctuations (Jackson, Hunt, Uhlmann, & Seward III, 1966) (Campanella, Charbon, & Rappaz, 2004). Jackson et al proposed the theory of the dendrite side branches constitutionally remelting in the ‘60s due to solute fluctuations around the growing dendrite (Jackson, Hunt, Uhlmann, & Seward III, 1966). Growth is stronger at the dendrite tip as it grows into the solute depleted bulk melt compared with the solute rich liquid at the neck of the dendrite. Melting temperature in this solute rich region becomes lower than that of the melt temperature causing remelting of the neck and the dendrite arm is removed and transported to the bulk liquid by

convective flows. The growth fluctuations are therefore due to the thermal-solutal fluctuations created by driving the melt through the slurry region of a cast and across the mushy zone. It is not so much that the melt temperature will be hotter than the melting point, but the melt that sweeps across the solidification front would at first be hot and replaced by colder melt (Jackson, Hunt, Uhlmann, & Seward III, 1966). This causes growth rate changes so the growth front is moving backwards and forwards within an isotherm due to the temperature gradient. The same effect happens with solute concentration. Rejected solute from the interface is swept away by the flow streams towards the centre, creating periods of low solute levels and then high concentration periods. This results in the growth rate speeding up and decreasing respectively, causing melting of the dendrite arms which are then swept into the slurry or transition region of the sump.

Forced flows also contribute to the survival of the crystal fragments by extending the constitutionally supercooled zone ahead of the interface as it carries solute to the central region of the billet. Jackson *et al* related the formation of a fully equiaxed zone to the ability of the crystal fragments reaching the centre of the casting as quickly as possible in order to survive (Jackson, Hunt, Uhlmann, & Seward III, 1966). Now they are ahead of the dendritic interface where they begin to block its growth in the constitutionally undercooled layer in front of it. Jackson *et al* then applied the theory to continuously cast aluminum with good agreement between the observed refinement due to stirring of the melt and the remelting theory (Jackson, Hunt, Uhlmann, & Seward III, 1966).

Remelting of the dendrite arms seems to be the mechanism that closely agrees with experimental observations. Jackson *et al* and Paradies *et al* both found that there was significant delay between the beginning of stirring and the onset of fragmentation (Jackson, Hunt, Uhlmann, & Seward III, 1966) (Paradies, Smith, & Glicksman, 1997). If fracturing was the mechanism, then it is logical to consider fragmentation to be relatively instantaneous. However, the mechanical effects of forced convection upon the fragmentation of crystals cannot be fully ignored.

In addition to the understanding of the nucleation mechanisms under convective flow, few studies have been devoted to the morphological evolution of grains under convective melt flow. A stability analysis by Vogel and Cantor concluded that

shearing destabilizes the solid–liquid interface and promotes dendritic growth contrary to the experimental observation (Vogel & Cantor, 1977). Observed microstructural features were consequently attributed to dendrite fragmentation due to intense shearing of the melt (Doherty, Lee, & Feest, 1984). Later theoretical work by Mullis shows that dendritic arm bending due to shearing the liquid might promote rosette type morphology (Mullis, 1999). Fan and co-workers studied systematically the morphological development of solidification structures under forced fluid flow by using a Monte-Carlo simulation (Das, Ji, & Fan, 2002). The model takes into account both diffusive and forced fluid flow, kinetics of atomic attachment at the solid–liquid interface and structural modification under the influence of capillary forces. It has been shown that the nature of fluid flow has a very significant influence on the morphology of the solidification structure. A laminar type flow is shown to destabilize the solid–liquid interface promoting dendritic growth for solid growing from a fixed substrate. Particle rotation under streamlined flow, or a periodic change in the fluid flow direction around the growing solid, however, has been shown to produce the rosette type solidification morphology. A turbulent type flow penetrating into the interdendritic region produces fine and compact solidification structures with or without liquid entrapment (Das, Ji, & Fan, 2002). Ji and Fan experimentally investigated the influence of intensive melt shearing on the morphological evolution in a Sn-15 wt pct Pb alloy system (Ji & Fan, 2002). It was found that forced convection increases the growth velocity and stabilizes the solidification interface, resulting in a transition of the growth morphology from rosette to spheroid type with increasing shear rate and intensity of turbulence. (Ji & Fan, 2002).

There are two types of main existing technologies that have been studied as a means of enhancing convections during casting, (1) ultrasonic treatment (UST) (Zhang, Le, & Cui, 2010) (Zhang, Eskin, & Katgerman, 2011); (2) electromagnetic processing (EPM) such as electromagnetic stirring (EMS) (Getselev, Kvasov, Cherepok, Varga, & Martynov, 1983) (Charles, 1989) (Charles, 1989) (Campanella, Charbon, & Rappaz, 2004) (Tang, Xu, Zhang, & Bai, 2010) and electromagnetic vibration (Charles, 1993).

Ultrasonic melt treatment (UST) introduces acoustic waves into a liquid melt at a frequency >17 kHz. Cavitation is generated by high frequency oscillations within the melt the causes intense mixing of the melt. Fragmentation and transport of the

crystals has been observed as a result with enhanced nucleation through local undercooling and wetting of primary intermetallics (Campanella, Charbon, & Rappaz, 2004). Eskin found that cavitation due to ultrasonic treatment created bubbles that formed on the aluminium-hydrogen-Al_2O_3 interface, wetting the impurities to such a degree that they become nuclei (Zhang, Eskin, & Katgerman, 2011). The cavitation bubbles form and then collapse rapidly creating more bubbles in a cyclic manner. The force of the bubbles collapsing sends a hydraulic pulse of 500 – 1000 MPa which forces matrix melt into cracks and fissures that are present on the oxide surface. This turns the oxides into wettable potent nucleation sites.

Electromagnetic stirring (EMS) is different from ultrasonic treatment, mechanical stirring techniques and shearing, because instead of inserting something into the melt to increase the forced convection, EMS is effectively a mouldless casting system. The immediate benefit of this system is the removal of the primary cooling as the melt is contained within a magnetic field as water - equivalent to that of secondary cooling on normal DC units – which cools the billet. This creates an extremely smooth surface with reduced segregation. The EMS process stirs the melt by eddy currents created in the electromagnetic field that once optimized can alter the flow patterns, homogenizing the melt chemistry within the (shallow) sump and refines the grain structure. The mechanism is similar to that of other stirring techniques in so far that dendrite fragmentation occurs due to forced flow and growth fluctuations, which act as heterogeneous nucleation sites ahead of the solidification front, after being transported there by the flow streams.

Extensive efforts have been devoted to the grain refinement by either chemical inoculants addition or physical field imposition. However, very little information has been reported in the literature on the correlation between grain refinement, which focuses on the refining of grain size, and the grain structural parameters, such as secondary dendritic arm spacing (SDAS), which is, in effect, more important for the distribution of intermetallic particles, which are formed in the late stages of solidification through eutectic or peritectic reactions (Easton, Davidson, & StJohn, 2011). Both the grain size and the SDAS are affected by alloy composition and cooling rate through constitutional undercooling (CU) parameters. The major difference is that the grain size is affected by the constitutional conditions as solidification begins, whilst the SDAS is more affected by the CU generated by the

liquid remaining near the end of solidification (Easton, Davidson, & StJohn, 2011). It is suggested that the ratio of grain size to SDAS can be used to define the grain morphology. At ratios less than two the grain morphology is spherical or globular, between 2 and 4 it is rosette-like or cellular and above 4 it is equiaxed dendritic (Easton, Davidson, & StJohn, 2011). The formation of different grain morphology in relation to the distribution of intermetallics will be part of the subject investigated in the present study.

2.2.3 GRAIN REFINEMENT THROUGH INTENSIVE MELT SHEARING

Intensive melt shearing (IMS) is a novel emerging technology of treating a liquid melt before it is processed in either DC casting, twin roll casting (TRC) or high pressure die casting (HPDC) systems (Jones, Prasada Rao, & Fan, 2013). The IMS system has evolved since its conception from the twin screw MCAST equipment (PCT Patent, Patent No. WO 01/21343 A1, 1999) to a far simpler rotor and stator unit (Patent No. WO2012035357 A1, 2012). The MCAST system consists of twin intermeshing, self-wiping screws inside a close fitting barrel heated to the liquidus of the metal being treated. Melt was fed into the barrel and extruded along the screws with extremely high shear rates. Good results were seen in aluminium, magnesium and zinc-aluminium alloys with appreciably improved structures compared to other methods of refinement (Fan & Liu, 2005) (Fan, Wang, Xia, & Arumuganathar, 2009) (Men, Jiang, & Fan, 2010) (Li, Wang, & Fan, 2012). Nucleation on $MgO/MgAl_2O_4$ oxide particles of □-Mg/□-Al phases after they have been dispersed into individual nuclei and distributed uniformly throughout a melt, significantly increasing the number density of active nucleating particles and thus refining the grain structure, has been evidenced as the grain refining mechanism in an AZ91 alloy and in Al-Mg binary alloys by Fan *et al.* (Fan, Wang, Xia, & Arumuganathar, 2009) (Men, Jiang, & Fan, 2010), (Wang, Fan, Zhou, & Thompson, 2011) (Zuo, et al., 2011) (Li, Xia, Jarry, Scamans, & Fan, 2011) (Li, Wang, & Fan, 2012). The effect of melt conditioning by the MCAST system was established as follows: (1) to homogenize the temperature and compositional fields in the bulk melt, (2) enhance heterogeneous nucleation by dispersion of naturally occurring oxides in the alloy melt, (3) reduce the thickness of the solute diffusion boundary layer at the solid/liquid interface, (4) significantly reduce the constitutionally undercooled zone, and (5) stabilize the solid/liquid interface.

A schematic of the IMS device of the rotor-stator mechanism is shown in Figure 2.2. It consists of a four-blade ceramic rotor in a ceramic stator driven by a motor at the top of the shaft. Intensive melt shearing is generated by ensuring a tight gap between the rotor and stator; providing a high shear rate or 10^5/s when the rotor is spinning at its highest operating speed of 15,000 rpm.

A large vortex is created below the device which sucks melt from the vicinity of the solidification front up into the device where it is sheared as described. This sheared

melt is jettisoned out of the device via a series of 2.5 mm diameter holes around the stator as shown in Figure 2.3. This creates areas of high turbulence below and within the shear device and as the melt exits through the holes. The IMS device is submerged below the surface of the liquid into the DC cast mould assembly so its treats the reservoir of melt directly during the solidification process. It is applied to DC casting (referred to as the melt conditioned direct chill casting: MC-DC process) as shown in Figure 2.4. Laminar flow streams form within the melt reservoir of the DC mould as a result.

Application of intensive melt shearing in the DC casting has the following effects:

- The dispersive mixing action will disperse inclusions and oxide films in the melt into fine and individual particles (usually on nano-scale), reducing/eliminating their usual harmful effects on the casting processes and quality of castings.
- The distributive mixing action will ensure the melt in the sump has a uniform temperature (a few degrees below/above the alloy liquidus), homogeneous chemical composition and well dispersed and uniformly distributed heterogeneous nucleation sites.
- The interaction between the macroscopic melt flow, i.e., the laminar flow paths as shown in Figure 2.3 and the solidification front provides a flatter and shallower sump profile and the potential for increased casting speed (Jones, Prasada Rao, & Fan, 2013) (Xia, Prasada Rao, & Fan, 2013) (Patel, et al., 2014).

Figure 2.3 Schematic of the shearing device stator with a cut away showing part of the four blade rotor. The device is inserted as shown into the mould of a DC caster creating the MC-DC process. A motor above spins the rotor inside the stator operating at speeds in the region of 3000 – 7000 rpm. Liquid is forced through the 2.5 mm diameter holes to be dispersed throughout the melt inside the mould.

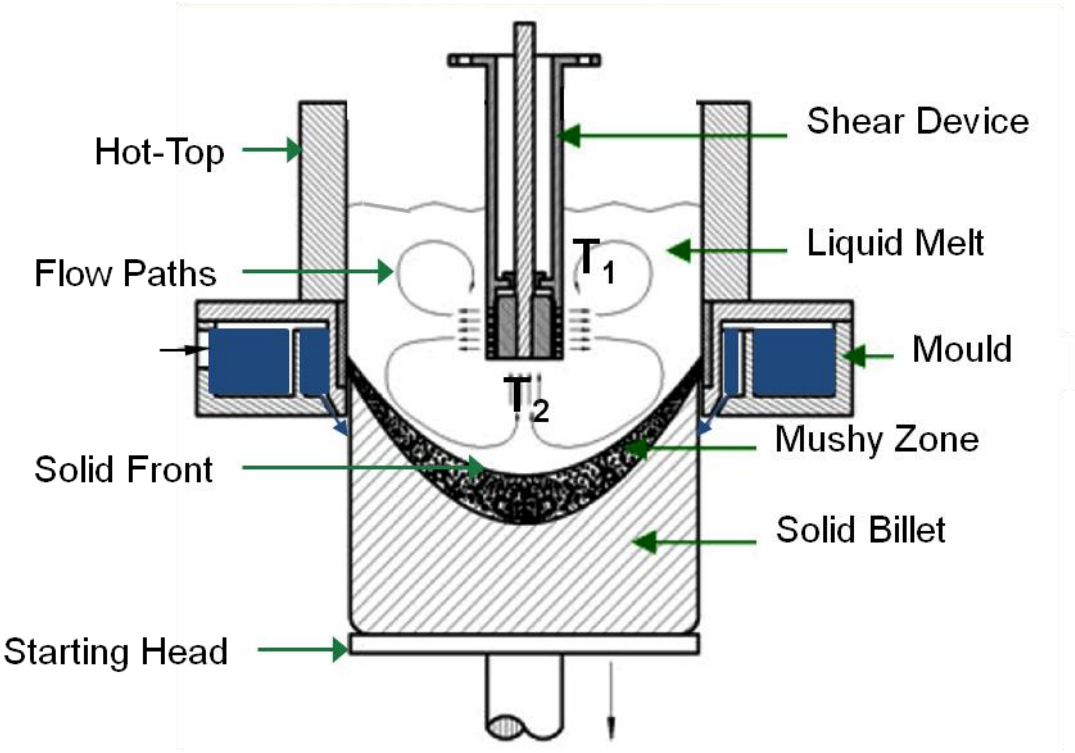

Figure 2.4 Diagram of the MC-DC process. The shear unit is submerged in the liquid pool of the sump inside the DC mould. The flow streams generated by melt conditioning are shown. Note how flow streams exist above the line of holes as well as below. T1 and T2 indicate thermocouple locations that monitor temperatures during operation.

Mechanisms for the refinement of grain structure by intensive melt shearing are:

1. Grain refinement through inoculation upon individual oxide particles (Fan, Wang, Xia, & Arumuganathar, 2009) (Wang, Fan, Zhou, & Thompson, 2011) (Li, Wang, & Fan, 2012) (Li, Xia, Jarry, Scamans, & Fan, 2011) (Zuo, et al., 2011). The shearing action of the device sufficiently breaks down and disperses the naturally forming oxides that are present in aluminium alloy melts. Therefore, intensive melt shearing (IMS) is believed to enhance heterogeneous nucleation in the sump of a DC billet through nuclei dispersion.
2. Promotes equiaxed growth through homogenisation of temperature and constitutional fields within the sump, ensuring the survival of newly created nuclei transported there. The melt within the sump has been shown to be held at around the liquidus temperature during shearing

(Xia, Prasada Rao, & Fan, 2013) (Patel, et al., 2014) providing a unique low thermal gradient, high growth conditions which contribute to the columnar to equiaxed transition (CET) as reported by Hunt (Hunt, 1984). In conventional DC casting, solidification proceeds by an advancing equiaxed (or columnar) dendritic front through a relatively narrow mushy zone delineated and bounded by the isothermal liquidus and solidus (Figure 2.5a). Both nucleation and dendritic growth occur in the mushy zone. The sump has a positive temperature gradient from the bottom to the top. In contrast, solidification in the MC-DC casting process proceeds by sedimentation of rosettes/equiaxed dendrites which nucleate and predominately grow in the sump with an almost isothermal temperature under the severe convective melt flow (Figure 2.5b) (Xia, Prasada Rao, & Fan, 2013).

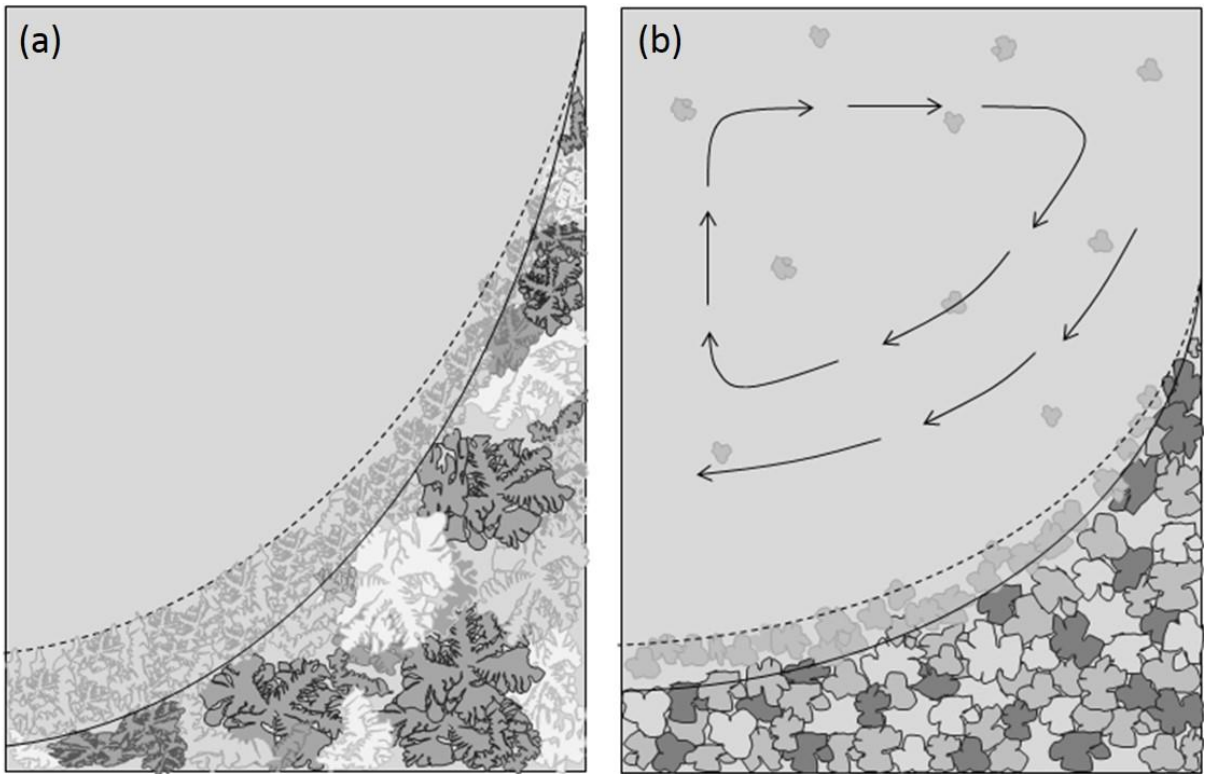

Figure 2.5 Sketch illustrates the solidification mechanism during DC (a) and (b) MC-DC casting (Xia, Prasada Rao, & Fan, 2013)

2.3 MACROSEGREGATION, GRAIN STRUCTURE AND DC CASTING PROCESS PARAMETERS

Macrosegregation, which is the non-uniform chemical composition over the length scale of a casting, is one of the major defects that occur during DC casting process (Flemings, 1974). This non-uniformity of species distribution, especially when it forms a high composition gradient or a poor distribution of secondary phases, can lead to a non-uniform distribution of mechanical properties and contribute to cracking during extrusion or forging of wrought alloys (Coangelo & Heiser, 1987). The fact that macrosegregation is essentially unaffected by subsequent heat treatment (hence constitutes an irreversible defect) leaves us with little choice but to control it during the casting stage (Vreeman, Schloz, & Krane, 2002) (Eskin, Zuidema Jr, Savran, & Katgerman, 2004) (Nadella, Eskin, Du, & Katgerman, 2008).

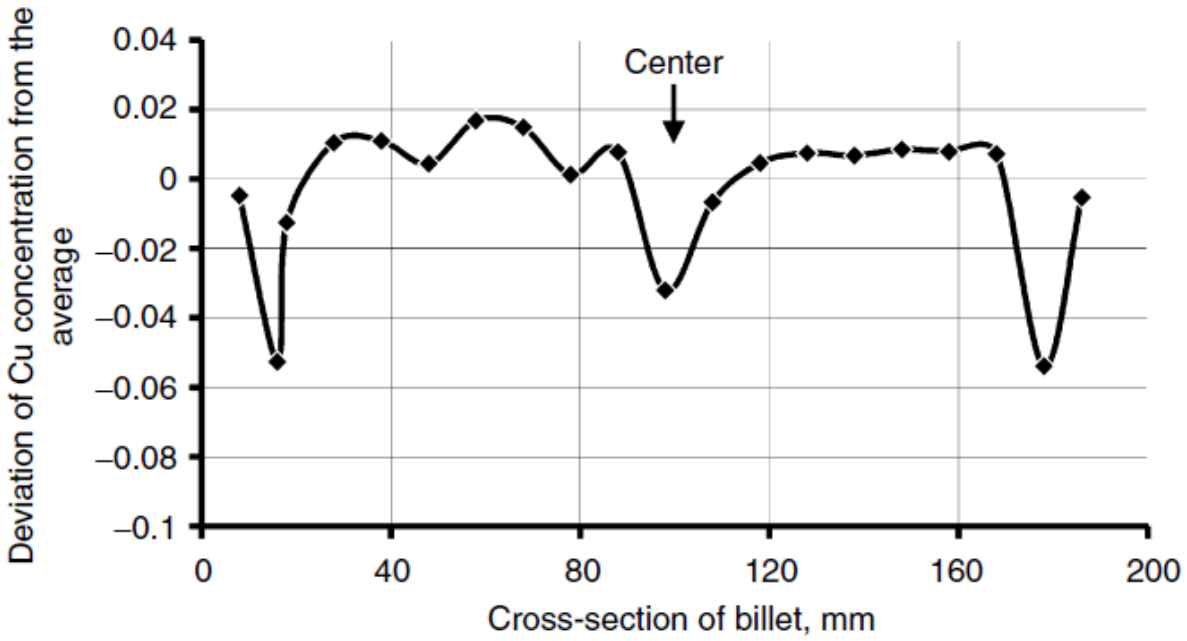

Figure 2.6 A typical pattern of macrosegregation in a 200-mm billet of an Al–4.2% Cu alloy cast at 120 mm/min. Note the negative segregation in the centre, positive at the surface, and a heavily depleted subsurface layer (Eskin D. G., 2008).

A commonly observed, surface to surface distribution of alloying elements at a transverse cross-section of a DC cast ingot reveals distinct regions of positive (solute rich) and negative (solute depleted) segregation (Yu & Granger, 1986). Figure 2.6 shows a typical pattern of macrosegregation in a 200-mm billet of an Al–4.2% Cu

alloy cast at 120 mm/min. Note the negative segregation in the center, positive at the surface, and a heavily depleted subsurface layer (Eskin D. G., 2008). Enrichment near the ingot surface is attributed to a combination of shrinkage induced flow of solute-rich liquid toward the surface and exudation induced by local remelting of the billet surface as the solid shell pulls away from the mould and the melt flow driven by the metallostatic pressure imposed by the melt head (Vreeman, Schloz, & Krane, 2002) (Mo, 1993).

Extensive studies have offered some insight into the mechanisms that control the negative macrosegregation at the centreline (Vreeman, Schloz, & Krane, 2002) (Nadella, Eskin, Du, & Katgerman, 2008). The current understanding of the macrosegregation mechanisms can be formulated rather simply: relative movement of liquid and solid phases during solidification in the presence of solute partitioning (microsegregation) (Nadella, Eskin, Du, & Katgerman, 2008) (Zaloznik, et al., 2011). On a phenomenological level, we can single out several types of such a relative movement that happens in the sump of a billet during DC casting: thermo-solutal convection in the liquid sump caused by temperature and concentration gradients, and the penetration of this convective flow into the slurry and mushy zones of a billet; transport of solid grains within the slurry zone by gravity and buoyancy forces, convective or forced flows; forced melt flow caused by pouring, gas evolution, stirring, vibration, cavitation, rotation, etc., which penetrates into the slurry and mushy zones of a billet or changes the direction of convective flows (Nadella, Eskin, Du, & Katgerman, 2008).

It is understood that the mass feeding stage can be extended by decreasing grain size, the limit being reached in the semi-solid forming process in which a fine non-dendritic grain size is obtained (Flemings, 1991); in this case homogeneous two phase (solid plus liquid) flow can be obtained at solid contents over 50%. Thus, improved mass feeding may be the main reasons why increasing the amount of equiaxed structure and decreasing grain size by grain refiner additions reduce macrosegregation (Flemings, 2000). However, grain refiner additions also promote the formation of free-floating coarse (slowly growing) grains (Zaloznik, et al., 2011). In non-grain-refined ingots free-floating grains either may not form or form in lower quantity by fragmentation. First attempts to include the influence of free-floating grains were made by Reddy and Beckerman (Reddy & Beckermann, 1995). To

further understand the mechanisms of macrosegregation by modelling the transport phenomena which control the segregation in DC casting, Vreeman *et al.* developed a fully coupled, single-domain, mixture model of the DC casting process which accounted for the transport of free-floating dendrites (Vreeman, Krane, & Incropera, 2000) (Vreeman & Incropera, 2000) (Vreeman, Schloz, & Krane, 2002). The model was used to predict macrosegregation distributions in Al-4.5 wt% Cu and Al-6.0 wt% Mg billets and the predicted surface-to-centerline distribution of macrosegregation was found to be consistent with observations in DC cast ingots discussed above. Negative segregation at the center of the billets develops as solute-depleted dendrites are advected along the interface of the rigid, mushy zone and settle near the centerline to form a uniformly packed region at the bottom of the sump, which increased with an increase in the packing fraction at which free-floating dendrites are presumed to coalesce into a rigid dendritic structure. As the free-floating dendrites settle near the centerline, the surrounding solute-rich liquid is displaced upward and experiences recirculation toward the surface of the billet and down into the interface of the rigid, mushy zone, establishing the region of positive segregation commonly observed in DC cast ingots (Vreeman & Incropera, 2000).

It has also been pointed out that grain morphology is an important factor to be considered to understand the mechanisms of macrosegregation (Lesoult, et al., 2001) (Joly, Grun, Daloz, & Lesoult, 2000). Lesoult et al. reported that grain refining caused more servere centreline segregation in a DC cast Al-4.75wt%Mg-0.35wt%Mn alloy sheet ingot. In their case, it was more dendritic in non-grain-refined ingot with less severe segregation; whist the grain was more globular in the grain refined ingot, with more severe centreline segregation (Lesoult, et al., 2001) (Joly, Grun, Daloz, & Lesoult, 2000). It has also been pointed out that grain morphology is an important factor to be considered to understand the mechanisms of macrosegregation (Lesoult, et al., 2001) (Joly, Grun, Daloz, & Lesoult, 2000). Lesoult et al. reported that grain refining caused more servere centreline segregation in a DC cast Al-4.75wt%Mg-0.35wt%Mn alloy sheet ingot. In their case, it was more dendritic in non-grain-refined ingot with less severe segregation; whist the grain was more globular in the grain refined ingot, with more severe centreline segregation (Lesoult, et al., 2001) (Joly, Grun, Daloz, & Lesoult, 2000). In contrast to the above observation, there is a study, which shows that grain refining results in positive centreline segregation (Finn, Chu,

& Bennon, 1992) (Nadella, Eskin, Du, & Katgerman, 2008). Finn et al. showed that grain refining with Al5Ti0.2B produced positive centreline segregation in 530-mm billets of an Al-4,5% Cu alloy; whilst the non-grain-refined counterpart exhibited the usual pattern of negative centreline segregation. It was proposed that the high permeability in the mushy zone with the addition of grain refiners, allowed advection of solute-rich liquid toward the centreline, thus changed the centreline segregation pattern (Finn, Chu, & Bennon, 1992).

Although numerous efforts have been devoted to the understanding the formation mechanisms of macrosegregation in DC casting, few approaches to implementing alleviated macrosegregation in DC casting have been reported in the open literature. It was reported that the application of a low frequency electromagnetic field during hot top DC casting can alleviate surface segregation (Zhang, Cui, & Lu, 2003). Frequency greatly influences solute concentration over the cross-section of ingot. Under a proper frequency, surface exudation and large-scale inverse segregation can be reduced effectively, which allows substantial savings on scalping operation (Zhang, Cui, & Lu, 2003).

In the current study, by introducing intensive melt shearing in the sump during DC-casting, in addition to the grain refinement achieved as reported in previous studies (Patel, et al., 2014) (Xia, Prasada Rao, & Fan, 2013), the flow patterns in the sump can be manipulated in such a way that the morphology/structures of the refined grains can be selected. This offers an opportunity to investigate the effect of melt conditioning on the formation of macrosegregation in DC casting, aiming at an alleviated macrosegregation.

CHAPTER 3 - EXPERIMENTAL PROCEDURE

The aim of this study was to investigate the effect of the high shear technology on the Direct Chill (DC) cast aluminium billet, focussing on reduced macrosegregation and grain refinement without deliberate additions of chemical grain refiners. The casting experiments in this work ranged from lab based DC to industrial scale DC but whilst the scale increased and thus the size of the mould, melt volume and size of log cast, the concept and process has always strived to be comparable to that of industry. Extrusion trials with mechanical testing of the profiles was planned in the original outline of this work, but unfortunately due to equipment issues and time constraints this was not achieved. However, it is outlined in the future work section of this work and casting trials to produce billet for extrusion will have been completed by the time this project completes.

The first experiments were performed in a static mould in the BCAST lab which consisted of a steel mould on a copper chill block, to simulate a flat solidification front (similar to directional solidification experiment) that travels towards the shear device which was held at a fixed position. Thus, over the course of the experiment, the distance between the shear device and solidification front reduced, increasing the intensity of the conditioning effect over the length of the billet. The second series of experiments utilised the DC unit at BCAST laboratory. This was the first time that MC-DC was achieved in practice, enabling direct comparison with industrial processes. Varying of the casting speed and device depth in relation to the mould allowed investigation in to the effect of shearing upon casting process changes. A third series of experiments were carried out on the Oxford Begbroke Science Park industrial scale DC unit. On this unit, investigation into the effect of varying rotational speeds upon the cast structure at different shear tool depths at an industrially comparable level, were carried out.

The casting methods and processes for each series of experiments will be addressed separately and described individually over this chapter, however the shear device remained the same throughout thus it will be described first as a point of reference.

3.1 THE SHEARING DEVICE

The shearing device is shown in Figure 2.3. It consists of a ceramic stator and rotor assembled as shown. The external diameter of the stator is 40 mm with a length of 200 mm originally that was extended to 400 mm for reasons outlined over the following sections. There is a very close fitting tolerance of the rotor and internal walls of the stator (< 0.25 mm) ensuring a high rate of shear during operation. Rotational speed of the rotor when inserted into the melt was controllable from 500 rpm to 7000 rpm but, typical operational speeds ranged from 3000 rpm up to the maximum permitted by the equipment.

For each experiment, the device was inserted into the melt after it had either been poured into the mould in the case of the static experiments, or steady state had been achieved in the case of the DC experiments. Before being inserted into the melt, the device was preheated to 700ºC, protecting it from thermal shock and reducing the amount of heat it could remove from the melt. After use, the device is extracted before the end of the cast and wrapped in Fibrefrax to ensure the thermal shock is kept to a minimum, prolonging the life of the tool. It must be noted here that the rotor is never spun when the device is dry or not in any type of liquid, be it water or melt, as the liquid acts as a lubricant to the device.

A motor drives the rotor which is attached at the top of the shaft. Both stator and rotor are supported by the motor above the melt, thus it is the motor that is lowered on its shaft when the device is being inserted into the melt. Care is taken to make sure the surface of the melt is clear of oxide films before insertion of the tool, ensuring that oxides are not added to the billet becoming inclusions that lead to problems down-stream; oxides could block the holes or cause a failure of the device if they become stuck between the rotor and stator.

3.2 STATIC MOULD EXPERIMENT

Static mould experiments were the first step along the path of this investigation. Before the investigation moved to the DC units, preliminary investigations into the

types of microstructure achievable when shearing was applied to a melt had to be established. The aim of these experiments was to shear the melt in its liquid and semi-solid states to physically refine the structure without the aid of additions such as titanium (Ti). The experiments were designed to hold the liquid at a temperature above the liquidus of the primary α-Al phase to allow melt conditioning of the liquid to occur. As the temperature reduced semi-solid melt formed and was in-turn sheared. Thus the effect of shearing upon the solidifying structure could be studied.

The apparatus was set up as shown in Figure 3.1. The mould consisted of a steel cylinder 60 mm in diameter with a 6mm thick wall and a slight taper to aid billet removal, wrapped in 6 mm thick fibrefrax felt and placed on a 50 mm thick copper block used for the chill face. The mould was preheated in the oven with the melt to 750 ºC whilst the copper block was at room temperature. The preheating of the mould ensured that the melt didn't cool too quickly thus solidifying before the shear device could be inserted, whilst the felt blanket kept the heat from dissipating rapidly, thus allowing shearing of the liquid state. Whilst the melt was conditioned, a thermocouple positioned 5 mm from the base of the shear device monitored the temperature. At 655 ºC the shear device was extracted from the melt. The head of the shear device was positioned just below the surface of the melt. Rotational speed was kept at 7000 rpm for each experiment.

3.2.1 MATERIALS AND SAMPLE PREPARATION

In each experiment the material was 6xxx alloy designated internally at Sapa as F22, which is an AA6060 wrought aluminium alloy, chosen for its use at Sapa and low alloy content as this could be a hindrance in this study, but success would mean the possibility for follow on work using this study as a template. The alloy composition and corresponding phase diagram providing using ThermoCalc database are provided in Table 3.1 and Figure 3.2 respectively. Approximately 800 g of commercial purity Al (99.7%) was melted in an electric resistance furnace at 750 ºC and alloyed to the base composition shown in Table 3.1. The Ti content of the alloy has a target of 0.014 wt% but for these experiments Ti was not added and thus was kept at trace levels.

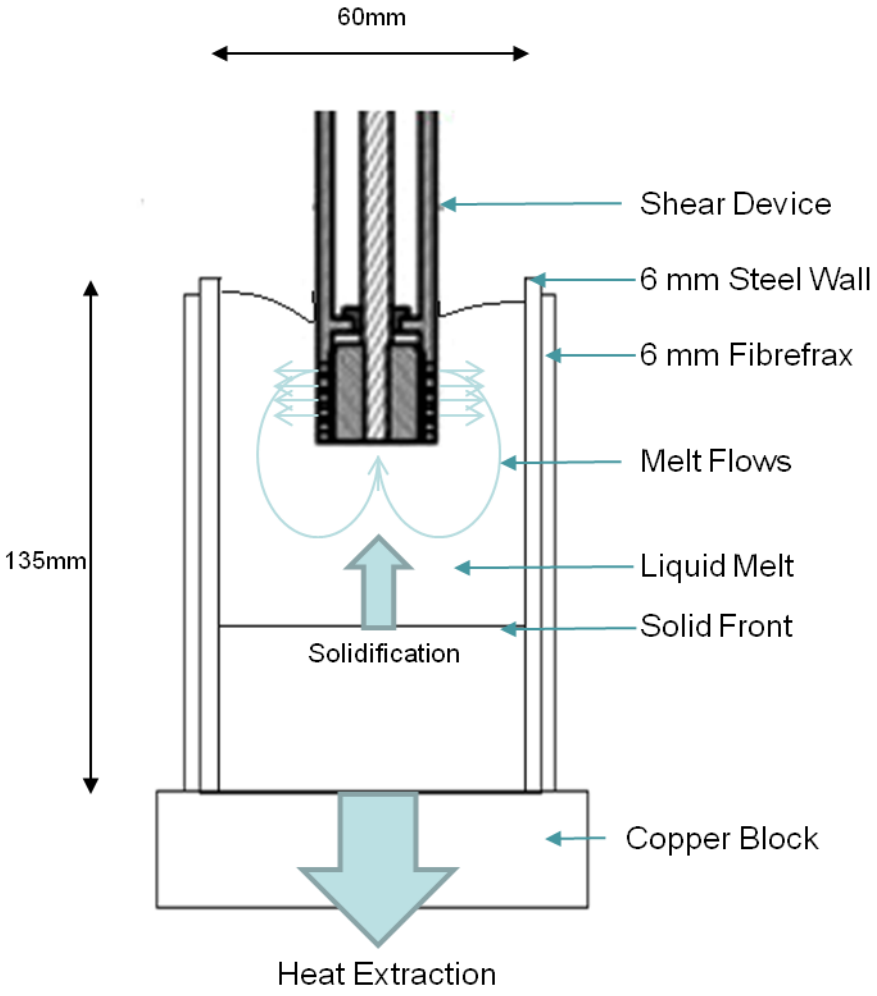

Figure 3.1 **Schematic of the static mould experiment apparatus. The shear unit is submerged in the liquid melt inside the steel mould. The steel mould is wrapped in Fibrefrax wool to reduce heat loss and thus cooling effect. Heat extraction is primarily provided by the copper "chill" block. The flow streams generated by melt conditioning are shown with the flat solidification front that rises towards the fixed shear device as solidification proceeds.**

Table 3.1 **Target composition (wt%) of the AA6060 Aluminum alloy used in the study**

	Composition (wt%)					
Elements	Si	Fe	Cu	Mn	Mg	Ti
Concentration	0.50	0.20	0.008	0.04	0.36	0.014

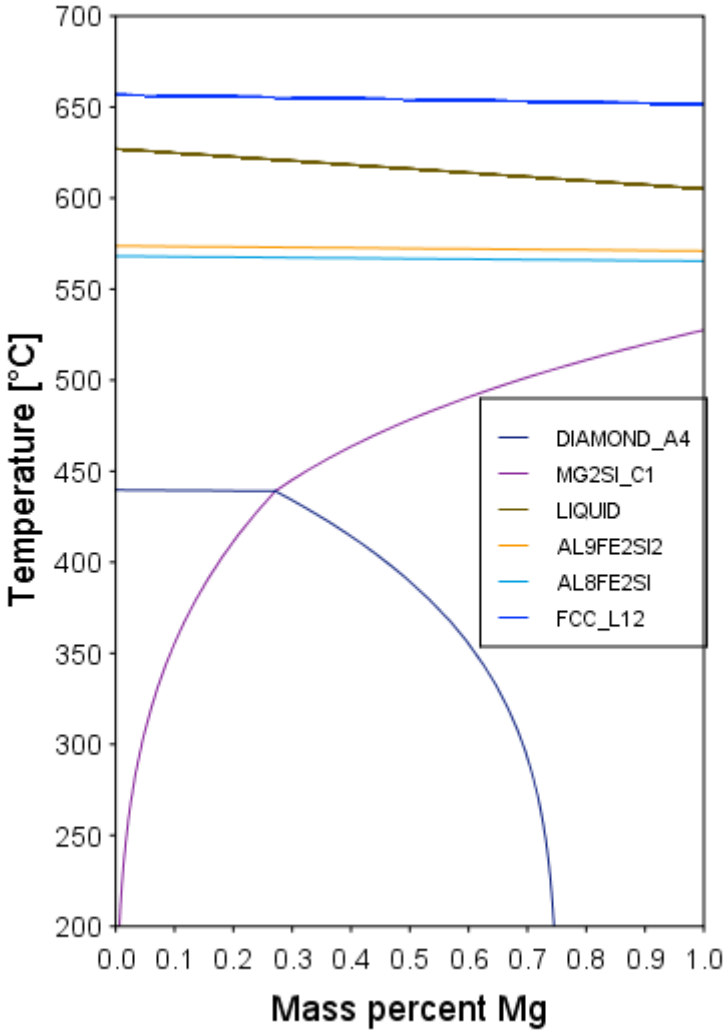

Figure 3.2 Phase diagram of 6060 alloy provided by ThermoCalc

For each experiment, the melt temperature and pouring temperature were kept constant at 750 ºC and 700 ºC respectively. The composition of the melt was checked by Optical Emission Spectroscopy (OES) on a Foundry Master. Alloying additions to the melt were made once the Al base had been melted fully, and was stirred into the melt to aid dissolution. Analysis of the melt composition was made 30 mins after the final addition, thus allowing time for each element to dissolve fully. Table 3.2 lists the alloy hardeners and element weight percentage.

Table 3.2 Concentrations of elements in the hardeners used to create the alloy studied

	Concentration (wt.%)				
Element	Si	Fe	Cu	Mn	Mg
Concentration	45%	80%	100%	80%	100%

Once the composition was correct and the temperature reached 750 ºC, the melt was removed to allow cooling to the pouring temperature. Prior to pouring, the melt was stirred, allowed to settle and a final skim to remove the surface oxide layer was done; it must be noted here that before any addition was made the melt stirred, oxide was removed first to ensure cleanliness of the melt and comparison with industrial practices.

3.2.2 METALLOGRAPHIC EXAMINATION AND IMAGE ANALYSIS

The cast billets were sectioned longitudinally down the centre. One half was ground flat using 600 grade silicon carbide (SiC) paper and macro etched using Tucker's solution which exposed the macro-structure enabling specific areas of interest to be chosen. From the selected areas a 10mm square sample was cut, mounted in Bakelite and prepared on 120, 240, 400, 800 and 1000 grade SiC paper respectively, polished with 9, 3 and 1 µm diamond paste on cloths, with final polish using OPS solution on cloth for a mirror-like finish for optical microscopy. Axio 4.8 image analysis software on a Zeiss polarizing microscope was used to obtain images of the microstructure at 10x and 50x magnification, before being anodized in Barker's solution. This revealed the grain structure enabling measurement of the grain size using the circle intercept method. Five images from each sample were obtained at 2.5x magnification and the average grain size for that area of billet determined.

Examination of the intermetallics was performed on the polished samples by a Philips XL30S scanning electron microscope (SEM). The software used to measure the particle size and morphology was the Oxford Instruments particle analysis software INCAFeature. Energy dispersive X-ray (EDX) was used to determine the composition

of the intermetallic particles found in the samples. Line scan analysis was also performed by SEM across the body of selected grains.

3.3 MC-DC CASTING AT BCAST LAB

3.3.1 MC-DC CASTING AT BCAST LAB

Direct chill casting on the unit at the BCAST laboratory followed the static mould experiments with melt conditioning (MC) applied during casts, the first time MC-DC had been achieved! In order to study the effects of shearing on the billet microstructure, the first experimental billet cast was not sheared or grain refined, as a means of providing comparison after melt conditioning. Three further experiments were completed with shearing applied to them using the device described previously in section 3.1. A schematic of the experiment apparatus is shown in Figure 2.4. The first MC-DC experiment was carried out with the head of the shear device level with the joint between the graphite ring and hot-top at a casting speed of 220 mm/min. The second experiment used the same set-up but the casting speed was increased to 240 mm/min to study the effect of increased casting speed upon the cast structure. The third experiment proceeded with the casting speed of 240 mm/min but the shear device was raised 25 mm above the edge of the graphite ring into the hot-top, increasing the distance from the solidification front and cooling effect of the mould upon the metal during casting. The speed was kept at 240 mm/min because at the slower speed and shearing in the hot-top reduced the temperature too quickly causing casting problems. The cooling water flow rate was kept constant at 27 litres/min during each experiment.

The rotation speed of the shear device remained constant at 3000 rpm for each of the experiments, the maximum that this unit would allow before bleed-out occurred. Two thermocouples were fitted around the device at positions T1 and T2 as shown in the schematic (Fig 2.3). Thermocouple T1 was positioned at the side of the device close to the holes to monitor the temperatures of these flow paths, whilst T2 was positioned 5 mm below the head of the shear device to monitor temperatures of the melt being drawn into the mould from the region of the solidification front, plus as a

safety measure to ensure the device did not get frozen into the melt if temperatures dropped below 655 ºC; if this occurred, the shear device would be removed immediately before it froze into the billet.

The DC caster consists of a water cooled aluminium mould with a graphite ring used for lubrication during casting. The starting head is made of Al and provides a solid ingot butt at the start that supports the billet during casting. A refractory basin known as the hot-top is fitted above the mould in contact with the edge of the graphite ring, in such a way that no melt can get between the hot-top and mould, as this would cause a hang-up and eventually a bleed-out. Feeding the melt into the hot-top is a short trough (launder) that is angled below the horizontal to aid flow into the hot-top; care is taken that the flow is not so fast as to cause splashing and turbulence in the hot-top. Both the water flow rate and casting speed were PLC controlled.

Before casting, the starting head is raised into the mould bore, sealing the mould at the bottom edge of the graphite ring thus when the melt enters the mould, it will not run-out into the pit. The refractory of the launder and hot-top were checked for cracking as a safety requirement, then recoated in boron nitride paint to ensure the melt does not stick to the surfaces. The launder and hot-top were heated to above 200 ºC to reduce heat loss to the system during pouring, as the ceramic would suck heat from the melt as they reach equilibrium temperatures. This could cause freezing in the mould and hot-tears at the start plus excessive cracking as a result of the cold melt. A significant safety requirement when working with molten metal is ensuring any tooling and alloying additions are dry and have been preheated to above 100 ºC, to remove moisture before contact with the melt.

Heating of the hot-top and launder is carried out by electric coil heater fitted into the hot-top and Fibrefrax felt is laid over the top to retain the heat. The starting head is lowered out of the mould during this time to allow heat to escape from the mould so the graphite does not deteriorate, or the starting head itself becomes too hot to provide cooling at the start of casting. Before casting, the starting head is brought up into the bore of the mould, level with the bottom edge of the graphite ring and then checked for any moisture. High temperature grease is applied to the surface of the starting head and graphite ring to provide lubrication during the holding time (where the shell of the billet forms before drawing down, out of the mould).

After alloying additions, the composition of the melt was checked by OES analysis on the Foundry Master and any corrections would then be made if needed. When the composition is at the target specification, and the melt temperature is 740 ºC casting was ready. At this point the heater and blanket are removed. The cooling water is started to make sure it achieves a good curtain for the billet to pass through as it exits the mould. Water ingress into the mould is checked; it goes without saying if this happened, the cast would be aborted. When the melt was ready it was removed from the furnace and allowed to cool to the pouring temperature of 720 ºC. The mould and hot-top are filled until level with the launder at which point the cast starts drawing down. The melt level in the hot-top was maintained at the launder level during the casts. Start speed was 140 mm/min but ramped up to the cast speed of 240 mm/min when the first solid billet exits the mould bore. It was at this point that the preheated shear device was inserted into the hot-top at its pre-determined depth. The cast was checked to make sure that the insertion of the device did not cause problems. Steady state of the cast was reached at this point so the shear device could be started with a speed of 1000 rpm. The rotational speed was increased to 3000 rpm as a maximum for these experiments.

3.3.2 MATERIALS AND SAMPLE PREPARATION

The composition of the material investigated had the same specification as the static mould experiments detailed in Table 3.1. The same base material was used (Al 99.7%) but the size of the melt was increased to approximately 6.9 kg per drop. The Al was melted in an electric resistance furnace heated to 800ºC which was reduced to 740 ºC when the Al was fully molten. The alloy was prepared to the specifications shown in Table 3.1 with hardeners added to the crucible of molten Al in the furnace. Before each addition was made, the oxide layer formed on the surface was carefully removed and the melt stirred to aid submerging and dissolution of the additions, which were then further stirred. This is especially crucial for manganese (Mn) which would float on the surface and oxidize so required assistance to become submerged and dissolve into the melt. Magnesium (Mg) additions were made last and were held under the surface by a suitable tool to ensure they did not float and oxidize at the surface. Grain refinement and titanium additions were omitted from these experiments.

The ingot was sectioned longitudinally with the face ground flat using 600 grade SiC paper and macro etched using Tucker's solution, which exposed the macro-structure enabling specific areas of interest to be chosen. The surface zones and bulk of the material were analysed. A sample was taken from the sheared zone and prepared for image analysis as detailed in section 3.2.2.

3.3.3 METALLOGRAPHIC EXAMINATION AND IMAGE ANALYSIS

The samples that were analysed were sectioned form the ingot such that the billet surface and the bulk through to the billet centre were within the same sample. The image analysis methods used were the same as those detailed in section 3.2.2.

3.4 MC-DC CASTING AT OXFORD BEGBROKE SCIENCE PARK

The final series of experiments were carried out on the DC casting unit at Oxford Begbroke Science Park. This unit has the capacity to cast two 1900 mm length billets at a diameter of 206 mm. However, for the experiments carried out in this section of the study, only one mould was used at a time for convenience. The purpose of carrying out experiments here was to scale up the lab based experiments to an industrially comparable level. The melt conditioning process in this study had not been investigated on such a scale before and the aim was to determine if melt conditioning could refine the structure in a larger diameter billet, over a continuous period of time. The scale in question here is comparable to industry where log diameters of 6 inch to 21 inch are available. So far we have only investigated at the lab scale. We needed to investigate what effect the melt conditioning device in its current form would have on a considerably larger diameter billet, with continuous melt addition and cooling rates, similar to industry. To understand the microstructural formation with the change of processing parameters, another consideration for this series of experiments was the interaction of the shear device and the forced flows it generates during melt conditioning, with a different hot-top and mould geometry. Thus a series of experiments were undertaken with the shear device at different positions within the hot-top, mould opening and mould itself. The positions are denoted as P1, P2 and P3 and are indicated on the scale drawing of the DC unit and shear device in Figure 3.2. In Figure 3.2, it is clear that the ceramic transition plate provides a sloped face from the thimble to the graphite ring of the mould wall. This sloped feature is absent from the BCAST lab hot-top. In industry there are many different mould package styles, thus it is important to consider these factors in choosing how to proceed with a particular DC unit. Therefore, not only was this experiment a key test to determine if the shearing effect of the MC-DC process worked in a substantially larger billet, but what effect mould design had on the MC-DC process. It also goes some way to validating the shear device flexibility to industry.

At each position, the rotation speed of the shear device was varied from 4500 rpm to its maximum rotation speed in this volume of melt, 6400 rpm. Rotational speed and its effect on the microstructure as a factor of distance could therefore be studied. Quantification of melt conditioning at each speed and device position upon the sump

profile, temperature profile and the forced flows it created is provided through in-depth analysis of the microstructural formation in the MC-DC cast billets.

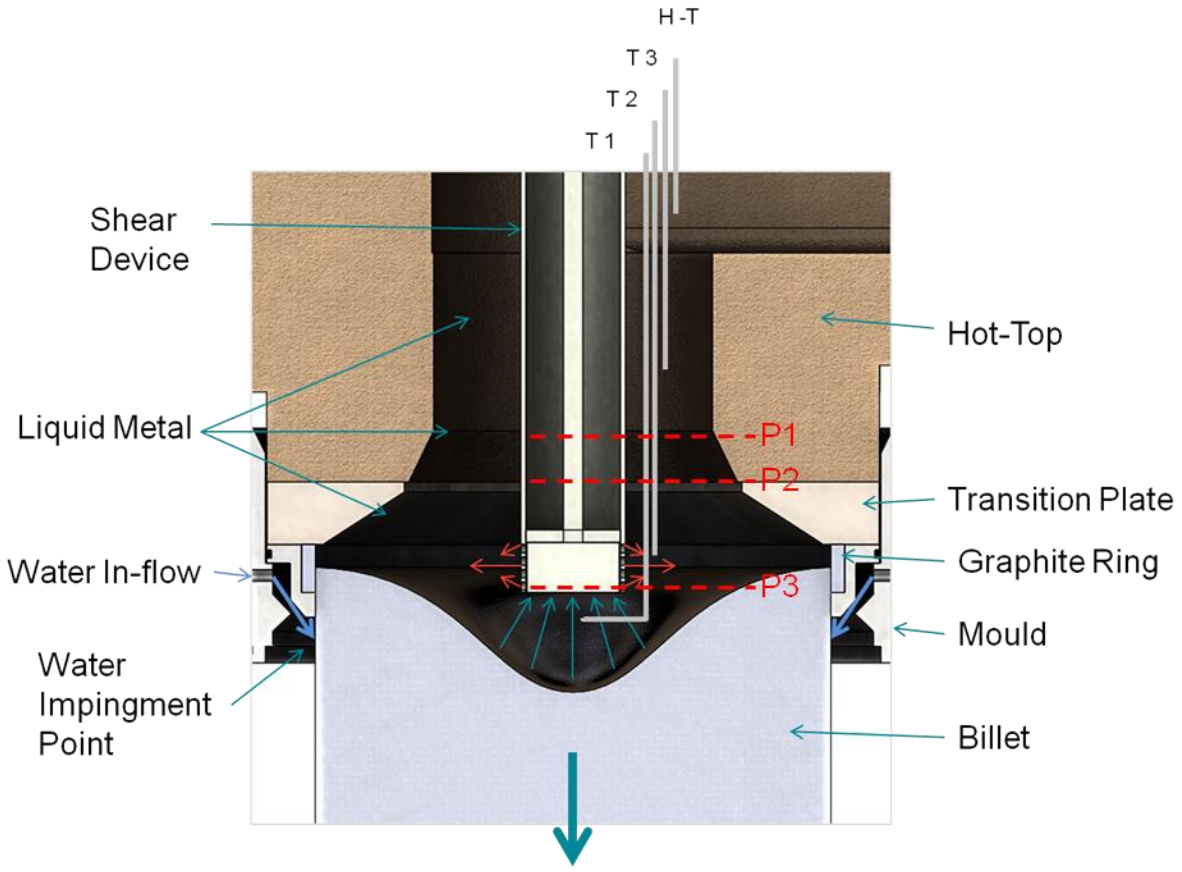

Figure 3.3 Schematic of the MC-DC process at Oxford Begbroke. The shear device is submerged in the melt within the mould, and labels P1, P2 and P3 show the positions of the shear device during each experiment. The hot-top and shear device are scale drawings. The shear device was the same as used in the previous experiments.

3.4.1 MATERIALS AND CASTING PARAMETERS

The alloy used in this study was an AA6063 to the target specifications in Table 3.3. This alloy is similar to that of the AA6060 material cast in the previous experiments; sections 3.2 and 3.3. and the phase diagram is provided in Figure 3.4. The phase diagrams between the 6060 and 6063 alloys used are similar as the compositional difference is very slight. The reason for the change was Oxford Materials department had been studying the intermetallics formed in this alloy, so the decision to produce material for this study during these experiments was made due to similarities of the

alloys. Approximately 350 kg of commercially pure Al 99.7% was used for each cast. The ingots of pure Al (99.7wt.%) were loaded into the furnace by crane.

Table 3.3 Target composition (wt%) of the AA6063 aluminium alloy used in this study

	Composition (wt%)					
Element	Si	Fe	Cu	Mn	Mg	Ti
Concentration	0.41	0.20	0.002	0.035	0.45	Trace

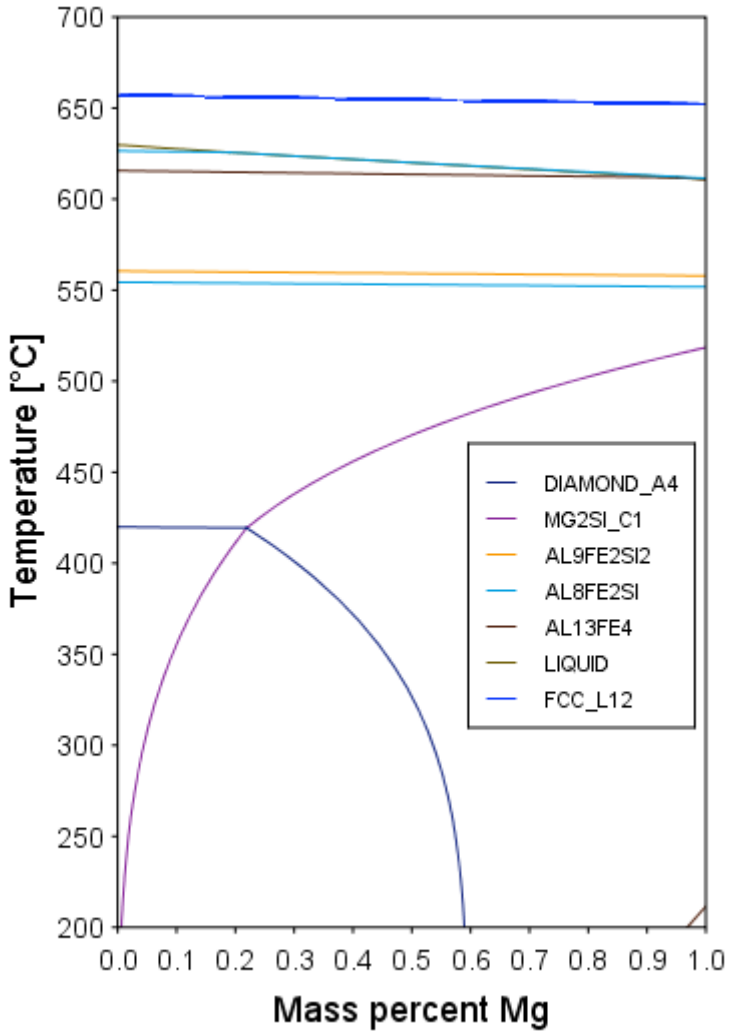

Figure 3.4 Phase diagram of 6063 alloy provided by ThermoCalc

The ingots of base alloy Al (99.7wt.%) were preheated at the top of the furnace before immersing slowly into the melt. Additions were calculated and prepared then preheated to above 100 ºC in a separate oven before being added to the melt. This ensured that the material was dry and safe to add to the melt.

Al ingot was melted in a gas fired furnace heated to 800 ºC which was reduced to 765 ºC when the Al was fully molten. The furnace is a hydraulically operated tilting furnace, manually controlled by an operator. The melt is transferred to the hot-top through a launder system made of Pyrocast AL 60, with a depth of 100 mm and 90 mm wide. The launders were coated in white boron nitride and heated by gas torch to ensure no moisture remained and reduce heat loss from the melt to the system. The melt was poured into the launders through a glass filter material to reduce inclusions. A schematic of the furnace and launders is shown in Figure 3.3.

The hot-top is made of the same ceramic material as the launders, Pyrocast AL 60 and is fastened to the casting table above the mould, see Figure 3.3. Between the ceramic hot-top and the mould is the transition plate. This ring of ceramic made from Pyrotec N17 material, which tapers from the opening of the hot-top into the mould at 33º. This transition plate is coated in boron and is tapered to ensure no hang-ups by the metal during casting. The diameter of the hot-top thimble is Ø 112 mm and Ø 133 mm at the inlet to the mould. The thimble measures Ø 200.8 mm at the point where it contacts the mould. The hot-top is held in place by a metal plate which was used to support the motor frame that drives the shear unit.

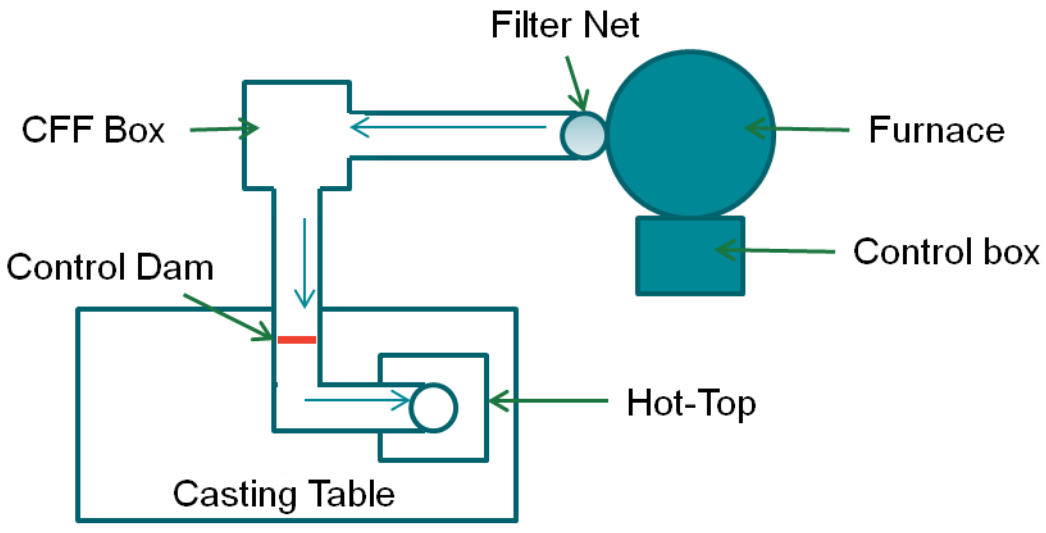

Figure 3.5 Schematic of the furnace and launder layout to the casting table of the Oxford Begbroke DC casting unit. The control dam was used to control flow from the furnace to the mould before casting. In the cases with grain refiners added, TiB_2 grain refiner rod was added in this area.

For each cast during this program of study, the casting parameters (casting speed, water flow rates, and melt temperatures) were kept constant and determined before any experiments were carried out. This ensured that the shear device position and rotation speeds were the only variables to affect the cast structure. The parameters were set as thus;

- Start casting speed: 90 mm/min
- Casting speed: 110 mm/min
- Ramp Rate: Steady state speed by 100 mm/min
- Water Flow: 240 ltrs/min
- Pouring Temperature: 765 ºC (Measured in furnace)
- Cast Temperature: 710 ºC (temperature at which melt released to mould)

The high pouring temperature was necessary to combat heat loss from the melt through the launder system during casting. As can be seen above, the cast temperature is considerably below that of the pouring temperature. This was controlled by allowing melt to flow to a certain point in the launder system, where a dam held the melt from entering the hot-top until the temperature (measured by K-type thermocouple) reached 710 ºC. The melt was then released into the mould. The mould filled up to the level of the launder base at which point the cast was started. The start casting speed is slower than at steady state to ensure a good shell and butt was achieved to support the cast. The casting speed was set to ramp up to the steady state speed by 100 mm/min of log cast.

Before the experiments with melt conditioning could be carried out, comparative material in the form of grain refined and un-refined billet was required. To simulate industrial practice, the grain refiner was a typical AlTiB rod that was added to the melt during the cast, by feeding it into the launder section between the CFF box and control dam, marked in Figure 3.3. The un-refined billet was cast without melt conditioning or grain refiner additions, thus the structure was created by the alloy system and casting parameters which typically create a structure of large (feather) grains and centreline cracked logs.

Experiments P1, P2 and P3 followed and were very similar in method; the cast begun prior to the shear device being inserted once a steady state had been achieved at

approximately 100 mm. Shearing began at approximately 250 mm. The rotational speed was increased to the first set point of 4500 rpm by 500 mm. This ensured that the shock to the system was not severe enough to cause a bleed out, by increasing the flows inside the shell too aggressively. The rotational speed remained at 4500 rpm for approximately 400 mm of log cast. The rotational speed was then increased to the maximum speed of 6400 rpm and continued until 1800 mm of log had been cast. At this point, the shear device was stopped and removed and 100 g of pure molten Zn was poured into the top of the mould to freeze the sump shape at the top of the log. The furnace was tilted back at approximately 1850 mm to ensure that the log did not exceed 1900 mm thus it could be removed from the pit without complication. This process was repeated for each of the three experiments.

An additional rotation speed was added to the experiment P3. At 400 mm, the rotational speed was held at 3000 rpm for 400 mm; increased to 4500 rpm for a further 400 mm; increased to the final (maximum) rotation speed of 6400 rpm for the remainder of the log. This was to study if a low speed had a similar effect to high speed shearing, with the shear device being in such close proximity to the sump at position P3.

A second experiment was carried out with grain refiner additions made to the cast as it was melt conditioned; MC-DC-GR. The experimental procedure carried out in trial P2 was used for this study. Analysis of the billet produced from the three trails P1, P2 and P3 suggested that position P2 was the optimum studied. The grain refiner was added as previously described for the reference billet.

It should be made clear at this point that the same device used in the previous lab based experiments and shown in Figure 2.3, was used during the experiments outlined above at Oxford. Although the mould size and casting unit was up-scaled, the device tooling was not, including the motor that drives the impeller.

3.4.2 SAMPLE PREPARATION AND METALLOGRAPHIC EXAMINATION

The billets were sectioned as shown in Figure 3.3. For each log cast, slices approximately 100 – 150 mm thick were removed from each area where the shear

rotation speed was different, indicated by the red shaded boxes in Figure 3.3. The slices were sectioned longitudinally; the surface milled flat and etched using Tucker's solution, exposing the macrostructure. The same process was applied to the section from the top of the log that contained the Zn addition, exposing the sump shape where the Zn froze. Adjacent to the large slices used for macro analysis, billet slices approximately 25 mm thick were taken for in-depth analysis of microstructure. These slices were sectioned as shown in Figure 3.4.

A 25 mm wide strip of the billet was cut from the centre of the billet and then halved so that separate Optical Emission Spectroscopy (OES) and Microscopic analysis could take place. For the OES analysis, the strip of billet was cut into 11 equal pieces with a width of 9 mm. The surface of the billet was the start point of the measurements and each surface adjacent to the surface was measured. The measured surface was ground on 600 grade SiC paper in water and washed with ethanol. Each sample then had three sparks made on the prepared face, and the average taken. The OES machine used was a Spectrolab S.

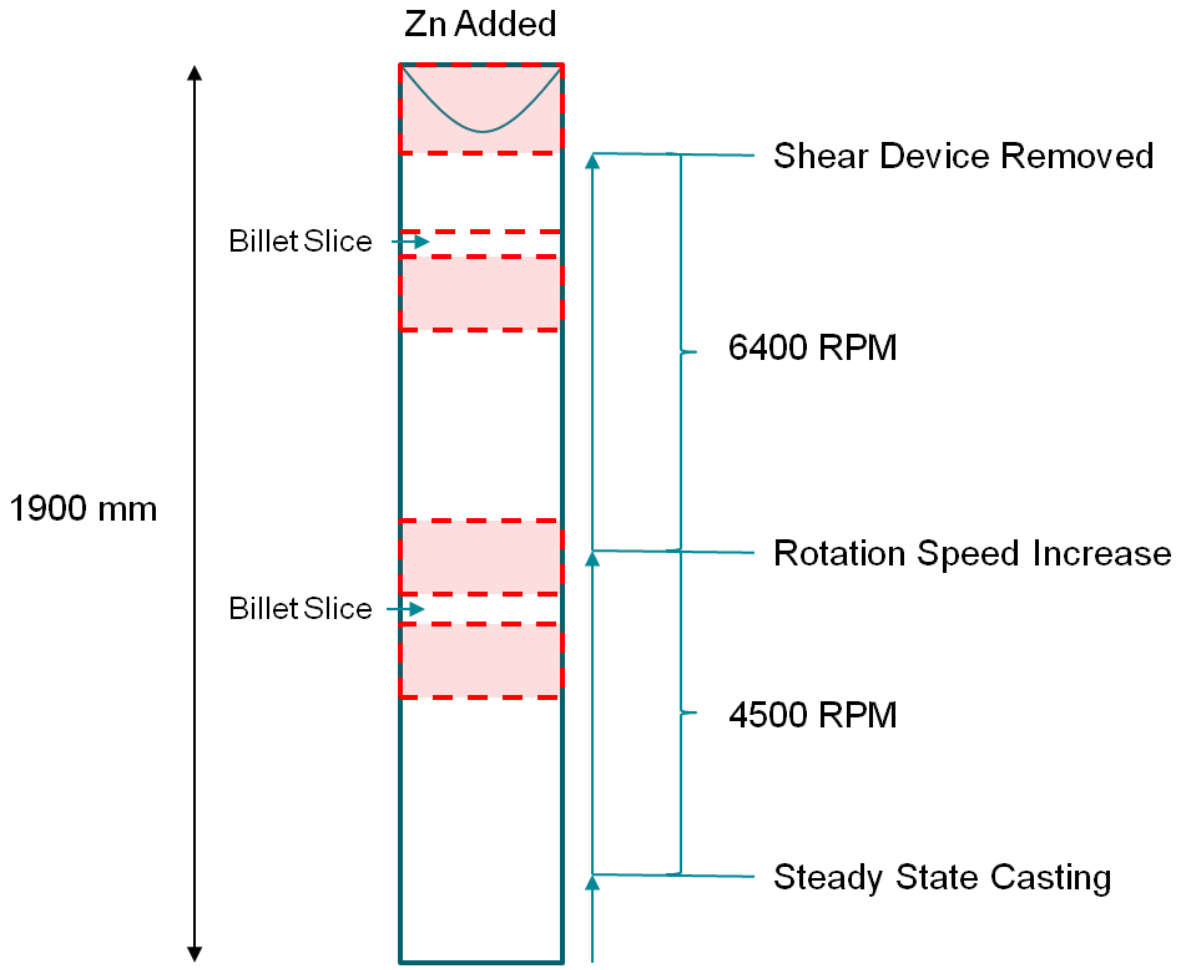

Figure 3.6 Schematic of a cast log and the areas where the sections and billet slices were taken.

The section of billet that was used for the micro-analysis was cut into three samples for ease of preparation and due to the size limitations of the SEM. The sample face that was prepared for analysis was of the longitudinal direction. Each piece was ground on 220 and 500 grade SiC paper respectively, before polishing with 9 µm diamond paste and lubricant using a Struers MD Largo abrasive plate. Following this step, 3 and 1 µm diamond paste with lubricant was used on MD Mol and MD Nap cloths respectively. The final polish using OPS solution mixed with ethanol in a 10% OPS to 90% ethanol ratio on an MD Chem cloth for a mirror-like finish. This step was followed by a 20 second wash using another MD Chem cloth with ethanol only to wash away the OPS particles. Water was used to wash the samples in between each step with ethanol to clean the surface during drying. However, water was not used for

the final OPS polish and ethanol wash, to protect the samples from the etching effect of water.

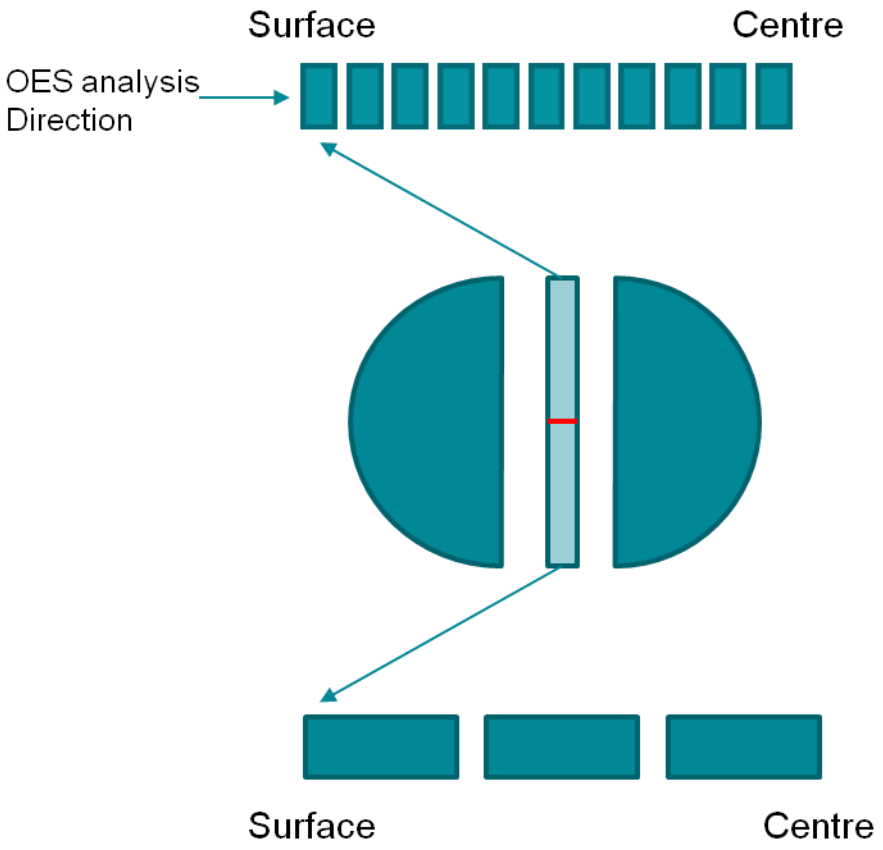

Figure 3.7 Schematic of the billet slice sectioned for analysis. The red line shows where the strip of material was halved for separate analysis preparation.

KAPPA Image Base image analysis software on a Nikon Eclipse LV150 was used to obtain images for intermetallic analysis and *P** measurements. 12 Images of the microstructure were taken at 10x and 50x magnification at 5 mm intervals across the 3 microstructure samples from the surface towards the centre. The *P** value provides an average measurement of particle free zones in as-cast microstructures. It can be used for as a measurement of solidification rate similar to dendrite arm spacing (DAS) except the difference is alloy dependant. The spatial distribution of the particles is measured using a mathematical image processing algorithm. For a particular alloy, low *P** values suggest high growth rates and vice-versa. It is based on a classical dilation-erosion algorithm applied to aluminium alloys and was developed at the Pechiney Research Centre (Ph. Jarry, M. Boehm, S. Antoine).

A Zeiss polarizing microscope was used to obtain images of the grain-structure after being anodized in Barker's solution. Measurement of the grain structure was carried out using the circle intercept method. Five images every 10 mm from each sample were obtained at 2.5x magnification and the average grain determined.

Examination of the intermetallics was performed on the polished samples by a Philips XL30S scanning electron microscope (SEM). The software used to measure the particle size and morphology was the Oxford Instruments particle analysis software INCAFeature. Energy dispersive x-ray (EDX) was used to determine the composition of the intermetallic particles found in the samples. Line scan analysis was also performed by SEM across the body of selected grains.

3.4.3 SIMULATED FLOW DIAGRAMS

In the following chapter, diagrams have been provided simulating the fluid flows inside the mould when the shear device is active. The diagrams are a visual aid to refer descriptions of the microstructure back to and to assist the reader in visualising the turbulence inside the sump.

The simulations were solved for steady state using fluid properties of water at 273.15K created using Solidworks Flow Simulation software. They are a 3D simulation model where the fluid domain is geometrically defined by the boundaries of the mould, shear device and the estimated sump shape. The shear device and mould are to scale with the hot-top, transition plate, graphite ring and mould body being that of the Oxford equipment used during the up-scale experiments. The estimated sump shape was taken from a DC cast billet produced at Oxford, inoculated with TiB grain refiner and doped with Zn at the end of the cast to measure the sump depth. All of the boundaries to the fluid domain apply the no-slip condition thus the fluid velocity at the boundaries is 0. At the top of the domain is a pressure opening boundary condition applied with environment pressure.

The impellor position is defined as a rotating region simulated using different angular velocities of 4500 rpm and 6400 rpm. A local rotating region is defined around the impeller inside the shear device stator housing. The stationary and rotating regions

are coupled by an averaging interface, thus flow parameters within the rotating regions are calculated using a steady state approach and averaged circumferentially on the rotating region boundaries.

CHAPTER 4 – RESULTS-PROCESS DEVELOPMENT

Melt conditioning by intensive shearing as an emerging technology has been established at BCAST (Fan, Bevis, & Ji, 1999) (Fan, Jiang, & Zuo, 2012) whilst DC casting is the principal method for semi continuous casting of wrought aluminium billets for extrusion purposes. The results presented in this chapter show how the two technologies of shearing and direct chill (DC) casting were brought together, creating the MC-DC process. This chapter is split into three sections; Process Development, how shearing and DC casting work together and the parameters fundamental to the process; Microstructure Evolution which goes into detail about how the microstructure is improved by the MC-DC process; Intermetallics, as the morphology, size and type of intermetallic are crucial to the performance of the billet and are an accurate measure of quality.

It is prudent to first describe the melt conditioning technology and its process development at BCAST as this will facilitate the understanding of how the MC-DC process came to be. Fan et al have made numerous studies into melt conditioning of magnesium and aluminium alloys previously, by twin screw mechanism and then rotor and stator mechanism (Fan, Liu, & Hitchcock, 2005) (Fan, Jiang, & Zuo, 2012). Fundamental studies examined the mechanisms of grain refinement through melt conditioned DC casting which allowed an understanding of fluid flow and tool positions within the melt (Fan, Jiang, & Zuo, 2012) (Jones, Prasada Rao, & Fan, 2013) (Xia, Prasada Rao, & Fan, 2013) (Patel, et al., 2014).

4.1 PROCESS DEVELOPMENT

4.1.1 FLOW PATTERNS INSIDE THE SUMP

4.1.1.1 High shear device

The key parts of the melt conditioning technology device are shown in Figure 2.3. It consists of a ceramic stator in which a ceramic four-blade rotor spins at 1000 rpm to 7000 rpm. This assembly is inserted into the melt within the mould through the hot-top as shown in Figure 3.2. The shearing device became an integral part of the casting process without adversely affecting the outcome, such as causing bleedouts through remelting of the solidified surface or forcing melt through the shell. The most critical time for a cast is the start and this raised the question of when to begin shearing, or even, when to introduce the device into the mould. At the start of casting, the starting head is positioned within the mould sealing the reservoir and forming the solid butt of the billet, whilst providing support for the ingot as it is withdrawn from the mould. The melt is held inside the mould by the starting head until sufficient time for the solid butt and shell to form (holding time), and then the billet is drawn away at an increasing speed till steady state is achieved.

This rapidly solidifying metal of the billet base poses a risk of freezing the high shear device into the butt, thus shearing could not begin until after the holding time and the billet begins to draw down. However, the device was inserted into the mould once it had filled, ready to begin shearing at the point the solidified butt emerged from the mould. It was at this point that it was deemed safe to begin shearing; at approximately 50 mm of cast length. A steady state casting speed was achieved by 100 mm of cast billet, as was the maximum speed of the shearing device. Determining that shearing could begin so soon within the casting was a result of the previous casts that showed even at 6400 rpm, there was no risk of bleedouts. Having the shear device inserted within the mould and operating at an optimum speed by 100 mm means that waste is kept to a minimum.

To prevent further freezing of the shear device, it was heated to 750 ºC, thus some 40 ºC above the metal temperature, prior to insertion into the mould. Heating the device also reduces the thermal shock to the shearing device, which is considerable when immersed into the melt when the tool is well below the metal temperature. After casting, the tool is simply switched off and extracted and if it is to be used again, heated at 700 ºC again to prevent thermal shock. The temperature is raised at a suitable time before casting to the required 750 ºC and the process repeated. This procedure has seen the shearing device withstand considerable use without failure.

4.1.1.2 Flow patterns induced by high shear

Understanding of the melt flows in the sump during DC casting is very important in order to understand the mass transport, the temperature profile of the solidus and liquidus, and the resultant sump profiles (Du, Eskin, & Katgerman, 2005) (Vreeman, Schloz, & Krane, 2002). In the current study, the flow patterns have been approximated using Solid Works for the different shear device positions, P1, P2 and P3 which are shown in Figures 4.1, 4.2 and 4.3 respectively. The fluid flows are estimated using a scale drawing of the mould, hot-top assembly and shear device. The measured sump depth of 60mm used for the estimation was taken from the DC billet sump profile without shearing. The medium used is water due to its similar viscosity to liquid aluminium. No temperature gradients have been added so it is assumed all of the medium is at room temperature whilst no account of the mushy zone has been added. The flow patterns have been generated by the software with the shear device at the three different positions of P1, P2 and P3 at rotation speeds of 4500 rpm and 6400 rpm. The purpose is to simply offer a visual representation of the flow patterns using the shear device inside the mould and hot-top arrangement at Oxford Begbroke. Accurate modelling and simulation of flow and solidification effects will be part of the work following this study.

Figure 4.1a and b are simulated flow patterns generated during shearing at 4500 and 6400 rpm at position P1; MC-DC-P1. Flow is clearly most powerful at its exits the shear device through the holes in the stator, similar to high pressure jets of water. This is indicated by the red shading at the sides of the shear device. These flows are shown to be distributing melt drawn-up from beneath the shear device out to the sides through the cross-section of the billet. The melt being drawn-up is at a lower temperature to that of the melt around the tool when the device is started. Rapidly the melt mixes and the temperatures equalize within the mould. The size of this field of mixing and its influence upon the cross-section of the billet is clearly dependent on the internal shape of the mould and the shear device’s position relative to it. From the diagrams it becomes apparent that the flows are confined by the thimble of the hot-top when the shear device is at P1. The jets rebound from the thimble walls and flow

upwards as well as down into the mould, yet there is a flow towards the graphite ring

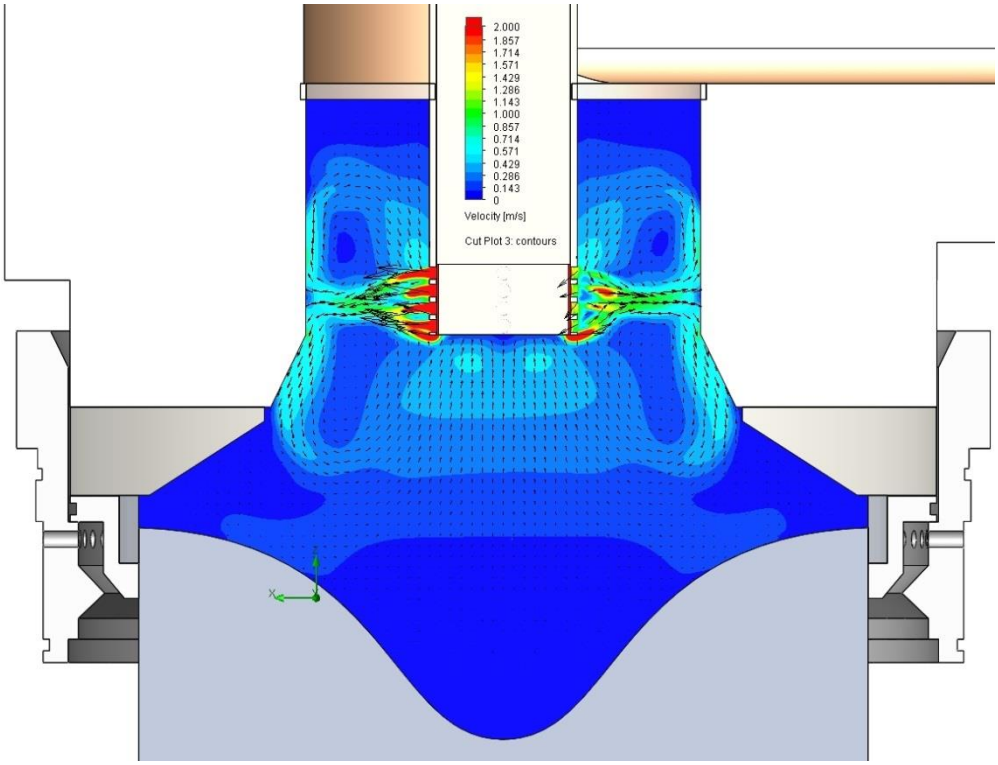

of the mould

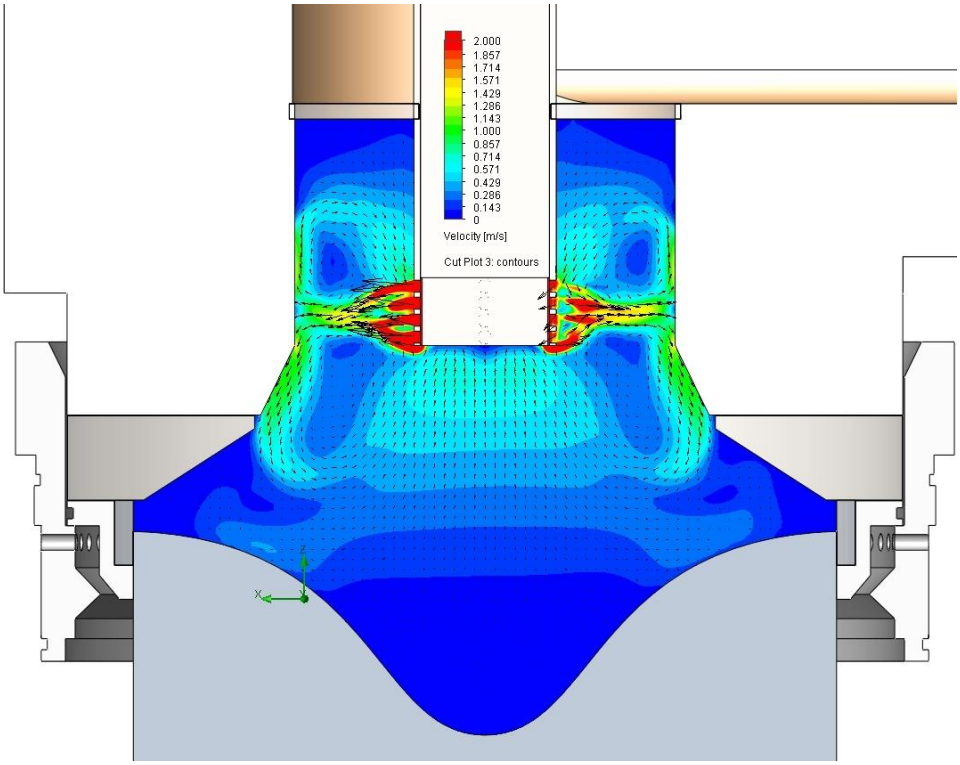

Figure 4.1 Simulation of the flow patterns created on SolidWorks software for MC-DC-P1 billet. The medium used is water with no temperature boundary conditions or porosity simulating the mushy zone. The sump profile was extracted from the sump formed without shearing or grain refiner. a) the rotation speed was 4500 rpm b) the rotation speed was 6400 rpm.

where primary cooling and solidification takes place. Therefore, the body of melt that the shear device is acting upon is less than those when the shear device is at P2 and P3.

The simulated flow patterns for the MC-DC-P2 billet are shown in Figure 4.2. With the shear device 20 mm lower at position P2 the high velocity flows take advantage of the sloped profile of the thimble exit and ceramic transition plate (t-plate). This significantly enlarges the size of the field conditioned by the shear device compared with those of MC-DC-P1. There is considerably more flow towards the graphite ring and primary cooling of the mould illustrating how the two technologies (MC-DC) can work together. Naturally flow towards the graphite ring will be competing with flows moving away from the graphite ring due to natural convection, caused by large undercooling from the mould (primary cooling). Cooling from the DC system is most acute in this area as the secondary cooling effect from the water impinging the surface takes place here, contributing 80% of the billet cooling.

Additional to the horizontal jets of melt from the shear device, laminar flows are created across the solidification front and above the jet flows, around the thimble and t-plate of the mould thereby mixing with the incoming melt, as indicated by the curved flow patterns above the jets. These arrows show the dispersive path of particles and melt within the mould. The most turbulent areas of the melt are directly beneath the shear device where the melt is spinning as it is drawn-up into the device and where the jets exit the holes. Melt leaving the device, is directed to the periphery rapidly, though the speed reduces over distance due to moving through the melt, yet evidently maintaining enough strength in the flow to deflect down into the sump and up into the thimble from the sloped profile of the thimble exit. Inside these up and down flows are eddies or voids in the flow, indicated by the darker blue colouring. The eddies are larger at 4500 rpm, Figure 4.2a, than at 6400 rpm, Figure 4.2b. It will

be shown in the following sections that microstructural in-homogenities varied between the two MC-DC-P2 speeds relative to these eddies.

When we compare the diagrams of MC-DC-P3 in Figure 4.3 against MC-DC-P1 and P2, the strength of the flows in the centre of the sump are significantly larger. Naturally, as the distance between the device and sump base reduces the strength of these flows would increase but it is also shown that they are also very constricted by

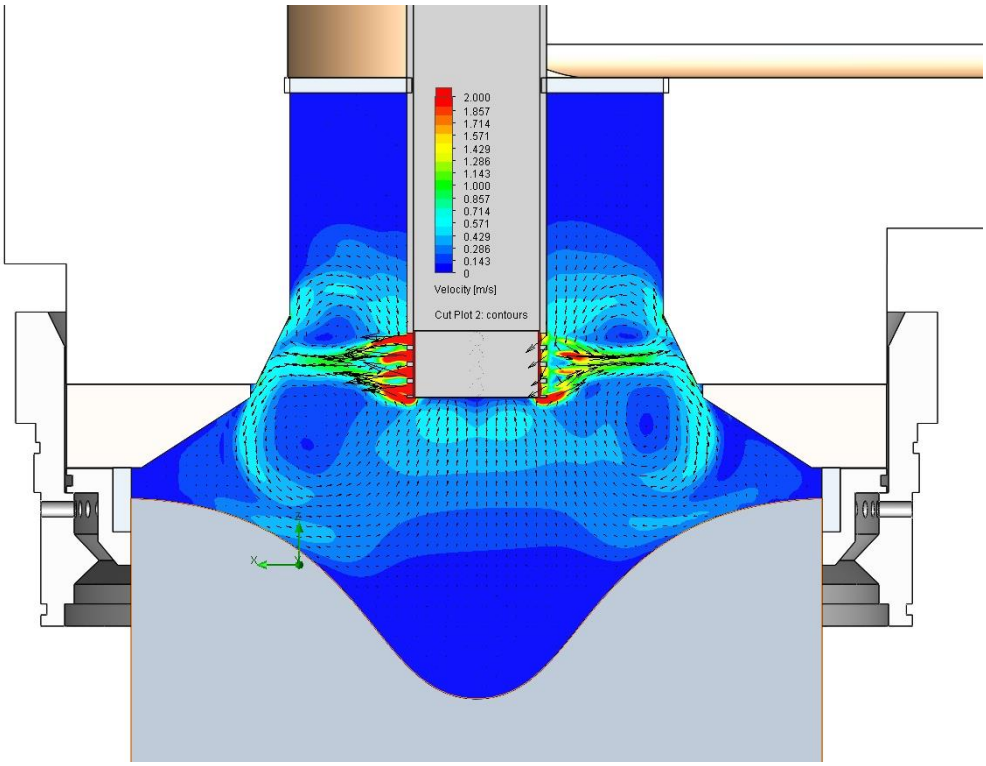

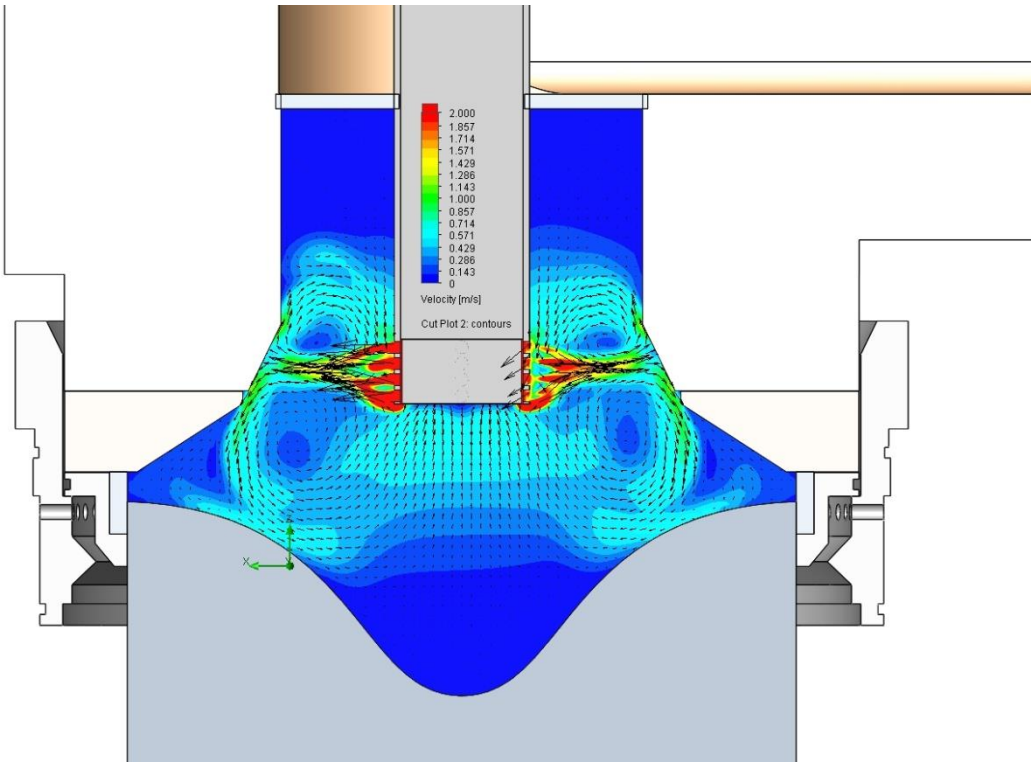

Figure 4.2 Simulated flow patterns created on SolidWorks software for MC-DC-P2 billet. The medium used is water with no temperature boundary conditions or porosity simulating the mushy zone. The sump profile was extracted from the sump formed without shearing or grain refiner. a) the rotation speed was 4500 rpm b) the rotation speed was 6400 rpm. Note the eddies that formed and how they reduce at the higher rotation speed in Figure b.

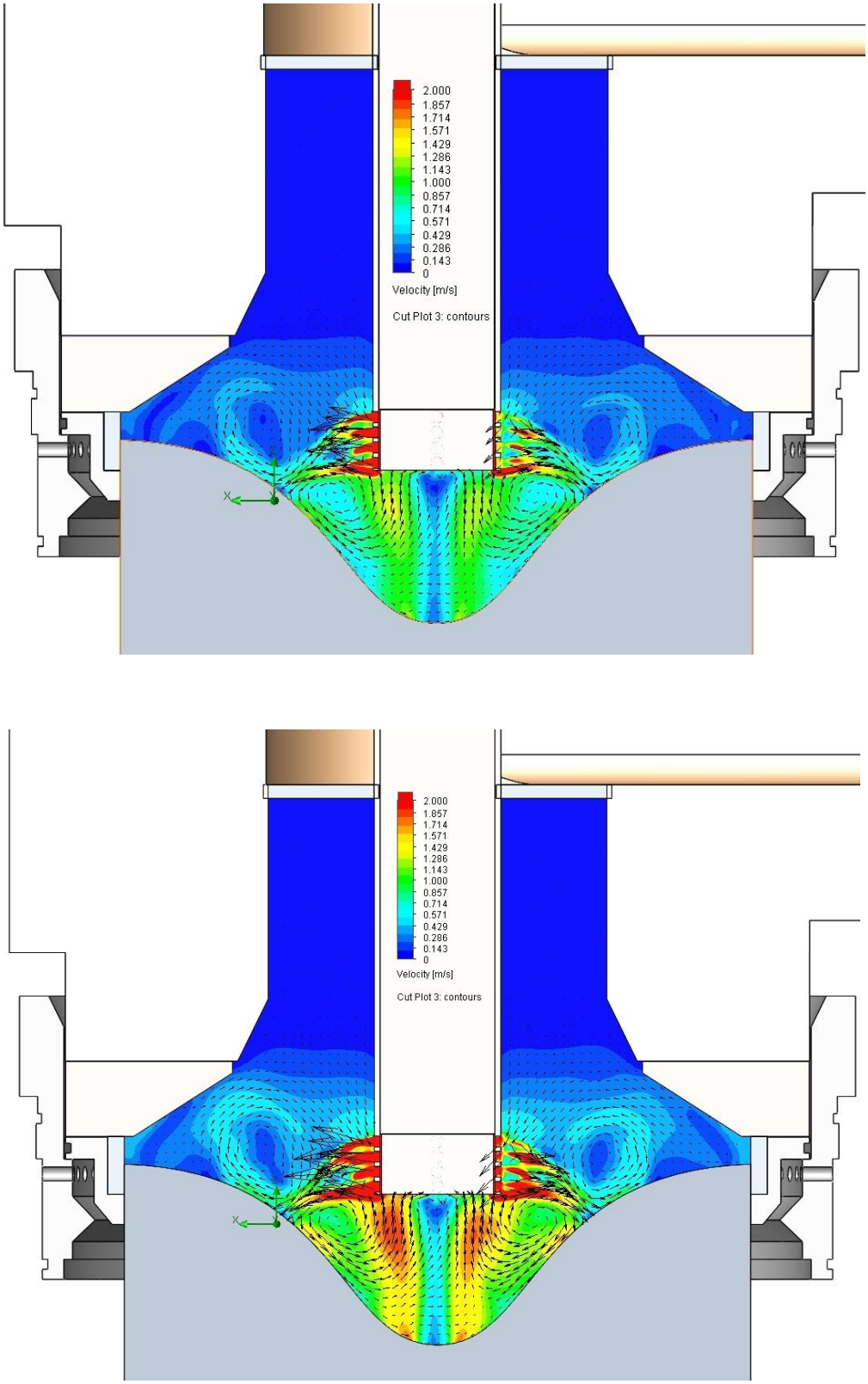

Figure 4.3 Simulated flow patterns created on SolidWorks software for MC-DC-P3 billet. The medium used is water with no temperature boundary conditions or porosity simulating the mushy zone. The sump profile was extracted from the sump formed without shearing or grain refiner. a) the rotation speed was 4500 rpm b) the rotation speed was 6400 rpm. Note the different form the eddies take compared with the MC-DC-P2 billet. Due most probably to the confinement of the strong jet flows within the core of the sump.

the sump profile. The jets from the tool are also directed downwards at a more severe angle due to pressure from the melt flowing into the mould above. Another change is that the flow patterns are contained within the mould reservoir itself and not interacting with the In-flow at the hot-top as during MC-DC-P2.

The effects of the MC-DC process at P1, P2 and P3 are related to the flow streams in these diagrams, specifically the effect that reducing the distance from the base of the device and the solid front had on flattening the profile of the sump base, due to the increase of the sucking forces. This would be most acute in MC-DC-P3 material. In the following sections of this chapter, sump profiles have been captured by the process of pouring liquid Zn into the top of the log at the end of casting.

Additional to the flows described above are those shown in Figure 4.4. Within the macro-etched billet slice shown, there is clearly a swirl effect caused by the rotation of the melt within the billet. The spiraling is visible due to different solidification structures within the billet section. This will be discussed in a later section but provisional investigation of this image suggests that this is the case. Certainly, the variation in structure is evident after etching. As the rotor spins, this action causes the melt drawn-up from the solidification front to spin. The melt around the shear device within the mould also spins as a result thus creating a vortex around the stator. Looking at the spiral pattern in figure 4.4 it appears that the spinning melt is contained within a thick band (approximately 10 mm wide) of coarse structure.

The reason for this banding is a change in temperature gradient at this point in the billet cross-section, where the cooling effect from the surface zone meets that of the conditioned melt in the sump, creating a region where coarse grains grow. Coarse grains from this band could then be moved to the central section of the sump by the spinning melt. A spinning melt inside the mould during casting could be a cause for concern if too severe, with images of the vortex similar to whirlpools spiraling into the mould around the shear device being generated in operators minds. This was not the case however. The surface of the melt in the hot-top showed no sign of turbulence during melt conditioning, even at 6400 rpm. However, the surface of the melt gently rocked in a manner similar to that of the melt surface in multi strand castings, with the “rocking” surface a feature of the technology, created by the ebb and flow of the melt

in and out of the mould during casting. The forced convection of MC-DC is contained within the mould reservoir beneath the ceramic hot-top; its effects mitigated by the system demonstrating how the MC technology can be integrated with DC technology.

In summary, the melt conditioning high shear device position relative to the mould assembly, rotation speed, etc., and DC casting process parameters, melt temperature and casting speed, etc., all have significant effect on the flow patterns inside the mould assembly (thus, inside the sump), and therefore on the microstructural formation.

Figure 4.4 Surface of billet slice taken from the MC-DC-P2 billet sheared at 4500 rpm showing the spiral pattern created by the spinning melt in the sump. Note the spirals did not enter the surface region as they are contained within the band of coarse grains.

4.1.2 SUMP PROFILE

The DC casting process variables determine the thermal conditions of casting and, therefore the temperature distribution in different sections of the billet (Nadella, Eskin, Du, & Katgerman, 2008). Together with the alloy composition this decides the dimensions and geometry of the transition zone in the billet between liquid and solid and therefore the profile of sump. Macrosegregation is linked to the flow of melt within the sump, solute rejection to the melt, grain morphology and solidification shrinkage. Both macrosegregation and sump depth are affected most acutely in the central region of the billet (Nadella, Eskin, Du, & Katgerman, 2008). The incorporation of a high shear device into the DC casting has also an effect on the sump profile. To understand the solidification mechanisms of MC-DC casting, in the current study, the sump profiles were frozen and delineated by pouring of liquid Zn into the melt in the hot top immediately after the shear device was taken off from the mould assembly. The casting speed was kept constant throughout the casts for consistency as was water flow, cast temperatures and composition. This left the application of shearing in the mould as the only variable with respect to the DC casting process.

4.1.2.1 Sump Profile Without Shearing or Grain Refiner

Figure 4.5(a-d) shows the sump profiles of four separate casts, (a) without melt conditioning, (b) with melt conditioning and the shear device at position P1, (c) shear device at position P2 and (d) with melt conditioning and the shear device at position P3.

The sump profile under normal DC casting is shown in Figure 4.5a without melt conditioning or additions of grain refiner, therefore the melt solidified naturally, without any external interference. This resulted in large feather grains that dominated the structure after the initial equiaxed grain structure at the surface, followed by the columnar grain region. The zone of fine equiaxed grains at the billet surface nucleate

when the melt contacts the mould wall (primary cooling), undercooling the metal and creating the billet shell.

The surface of the billet (shell) contracts away from the mould wall when cooled without any resistance from the molten metal inside, creating an air-gap between the shell and mould wall. This immediately reduces the heat transfer coefficient of the mould, allowing the melt temperature inside the shell to rise from the in-flow of hot melt and the released latent heat of solidification. This rise in temperature and reduction in cooling allows the coarse structure to develop, hence the region of columnar grains observed. This region of columnar grains will continue until the cooling rate increases sufficiently to undercool the melt for nucleation to occur. When the billet exits the mould, cooling water (secondary cooling) impinges the billet surface increasing the heat transfer coefficient by one or two orders of magnitude (Eskin D. G., 2008), reducing the melt temperature and increasing the solidification rate resulting in the solidifying grains having an equiaxed structure.

Feather grains clearly dominate the structure in the core of the billet when the billet is cast without shearing; an indication of steep temperature gradients and high cooling rates (Henry, Minghetti, & Rappaz, 1998) which is a factor of casting speed and secondary cooling provided by the forced cooling water from the mould. Of course, the structure observed here is not industrially acceptable but regularly occurs if no grain refiners are added. Feather grains can be eliminated by stirring of the melt or sufficient inoculation practices (Emley, 1976). Due to its effectiveness and cost efficiency, inoculation is currently the most practical and productive method of preventing feather grains (Turchin, Zuijderuiyk, Pool, Eskin, & Katgerman, 2007).

The feather grains have grown from the edge of the short columnar grain region that developed at the air gap (between mould and billet surface). They dominate the growth competition such that they are the only grain morphology present into the core. It is at this point in the billet that the temperature gradient is most acute. The solid shell and columnar grains act as a heat sink for the hotter core melt as the cooling water extracts the heat through the billet surface. Feather grains have been found to grow in the gradient direction with trunks in the <110> direction (Henry, Minghetti, & Rappaz, 1998) (Henry, Jarry, & Rappaz, 1998) (Henry, Gruen, & Rappaz, 2004). Growing with the temperature gradient facilitates dominance over the

competing grain morphologies to the point where the fans of the feather grains consume other grains as they grow larger. The feather grains grow vertically towards the in-flow of hot melt which is to say, the direction of the temperature gradient.

(a)

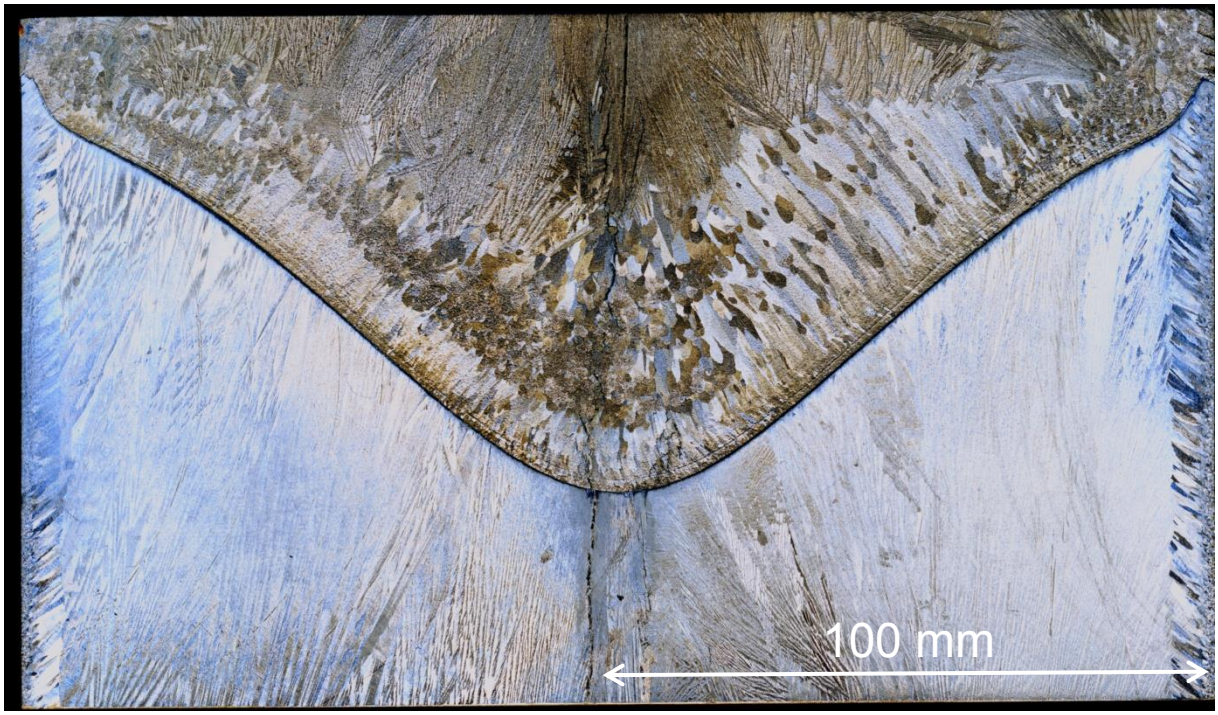

(b)

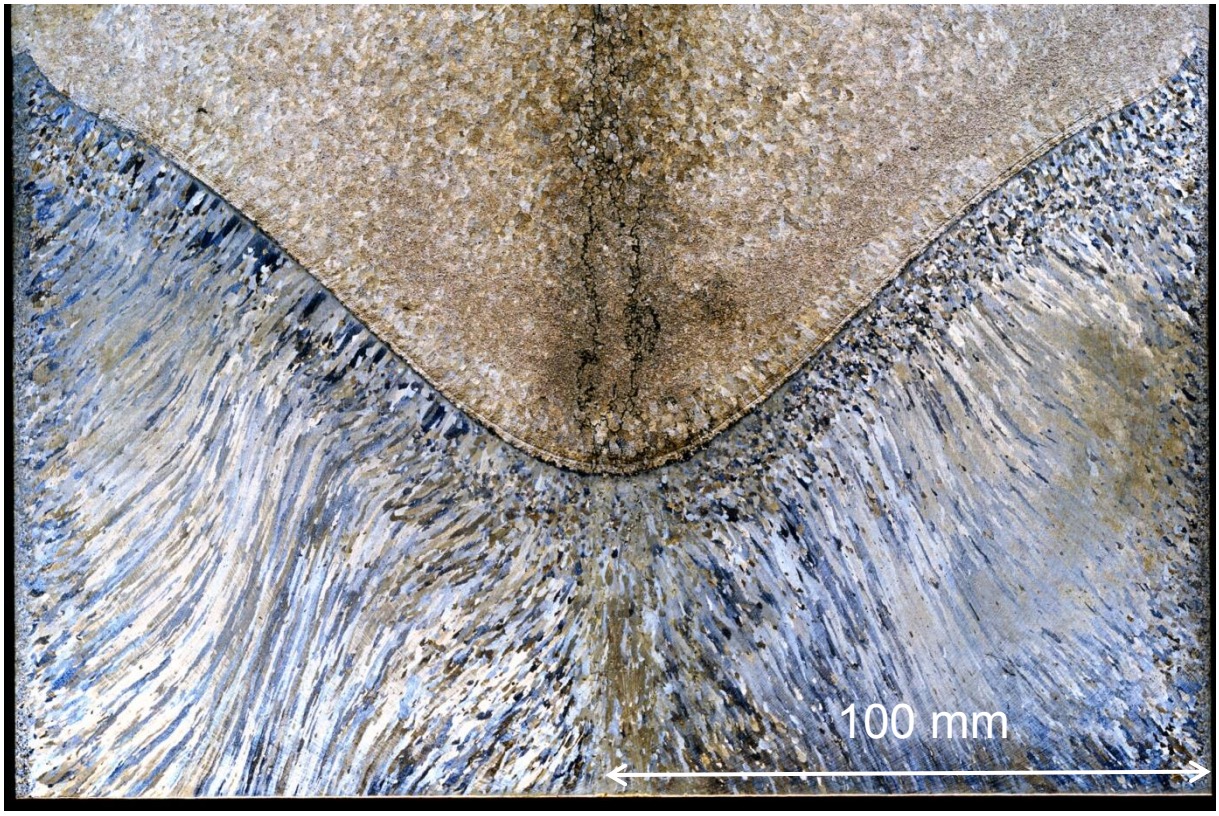

(c)

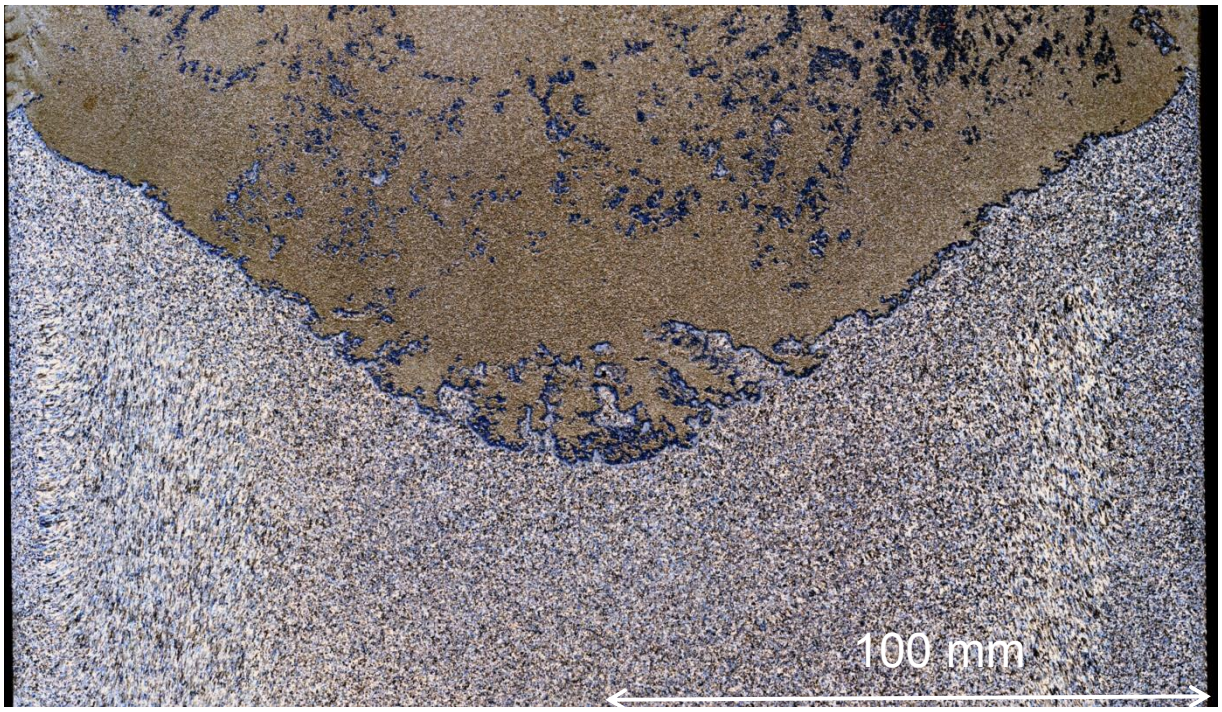

(d)

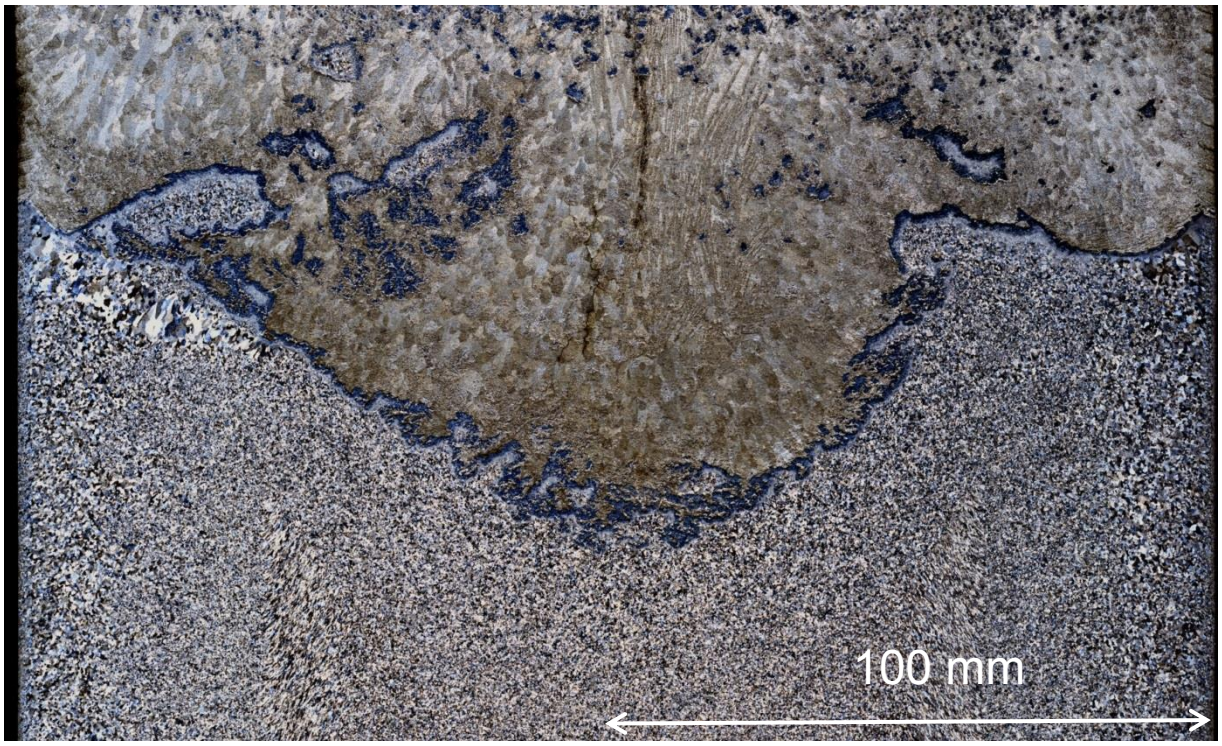

Figure 4.5 Macrographs of 206 mm billet vertical cross-section showing sump profiles delineated by pouring liquid Zn into sump. (a) Cast without shearing showing large feather grains and centerline crack; sheared sample (b) MC-DC-P1, (c) MC-DC-P2, (d) MC-DC-P3. Grain refiner was not added to any of the casts shown above.

A centerline crack can be seen in Figure 4.5a and b. This is common in alloys that are not grain refined and cast too fast or too hot. To eliminate cracking, industrial practice is to add grain refiners to the melt to the ratio of 0.8 – 1.2 kg/tonne of melt, notably the same practice used to eliminate feather grain growth. Casting slower or reducing melt temperature has similar effects to that of grain refinement, but this affects productivity negatively and across multi strand tables reducing temperatures could result in melt becoming too cold at the thimble. The crack is a result of thermal stresses due to shrinkage, pulling the material apart at the centre of the billet inter-granularly, with insufficient melt flow at this point in solidification, for liquid to get through the dense fans of the feather grains. Thus a void appears that cannot be filled and a centerline crack propagates. As the mushy zone of the cast becomes more and more coherent (solid) the amount of liquid that is able to flow becomes less. The shrinkage is due to metal contraction from the coherency isotherm at the limit of the mushy zone, to the solid, upon cooling and results in shrinkage induced flow. The crack in our material runs from the base of the billet to the top, as do these ultimately unwanted, feather grains.

4.1.2.2. MC-DC- P1 Sump Profile

The sump profiles in Figures 4.5 (a) and (b) are comparable to each other. The shear device was positioned at position P1, 50 mm from the base of the mould, inside the thimble of the hot-top. This suggests that the depth of the tool was not sufficient to affect the sump profile by drawing cold melt from the sump up through the tool whilst forcing hotter melt in the mushy zone. As described previously, this was due to the proximity of the tool to the thimble walls restricting the forced melt flow of the jets exiting the shear device. However, the structure of the billet in Figure 4.5b (sheared) is clearly different to that of Figure 4.5a (un-sheared), so whilst the sump profile may have remained unaffected, the bulk of the material clearly hasn’t developing a feather grain structure throughout the billet cross-section. The columnar grains developed at the air gap between the base of the mould and the cooling water impinges the surface of the billet, after the fine equiaxed grain structure of the shell is established. When the secondary cooling water impinged the billet surface, the columnar grains grow out from the periphery and upwards against the heat flow. There is no

restriction on the growth of these grains from solute due to the dilute nature of the alloy or an equiaxed grain structure due to lack of nuclei within the melt, thus columnar growth was dominant from the base of the billet to the top.

The columnar grain in this billet is similar to that without shearing but there were simply more nuclei generated by shearing to increase the number of columnar grains thus forming a columnar structure of many grains instead of one with relatively few grains, where the fans consume other nuclei/ grains. Columnar growth then still succeeds over other grain morphologies during the growth competition, but dendrite fragments caused by the increased flow became nuclei and increased the number of grains. Obviously, it is the increased turbulence through shearing of the melt that has had this dramatic effect on the structure of the billet. Turbulent or forced convection creates more fragments than normal convection as we can see when we compare figures a and b, with and without shearing respectively. There are clearly more grains in the sheared material than without and the only difference between the two casts is shearing, increasing the turbulence and thus the fragmentation rate. It is these increased flow patterns that also influence the angle and deflection of the grains as they get closer to the centre. This is most obvious on the left side of the section. Turchin et al (Turchin, Zuijderuiyk, Pool, Eskin, & Katgerman, 2007) described how dendrites deflected in the direction of the flow when forced flow was applied to the solidifying melt and there is a change in the growth direction in the grains on this side. The flow patterns shown in Figure 4.1a demonstrate that the flows are very similar but not entirely symmetrical which suggests an increase in flow rate could be possible at opposite sides of the billet, thus creating the deflection in the growth direction of the grains.

In the centre of the billet, coarse grains have collected here directly under the solidification device. There were too few to block the columnar growth or heal the crack which, would have started in the butt of the billet and spread along the centerline to the top. They were transported here by the growing front and flow paths that naturally transport grains to the centre. Increasing flows transport grains to the core quicker than normal convection whilst simultaneously creating more grains through remelting of the dendrite arms (Jackson, Hunt, Uhlmann, & Seward III, 1966). Sufficient number of nuclei and an undercooled region for growth results in an equiaxed grain structure that blocks the columnar front. Although grain multiplication

has taken place here in our billet as a result of shearing, there were insufficient grains to block the columnar growth or heal the centerline crack.

4.1.2.3 MC-DC-P2 sump profile

The sump profile of Figure 4.5(c) is shallower compared to those of (a) and (b). The shear device was lowered to position P2 which brought the head of the device 25 mm closer to the solidification front. At this height, it took advantage of the sloped profile of the t-transition plate to better distribute the jets of melt from the shear device. This is also demonstrated in the simulated flow patterns shown in the MC-DC-P2 SolidWork diagrams in Figures 4.2a and b. It can be seen clearly that this has had a dramatic effect on the formation of structure of the billet.

The structure of the sump looks to be semi-solid in nature as there are different phases of already solidified material floating above the solidification front, identified as the dark regions within the brown Zn enriched zone. This solid has not mixed with the Zn and thus stands out as a different coloured section when etched. At the centre of the sump, the profile has become irregular suggesting an unstable interface between the liquid and solid phases, in the region of the mushy zone. This instability could be a result of conditioning being stopped as the shear device had been removed when the liquid zinc was added. By stopping the shear device, the forced flows rapidly decrease which revert the sump back to natural state during DC casting. Hot inflowing liquid from the melt stream interacts with the solidifying zone causing remelting of the solid phase close to the sump base. Thus the sump may actually be shallower and flatter than shown here during shearing, but the depth increased as melt conditioning stopped. Indeed, if we look at the area just above the broken sump interface at the centre, there is a region of zinc that has no semi-solid in it and could be considered fully liquid as it has reacted completely with the zinc. There is certainly a large amount of solid particles floating within the sump implying a significant amount of grain fragmentation is taking place with ample nuclei for grain growth to block the columnar growth and facilitate the columnar to equiaxed transition. This is supported by the refinement of the billet structure through the MC-DC process (Figure 4.5c).

There is a difference in the grain structure across the billet with two columns of coarser structure at both sides of the sample, approximately 20 mm from the surface (Figure 4.5c). The profile of the sump is not symmetrical or smooth either with steps in the profile of the sump evidently correlating with the columns below them. It would be beneficial to consider the cross-section in Figure 4.5c and the flow patterns in Figure 4.2 together at this point; the flow patterns influence the structure of the billet considerably. In Figure 4.5c, the step at the right side of the sump is more distinct than that of the left and higher suggesting uneven flow. This is supported by what appears to be solid phase floating in the top of the sump, with more solid present on the right side than the left. The coarse grain column on the left of the billet below the sump is wider and closer to the surface than the right side. Explaining this could be down to the fact that the shear device was not positioned directly along the centerline. However, the SolidWorks images show that even with the tool perfectly centred, there are uneven flow patterns. Flows and vortices are rarely even so there will be variance in velocities relative to the centerline of the vortex. The jet flows out of the shear device towards the left are stronger than those of the right in Figure 4.2 accounting for the bias in flow intensity on the left side of the schematic. This can be considered as the reason for the deviations across the section and sump profile.

It is interesting to see that there are eddies within the flows either side of the jets. Even more interesting is the difference in size from left to right and the relation of the eddy positions with those of the coarse grain columns. The coarse grain column at the left of Figure 4.5c is larger than that of the right which matches the larger eddy in the flow patterns of Figure 4.2a-b. This implies that the eddies facilitate the creation of these coarse grain columns. The cause of the columns of coarse dendritic grains is most likely a temperature gradient within the void. Eddy currents within the melt flows are zones in which the temperature will stabilize and possibly remain unaffected to a lesser degree than the rest of the melt, creating the required thermal gradient required for dendritic growth to dominate.

4.1.2.4. MC-DC-P3 Sump Profile

The sump profile in Figure 4.5d appears to take the stepped profile in Figure 4.5c further by having a flat profile at the periphery of the billet, which curves towards the billet centre arguably at the height at which the water impinges upon the billet surface. Shearing has been established during steady state casting for the entire cast at this point, which has to be considered when discussing this phenomenon. Because the casting speed, melt temperatures and water flow rates have all been kept the same, the sump shape and depth at the start of casting before shearing began would have been the same for each cast. Therefore, it is the closeness of the shear device at MC-DC-P3 to the solid front that has dramatically altered the sump profile to the point where it is essentially flat. With the shear device this low in the sump, the sucking force of the device has a much larger effect on the profile, effectively bringing it level with the bottom of the mould, or where the water impinges the billet surface. This reduces the transition region - slurry zone and mushy zone - in the centre where this zone would usually be largest. The complex heat transfer mechanisms from the superheat entering the mould, conduction through the solid to the surface, extraction by cooling water impinging the surface (secondary) and cooling of the mould (primary), are operating within a reduced area due to the shallow sump profile. This could result in the secondary water having a larger impact on the cooling rates at the billet centre.

Evidently there is an exaggerated stepped profile to the sump in image (d). When compared to the sump of MC-DC-P2, image (c), a step in the profile is evident also but far less pronounced. This is due to the remelting of the solid below the sump after the shear unit was removed and the incoming melt being sufficiently hot to induce remelting at the solid-liquid interface. The structure inside the sump indicates this quite well. There is evidence of remelting back into the solid at the edges of the sump and under the flat steps of the profile. The reason for this being that the steps are still cooled sufficiently by the water and the mould remains solid. The temperature increases in the centre of the billet as it is the farthest point form the cooling effect of the water. The liquid zinc has thus flowed into the remelted zone at the centre of the billet.

Another factor of the shear device being removed is the appearance of a centerline crack and feather grains around it. The overall grain structure of the solid in the sump is coarse on a macro-scale, again different to that experienced by the sump of position P2, implying a reduction in cooling rate as a result of melt conditioning stopping. The centerline crack is a feature of un-grain-refined or insufficiently grain-refined DC cast aluminium billets, but there is no centerline crack present in the material until after melt conditioning has stopped.

4.1.3. STEADY STATE TEMPERATURE PROFILES OF THE SUMP IN MC-DC CASTING

Figure 4.6 shows the measured temperature profiles during MC-DC castings. The plots display temperatures measured by thermocouples positioned at fixed but varied heights during casting; below the shear device (Therm 1), around the shear device exit holes (Therm 2), in the thimble through which the melt flows to the mould (Thimble) and in the Hot-Top (Hot-Top).

Figure 4.6a plots the temperature profiles measured when the shear device was at position P3. It is clear that the temperature was becoming uniform during shearing. As shearing begins the temperature profiles measured by Therm 1, Therm 2 and Thimble, drop dramatically with Therm 1&2 temperatures equalizing. Temperatures within the thimble follow the same profile as that of Therm 1&2 but remain 2-5°C hotter due to constant in-flow of hot melt. Half way through the cast the temperature increased rapidly at the point shearing stopped. Both this increase and the temperature decrease as shearing begins happen almost instantaneously. The temperature below the shear device (Therm 1) rises approximately 12 ºC from 660 ºC to 672 ºC, whilst the temperature around the shear device increases from 660 ºC to 675 ºC when shearing began. The fact that the temperatures below and around the shear device are so close indicates good mixing of the melt creating a homogeneous temperature field.

Above the mould in the hot-top, the temperature fluctuates during shearing whilst decreasing from its normal steady state temperatures. Of course with the in-flow of hot melt supplied by the furnace the temperature should not decrease as severely as

inside the crucible reservoir of the mould, but a reduction is measured nonetheless. To reduce the temperature in the hot-top similar to the reduction within the mould, risks freezing the melt in the hot-top and launders; this would result in a lost cast and considerable down-time. However it is significant that the hot-top temperatures are affected by shearing as it demonstrates significant up-flow due to vortices past the shear device.

In Figure 4.6b the temperature plots are much more erratic than those of Figure 4.6a, (ignoring the sudden change in temperature due to shearing being stopped). During this cast the rotation speed and height of the shear device was varied from 3000 rpm to 6400 rpm and positions P1 to P2 respectively. The areas of change are identified in the diagram, Figure 4.6b and attributed to the steady state temperature fluctuations. Although the temperature plots display a rapid reduction in temperatures and swift alteration in the melt condition at the point where shearing begins, there is a delay between changes. It must be noted here that only parameters exclusively related to melt conditioning were varied, thus; casting speed, water flow rates, melt temperature, melt level and alloy composition remained unchanged throughout.

Shearing began at height P1 in the thimble of the hot-top. Rotation speed was 3000 rpm and increased to 4000 rpm after 100 mm. The shear device was then lowered to position P2. This is indicated by the first large reduction in temperature in the diagram. To lower the device to position P2, which is in the mould, it felt prudent to reduce the rotation speed to 3000 rpm again as a safety precaution, reducing the risk of a bleedout due to unsettling the melt whilst lowering the shear device. It also offered the opportunity to compare the effect on temperatures at rotation speeds similar to those at position P1, but with the tool closer to the solidification front. The rotation speed of the shear device was then increased through 4500 rpm, 6000 rpm and finally 6400 rpm.

The temperature profile of P1 spinning at 3000 rpm showed an increase in temperature, measured by Therm 1 below the shear device. It is a very sharp increase in temperature of 15 ºC and it can be argued that the temperatures measured around the shear device (Therm 2) and in the thimble also rose by a further 2–3 ºC at the start of shearing. Not surprisingly, temperatures Therm 1, Therm 2 and Thimble equalized together closer than those measured at P2 or P3. What is

interesting is that the temperature within the hot-top above the thimble rose by the same 2-3 ºC at the start of shearing.

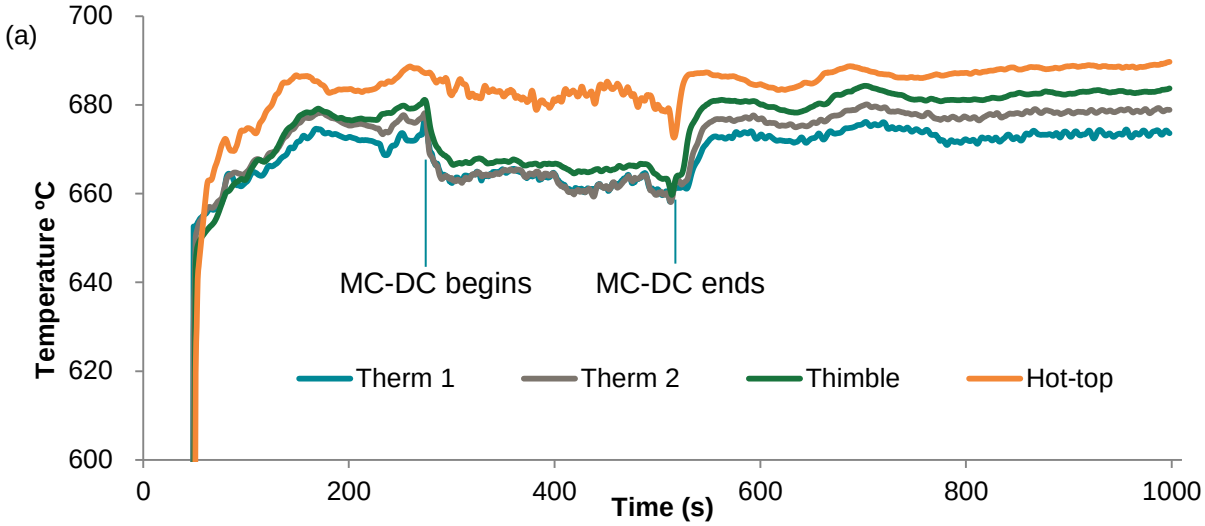

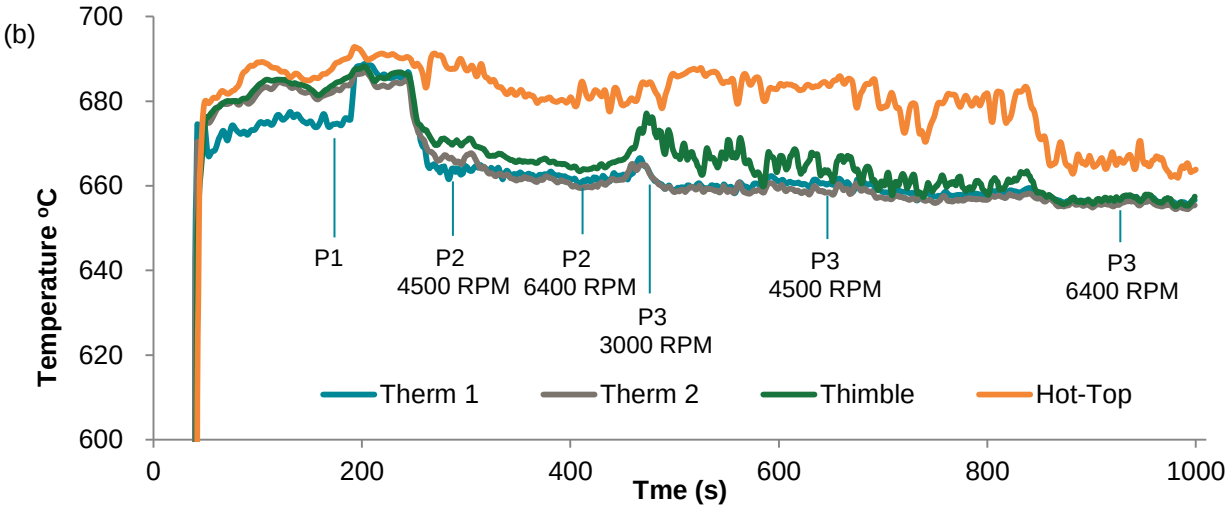

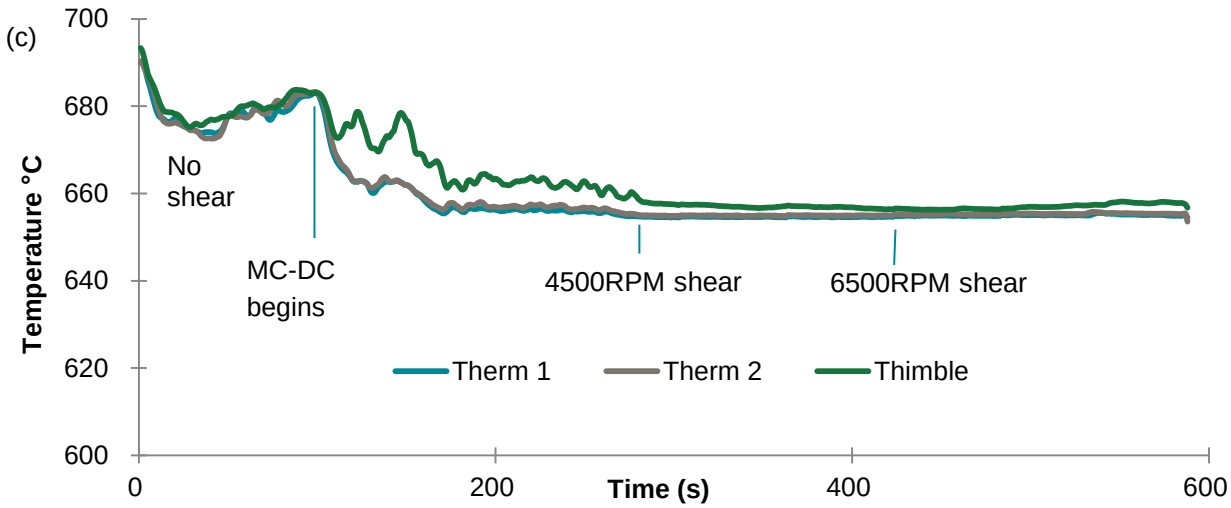

Figure 4.6 Temperature profiles of MC-DC billets cast in 8" diameter mould. (a) Shows profile with shear device at height P3. The shear was stopped halfway through the cast. (b) Shows temperature profile with both rotation speeds and shear device heights varied. (c) Full length cast at height P2 & varied speed. Temperature drops with stable conditions during casting were seen in the experiments carried out in this study whenever MC-DC was active.

This suggests that the forced flows generated by the shearing device spinning at 2500 rpm, are not sufficient to condition the melt at the solidification front/ mushy zone at position P1, but rather interact with the hotter melt entering the mould. Instead of drawing colder melt and solid from the mushy zone up through the shear device into the slurry zone, increased flow is happening at the hot-top which circulates hotter melt around the shear device in a much more confined area. At this position there is greater restriction upon the jet flows out of the shear device compared to positions P2 and P3 which are lower in the mould.

Below the shear device and at the top of the thimble the temperatures oscillate and decrease by 4 ºC to 684 ºC whilst Therm 2 measures temperatures 2 ºC cooler, 682 ºC. This thermocouple is positioned at the point where the jets exit the device. An explanation for the difference in temperature could be eddies' of stagnant flow around the shear device caused by jets rebounding off the walls of the thimble. These rebounding flows compete with the jets exiting the shear device forcing melt up and down which compete with incoming melt flow and natural convective flow from the mould respectively creating the eddies around the shear device.

As the rotation speed is increased to 4000 rpm the melt temperature drops 10 ºC in 10 seconds across thermocouples Therm 1, 2 and Thimble. There is a noticeable

step in the profile at approximately 675 ºC which relates to an increase in temperature at the hot-top. This could have been caused by an increase in melt temperature from the furnace or metal head at the hot-top. Its significance is indicated by the fact that this rise in temperature above the mould can affect the temperatures of the melt being sheared instantaneously, suggesting intense mixing of melt. The temperatures continue to drop with the temperatures below and around the shear device reducing further than that of the thimble. Colder melt from inside the mould is being drawn up through the shear device, indicated by the lower temperatures of Therm 1, and mixing around the shear device. The hotter temperatures of the thimble thermocouple show that although the melt in the thimble is mixing well with the colder melt of the mould, the hotter melt entering the mould keeps its temperatures above that of Therm1 and 2.

After 400 mm of cast log, the shear device is lowered to position P2 and the rotation speed reduced to 2500 rpm. Reducing the rotation speed and lowering of the device caused a rise in the temperature of the melt which validates the decision to lower the rotation speeds before doing so. This is to be expected as the velocity of the forced melt flow decreases caused by the delay whilst the melt adjusts to the new flow speeds. Stabilization of the temperatures below and around the shear device was swift and well equalized at 660 ºC. Above the head of the shear device, the temperatures in the thimble oscillated greatly in comparison. Such a low rotation speed does not offer enough mixing in this volume of melt also.

The temperature in the thimble decreased and didn’t stabilize until the rotation speed reached 6000 rpm. At 6000 rpm the temperature in the thimble equalizes with the temperatures within the mould, accompanied by a large drop in temperature in the hot-top also. This indicates that forced flows within the mould are able to mix melt from the hot-top and condition it with that of the colder melt from the mushy zone. Not only is the melt being drawn upwards into and through the shear device, then jetted out to the sides of the billet, but it also spins as shown by the spirals in Figure 4.4. This spinning melt could create the mechanism that draws the hotter melt down, as well as sending colder melt upwards past the shear device into the thimble, mixing it together reducing the temperature gradient from the solidification front to the hot-top. It can be argued that melt temperatures naturally drop during the cast due to loss through the launder system to the mould, thus the start melt temperature is hotter to

allow for this. However, the temperature loss of the melt is too large to be attributed to the system and can only be caused by mixing of the hot-in-coming melt with the colder melt at the solidification front, via melt conditioning.

In Figure 4.6c, the temperature plots are much more uniform during prolonged shearing compared with those of the Figures 4.6 a and b. This is due to the shear device being fixed at position P2 for the whole cast. Rotation speeds were increased from 4500 rpm to 6400 rpm after 1000 mm of log was cast. Thus steady state had been reached and fully developed during which time the log was conditioned at 4500 rpm. Then after a further 400 mm, the speed was increased to 6400 rpm until the end of the cast. The rotation direction and subsequent flow directions were kept the same; only the intensity increased thus steady state temperature profiles remained. The start of shearing is accompanied by the observed reduction in melt temperature in the regions around the shear device and thimble. The temperature plots fluctuate as the rotation speed increased to 4500 rpm at the start. This fluctuation is most apparent when comparing the temperature within the hot-top/thimble which is higher than that of the melt around the shear device. The temperature profiles of each thermocouple mirror each other but there is understandably a delay between the melt temperatures measured at the thimble and the shear device. The high flow intensity at the shear device stabilizes the temperatures faster within the mould. The results suggest that lower shearing speeds take longer to stabilize the temperatures and a swift increase of rotation speed up to the minimum of 4500 rpm is preferable.

This is only based on temperature results as any microstructure analysis to support this will be discussed in a later section. The DC cast billet appears to be able to withstand a rapid increase in rotation speed and the intense flows that are created. At 4500 rpm all melt temperatures within the thimble and mould are equalized and stable at 655 ºC, approximately the liquidus of this alloy. The temperatures remain stable at the liquidus even after the rotation speed is increased to 6400 rpm, suggesting that this is the maximum conditioning effect permitted by nature and the system. Thus the molten pool of metal within the core is conditioned with the incoming melt, creating a homogeneous temperature field at the liquidus temperature suitable for nucleation and survival of particles, facilitating the production of a fine grain structure.

4.1.4 MACROSEGREGATION

Spatial non-uniformity in the chemical composition on the scale of a solidified casting is a definition of macrosegregation (Nadella, Eskin, Du, & Katgerman, 2008). The fundamental reason for segregation is the partitioning of solute elements between liquid and solid phases during solidification (Eskin, Nadella, & Katgerman, 2008b). However, the partitioning of the elements during solidification and even their inhomogeneous distribution at the scale of a grain, induced by incomplete diffusion (so-called microsegregation) do not cause big problems in practice. Microsegregation can be eliminated by homogenisation treatment of the casting. What translates the microscopic partitioning and segregation to the macroscopic scale is the relative movement of liquid and solid phases in the two-phase zone (mushy zone) during casting (Eskin, Nadella, & Katgerman, 2008b). Because macrosegregation is at the scale of the casting, it cannot be eliminated or reduced through homogenisation practices, but rather by the parameters of casting. Thus the mushy zone is critical to the extent of the macrosegregation in a cast, which is mainly dependent upon the casting speed which extends or reduces the mushy zone hence macrosegregation is known to increase with casting speed. This links macrosegregation to the solid fraction of the mushy zone and the increasing solid phase there with the flow of liquid. This is of importance when we consider the explanations of the previous sections concerning the high turbulence and increased flows of melt conditioning and its effect on the mushy zone. The following section describes the results of compositional uniformity across the section of the MC-DC casting based on macro-levels.

4.1.4.1 OES Analysis of DC and DC-GR billet

Figures 4.7a, b and c plot the deviation in concentration of Si, Mg and Fe about the average of the material respectively. The measurements were taken across the radius from the surface of the billet to the centre. Shearing was not applied to the

melt of either cast but TiB_2 grain refiner in the ratio of Ti:B=5:1 at the rate of 1.0 kg per ton was added in billet DC-GR. Silicon (Si), magnesium (Mg) and (Fe) are the elements that contribute greatest to the material, forming the constituent particles that influence the performance of the material.

The three diagrams show very uniform trends with little deviation from the average or between each cast. However, silicon does show a negative trend below the billet average across the whole section (Figure 4.7a). An inverse segregation zone (ISZ) is present at the surface of both casts due to the high cooling rates of the mould (primary cooling). However, it is very much reduced compared with that of the DC-GR billet. Following on from this there is a zone of negative segregation identified by the dip in the plot at 9 mm form the surface, which is typical of a depleted zone found in DC castings due to the ISZ of the surface. The remaining trends are very uniform with the Mg and Fe results showing excellent correlation with the measured average for the billet.

The trends for each of the elements and billets describe a uniform distribution and suitable casting practice to develop quality billet for extrusion purposes and further processing. Analysis of the structure and constituent phases in further sections will

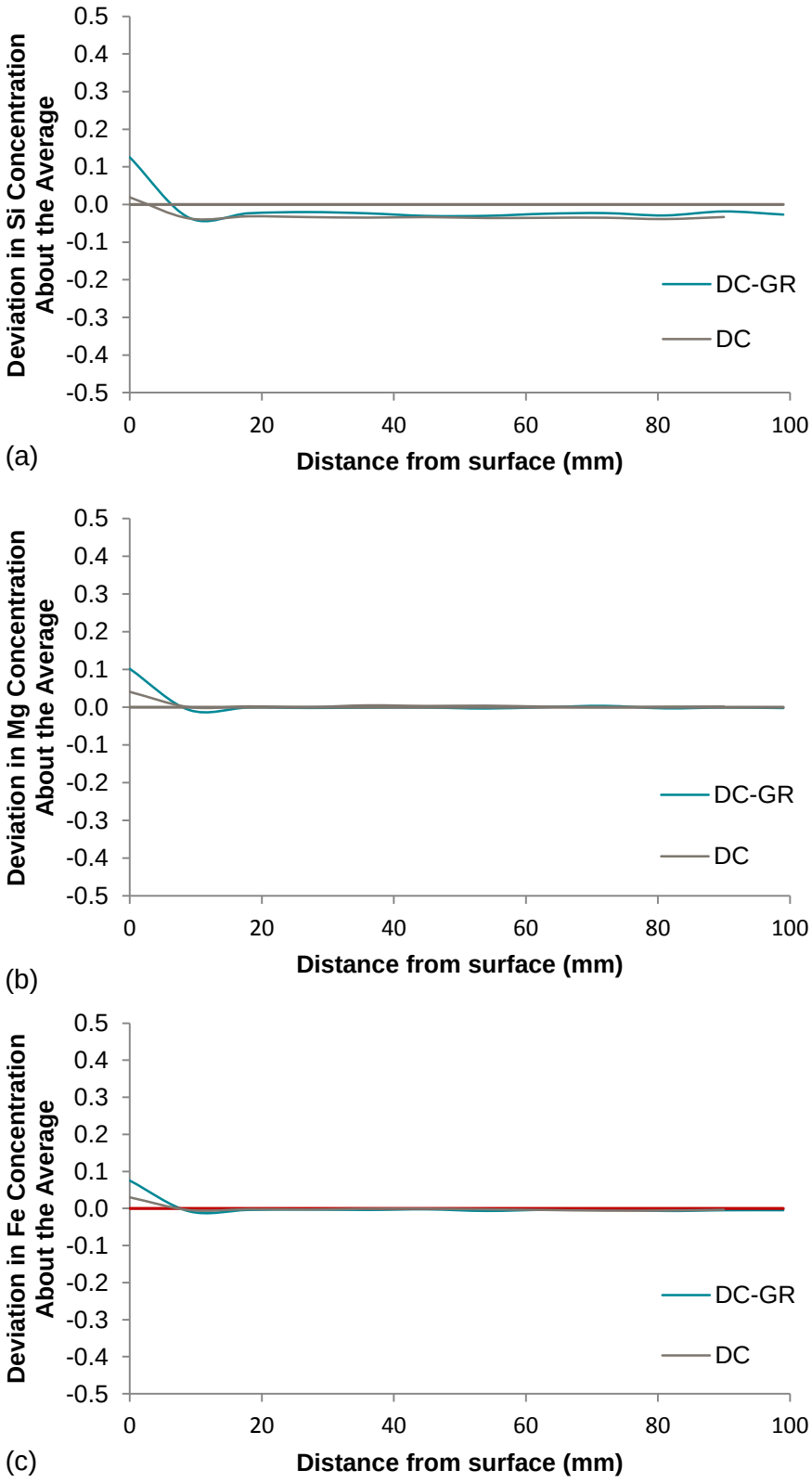

Figure 4.7 Deviation in the concentration of (a) Si (b) Mg and (c) Fe across the billet radius of DC cast billet containing TiB_2 grain refinement additions.

determine the accuracy of this statement. It is surprising considering the coarse nature of the un-grain-refined material that there isn't anything that could be regarded as macrosegregation occurring across the DC billet. Especially as the result is near identical to the DC-GR billet. This would certainly suggest that the process parameters are sympathetic to solutal gradients within the sump.

4.1.4.2 OES Analysis MC-DC-P2

The deviation in concentration of Si, Mg and Fe in MC-DC-P2 is presented in Figure 4.8. Shearing was applied during the cast with the device at position P2 and rotation speeds of 4500 rpm and 6400 rpm. What is noticeable is the difference in deviation from the average billet values between the two speeds. At 6400 rpm, deviation is positive above the average but becomes negatively segregated after the coarse grain bands, passing the average from a positively segregated concentration to a negative concentration halfway through the coarse grains. The deviation value for each of the measured elements remains below the average to the centre where there is a slight rise. In terms of plot profile for each of the elements, the trends mirror each other where the positive and negative values are. But Si again deviates negatively away from the average concentration across the billet as seen in the DC cast billet result (Figure 4.7).

This is not the case for the concentration profile at 4500 rpm. This trend is much more uniform to the point where the depleted zone seen after the ISZ of the surface is gone but is clearly present at 6400 rpm. Deviation from the average at the surface at 4500 rpm for Si is 0,058, Mg 0,074 and Fe 0,045 wt.%. This is lower than at 6400 rpm meaning that the size of the inverse segregation at the surface is reduced when sheared at 4500 rpm. At the centre of the billet where shearing is most intense, Si shows a negative value at -0,014 wt%, whilst Mg and Fe are 0.015 and 0.003 respectively. If we compare that with the same position at 6400 rpm, Si -0.086, Mg -0.043 and Fe -0.030, negative segregation occurs more severely at the higher speed.

It is interesting that the negative segregation at 6400 rpm occurs where shearing is most acute in the core of the billet implying more solute transport occurs at higher rotation speeds. If this result is compared to that of the DC billet, cast with the same

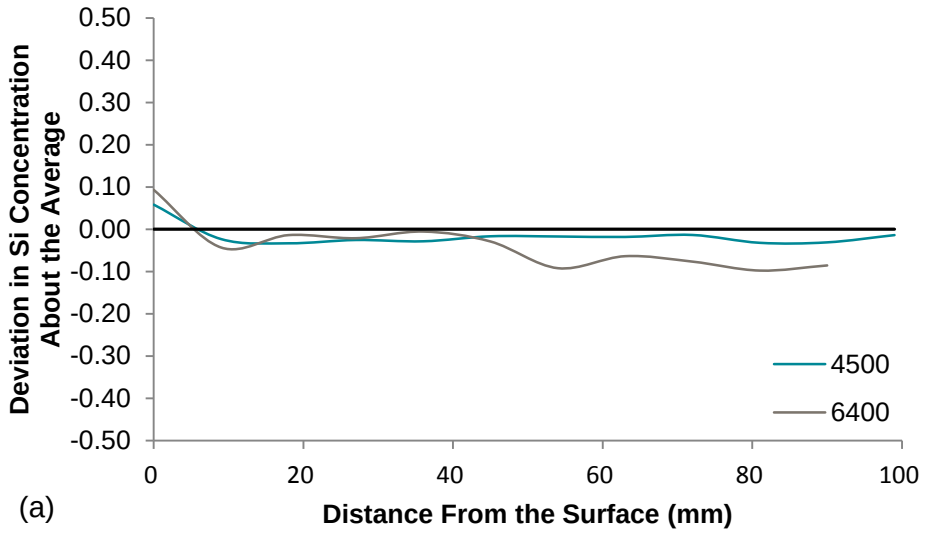

(a)

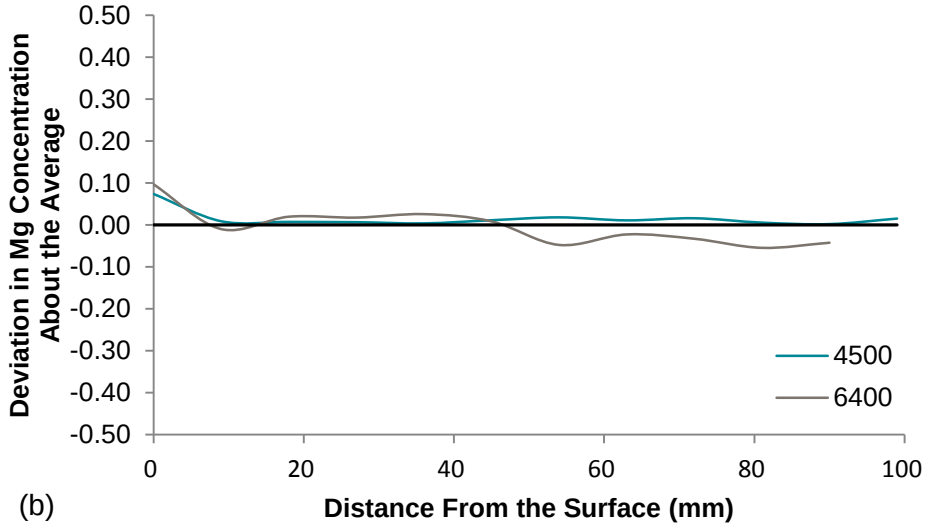

(b)

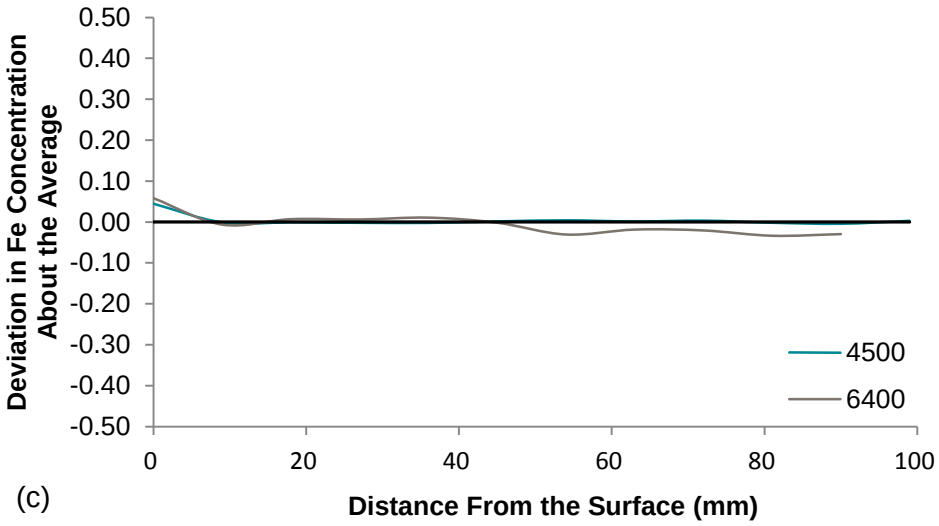

Figure 4.8 Deviation in the concentration of (a) Si (b) Mg and (c) Fe across the billet radius of MC-DC-P2 billet at 4500 and 6400 rpm.

process parameters, then macrosegregation has been enhanced by shearing especially in the centre where the element concentrations tend towards the negative, similar to the DC billet result. This would suggest that shearing does not adversely affect the segregation of Si at lower rotation speeds (4500 rpm). This is supported by the lack of segregation experienced by the Mg and Fe trends at 4500 rpm which deviate <0.010 from the average.

4.1.4.3 OES Analysis MC-DC-P3

The shear device was positioned at depth P3 for these series of experiments and an additional rotation speed of 3000 rpm has been included. Comparison with the results when the shear device was at P2 shows that this reduction in distance from the solidification front affects the distribution of the solute elements across the billet radius to a greater extent. The plots show little uniformity in concentration about the average with each diagram showing negative segregation trends until half radius.

After the coarse grain bands at 45 mm the trends for each of the three rotation speeds became positively segregated. There is a variation in effects between the three rotation speeds, 3000 rpm, 4500 rpm and 6400 rpm indicating that the rotation

speed determines the mass transport of the solute; thus flow patterns and amount of solid within the mushy zone are critical to the distribution of solute across the melt. Each element shows an increase in concentration after the coarse grains bands with 6400 rpm showing the largest increase; Si 0.087, Mg 0.141 and Fe 0.035 wt% compared to Si 0.009, Mg 0.081, Fe 0.005 wt% at 3000 rpm and Si 0.017, Mg 0.088, Fe 0.008 wt% for 4500 rpm. At 6400 rpm the vortex created would be strongest of the three speeds thus able to transport more solid and solute as seen previously. It follows that the inverse segregation at the surface concentration at 3000 rpm is largest of the three speeds and the deviation from the average is lowest just after the surface. This is due to the low rotation speeds and reduced flows trying to move sufficient melt. These flows will naturally be smaller than those of the flows generated at rotation speeds of 4500 and 6400 rpm as shown in Figures 4.1 to 4.3. Hence the deviation in concentration about the average at 4500 rpm falls between 3000 rpm and 6400 rpm and, is arguably the closest of the three speeds to achieving a uniform distribution of solute.

Noticeably, the trends for each of the elements and speeds drop towards the negative values at the centre due to the removal of solute at the solidification front.

The trend being similar for each rotation speed is most likely a cause of the close proximity of the shear device to the solidification front, resulting in the sucking force of the device being strongest here. The solute is most likely unable to be distributed because of the shape of the sump, trapping the solute within the core resulting in the increase in concentration after the coarse grain bands. Interestingly, whilst both Fe and Si concentrations fluctuate about the average, negatively and positively, the Mg concentrations are constantly positive. The partition coefficient *k* of Mg is 0.51 which means that more solute is held within the solid.

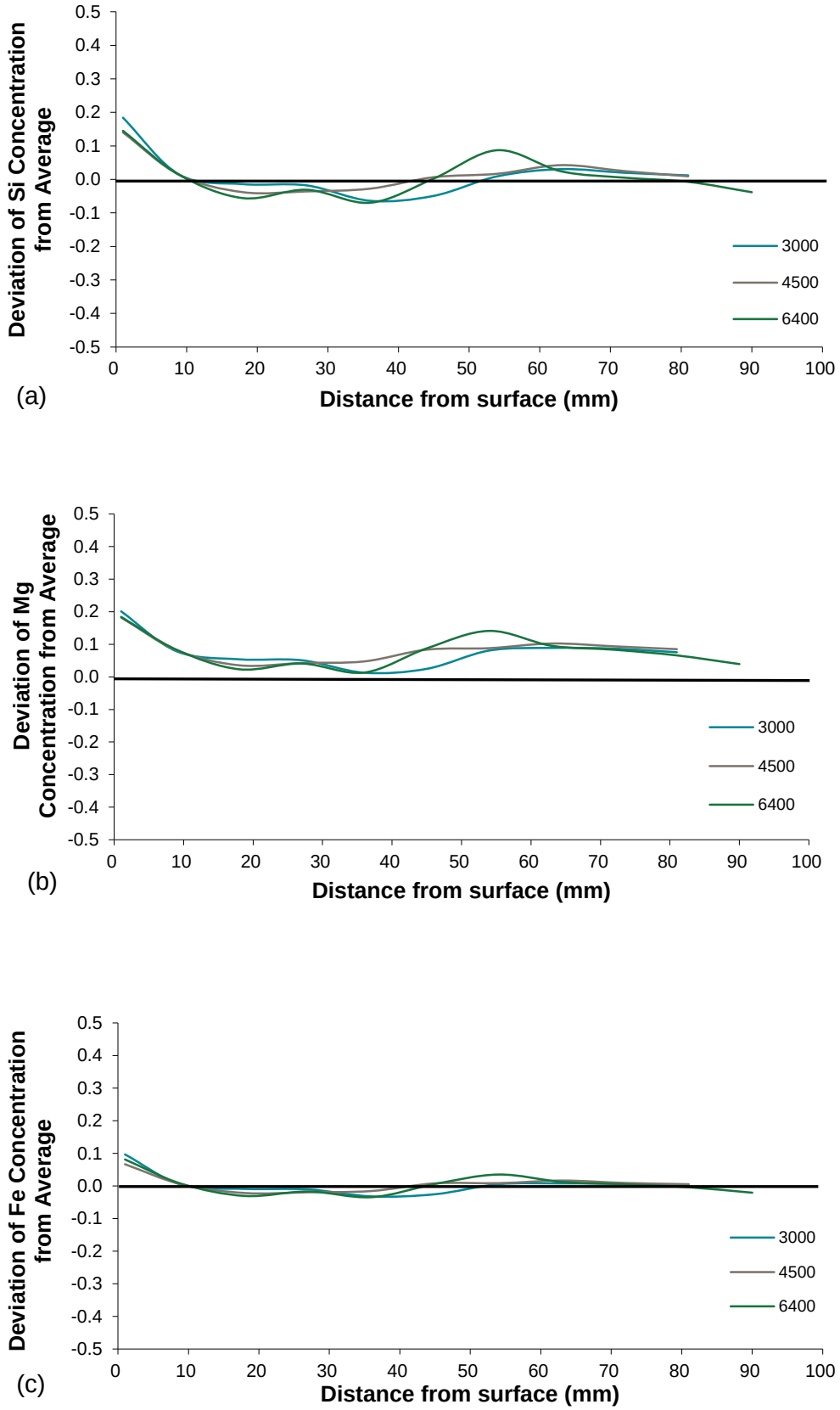

Figure 4.9 Deviation in the concentration of (a) Si (b) Mg and (c) Fe across the billet radius of MC-DC-P3 billet at 3000, 4500 and 6400 rpm.

4.1.4.4 OES Analysis MC-DC-P2-GR

Figures 4.10 a-c plot the elemental deviation from the average billet concentration across the radius of the billet that was cast with shearing and grain refiner combined. TiB_2 5:1 grain refiner was added to the melt at 1.0 kg per ton whilst the shear device was inserted at position P2 and operated at 4500 rpm and 6400 rpm. Again, Si, Mg and Fe are the elements measured.

What is apparent from the plots is the variation in concentrations between the two rotation speeds. The deviation from the average is greatest at 6400 rpm, similar to the results discussed previously, with larger ISZ at the surface and depleted zone extending 20mm into the billet. The overall trend for each element at 6400 rpm is increasingly negative towards the centre from approximately 45 mm or half radius of the billet. Between 25 and 45mm is a zone of enriched material which is positively segregated above the average before decreasing to negative values.

As seen previously 4500 rpm is considered to have the most acceptable plots compared to 6400 rpm but it is not comparable to the previous billets. The results fluctuate from positive to negative similar to that of the 6400 rpm concentrations but to a lesser extent. Deviation from the average is Si 0.0475, Mg 0.0375 and Fe 0.0247 wt% compared to Si 0.0733, Mg 0.0549 and Fe 0.0372 wt% at 6400 rpm describing a much larger shift between values about the average for shear speeds of 6400 rpm than 4500 rpm. The depleted zone is much less distinct at 4500 rpm with a positive trend that deviates Si 0.060, Mg 0.042 and Fe 0.004 wt% from the average at its largest. The 4500 rpm trend does not become negative until after 60 mm from the surface and even then the deviation is less than at 6400 rpm. This strengthens the argument that 6400 rpm may be too high a shear speed for this material at this cast speed and tool depth.

It is however interesting to compare these values with those of the DC and DC-GR billets. The plotted values were extremely uniform in these two billets with a short depleted zone and very small deviation from the average seen in the Si result only. Compared to the MC-DC-P2-GR material the result was very different. Large negative concentrations especially at 6400 rpm from the half radius point of the billet

through to the core are recorded implying an enhancement in the potential for macrosegregation.

In summary, although the trends of the MC-DC material were not as uniform as that of the grain refined billet, at 4500 rpm and MC-DC-P2, the concentrations were acceptably homogeneous with little deviation from the average. The deviation was in fact lowest of all the material tested including that of the grain refined material suggesting that processing optimisation is certainly required, but there is potential for MC-DC billet to be cast without macrosegregation.

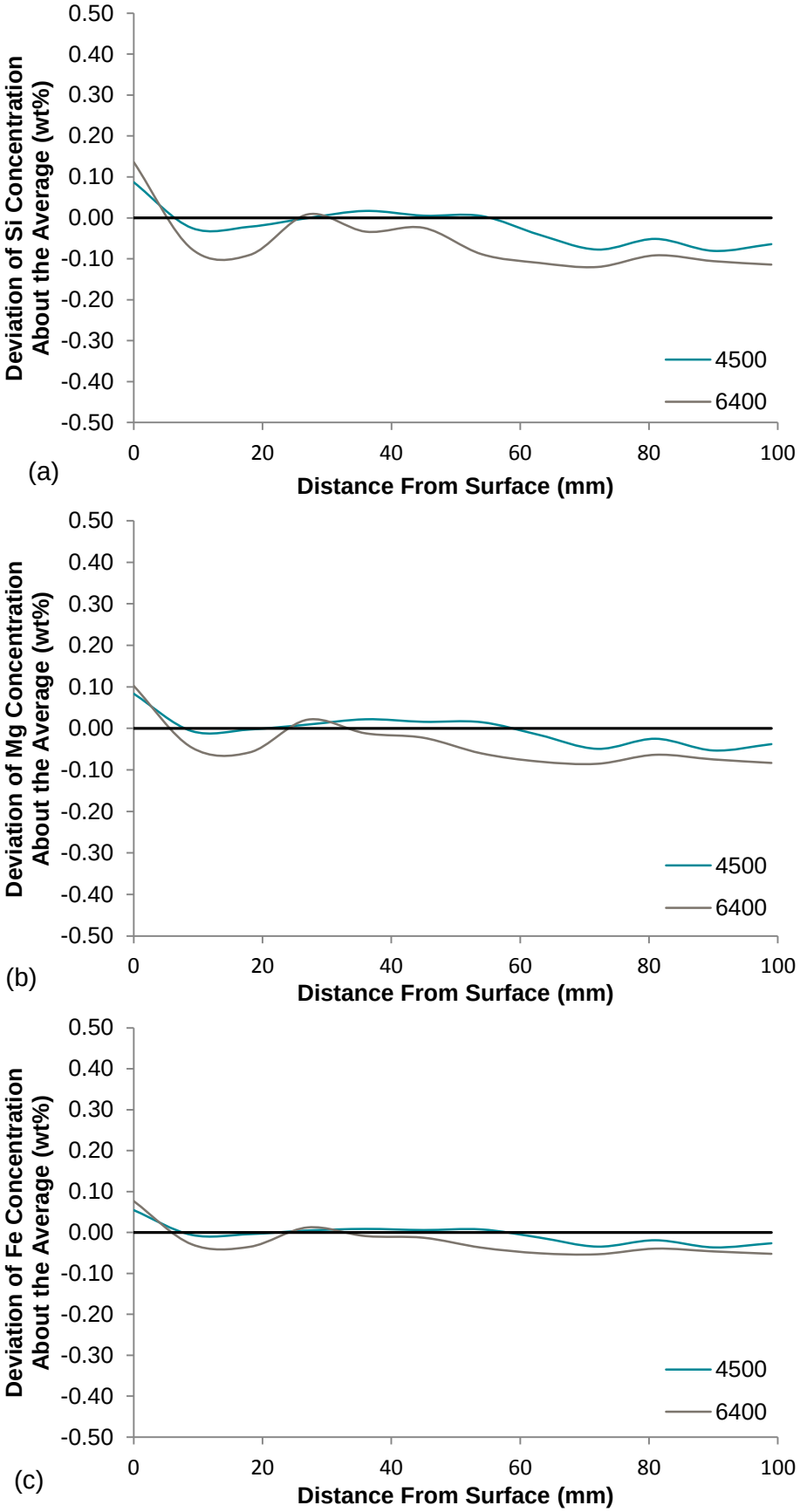

Figure 4.10 Deviation in the concentration of (a) Si (b) Mg and (c) Fe across the billet radius of MC-DC-P2-GR billet at 4500 and 6400 rpm.

CHAPTER 4.2 – RESULTS - MICROSTRUCTURE EVOLUTION

This chapter presents the metallographic findings of samples taken from the static mould experiments and DC castings performed at the BCAST laboratories, as well as billets cast at the Oxford Begbroke Science Park. The samples have each been analyzed similarly to ascertain the evolution of the structure when conditioned by shearing. The static mould experiments provided fundamental studies of material solidified and will be discussed first. The first MC-DC billet was cast using the lab scale DC caster at BCAST laboratory where we successfully combined high shear technology with DC casting technology. This success was then scaled-up at the industrial scale facility at Oxford Begbroke Science Park.

Over the coming pages the microstructure of the sheared billet will be presented along with the grain sizes and, comparison of the different morphologies that are found within the structure of a DC cast billet and what this means for the quality of said billet. Quality is determined by the performance of the material during down-stream processing and it is billet that is at the start of the process. A well-defined, uniform cross-section of equiaxed grains has long been established as the ideal structure for castings, offering peak productivity by reducing surface defects such as pick-up and streaking as well as increased extrudability. The properties relating to the mechanical aspects of the material are a factor of the elements in solid solution and intermetallics formed during solidification and modification by subsequent homogenisation. The intermetallics will be covered in the following section but it must be considered that the grain structure of the material is by no means absent from determining the strength of the material through the distribution of the constituent phases during solidification.

4.2.1 STATIC MOULD CASTING WITH MELT CONDITIONING

Four distinct zones are clearly visible in the macro-etched sample of Figure 4.11. Zone 1 contains the columnar grains of the ingot base; zone 2 is where a second band of angled columnar grains developed, edged with bands of fine equiaxed grains; zone 3 is the area around the head of the device consisting fine equiaxed

grains; zone 4 developed after the tool was extracted and is above the sheared area, consists of large dendritic grains. Note how the proximity of the solidification front to the shearing device affects the growth patterns of the zones.

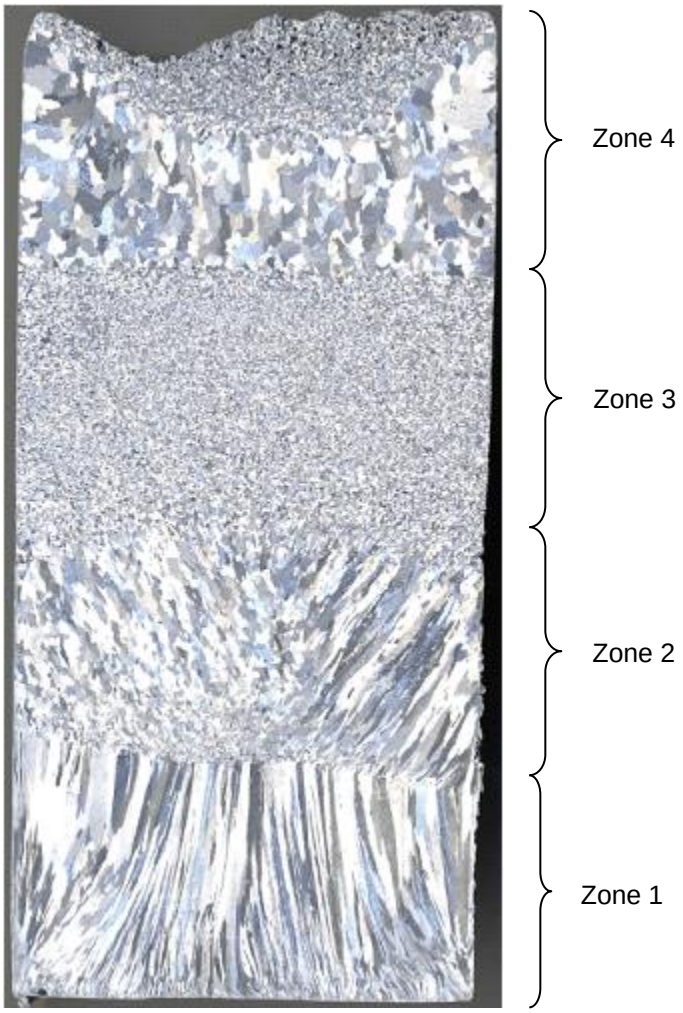

Figure 4.11 Macro etched sample showing static mould solidified billet after shearing, (Zone 1) contains columnar grains that grew away from the base into the hotter liquid, (Zone 2) mixed microstructure of coarse and columnar dendritic grains directly affected by shearing (Zone 3) the zone where the shearing device was inserted with a fine equiaxed grain structure, (Zone 4) coarse grain structure as a result of the shear device being removed and equilibrium returning to the melt.

The microstructure in zone 1 is columnar in nature with large grains growing vertically away from the copper base into the hotter melt, the microstructure of which is shown in Figure 4.12. The solidification front would have been essentially planar as there is a reduced cooling effect from the mould walls, as the mould was heated to the same

temperature as the melt and insulated to reduce heat loss. The columnar grains grew vertically and formed prior to the shear device being activated and as a result, zone 1 is assumed to be unaffected by shearing.

Zone 2 developed under turbulent flows generated by the shear device. Although it was not directly around the device, it was in contact below it and the sucking vortex created beneath the device was at its most intense here. This is evident by the shape of the equiaxed grains directly below the shear device which rise along the centerline towards the shear device. Irregular motion in zone 2 produced by the turbulence caused fluctuations in growth rates that facilitated the remelting of the dendrite arms, creating the grain fragments for nucleation.

Zone 3 is clearly equiaxed with a larger number of grains nucleating compared with the other zones. Here shearing was most intense, conditioning the liquid melt to a greater degree than other zones as the solidification front advanced. Above, zone 4 is coarse equiaxed in nature indicating a different growth rate compared with zone 3.

The coarse equiaxed grains of zone 4 develop after the tool is extracted suggests that the melt in this experiment was not conditioned on a whole by shearing, but conditioning was in fact localized around the tool. The cooling rate could also be less for the top section and the lack of equiaxed grain structure at the mould wall, suggests a reduced temperature gradient across the ingot. However the structure is equiaxed as fragments will have travelled to this part of the ingot also, transported by the vortex present from the transition between zones 1 and 2 until the surface. Into this vortex, fragments were inserted by the jets exiting the shear device. These jets will swirl around the holes of the shear device due to the close proximity of the mould walls; they simply had nowhere else to go but back against the jet flows coming from the shear device, creating swirling eddies similar to those seen at Position P1 in the previous section.

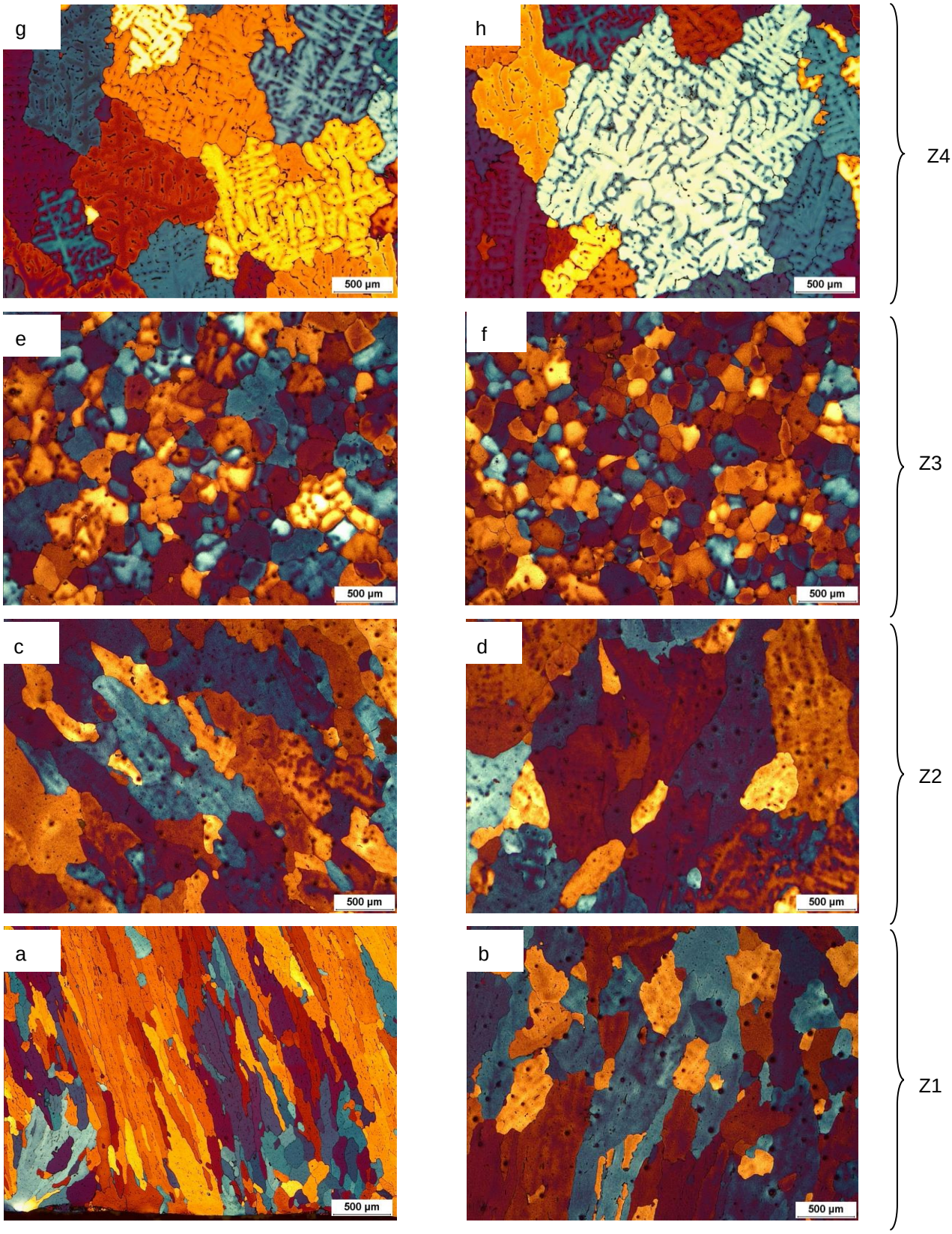

Figure 4.12 Micrographs obtained from the four zones of the material solidified in the static mould experiment. Zone 1 (a) shows elongated narrow columnar grains whilst image (b) shows the transition from columnar to cellular. Zone 2 (c) shows elongated cellular grains angled towards the height flow, image (d) from Zone 2 shows larger grains are present yet still angled. Images (e) & (f) of Zone 3 display a mix of dendritic and cellular equiaxed grains respectively. Images (g) & (h) of Zone 4 show large dendritic grains.

The vortex is able to move liquid up and down, transporting colder melt from and hotter melt to, the solidification front and vice versa, with the heat extracted through the solid phase, increasing cooling. The remelting of the dendrite arms is not necessarily down to hotter melt forced through the inter-dendritic regions alone, although it will clearly speed up the process, but rather fluctuations in heat and solute content interacting around the dendrite arms. A sudden decrease in growth velocity coupled with increased flow could radically alter the amount of solute and heat fluxes about the dendrites, causing local recalescence resulting in the remelting of the arms (Jackson, Hunt, Uhlmann, & Seward III, 1966). Growth velocity is reduced by the equalizing of temperatures and reducing the temperature gradients facilitating coarse dendritic growth with little fragmentation. It needs to be mentioned that the author does not discount the fracturing of dendrites through the initial “shock” of intense shearing upon the columnar grains of zone 1. Mechanical fracture would result in the instantaneous emergence of finer grains which, it can be argued, is exactly what has happened at the boundary of zones 1 and 2 blocking the columnar growth. Ahead of these grains remelting occurs in the zone as described previously. In Figure 4.11, between zones 1 and 2, crystals are seen trapped between the columnar grains. These crystals are 550 ± 80 μm and are effectively too large to be picked up and moved with the flows and therefore settle here. These crystals may have been caused by the initial shock of the increased flow rates and thus are a result of mechanical fracture rather than remelting. These grains are of a size and quantity sufficient to block columnar growth which is evident here.

It is obvious that along with the equiaxed and coarse dendritic grains, to the right of the centerline there is clearly a region of growth dominated by columnar grains angled away from the vertical. Angled growth of the columnar grains is towards the flow of hotter melt and solute gradient. The solute rejected in zone 2 is stirred and transported around the zone, but the hotter melt above is dilute as it has not been enriched by the rejected solute. It has been identified by others that flow rates alter the angle of columnar grains with increases in forced flow increasing the angle or deflection of the grains (Turchin, Zuijderuiyk, Pool, Eskin, & Katgerman, 2007). The grains to the right of zone 2 are more columnar then the grains on the left which are coarse dendritic, suggesting uneven flow by the shear device being off centre. However, the dominance of the columnar growth is most likely due to the sweeping of

solute from this section in comparison to the left. With the diameters of the mould and shear device stator being so close (mould Ø 55mm: stator Ø 40mm) any deviation from the centerline would be intensified resulting in preferred flow paths where the gap between the mould wall and stator is greatest. There are also a larger number of grains on the left side of the billet due to increased fragmentation or build-up of nuclei. There is clearly a slope in the transition between zones 1 and 2 from left to right, being higher with feather grain growth plus a larger number of equiaxed grains to the left of the centerline. Having an increased number of dendrite fragments, there is an increase in the number of grains resulting in a finer structure as more nuclei survive meaning more growth, less space to grow and finer structures. The reason for the coarse grain structure here is that the forced flow extracts the dendrite fragments from this zone and with increased cooling through the solid of zone 1, the gradients are sufficient for dendritic columnar growth to dominate. These grain fragments nucleate easily because being dendrites themselves or part of at least, they already have the same lattice structure of the bulk material thus they have lower interface energy.

Zone 3 is directly influenced by shearing and has a fine equiaxed grain structure with an average grain size of 150 ± 20 µm which is uniform throughout the cross-section. Fragmented grains will most likely have been transported to zone 3 from the solidification front and settled above the columnar mushy zone 2. These fragments became low energy nucleation sites for α-Al grains. Note that the grain morphology has changed from dendritic in zones 1 and 2 to cellular under direct effect of shearing, figure 2 zone 3. This would indicate that the growth rate has decreased along with the temperature gradient. Secondary dendrite arm spacing (SDAS) is finer if the morphology of the grains is dendritic. However in the case of the grains in zone3, they are more cellular in morphology with good uniformity. A reduction of grain size is systematic of an increase in cooling rate and or an increase in nucleating particles, with a high number surviving and becoming active nucleates. The flows created by the shear device transport melt up and down so in zone 3, the fragmented particles are transported here and mixed into a melt field that is homogeneous in temperature and solute. The fine equiaxed grains again block the columnar growth, this time from zone 2, with a clearly defined transition from columnar to equiaxed grains. The uniformity of the grain structure of zone 3 is evidence of the uniformity of

the melt here. The cooling rate and thermal-solutal distribution was the same throughout. As the solidification front moved upwards, at the point it was 5 mm (measured by thermocouple) from the base of the shear device, the shear device was turned off and removed. The void was filled by the fragmented melt and growing crystals that settled in this zone.

4.2.2. BCAST LAB SCALE MC-DC CASTING

These experiments were designed to implement MC-DC casting in a similar casting process to that of industry. Thus the billet would now be drawn down away from the water cooled mould with the metal fed to the mould via a hot-top system. As a reference sample shearing was not applied to the first cast, after which shearing was applied to all other casts. The four casts analysed in this section are;

- With no shearing and a casting speed of 220 mm/min
- Shearing device depth of 25 mm above the edge of graphite ring and a casting speed of 240 mm/min
- Shearing device level with the edge of the graphite ring and a casting speed of 220 mm/min
- Shearing device level with the edge of the graphite ring and a casting speed of 240 mm/min

Rotation speed of the high shear device was kept constant at approximately 3000 rpm with the device inserted and started as the billet begins to exit the mould for each of the casts. The alloy remained as AA6060 with no grain refiner additions during the casting.

The macro image in Figure 4.13a-b shows the polished vertical cross sections of a billet that was cast at 220 mm/min with shearing and no grain refiners added using the BCAST lab facilities. The billet was cut in half to aid polishing of the surface for macro etching. Shearing did not begin immediately to ensure the cast got underway without any bleed out problems. This resulted in a typical un-conditioned structure forming at the base, Figure 4.13a, consisting of fine equiaxed grains at the surface, followed by large columnar grains grown against the heat flow, and a coarse

equiaxed structure in the centre. The centreline crack present is a consequence of DC casting without grain refiner hence due to the solidification rate and cast speed. The crack began in the base of the billet (this has been removed from below the cross-section presented in Figure 4.13a) and progressed until the structure began to refine through shearing. In Figure 4.13a the crack heals a short way into the region of refinement. The transition from coarse structure occurs around 20 mm from the base of the sample and again there is a definitive zone where shearing begins, as the sump profile reacts to the forced flows as does the morphology of the billet structure.

At the point where the crack moves through the transition it appears to deviate from a straight line as it flows around large coarse grains that would have originally been floating crystals. These crystals may have been brought to the centre of the billet by the forced convection of the shear device.

The width of the billet sump becomes wider at the base, flattening the sump profile at the point where the crack heals, approximately 45 mm from the base of the sample. The sump width increases with shearing time thus, the refined structure of the billet increases in volume as more melt is conditioned all the way out to the billet surface. Therefore, the refined structure of the billet appears contained within a boundary of columnar grains forming a cone that increases in width as more billet is produced and the refinement spreads across the billet cross-section. This suggests that the sump profile in this billet became flatter as previously experienced in section 4.1. Layers of coarse grains that are present at 105, 95, 70 and 60 mm is evidence of this profile change as these coarse grains settle within the mushy zone of the sump when they become so large they can no longer be transported by the flows. Thus, they outline the sump profile as a layer of coarse grains. The profile becomes flatter as the region of refined grains becomes wider but is still essentially confined within the columnar grain boundaries that develop in the region of highest temperature gradient. The layers are not present within the top section of the billet indicating a much more uniform morphology with a reduction in the number of floating crystals.

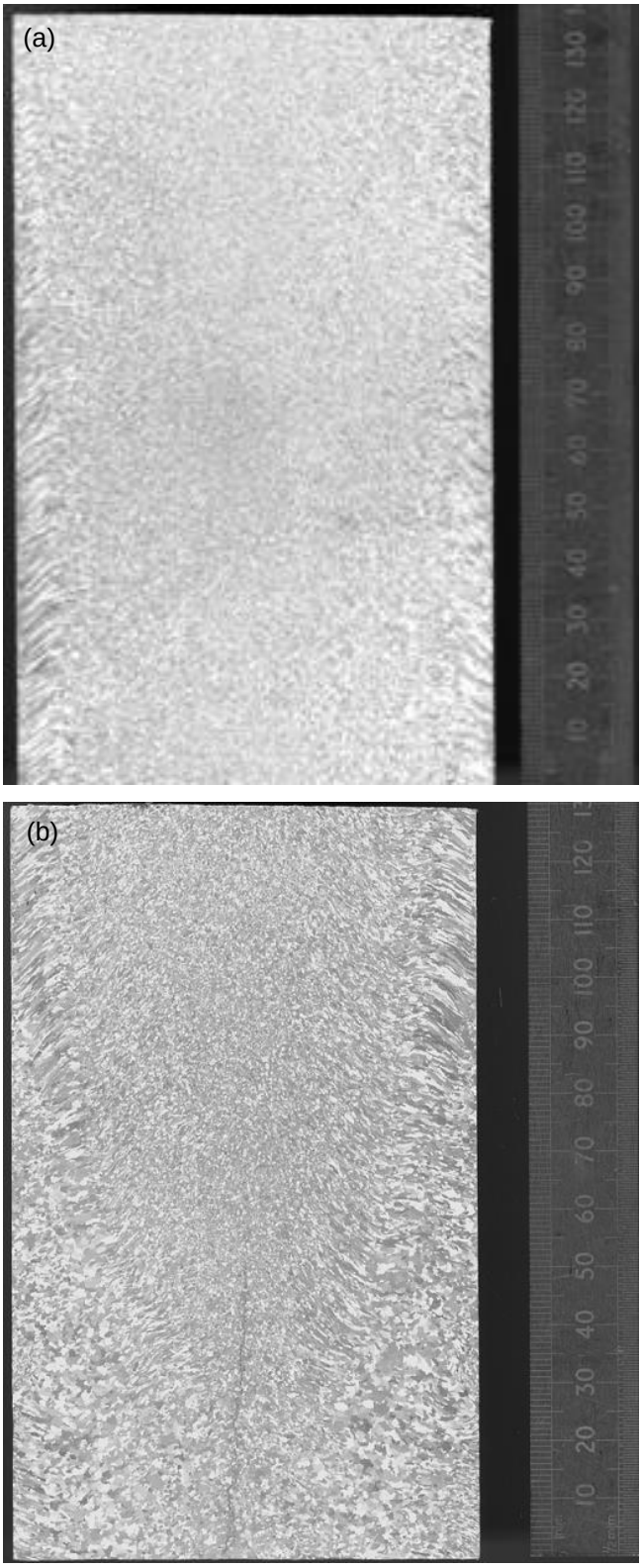

Figure 4.13 (a) Macro image taken from the base of a billet cast using the pilot scale DC unit at BCAST. Note the centreline crack that heals approximately 50 mm form the base of the sample as the grain structure becomes increasingly refined, (b) Top section of pilot scale MC-DC billet cast at BCAST. It shows increased refinement of the billet continues as melt conditioning progresses.

The columnar zone develops dendritically with arms growing along preferred crystallographic directions (<100>) towards the centre of the billet against and parallel to the direction of heat flow (Henry, Minghetti, & Rappaz, 1998) (Henry, Jarry, & Rappaz, 1998) (Henry, Gruen, & Rappaz, 2004). This growth is blocked by the establishment of the coarse equiaxed zone in the centre of the billet which is the reason why large feather grains aren't dominant in this billet. Thermal-solutal convection remelting the dendrite arms at the root and moving them to the centre is a possible mechanism for this phenomenon, whilst a constitutionally undercooled field in the core allows the nucleant particles to survive. The mechanism is different during shearing which also decreases the temperature gradients across the melt but enhances heterogeneous nucleation through the significant increase in the number density of nucleating particles and subsequent intensive melt convection. Rapid transportation of nuclei to the core of the billet increases the number of grains inside the core, thus resulting in the finer structure present. There is a very definite change between the non-sheared and sheared region of the casting suggesting some mechanical aspect to the fracturing of the dendrites. However, in the present study, due to the near isothermal temperature field and uniform constitutional field by intensive melt convection, dendritic growth is impossible in the sump (Ji & Fan, 2002). Solidification is suggested to proceed through enhanced heterogeneous nucleation on dispersed oxide particles and subsequent equiaxed globular or dendritic growth. This condition would rule out the remelting mechanism.

The columnar grains appear to form at the point where shearing begins close to the centreline and moving progressively out towards the surface with increasing length of billet and shearing time, to the point where they essentially vanish as the gradients near the surface decrease. For the coarser columnar grains formed near the surface, the angled orientation developed with growth towards the flow of hotter melt, away from the cooled surface. The wider regions of the coarser columnar grains in the current study are due to the specific mould assembly in BCAST with larger mould height.

The grain structure is shown in Figure 4.14a-h. Without shearing the grains have a coarse dendritic structure throughout as shown in Figures 4.14a and b with thicker branches and larger arm spacing at the core of the grain, with finer arms and spacing at the periphery. Cooling rate differences are attributed to this coarsening as across

the billet the cooling rates vary due to the very nature of DC casting. Cooling rate is greatest in the region where the water impinges onto the surface of the billet, reducing with distance from the surface to the centre. However, cooling rate can increase through increased growth rates as the solid around the equiaxed grain acts as the heat sink for cooling. Naturally occurring convection carried the dendrite fragments from the solidification front to the centre where these grains will have coarsened. When the grains became large enough, they sank and settled in the sump. This settlement resulted in contact with solid increasing the heat extraction from the grain thus increasing the cooling rate and refining the dendrite arm spacing. The main stems of the dendrites are coarse with the arms becoming finer with increasing distance from the core of the grain.

The grain morphology in the billets cast with shearing in the hot-top above the graphite ring substantially decrease in size compared to the billet grain size without shearing, whilst retaining a dendritic morphology. It is clear from the images in Figure 4.14b - c that the grain morphology changes significantly through the cross-section of the billet. At the surface, the grains are coarse dendritic in nature with thick dendrite arms compared with the dendritic grains in the billet centre. Also, the arm thickness is similar throughout the grain rather than coarse arms in the core that become finer at the periphery, indicating uniform growth conditions. The majority of the grains at the centre take on globular/rosette morphology with larger dendritic floating grains present that have a much finer DAS compared with the surface region, suggesting higher cooling rates.

Figure 4.14e-f shows the structure of the billet cast at 220 mm/min with the shear device positioned at the edge of the graphite ring. The grains are predominantly globular from the surface to the core of the billet. The average grain size is 139 ± 14 µm with the smallest grain size at the surface, 121 µm due to the increased cooling rate at the point of contact with the mould and water impingement. The grain size increases towards the centre due to the decrease in cooling rate compared with the surface but the standard deviation suggests a relatively uniform structure with a variation in size of 14 µm across the billet radius. There are agglomerations of dendritic grains within the globular structure that increase in volume towards the centre and may be attributed to the grain size variation as they grow into larger grains then the globular grains. What are interesting with the structure are the grains that

formed as rosettes but became dendritic at the periphery of the grains. This is indicative of an increase in cooling rate during the final development of the grain which indicates the grains grow in a globular fashion from increased nuclei being present, sank when too large to be transported further, coming into contact with the solid that increased the cooling rate causing the dendritic morphology. The globular grain structure creates segregation of the constituent particles to the grain boundaries whilst in the equiaxed dendritic grains the constituent phases are more inter-dendritic. The shell zone as seen in the macro section is large in this billet which is a factor of the mould technology used, as it has a large graphite ring depth and high cooling.

The grain size of the billet cast at 240 mm/min with shearing at the edge of the graphite decreases further so that it becomes the lowest of the four casts analysed here at 120 ± 12 µm. The increase in casting speed must be considered a factor in this decrease of grain size (Eskin, Zuidema Jr, Savran, & Katgerman, 2004). However, it is obvious in Figure 4.14g - h, that the grains at the surface are very columnar dendritic in nature. This is different to the other casts and could be attributed to the faster casting speed that increased the gradient at the surface by introducing the cooling effect of the water onto the surface quicker, providing the driving force for increased growth rate. Another factor could be that the increased casting speed did not allow sufficient nuclei to be transported in time to restrict the growth before the columnar grains grew. However, overall the grains have a fine equiaxed rosette morphology giving a lower average compared with the billet cast at 220 mm/min.

Plots of the grain size values across the radius of the billets for the four casts analysed here are shown in Figure 4.15. There is a clear decrease in grain size when shearing is applied to the melt compared to without shearing as expected but, significantly there is a decrease in grain size when the shear unit is lowered to the edge of the graphite ring, ultimately reducing the distance between the solidification front and shear device.

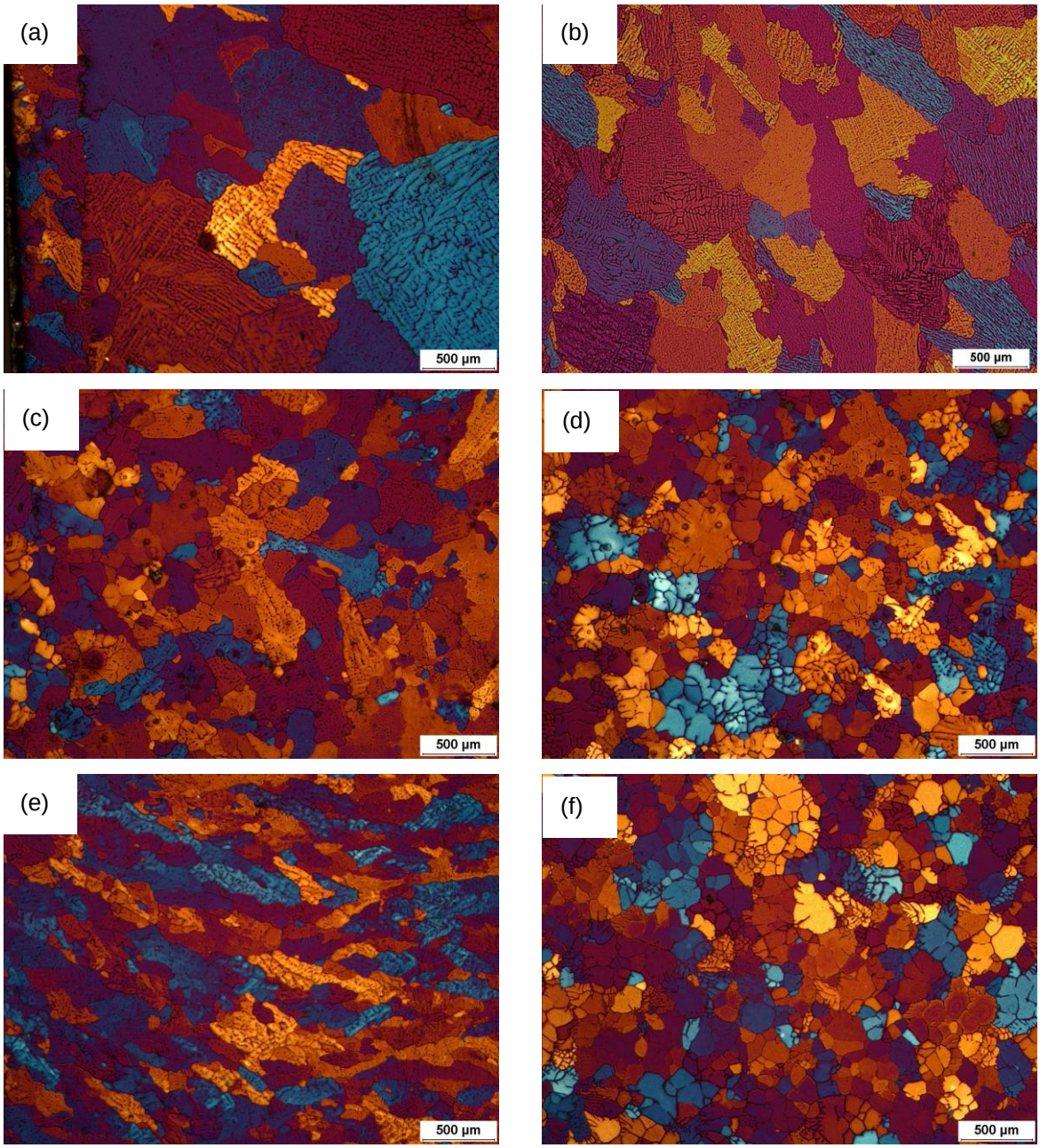

Figure 4.14 Grain structure images for MC-DC billet cast at BCAST. Each group of images shows the surface and centre zones respectively a-b) No shear, c-d) MC-DC level with the graphite ring at 220 mm/min, g-h) MC-DC level with the graphite ring at 240 mm/min.

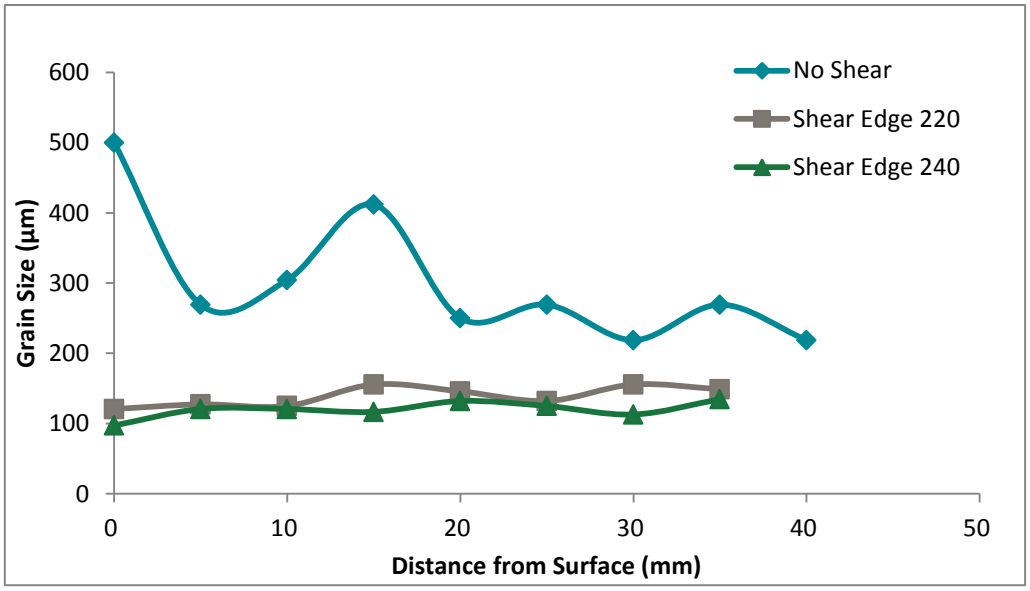

Figure 4.15 Diagram showing the average grain sizes across the billet radius. The billet was cast on the BCAST pilot scale DC unit at varying casting speeds and with high shear device positioned level with the edge of graphite ring in relation to the mould.

When shearing is applied at the edge of graphite ring, the average grain size is below 160 µm across the radius for a casting speed of 220 mm/min, whilst increasing the casting speed to 240 mm/min caused the average grain size to be below 140 µm. Both of these average grain sizes would be acceptable for industry, which are typically 100 µm or less with a globular morphology across the billet cast with grain refiner additions.

4.2.2.3 P* Analysis of lab scale cast billet

Figure 4.16 plots a quantitative assessment of the distance between precipitates, named P*, the average size of particle free zones in as-cast structures. The P* assessment gives a good indication of the grain morphology through the repartition of the final liquid at the end of solidification; whether the constituent phases are in the interdendritic spaces or at the grain boundaries, indicates the size and morphology of the grains. Those grains with high P* values indicates globular grains formed with slow growth velocity whilst low P* values reveal fast growth conditions that lead to dendritic grains being dominant. The lower values are of course due to the finer arms

of the dendritic grains compared with those with rosette morphology, which have a much larger arm thickness almost on the scale of the grain size.

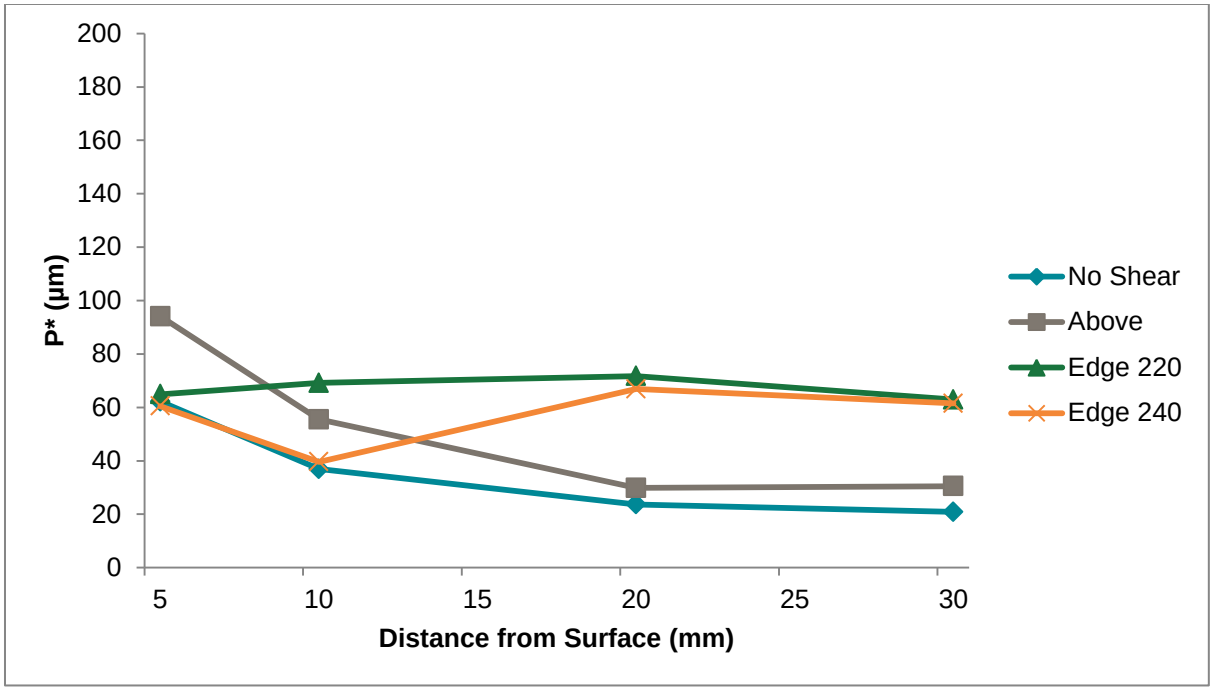

Figure 4.16 Diagram showing the average P* value across the billet radius. The billet was cast at BCAST using the pilot scale DC unit. The P* value gives an indication of growth rates by measuring the distance between constituent particles. A high P* value denotes a low growth rate and vice versa.

Accompanying the P* values in Figure 4.16 is the series of micrographs in Figure 4.17. These are microstructure images of the grains from light optical microscopy, used in the measurement of particles for the P* analysis. These images relate the P* values to the corresponding microstructure, illustrating the coarseness of the dendrite arms or rosette morphology at the largest P* values, or refinement with the lowest. In Figure 4.16 there is a clear divide between the billets cast with the shear device level with the graphite ring and the billets without shearing and the shear device in the hot-top. Therefore, the analysis of these casts will be split and summarised at the end of the section for clarity. The analysis of the trends in Figure 4.16 will be accompanied by the associated images of Figure 4.17 so; images of the billet without shearing are, a and b; images with shearing in the hot-top are c and d; images with shearing when

the shear device is level with the graphite ring cast at 220 mm/min and 240 mm/min are e – and f, g and h respectively.

The billets cast without shearing and with shearing above the graphite ring have similar trends but differing P* values, indicating a difference in the growth rates when shearing is applied. If we consider the microstructure images of Figures 4.17 a, b, (without shearing) and c, d, (shearing above the graphite ring) the structure became more equiaxed with cellular and equiaxed dendritic grains having formed when shearing was applied. The overall morphology of the microstructure for both casts is dendritic with refinement of the dendrite arms increasing towards the centre of the billet, but there has clearly been a coarsening of the dendrites at the centre and globular/ rosette grains are present. Rosettes are indication of grain refinement and this is clearly as a result of shearing, most probably through unique grain growth under high shear due to forced intensive convection (Ji & Fan, 2002). What is apparent from Figure 4.16 is that the surface region of the billet cast with the shearing device stands out from the three other casts with a higher P* value, thus larger distances between the constituent particles. A larger P* value signifies slower growth rates that leads to coarsening of the structure and a rosette structure is dominant at the surface. This contrasts against the surface structures of the three other casts which are dendritic columnar and dendritic equiaxed. There is obviously increased nucleation at the surface of the billet compared with the other casts when the shearing has been within the hot-top, which could possibly be due to the multiplication of grains within the melt through dendrite remelting, before the surface makes contact with the mould wall (cooled graphite ring) thus modifies the structure of the surface, whilst the shearing inside the mould does not have the chance due to increased cooling rate and subsequent higher growth rates.

We now consider the P* values of the billets cast with the shearing device level with the graphite ring. The trend for the billet cast at 220 mm/min is certainly the most uniform of the four casts displayed here with low growth rates across the billet radius. These growth rates reduce from the surface across the billet radius but naturally increase at the core region towards the centre where shearing is most intense. The microstructural photos (Figure 4.17 e, f) show a globular/ rosette structure throughout the cross-section of the billet radius that become more dendritic as the growth rates increase at the billet core, collaborating with the P* values. The uniform nature of the

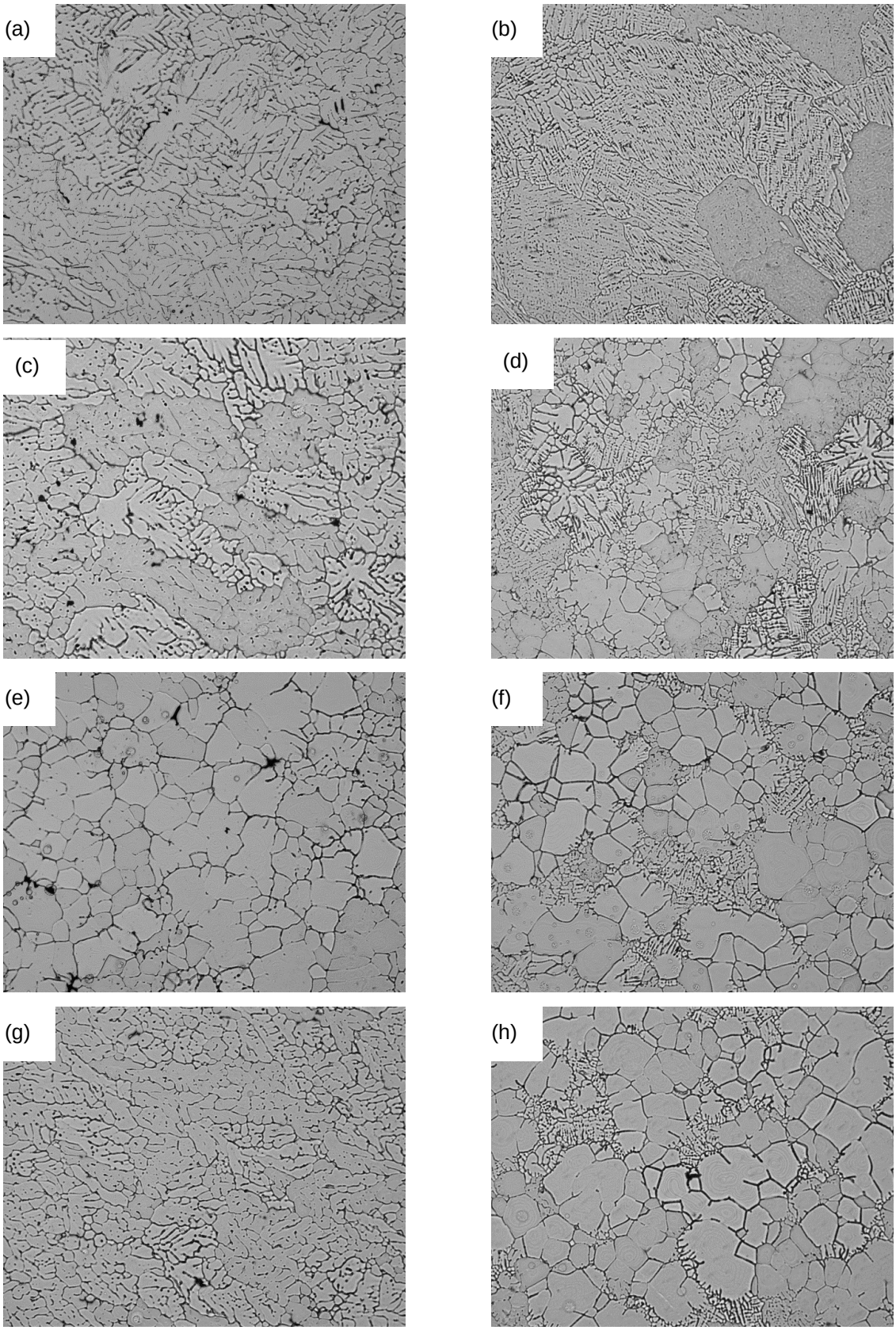

Figure 4.17 Microstructure images that correspond to the P* values of the BCAST DC pilot scale billet. Each group of images shows the surface and centre zones respectively a-b) No shear, c-d) MC-DC 25 mm above graphite at 240 mm/min, e-f) MC-DC level with the graphite ring at 220 mm/min, g-h) MC-DC level with the graphite ring at 240 mm/min.

growth rates suggests a homogeneous melt with reduced thermal and solutal gradients as the growth rates are similar across the billet with a relatively uniform structure. Analysis of the intermetallics will determine the level of solutal homogenisation which is covered in the following section. In the meantime this is a reasonable assumption due to the evidence presented up to this point.

When comparing the P* values of the billet cast at 240 mm/min there is a clear difference to the P* values at 220 mm/min, to the point where the growth rate can arguably be considered changeable from the surface to the billet centre. The growth rates increase after the surface similar to those of the un-sheared billet, changing the microstructure from coarse dendritic grains to a rosette structure as the growth rates decrease. Figures 4.17e, h shows the morphology change from dendritic to a more cellular/rosette type similar to that of the cast at 220 mm/min; however the increase of cast speed appears to have un-stabilised the process from the uniformity of the slower cast. High growth rates are most likely a result of the cooling and solidification rate increase when the casting speed is increased. The grain size is smaller than those measured in the billet cast at 220 mm/min which is refinement one would expect to find when increasing the cast speed. Couple this with refinement generated by shearing and there is evidently an argument for the potential to increase productivity and achieve a uniform, refined structure with the MC-DC process.

4.2.3 INDUSTRIAL SCALE MC-DC CASTING

4.2.3.1. Industrial Scale DC Cast Billet With and Without Grain Refiner

For the first time, an industrial trial of melt conditioned DC casting was successfully performed at Oxford University's Begbroke Science Park. The sump profile presented in the previous section show a clear evolution in the billet structures from coarse un-conditioned and un-grain-refined billets consisting of large feather grains, to refined structures of equiaxed grains in MC-DC billet. Achieving fine equiaxed structures industrially requires the common practice of inoculation through grain refiner additions that saturate the melt with nucleant TiB_2 particles. That is where this section begins, with the analysis of grain refined billet that had TiB_2 5:1 grain refiner rod

added at the ratio of 1.0 kg/tonne during the cast. The rod was fed into the melt before it reached the mould. Apart from this addition to the casting practice, none of the process parameters were changed over the non-grain-refined, un-sheared and sheared billets. Figure 4.18 shows the macro etched vertical cross-section of the billet. A fine equiaxed structure is evident typical of the type seen by industrial techniques when grain refiner is added. The structure appears extremely uniform with a small shell zone and no evidence of coarse structures or defects large enough to the naked eye. It is certainly of a comparable level to that of industrial billet.

Figure 4.19 is a micrograph of the grains accompanying Figure 4.18. The microstructure was observed by light optical microscopy (LOM) after being anodized to facilitate observation of individual grains using polarized light for grain size measurement. Considering the morphology of the grains in the image, it could certainly be considered dendritic as dendrite arms finer than the size of the grain are present; if the dendrite arm spacing was only slightly smaller than the grain it would be considered a rosette or cellular and if no dendrite arms were present in spherical grains then that would be a globular structure. A dendritic grain structure can represent a coarsening of the structure over the industrially typical globular grain structure that is seen when grain-refiner additions are made during a cast. The average grain size is usually smaller for industry with the grain sizes as low as 60 – 80 µm being the norm, something industry strives for in the belief that smaller, finer grains are the most beneficial. Without a doubt, small equiaxed grains structures are the optimum for performance downstream but the structure achieved here is certainly acceptable for industry despite being dendritic in nature. The cause of the dendritic structure is most probably an optimum amount of grain-refiner used compared with over additions made routinely in industry, coupled with a high cooling rate.

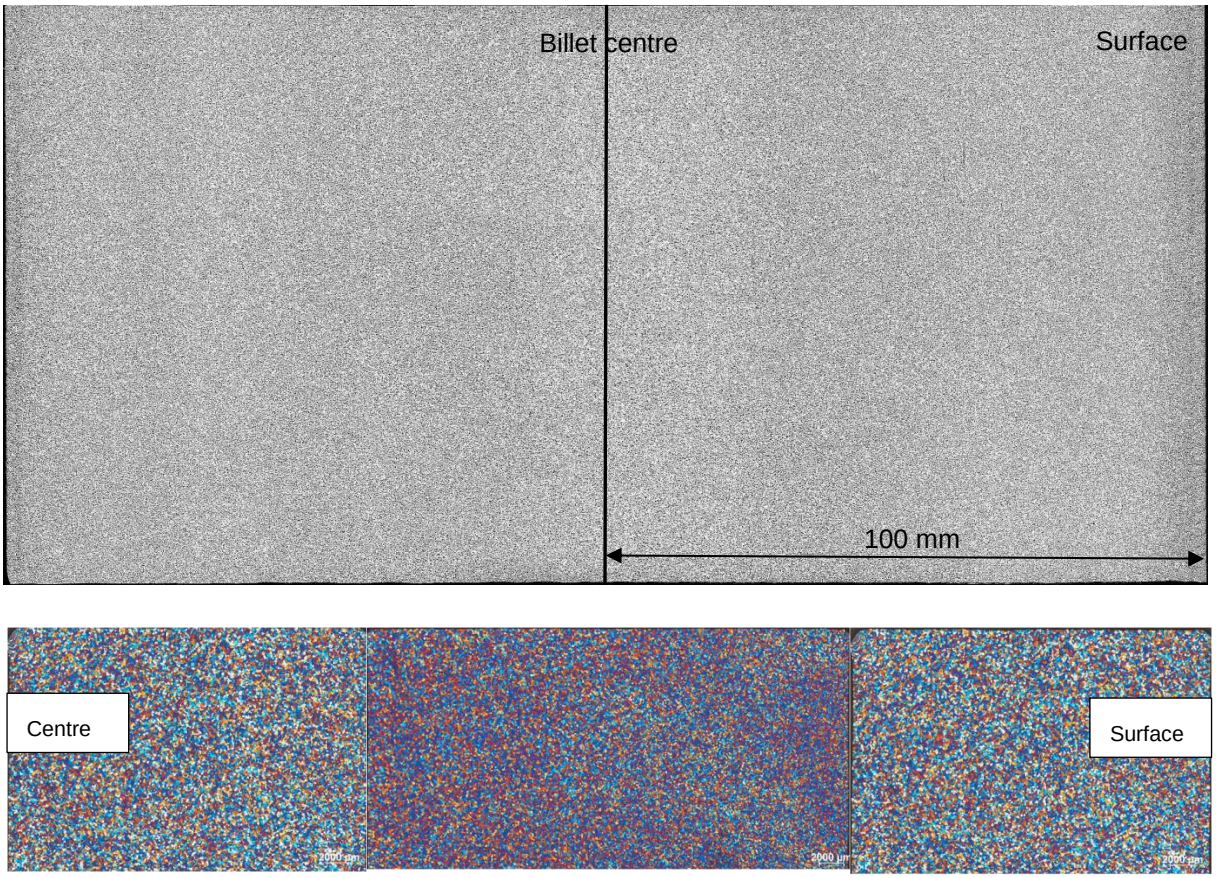

Figure 4.18 Macro-etched vertical cross-section of the DC-GR billet. TiB=5:1 AlTiB grain refiner was added during the cast but not shearing. Mosaic of images showing the microstructure across the DC-GR billet radius and is 100 mm across from surface to centre. Scale bar reads 2000 µm.

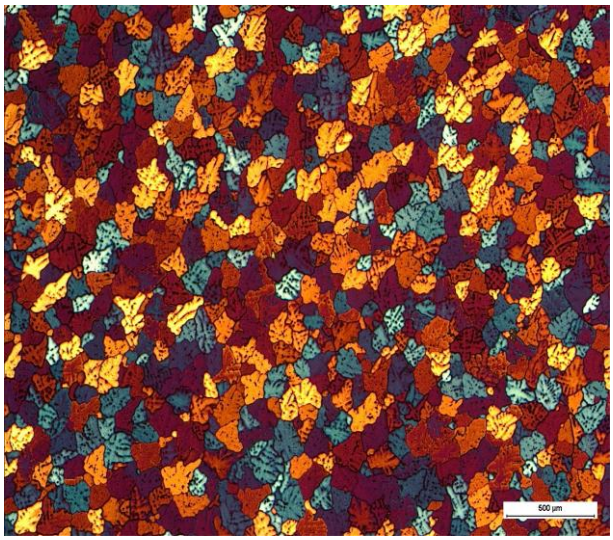

Figure 4.19 OM image of the microstructure of the grain-refined billet (DC-GR) cast at Oxford Begbroke Science Park.

Measurement of the grains was by circular intercept method and the average of 10 images taken every 10 mm across the billet radius is given as 91 µm ± 9 µm. The standard deviation is a statistic that quantifies the spread of data about the average value. The standard deviation here is 9 µm for the values measured across the billet radius suggesting that the grain size is very uniform across the billet. This result is to be expected when using grain refiner and as such is a good assessment of the process parameters and achievable quality of the billet produced by the technology, thus a bench mark to compare the sheared material with.

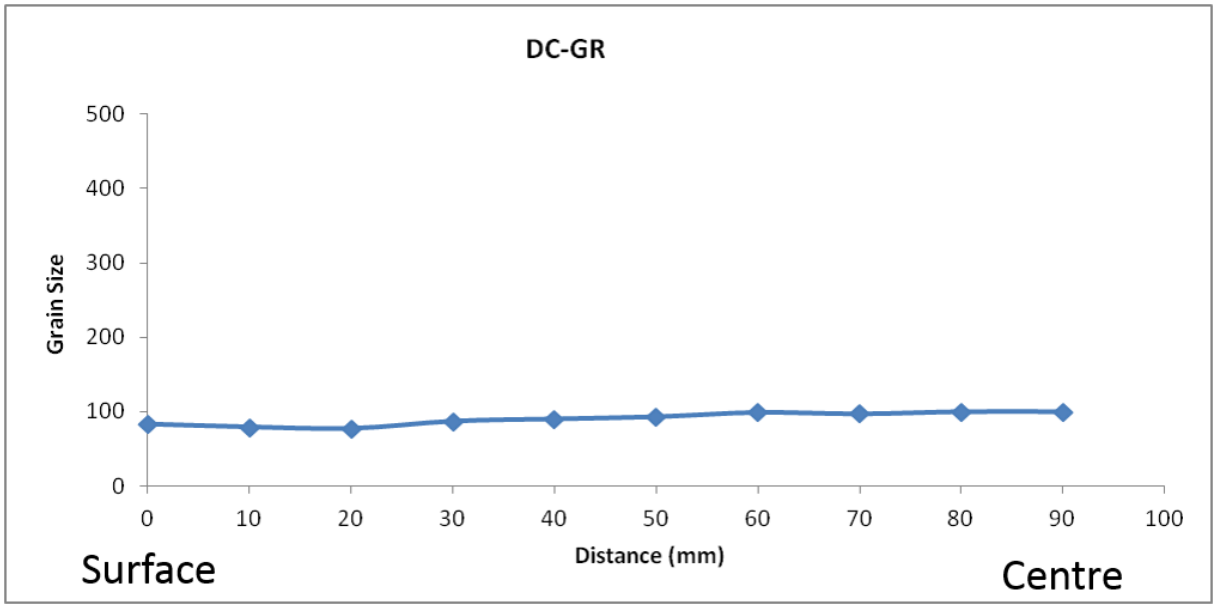

Figure 4.20 Graph of the average grain size of the grain-refined DC billet across the radius of the billet from the surface to the centre.

4.2.3.2 Industrial Scale DC Cast Billet with Shearing Applied: MC-DC Billet Macrostructure

Following on from the billet cast with and without grain refiner, a billet with shearing applied was cast and its structure is presented here from the base through to the first 650 mm of the 1600 mm billet length, plus a cross-section taken from 1400 mm. No grain refiner additions were made to this cast and the device was positioned at

position P2, subsequently known as MC-DC-P2 from this point forward. Sections were cut from the billet and halved along the vertical axis where etchant was applied after being machined flat, revealing the macrostructure. The macro-graphs are arranged over the following three pages in series from the base of the billet where the rotation speed of the high shear device was 4500 rpm, through to the top of the billet where the shear rotation speed had been increased to 6400 rpm. The region of billet where the speed was increased at 600 mm cast is included.

The series of images are listed below as part of Figure 4.22:

a) Cross-section of billet base, 0 – 250 mm from the base;
b) Cross-section of sheared material at 4500 rpm, 300 – 400 mm from the base; indicating the delay between starting running of the shear device and structure change;
c) Cross-section of sheared material at 4500 rpm showing CET, 400 – 500 mm from the base;
d) Cross-section of sheared material at point of increase from 4500 – 6400 rpm, 550 – 650 mm from the base;
e) Cross-section of billet sheared at 6400 rpm.

The figures are arranged such as they were when part of the billet so, for example, Figure 4.22b is below Figure 4.22c on the page; Figure 4.22d is below Figure 4.22e. By viewing the cross-section of the billet from the base through to 600 mm we can track the evolution of the microstructure through the billet and the transition from columnar to equiaxed grains. The reason it has to be done in series over the course of three pages is, to preserve the detail that would be lost if the images were reduced to fit as one complete 650 mm sample.

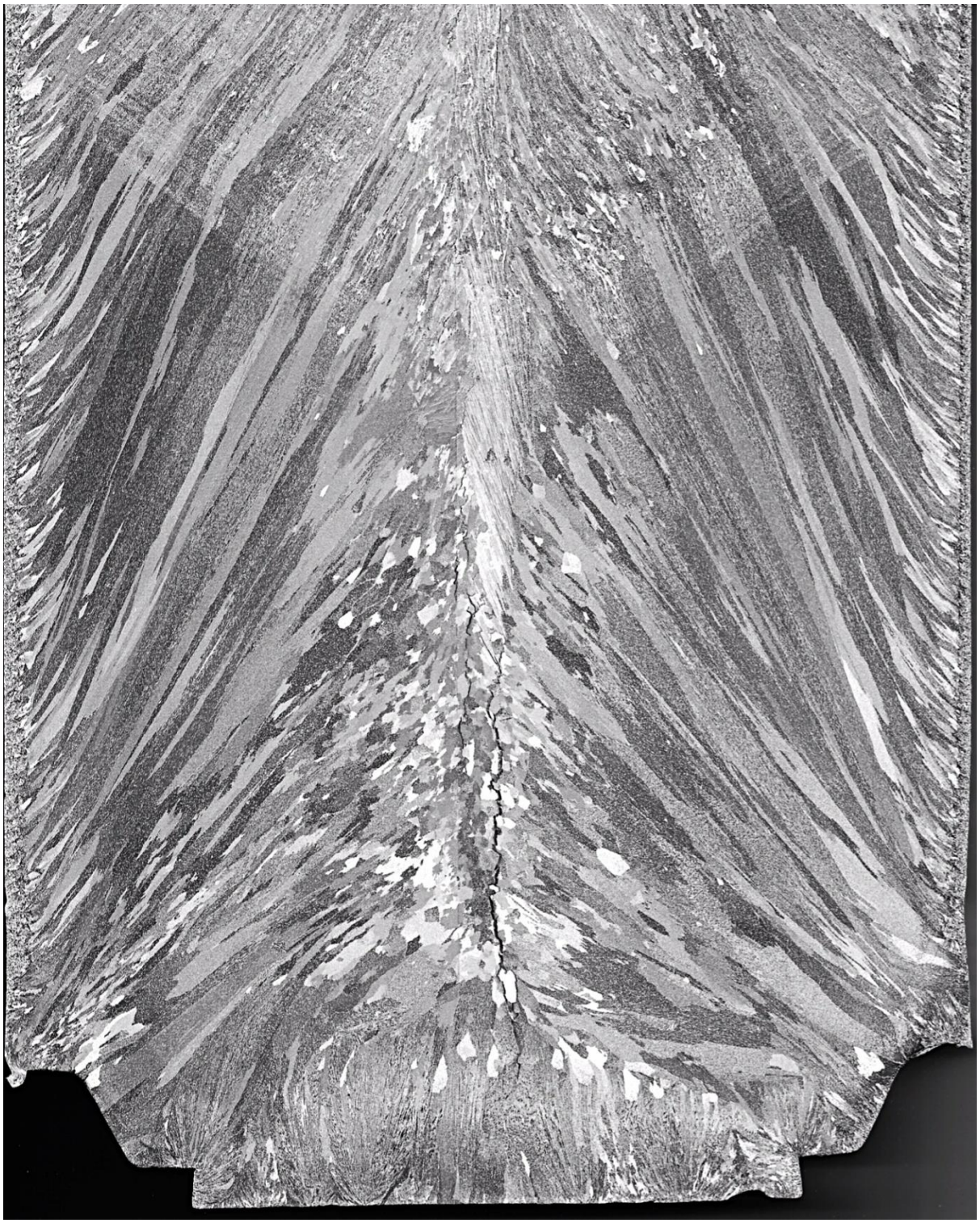

a

c

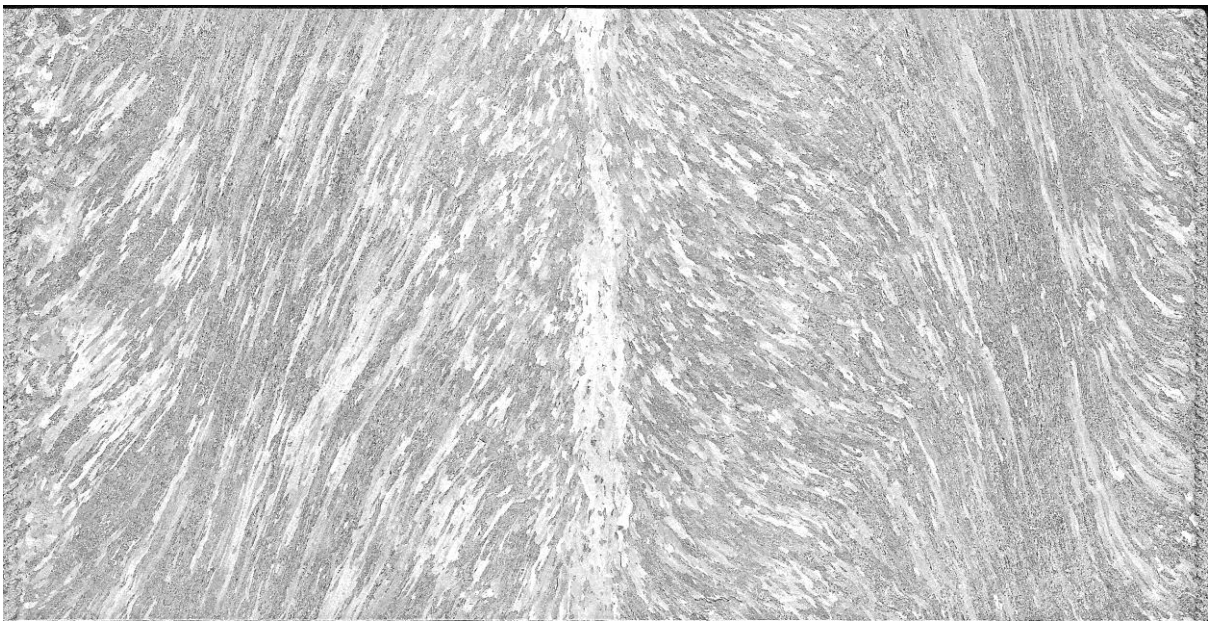

b

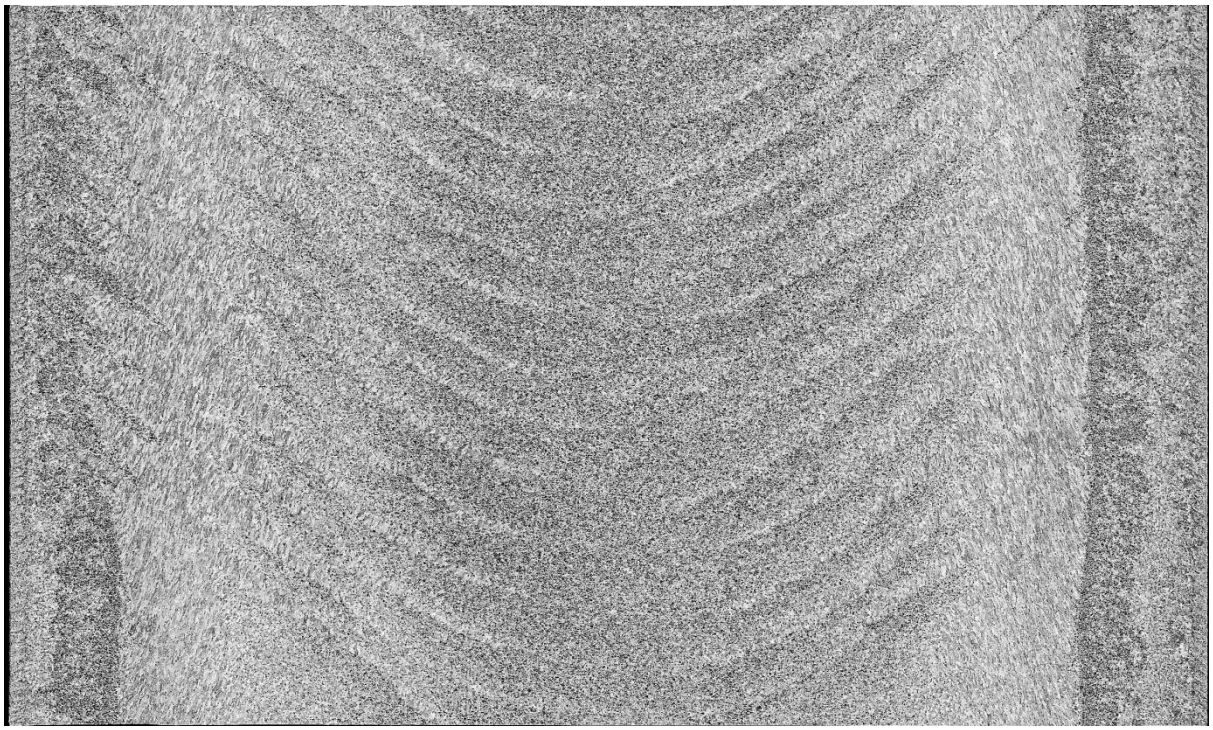

e

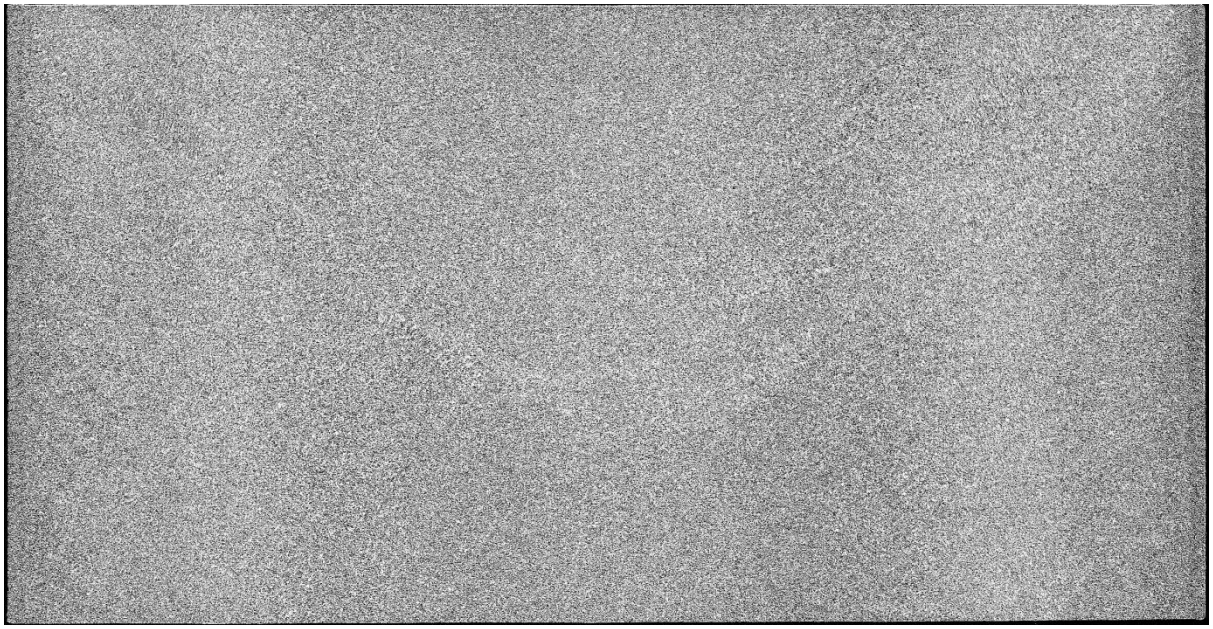

d

Figure 4.21 Macro images of the MC-DC-P2 billet cross section. (a) 0 – 250 mm from the base, (b) 4500 rpm, 300 – 400 mm from the base, (c) 4500 rpm showing CET, 400 – 500 mm from the base, (d) 4500 - 6400 rpm, 550 – 650 mm from the base (e) 6400 rpm. Note the heavy layering that occurs at 6400 rpm. Each image is of complete 203 mm billet cross-section.

Figure 4.22a is a vertical cross-section of the billet sump which shows the microstructure for the first 250 mm of the billet. It is important to note at this point that the shear device was inserted into the melt at 100 mm and shearing started at 250 mm of billet cast, thus the base of the shear device was level with the top of this sample when shearing began. The structure of the billet consists of large columnar grains that grow towards the centre of the billet from the surface.

With increasing distance from the base the columnar grains become progressively more vertical as they grow towards the heat flows. This allows the grains to become elongated compared to those near the base of the mould, which grow at a shallower angle and who's growth is blocked by coarse dendritic grains at the centre of the billet. These coarse grains are typically found in the central zone of un-grain-refined billets, transported there by the convective flows of the process where they block the columnar growth forming an equiaxed but coarse structure. At the base feather grains develop rapidly against the cooling effect of the starting-head forming a solid base of dendrites. Ahead of these grains are what appear to be crystal fragments which, were probably caused by the hot melt entering the mould, flowing across the solid front, remelting dendrite arms and transporting the fragments into the sump of the forming billet. These fragments can be seen just ahead of the feather grains, where they became nuclei for the coarse and columnar grains, blocking the feather structure.

Feather grains are present at the centerline approximately 120 mm from the base and continue to the top of the sample. They only occur along the centerline contained within the coarse equiaxed and columnar grains, suggesting a temperature gradient is present along the centerline during steady state casting.

Approximately 170 mm from the base, what appear to be layers of melt in the shape of the sump profile have formed. These layers may be the build-up of solute and grain fragments at the solidification front and almost certainly a result of shearing having begun above. It is not enough to stop the growth of the large columnar grains as they are still growing through these layers, but there are still obvious effects of shearing that initiate from this point. The columnar equiaxed transition happens further up the billet at 430 mm from the base, Figure 4.22 c, which is approximately 180 mm after shearing began. However, within the layers it can be argued that the

amount of grain fragments that are present increases accompanied by a narrowing of the columnar grains and widening of coarse grain zone at the centre.

The centerline crack that is present also narrows as it passes through the sheared zone of the billet. The crack itself is widest at the base during the start as the speed quickly ramps up to the steady state speed (0 – 110 mm/min by 100 mm cast). At 100 mm, the region of the crack envelopes the coarse grain zone with the crack propagating inter-granularly between the columnar and coarse grains, then becoming most prominent around the feather grains along the centerline. As the width of the coarse central region narrows with shearing, so too does the crack region as it passes through the shear affected zone. The structure along the centerline is still coarse but the feather grains disappear with twined columnar forming within the crack.

Figure 4.22b shows the structure 300 – 400 mm from the base of the billet. The structure is still columnar but the grains are markedly thinner than the columnar grains of the base sample in Figure 4.22a. The volume of coarse grains has also increased but again there is a disparity between the left and right side of the sample, with the right side containing an increasingly dominant coarse equiaxed structure, whilst the left is clearly columnar grain dominant. Looking at each side of the sample from the surface to the centre, the differences start at the periphery. The columnar grains still grow towards the heat and melt flows which obviously must change some distance from the surface as the angle of growth changes towards the vertical. There is a temperature gradient generated by the cooling water at the surface driving the growth of the columnar grains towards the centre. As the flows change in the sump as a result of shearing, the grains deflect towards these new flows that now will not be emanating from the centre but are now travelling down the periphery of the billet and mushy zone due to dispersive action of the shear device. As the fragments and flows move along the solidification front they transport fragments to the centre creating the coarse grain structure at the centre.

On the right side of the sample, the columnar grains appear blocked by coarse grains that have been transported to the centre and have increased in volume, whilst noticeably decreasing in size. It is evident that these grains are flowing as if drawn to the centre and upwards, which is understandable considering the drawing action of

the shear device. The centerline cracks are still present with a coarse structure present between them. Thus the amount of shearing affected upon the cast has been insufficient at this point to complete the transition from columnar to fully equiaxed.

The columnar to equiaxed transition (CET) occurs approximately 430 mm from the base of the billet; 180 mm after shearing has started and is shown in Figure 4.22c. The transition is obvious in this sample and appears quite suddenly. The coarse and columnar structure around the transition zone is not too dissimilar from that of the structure in Figure 4.22b where the volume of coarse grains in the central region is increasing steadily with the shearing time, but not enough to cause the transition. The equiaxed structure clearly develops first in the central region of the billet creating a coherent fine equiaxed structure that widens with the sump profile, blocking the columnar growth over an increasing cross-section of billet. The volume of grains has increased and the grain size decreased with the survival of nuclei in the homogeneous temperature field created by shearing. Out to the periphery of the billet, the columnar grains still dominate creating a coarse structure between the equiaxed zone and the billet surface but, the coherent equiaxed structure at the core of the billet is now well established at this point to overcome the growth of columnar grains and dominate the growth competition. This allows a fully equiaxed grain structure to develop from this point and for the remainder of the billet. It could be argued however that this coarse columnar structure is beginning the transition to equiaxed at the top of the sample, 500 mm from the base.

Even though the structure has become equiaxed the centerline crack is still present but far less defined than in previous sections of the billet (Figure 4.22b). This implies that the crack is healing supported by studying Figure 4.22d as the crack has healed by the start of this section, 550 mm from the base. The crack remains healed for the duration of the cast confirmed by its absence in Figure 4.22e which was taken close to the top of the billet.

A fully fine equiaxed grain structure has evolved since the section of billet in Figure 4.22c such that a uniform structure is presented in the billet cross-section of Figure 4.22d. Intensive shearing has been well established by this point in the billet and the resulting structure is fine equiaxed, the exact specifications of which will be detailed in the following sections. Figure 4.22d is the transition point where the speed was

increased from 4500 rpm to 6400 rpm. Within this sample there is a line of coarse grains that are a result of the speed change. It is obvious that such a change as this will alter the state of the casting which with remarkable efficiency resettles itself to steady state and the coarse structure is eliminated from the centre of the structure.

Although a fine uniform structure is visible through the cross-section, there is evidence at the periphery of a coarse structure identified by different shading within the sample. If we compare image Figure 4.22d with e, the different structures become much more apparent. These structures and the zones they inhabit are similar in width and type for both samples; they have simply developed significantly more when the rotation speed has been increased to 6400 rpm.

Due to its complexity, Figure 4.22e requires separating into its key components first so that the reader will better understand the areas being described.

1. Shell zone
2. Coarse structure at periphery next to shell zone
3. Fine equiaxed grain region at periphery
4. Coarse grain structure columns
5. Layers of coarse grains

There is a clear divide between the billet structure at the periphery, zones 1 – 3, and the core of the billet. Separating these zones are the columns of coarse grains as if they were a wall stopping the structure at the surface developing further into the billet. Instead of forming columnar grains at the surface as seen previously in Figures 4.22a-c however, a finer structure has developed here suggesting that melt conditioning does still determine the structural evolution at the billet surface. As the micrograph shows, there are fine equiaxed globular grains at the interface where the coarse angled grains begin, whilst at the surface the grains are much larger and dendritic. The grain structure from the surface up to the start of the columns, zones 1-3, gets steadily finer creating this distinct interface between the surface region and the columns. It is still a mixed grain morphology that formed through these zones consisting of dendritic and globular grains together, suggesting a varied temperature gradient and floating crystals were present.

In the previous section, it was stated that these columns, zone 4, could be related to areas of static flow such as eddy currents or voids. This is certainly feasible and the SolidWorks models of the previous section show that voids are theoretically present at the point where these columns develop. What this series of figures show is that these columns relate to the position of the columnar grains present before melt conditioning took effect, specifically the point where the grains deflect to the flow. Indeed, it should be noted here that if we compare the image in Figure 4.22e with 4.22d below it, the structural interfaces listed above mirror each other even at 4500 rpm, although not as evident as at 6400 rpm. This suggests that the columnar grains remain in the melt where the voids in the flow are, but become more and more refined until they evolve into coarse grains rather than columnar. These voids in the flow may have a different temperature and solute content to that of the melt around it especially that of the undercooled flow coming from the surface. This creates gradients which drive the development of the coarse structure in these columns.

Routinely, the drawing capacity of the shear device is able to extract grains from the columns resulting in the layers that are seen so clearly in Figure 4.22e extending into the core of the billet. At the core they are one grain layer as these grains are able to be transported further before attaching to the solid forming the next layer of the mushy zone. Small grain fragments that are dispersed by the shear device move along and settle upon these layers creating solid layers of fine equiaxed rosettes between the coarse grain layers, shown in greater detail in the image accompanying the schematic. The layers are staggered so that the layers on the left of the sample as we look at it, are in-between the layers on the right at the core, again shown clearer in the schematic which relates to the uneven flow generated by the shear device.

4.2.3.3 Microstructure Evolution of the MC-DC-P2 and P3 Billet

The microstructures of the billet sheared at P2 and P3 are presented here as well as the billet sheared with grain refiner added during the cast. The figures were obtained by light optical microscopy (LOM) after anodizing to reveal the different grains and the average grain size measurements made using the circle intercept method.

Scanning Electron Microscopy (SEM) was used to analyse the microsegregation of elements through the individual grains and the samples were polished to high standard only, as etching can add and remove features from the samples. Before the grain size analysis is presented, mosaics of the each of the billet radius; MC-DC-P2 4500 and 6400 rpm; MC-DC-P3 300, 4500 and 6400 rpm, are shown in Figure 4.23. Mosaics of the material from the MC-DC-GR-P2 billets are shown in Figure 4.24. These mosaics were obtained by LOM on a controlled moving platform with multiple images taken and combined. The magnification was kept constant at 25x magnification for each sample for comparison.

The mosaics give a good indication of the different structures that formed across the billet. These structures have been described in the earlier section but the images show depth of the structures and their positions relative to the position of the shear and rotation speed. For example, the columnar zones in the material sheared at MC-DC-P2 (Figure 4.23a-b) are closer to the surface of the billet when compared with the MC-DC-P3 (Figure 4.23c-d). From the SolidWorks images of the flow patterns in the billets, the position of the device within the mould was critical in forcing flow towards the surface region and where the eddies were positioned. Eddies within the flows are considered by the author to be the cause of the coarse columnar grains formation. The variation in the depth of where the coarse zone begins between MC-DC-P2 and P3 support this hypothesis.

These mosaics of Figure 4.23 are a good indicator of the rotation speed effect of shearing. Consider the variance in structure between Figures 4.23a and b which are from the same billet and sheared with the device at position P2 but sheared at 4500 and 6400 rpm respectively. In Figure 4.23a, the coarse zone begins 20 mm from the surface but extends well into the mid radius of the billet, becoming finer after approximately 50 mm from the surface. The coarse region of the billet sheared at 6400 rpm in Figure 4.23b begins at approximately the same position but distinctive layers of coarse grains above the equiaxed have now developed. These layers are those seen in Figure 4.22e but at higher magnification. The coarse column that begins 20 mm from the surface shows layers within it that then extend outwards into the billet at the approximate shape of the sump. It is known that equiaxed grains can generate a large drift or settling velocity compared to columnar structures. The columnar structures may nucleate and grow on the equiaxed structures forming a

new mushy layer, which the equiaxed grains settle upon. This repeated so the structure resembles that shown in Figure 4.22e.

Mosaics of the images from MC-DC-P3 billet at rotation speeds of 3000, 4500 and 6400 rpm are presented in Figures 4.23c-e, respectively. What is noticeable from the first look at the images is that the coarse grain column moves closer to the surface region with increasing shear speed. The width of the column decreases also with speed increase, with the column in the billet sheared at 3000 rpm (Figure 4.23c) being wider and further from the surface then the faster speeds in Figure 4.23d (4500 rpm) and Figure 4.23e (6400 rpm). There are two distinct structures that developed either side of the coarse grain column (CGC) within these sections of billet. The surface region side is coarser at the lower shear rotation speeds as can be seen at 3000 rpm. A very coarse columnar grain structure developed after the initial shell zone formed that remained coarse for approximately 20 mm into the billet, before becoming a more refined equiaxed structure at the point where the coarse grain column developed. “Waves” of coarse grains are present within an equiaxed grain structure between the surface and the CGC for each of the rotation speeds, but at 4500 rpm this structure is more refined. At 6400 rpm, the waves are much more distinct and the layering that was prevalent in the material sheared at 6400 rpm and position P2, is evident.

The layering of columnar grains between equiaxed grains occurs as before but the length at which they extend into the billet core is shorter. This is most likely due to the closer proximity of the CGC to the forced flows from the jets out of the shear device and the turbulent flows within the core. The core of the billet sheared at P3 is well refined and equiaxed which is clear in the images (Figures 4.23c-e). The SolidWorks images suggest that larger flows developed within the core of the billet due to the shape of the sump containing the flows. The layers that formed are shallower than those in the billet sheared at position P2, suggesting that the sump shapes were different.

The SolidWorks images also show that there is considerably larger flows in the surface region beyond the eddies where the CGC originates. This would certainly support the changing structure in the surface region.

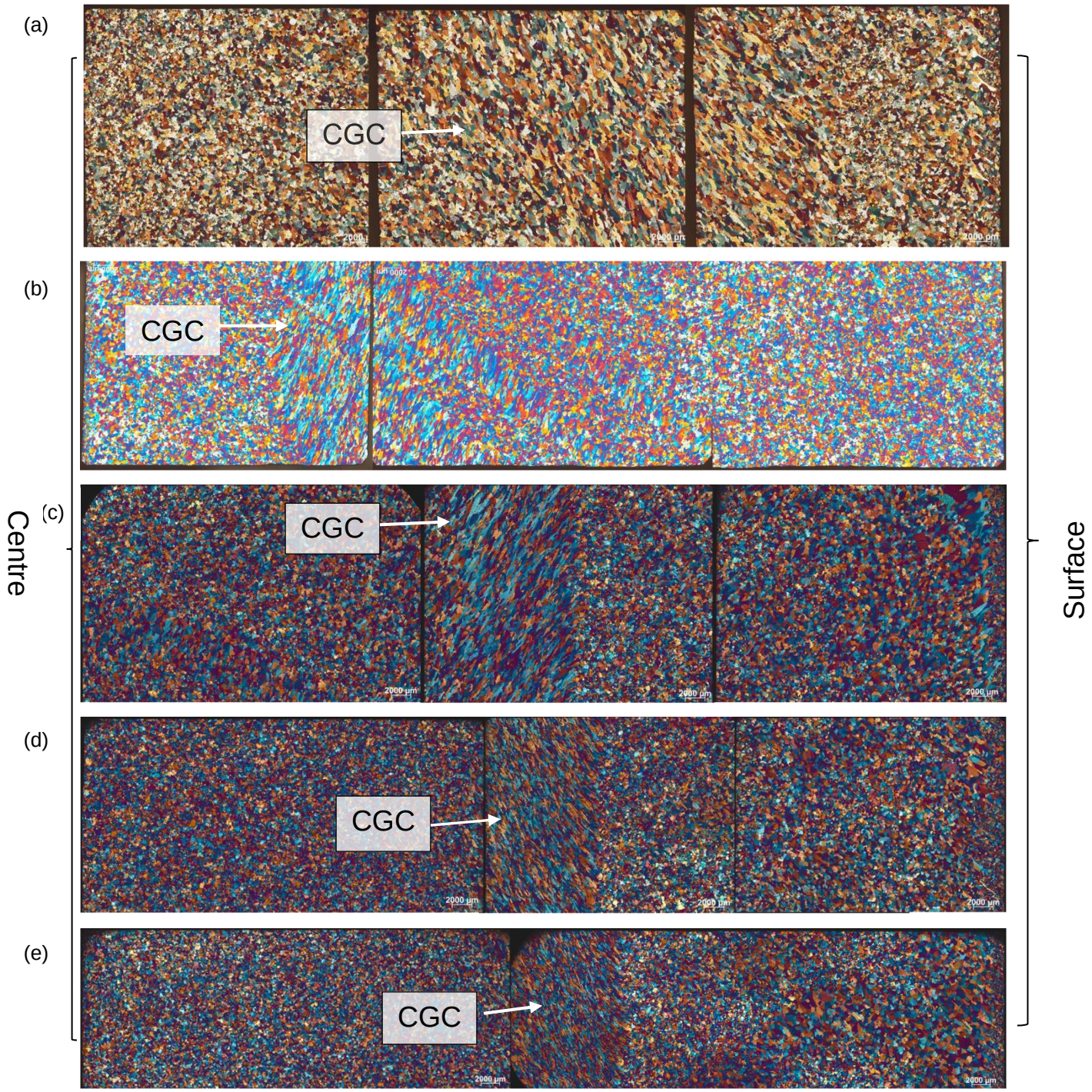

Figure 4.22 Grain structure mosaics from the MC-DC-P2 and P3 billet from the surface to the billet centre. (a) MC-DC-P2 at 4500 rpm, (b) MC-DC-P2 at 6400 rpm, (c) MC-DC-P3 at 3000 rpm, (d) MC-DC-P3 at 4500 rpm, (e) MC-DC-P3 at 6400 rpm. Note the coarse grain column occurs in each of the billets, getting closer to the surface with increasing rpm. Scale bar displays 2000 µm see Appendix 2

Mosaics of the billet radius taken from the MC-DC-GR-P2 material are presented in Figure 4.24. Figure 4.24a was obtained from the billet sheared at 4500 rpm, whilst Figure 4.24b was sheared at 6400 rpm. There is little difference between the two structures which both contain well refined equiaxed grains; however there does appear to be a coarse grain structure close to the surface in both billets. This structure resembles a CGC as seen in the MC-DC billets, but is considerably less coarse. Eddies will still have formed within the flows during shearing thus the CGC formed, however, grain refinement increased nucleation occurred reducing the effect and coarseness of the grains by restricting their growth.

The quantified average grain sizes are presented in Figure 4.25 as a means of quantifying the effect of shearing across the billet. Figure 4.25a displays the average grain size of MC-DC-P2 billet sheared at 4500 and 6400 rpm; Figure 4.25b displays the average grain size of MC-DC-P3 billet sheared at 3000, 4500 and 6400 rpm; Figure 4.25c displays the average grain size of MC-DC-GR-P2 billet sheared at 4500 and 6400 rpm. The grain sizes were measured across the radius of each billet in 10 mm intervals. Ten images per interval were taken at 2.5x magnification (25x) and the average value of each interval plotted on the graphs. The standard deviation at each interval was calculated to quantify the spread of data about the mean, giving an indication of how uniform the structure is at each measured point and, thus across the billet radius.

Figure 4.25 shows that the MC-DC billets have a larger grain size compared with that of the billets cast with grain refiner (MC-DC-GR). The MC-DC-GR billet trend is much more uniform than those of the MC-DC billet but, this is to be expected at this stage of development due to the potency of grain refiner and is comparable to the DC-GR result (Figure 4.25c). However, that variation in grain size is within 50 μm of those measured in the MC-DC-GR billet, especially after the CGC where shearing was most intense.

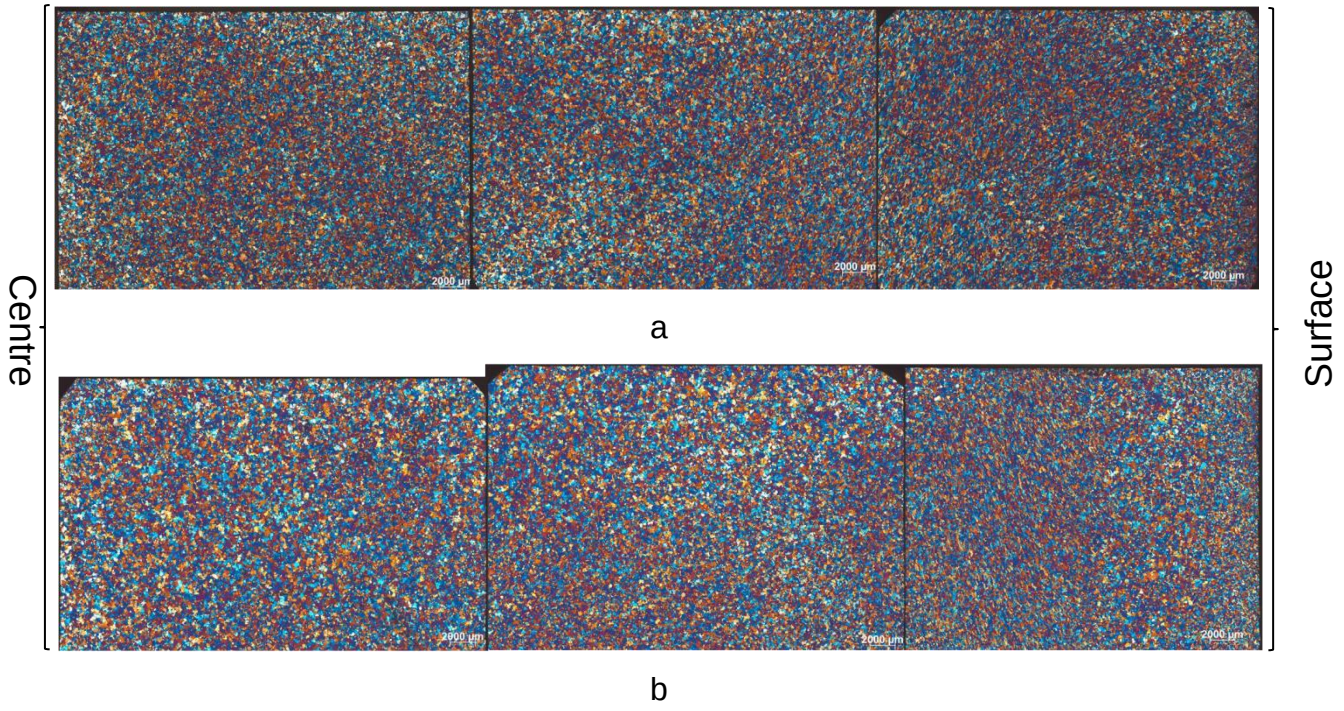

Figure 4.23 Grain structure mosaics from the MC-DC-P2-GR billet. (a) MC-DC-P2-GR at 4500 rpm, (b) MC-DC-P2-GR at 6400 rpm. Note the coarse grain column occurs in each of the samples at approximately the same position as the MC-DC billets indicating the effect of shearing or more specifically the voids in the flow streams.

For the MC-DC-GR-P2 billet, it was approximately 100 ± 7 µm at 4500 and 6400 rpm. The average grain size of the MC-DC-P2 billet at 4500 rpm is 185 ± 30 µm, decreasing by approximately 30 µm across the billet radius to 154 ± 30 µm after the rotation speed was increased to 6400 rpm. Each of the sheared samples showed a decrease in grain size after the speed increased to 6400 rpm. At position P3 the average grain size was 135 ± 28 µm and 157 ± 39 µm at 4500 and 6400rpm respectively. However, the standard deviation over the billet radius is a lot larger than that of the MC-DC-GR and DC-GR billet, due to the variation in grain morphology across the billets as shown in Figure 4.23a-e.

It can be seen in Figure 4.25a that there is a significant increase in grain size at the lower rotation speed of 4500 rpm over the grain size at 6400 rpm. It is unsurprising that the grain size reduces under higher rotation speeds as there would be a decrease in melt temperature and thus increased nucleation resulting in lower grain sizes. The average grain size at 6400 rpm drops significantly from 220 µm at the surface to 150 µm after 10 mm into the billet. 150 µm is the average grain size for

this billet sheared at 6400 rpm. If the CGC is ignored at this point and we consider the trend without this value, then the grain structure is very uniform and would consistently hover around the 150 µm value. Industrially this grain size would be acceptable for many applications. At 4500 rpm, the coarse structure extends from the periphery of the billet to the mid radius point. The largest grain size was 210 µm decreasing in size to 132 ± 5 µm at the centre. Figure 4.25a shows that this is similar to 6400 rpm size at the centre; 134 ± 12 µm. The standard deviation has reduced dramatically for both speeds indicating that there is a much tighter control in the grain size, with less coarse grains present. The standard deviation is still larger over the 6400 rpm grain sizes.

At shear position P3, the difference between the two speeds is much less. Shearing at 4500 rpm did decrease the average grain size by 20 µm when compared to 6400 rpm values; 4500 rpm: 135 ± 28 µm; 6400 rpm: 157 ± 39 µm. Again, the standard deviation is larger at the higher rpm suggesting a larger fluctuation in grain sizes. Within the core of the billet however, the standard deviation decreases with grain size when sheared at 6400 rpm more than at 4500 rpm; 100 µm ± 3 to 120 µm ± 11, respectively. Figure 4.25b shows that average grain size of the surface region is coarser whilst becoming more refined after the CGC when the billet was sheared at 6400 rpm.

It is noticeable that when the billets are sheared at P3, the grains at the surface are larger than the billet average (apart from the coarse grain regions of course). It is understandable when we consider the SolidWorks images that show the flows do not reach the surface fully, allowing the shell zone and billet surface region to form almost independently of shearing. The flows when the shear was positioned at P3 were restricted to a greater extent than when the device was at P2. It appears than that the grain structure in the core benefitted from the intensity of the melt conditioning at 6400 rpm when the shear device was at position P3.

By adding grain refiner to the melt during the cast, the average grain size becomes extremely uniform across the billet similar to the DC-GR billet with an average grain size of 100 ± 7 µm for both 4500 and 6400 rpm. The coarse grain structure has been eliminated from the MC-DC-GR billet with the addition of grain refiner that inoculates the cast with nucleants resulting in a more homogeneous structure.

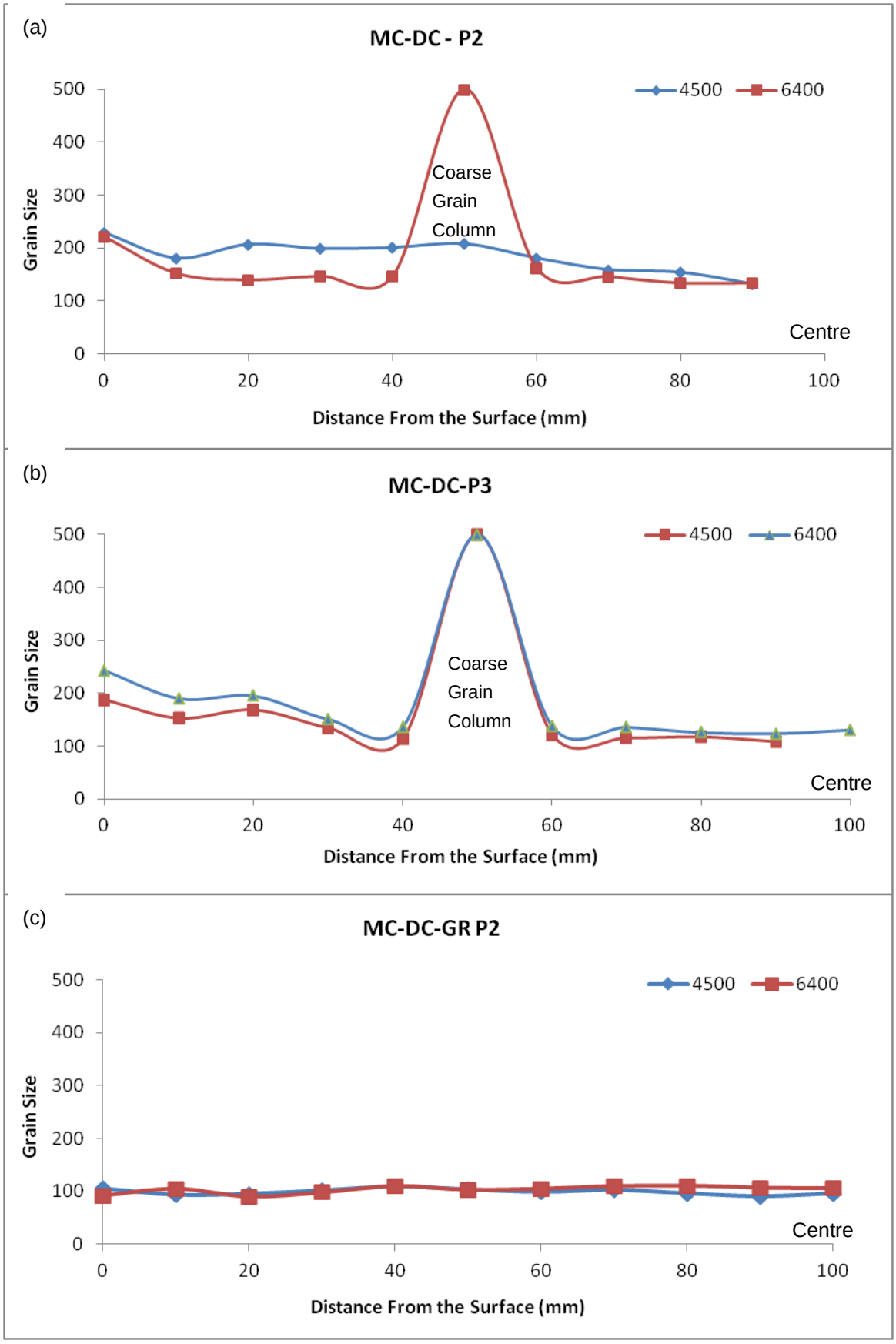

Figure 4.24 Average grain size plots for the MC-DC billets (a) MC-DC-P2, (b) MC-DC-P3 (c) MC-DC-P2-GR

Interestingly the grain size did not decrease further coupling the refiner addition with shearing – the average DC-GR grain size was 91 ± 9 μm and MC-DC-GR average grain size was 100 ± 7 μm – implying that the grain refiner additions dictated nucleation rather than grain multiplication through shearing. The slight increase in the grain size could be a coarsening of the structure due to the homogenising effect of shearing upon the temperature field allowing the nucleating grains to grow and coarsen.

4.2.4 MICROGRAPHS OF SHEARED BILLET

Micrographs of the sheared billet structure across the radius are presented in Figures 4.26 – 4.28 for a more in-depth analysis of the phenomena seen in the previous section. The micrographs display images from regions of the billet listed below, that were sheared with the device at position P2 and P3 without any grain refiner additions, at rotation speeds of 4500 and 6400 rpm. Regions shown are:

- Surface/ shell zone
- Coarse grain column (CGC)
- Mid radius
- Billet centre

It is not necessary to include every image of the microstructure as for each billet cast a micrograph was taken every 10 mm along the radius; however they are included within the appendix for reference.

4.2.4.1. MC-DC Billet Surface Region Grain Structure

Most wrought Al alloys are direct chill (DC) cast to produce ingots, the outermost shell of which is then commonly scalped off to remove the uneven cast surface and inverse segregation zone (Allen, Kumar, Carroll, O'Reilly, & Cama, 2001). Figure 4.26 shows the grain structure and meniscus at the surface of the MC-DC-P2 (Fig 4.26a-b) and P3 (Fig 4.26c-d) billets at 4500 and 6400 rpm respectively. The

meniscus is clearly larger in the billets sheared at 4500 rpm. The values are given in Table 4.1 along with the average grain size at this location. In Figure 4.26a and c, the structural band of the meniscus is clearly shown by the fine grain structure that accompanies it into the billet. Above this fine grain structure develops a coarse grain structure between the structure bands of the meniscus. As the billet moves down, melt flows over the fine grains of the solidified meniscus contacting the mould wall, where it solidifies and forms the new surface of the billet. The process repeats itself forming layers, the shape of which is a product of the mould geometry and casting speed. The curvature and depth of the meniscus is controlled by the wetting angle between the mould wall and ceramic of the transition plate (T-plate) and resulting air pocket. The surface tension of the free meniscus surface remains solid against this air pocket, similar to the meniscus of a liquid in an over filled glass. To ensure higher surface quality, meniscus control is paramount.

It is interesting that the average grain size at P2 is the same between the rotational speeds even though the meniscus is 3x deeper at 4500 rpm. If we compare that result to those at shear position P3, there is approximately 50 µm difference between the grain sizes. It therefore comes down to the position of the shear device in relation to the mould and the ability of the forced flows to affect the structure at the surface region. At 6400 rpm, more flow penetrates this region reducing the meniscus at P2 and P3, but the flows appear restricted at 4500 rpm and position P3. The surface of MC-DC-P3, Figure 4.26c, appears rougher than that of MC-DC-P2, Figure 4.26a. Both were sheared at 4500 rpm and the casting speed was 110 mm/min for both cases which suggests that the positioning of the device influenced the collapsing of the meniscus and subsequent formation of the surface. Both have the coarse grain structure above the fine grains but the average grain size at the surface of MC-DC-P3 is less than that of MC-DC-P2, implying that the primary cooling had more influence for MC-DC-P3 increasing the cooling rate and decreasing the grain size.

The average grain size of the surface zone sheared at 6400 rpm at P2 and P3 is 221 µm and 243 µm respectively. There is a clear increase in size between MC-DC-P2 and P3, obvious when comparing Figures 4.26b and 4.26d as Figure d has a much larger grain structure away from the surface. All four structures coarsen to large dendritic grains away from the surface after the meniscus but the increase in grain size is greatest for MC-DC-P3 at 6400 rpm.

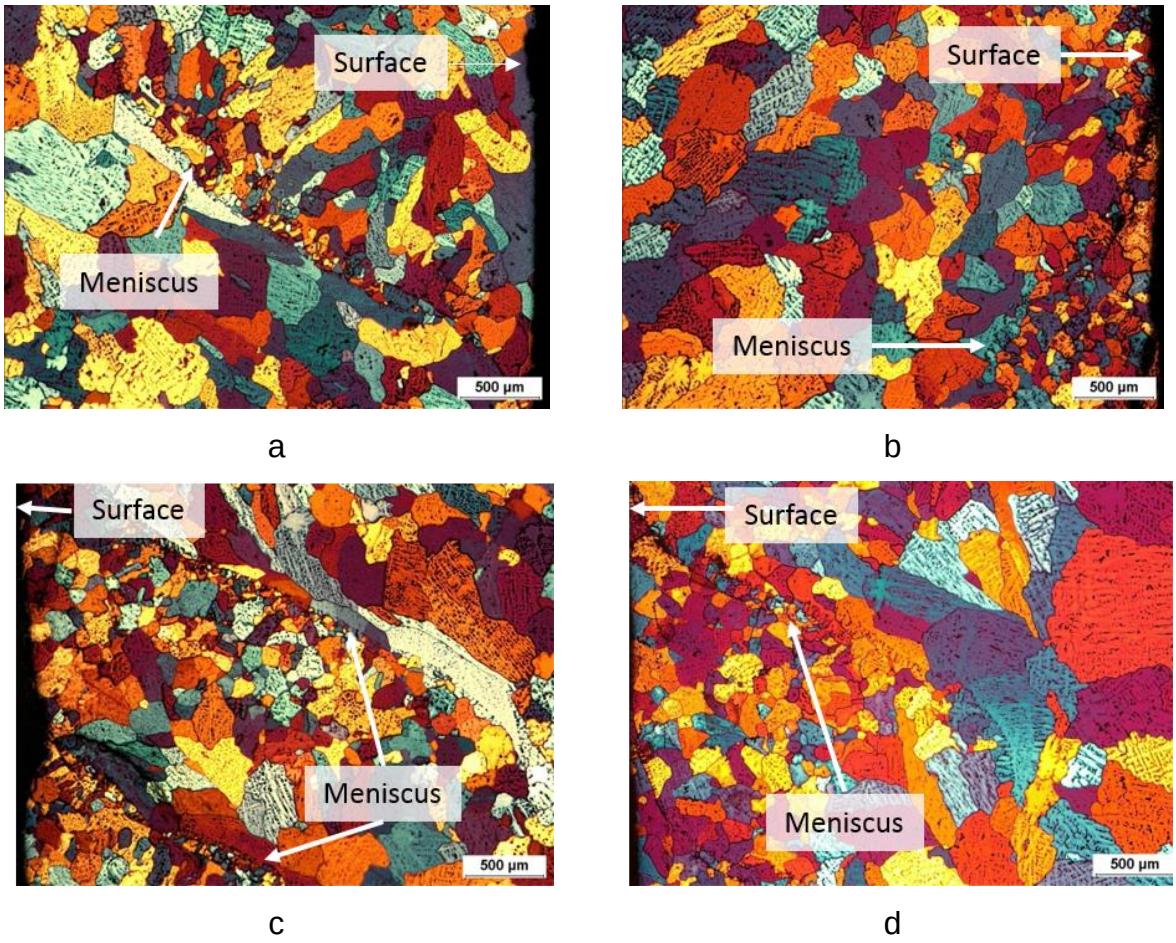

Figure 4.25 Micrographs obtained from the shell zone and surface region of the MC-DC billets sheared at varying tool depths and rotation speeds. (a) MC-DC-P2 at 4500 rpm with meniscus structural band extending from the surface into the billet with fine equiaxed grains covered by layer of coarse grains, (b) MC-DC-P2 at 6400 rpm shows coarse grain structure very close to the shell with much shorter meniscus and subsequent equiaxed zone, (c) MC-DC-P3 at 4500 rpm meniscus is highly developed again with large structural band into the surface region, equiaxed and coarse structure between meniscus layers present, (d) MC-DC-P3 at 6400 rpm coarse grain structure develops close to the shell zone, structural bands of meniscus evident with equiaxed structure between the meniscus layers.

Table 2.1 The average grain size at the billet surface for the MC-DC-P2 and P3 billets at 4500 and 6400 rpm. Included is the meniscus depths for each shear depth and speed.

Shear position	P2		P3	
Rotation speed (rpm)	4500	6400	4500	6400
Grain sizes (µm)	229 ± 41	221 ± 36	187 ± 20	243± 25
Meniscus depths (µm)	3000	1000	3000	1000

4.2.4.2. MC-DC Billet Coarse Grain Columns (CGC)

Figure 4.27a shows the microstructures of the coarse grain columns (CGC) that formed in the billet at MC-DC-P2 4500 rpm. Figure 4.27b shows the CGC structure of MC-DC-P2 at 6400 rpm. Comparing Figure 4.27a and b, the coarse grains in Figure b are much more columnar in nature and steeply angled than in Figure 4.27a. As described previously, a CGC formed in each of the MC-DC billets, except for MC-DC-P2 at 4500 rpm. In this billet a dendritic coarse equiaxed structure 18 mm from the surface developed which extended to the mid radius point of 50 mm. The CGC of the other MC-DC billets are elongated and could be argued to be columnar in nature. Evidence of this is provided in Figure 4.27c and d which show the long, steeply angled grains of the CGC from the billet sheared at 6400 rpm at tool depth P3. Again, as in Figure 4.27a, at 4500 rpm P3 the morphology of the grains are different to those at 6400 rpm. This is most likely a consequence of the increased flow at the higher rpm depositing grain fragments at the solid front, removing solute allowing growth but in a marginally more confined manner that at 4500 rpm.

An angled growth orientation away from the normal is evident in all figures suggesting that the structures were growing towards flows generated by shearing. Whilst the morphology is different, the dendritic nature of the grains is similar implying similar growth rates. The eddies that have been linked to these CGCs are larger in the MC-DC-P2 billet than the others when simulated by SoildWorks. This is only a rough approximation but the results do support this theory.

Outside of these eddies and subsequently either side of the coarse grains, the microstructure changes morphology becoming equiaxed towards the core of the billet. There was a sharp transition on both sides of the CGC from coarse steeply angled grains to equiaxed. A fine equiaxed grain structure formed on the surface side adjacent to the CGC of the MC-DC billets, whilst towards the centre this equiaxed structure grain morphology was more mixed.

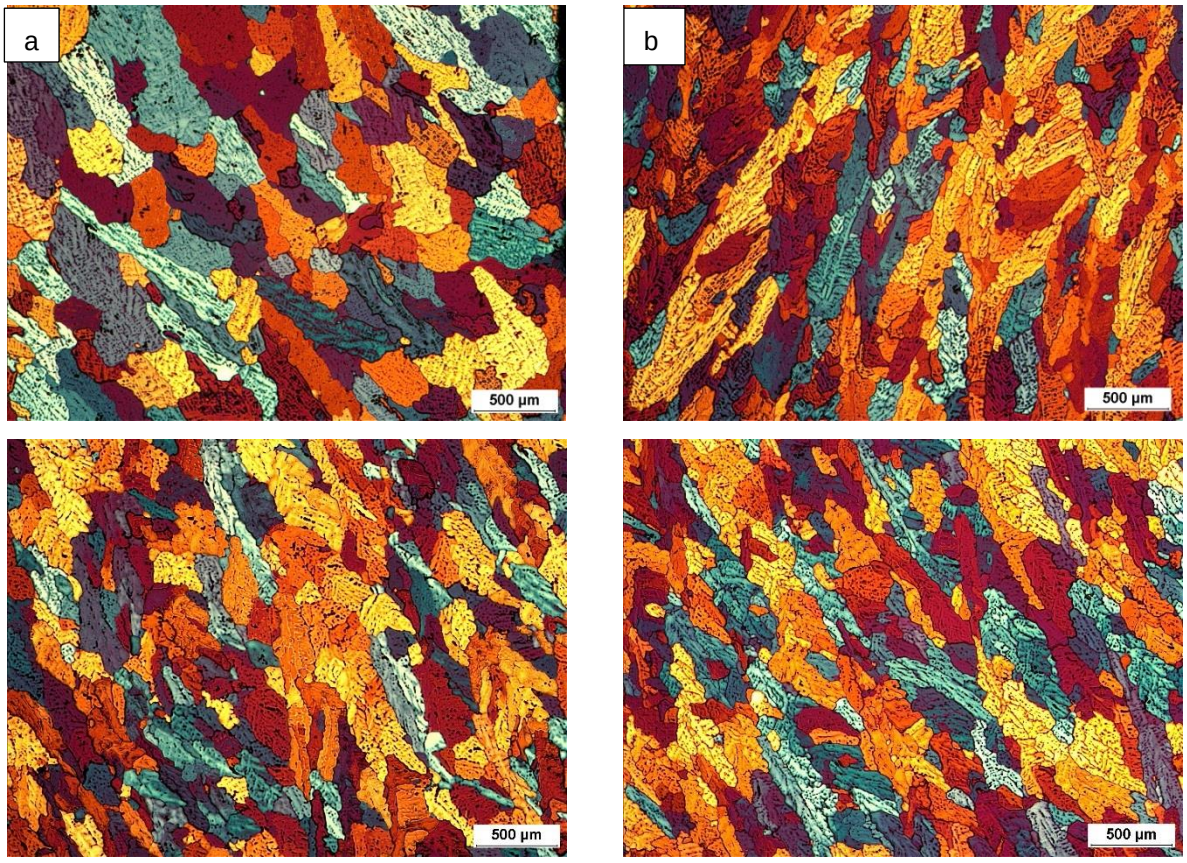

Figure 4.26 Micrographs showing the coarse grain structures present in the sheared billets. (a) 4500 rpm, depth P2 shows large dendritic grains that are angled without a columnar morphology, but appear to have grown in more unconstrained manner, (b) 6400 rpm, depth P2 grains are angled more towards the vertical and columnar in nature being thinner and longer than the grains seen in image a, (c) 4500 rpm, depth P3 showing steeply angled dendritic grains within the CGC, (d) 6400 rpm, depth P3 CGC which are more columnar than at 4500 rpm.

4.2.4.3. MC-DC Billet Mid Radius Grain Structure

At the mid radius of the billets the grain morphology is becoming equiaxed and finer toward the billet centre. For each sheared billet, the grain structure after the CGCs becomes increasingly refined towards the billet centre. However, the grain morphology is definitely becoming more mixed. Figure 4.28a-d show images obtained at 55mm from the surface, approximately after the coarse grain columns. Figure 4.28a-b consists of MC-DC-P2 at 4500 and 6400 rpm respectively. Figure 4.28c-d show the microstructures of MC-DC-P3 at 4500 and 6400 rpm respectively.

The average grain sizes are shown in Table 4.2. MC-DC-P2 sheared at 4500 rpm has the largest and most coarse structure at this point of the billet with an average of

208 ± 23 µm. The standard deviation suggests that there is variation in the grain size with pockets of smaller grains within the dominating equiaxed dendritic structure. Figure 4.28a shows these pockets of smaller grains embedded within the larger dendritic grains. These smaller grains are those which developed a rosette morphology under high shearing. These rosettes would have been transported by the forced flows as floating crystals.

Figure 4.28b shows the transformation from dendritic grain structures to a mixed morphology becoming much more established when the rotation speed was increased to 6400 rpm. Dendritic grains are still present but globular/ rosette grains have increased in number making for a very mixed structure. This has led to an overall reduction in the average grain size 162 ± 13 µm though. The morphology might be mixed but the low standard deviation value suggests that the grain size is relatively uniform. This reduction in grain size is most probably a result of increased nucleation, as the intensity of the MC-DC process is more acute here.

Table 4.2 shows that MC-DC-P3 produced a smaller average grain size than those of MC-DC-P2. Figures 4.28c–d display images of equiaxed grain structures created through MC-DC processing at 4500 and 6400 rpm, respectively. Both rotation speeds have low standard deviation values indicating a tight spread in the grain size measurements. Grain morphology of the 4500 rpm billet is fine dendritic interspersed with rosettes and globular grains. The globular grains became dendritic at their periphery, after contact with the solid increased their solidification rate due to increased heat extraction.

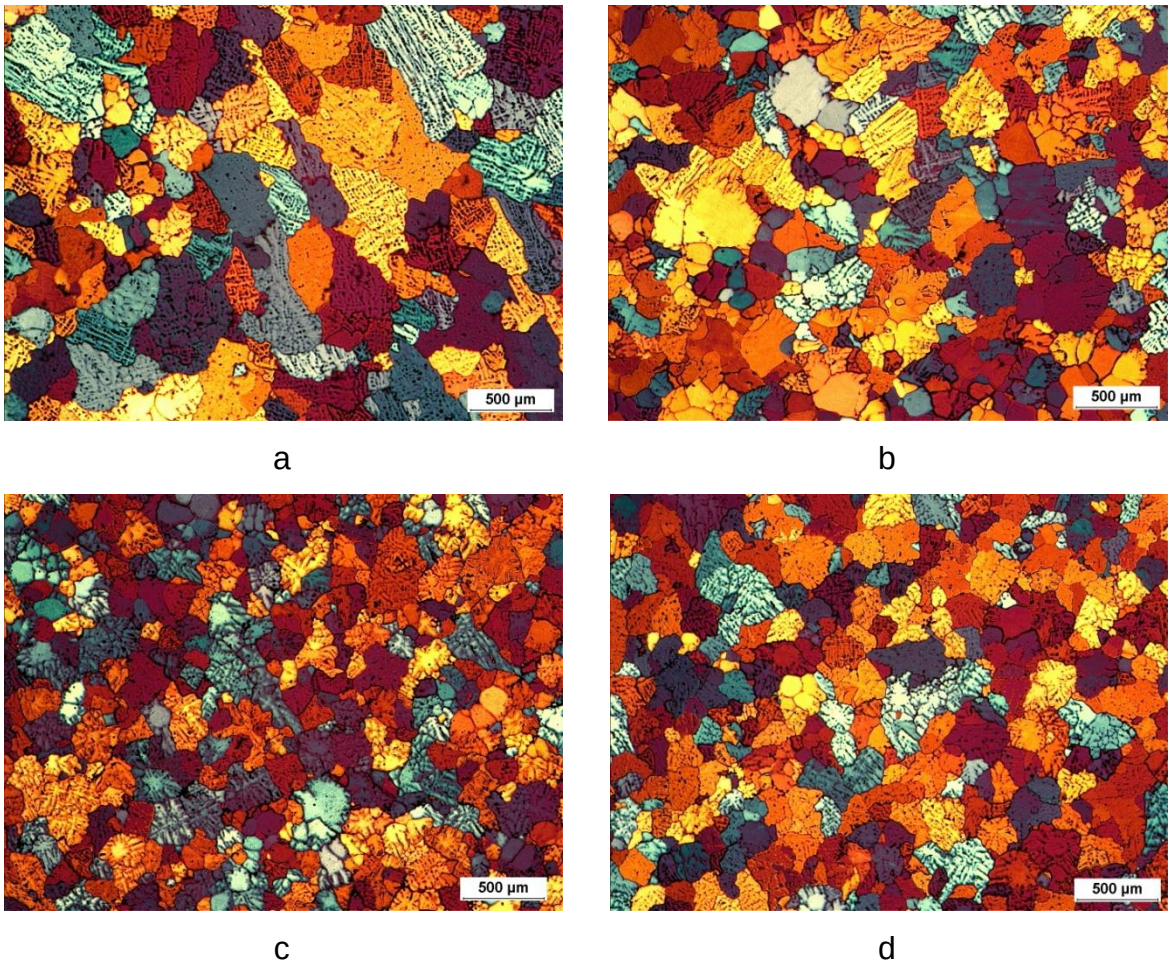

Figure 4.27 Micrographs obtained from the mid-radius point from the MC-DC billets sheared at varying tool depths and rotation speeds. (a) MC-DC-P2 at 4500 rpm, (b) MC-DC-P2 at 6400 rpm, (c) MC-DC-P3 at 4500 rpm, (d) MC-DC-P3 at 6400 rpm.

Table 4.2 Table showing the average grain size at the billet mid-radius for the MC-DC-P2 and P3 billets at 4500 and 6400 rpm.

Shear position	P2		P3	
Rotation speed (rpm)	4500	6400	4500	6400
Grain sizes (µm)	208 ± 23	162 ± 13	122 ± 13	138 ± 13

4.2.4.4. MC-DC Billet Centre Grain Structures

Figures 4.29a-b present micrographs taken from the central region of MC-DC-P2 sheared at 4500 and 6400 rpm, respectively. Figures 4.29c-d were obtained from the

central region of MC-DC-P3 sheared at 4500 and 6400 rpm, respectively. A globular morphology is present in all four of the billet samples shown. Only Figure 4.29a (MC-DC-P2) shows a dominant dendritic morphology. Due to these coarser dendritic grains the average grain size is the largest of the MC-DC billets at this point. It is evident from the images that the grain size is considerably smaller in the centre of the MC-DC-P3 billet at both 4500 and 6400 rpm. This is supported by the results shown in Table 4.3. The standard deviation is clearly much lower also. This implies a much more uniform structure was created within the core of the MC-DC-P3 billet compared with the MC-DC-P2 material. This is especially acute in MC-DC-P3 at 6400 rpm, where the grain size is 100 µm ± 3. The intensity of the melt conditioning is at its largest here due to the low positioning of the device and the confines of the sump restricting the flows.

First, at the core of the billet, this region is directly under the shear device resulting in intense flow patterns and turbulence in this area. Under the shear device are vortices that draw solute into the shear device consisting of fragments and solute form the solidification front. These fragments pass through the shear device and dispersed across the melt and drawn towards the centre again along the solidification front by the sucking force of the device. Concurrent to this, the rotation of the shear device spins the melt within the mould which becomes more intense at higher rpm. However, the flows around the voids also increase making the voids more substantial. This space is cooled through the action of the shear device as shown in the temperature plots previously thus helping to develop the finer grain sizes seen in the core region of the MC-DC-P3 billet.

Grain refiner was added to the melt during the cast at the ratio 1.0 kg/tonne in conjunction with shearing at rotation speeds of 4500 and 6400 rpm. The shear device was positioned at depth P2 thus this material is designated MC-DC-GR-P2 from now on. Grain refining inoculates the melt with TiB_2 particles that act as nuclei for grain nucleation similar to industry practices. Nucleation is therefore occurring before shearing has started in this case, ensuring a uniform equiaxed structure of fine grains develops. Previous MC-DC billet without grain refiner developed a mixed grain structure that was predominantly equiaxed dendritic grains, interspersed with rosettes and an average grain size of approximately 150 – 160 µm. In this section, the interaction of melt conditioning and grain refiner additions are to be analysed.

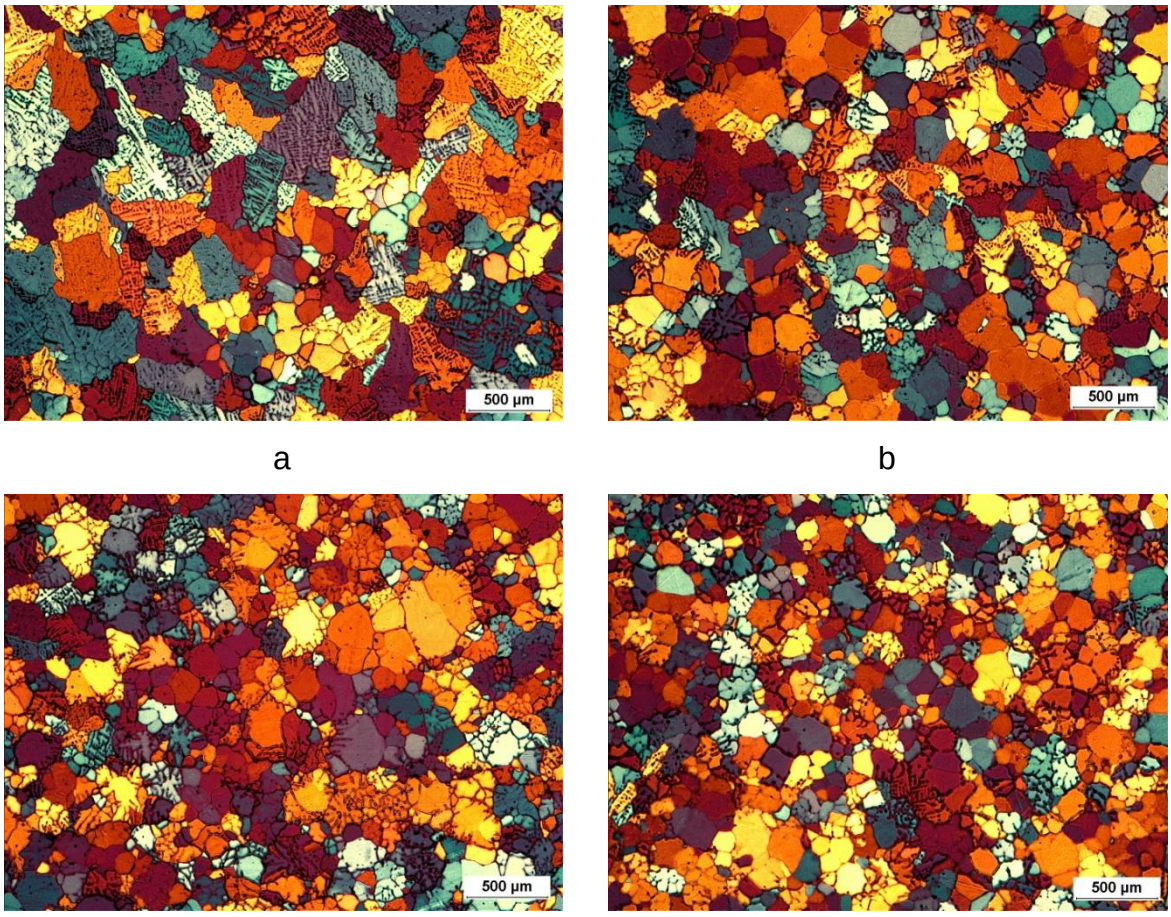

Figure 4.28 Micrographs of the MC-DC billet centre after shearing. (a) MC-DC-P2 at 4500 rpm, (b) MC-DC-P2 at 6400 rpm, (c) MC-DC-P3 at 4500 rpm, (d) MC-DC-P3 at 6400 rpm.

Table 4.3 The average grain size at the billet centres for the MC-DC-P2 and P3 billets sheared at 4500 and 6400 rpm.

Shear position	P2		P3	
Rotation speed (rpm)	4500	6400	4500	6400
Grain sizes (µm)	154± 16	134 ± 12	120 ± 11	100 ± 3

4.2.4.5 MC-DC-P2-GR grain structure

Figure 4.30a shows the billet microstructure at the surface region of MC-DC-GR billet sheared at 4500 rpm. The grain morphology is predominantly equiaxed globular with an average size of 90 ± 8 µm which is typical of a grain refined billet. The standard deviation alludes to the uniformity of the structure through its low value. This again is a function of the increased nucleation established by the grain refiner.

Figure 4.30b shows that there is in fact a coarse structure present 20 mm from the shell at a similar distance and morphology to that of the MC-DC billets. The grains are more elongated in nature and are angled to the flows that would have been present. The grains are evidently more dendritic compared with the structure the preceded them in Figure 4.30a. This means that there was a change in the growth conditions at this point along the billet radius. The most likely cause of this will be the voids in the vortex as a result of the eddies inside the flows. These eddies will have a different cooling rate and subsequent growth rate to the remaining billet. This is supported by the other images all showing fine equiaxed grain structures consisting of random globular/ rosette mixtures.

In Figure 4.30c the structure becomes uniform and equiaxed globular interspersed with larger rosettes, indicative of floating crystals transported through this region of the billet by the convective flows, coarsening as they travel before settling amid the fine equiaxed grains. At the billet centre, there is an obvious increase in the number of rosettes present in the structure, resulting in a slight increase in the average grain size. However at 96 ± 8 μm it is not cause to write off the quality of the billet on the grounds due to the mixed microstructure.

The microstructure at the centre of the MC-DC-GR-P2 billet is shown in Figure 4.30d. Here, the morphology of the grains becomes a mixture of rosettes and dendritic grains. These dendritic grains are typical of those that begun as floating crystals, which settled as rosettes and developed a dendritic structure at the periphery due to the increased cooling rate of the solid grain network. The average grains size at the centre is 96± 5 μm.

The rotation speed was increased from 4500 rpm to 6400 rpm after one metre of billet had been cast. A slice from the billet was taken as for the other casts made during this work and the microstructure obtained via OM after anodizing. The microstructure was similar to that of previous section of billet sheared at 4500 rpm. Overall the average grain size was larger when averaged out across the billet radius but only to a value that could be considered a statistical error. More definite was the replacement of the CGC with a dendritic grain structure shown in Figure 4.31a. This dendritic structure extends between 20 to 40 mm from the surface and is angled towards the heat flows. The structure shown in Figure 4.31b was obtained from the

billet centre. The grains in this image are considerably more globular in morphology and it could be argued that rosette grains are rare indicating rapid nucleation of well dispersed, plentiful substrates. The dendritic grains between the surface region and mid radius are a product of the increased nucleation from grain refining and shearing.

4.2.5 P* ANALYSIS OF THE MICROSTRUCTURE ACROSS MC-DC BILLET

P* analysis has been performed on the three sheared billets, MC-DC-P2, MC-DC-P3, MC-DC-GR-P2 at 4500 and 6400 rpm. Across the radius, twelve micrographs were obtained by OM on polished samples every 10 mm. The spatial distributions of constituent particles are then measured using a mathematical image processing algorithm, producing an average of the particle-free zones in the microstructure expressed in µm. The measurement can be used to quantify the growth rate (similar to dendrite arm spacing measurements DAS) but is alloy specific, hence the P* value for 6063 cannot be compared with the P* value of 6082. Low P* values approximate high growth rates and vice-versa.

The P* values for MC-DC-P2 are presented in Figure 4.32a. The plot of the graph shows 4500 rpm having a relatively stable and uniform growth rate across the billet radius. Highest value and subsequent lowest growth rate is at the billet centre at 68 ± 9 µm where the mixed structure developed. Large dendritic grains are present with small cellular grains which accounts for the uniformity of the growth rate according to the P* values. Across the MC-DC-P2 billet radius, dendritic grains are dominant thus the average P* value will be similar. In billets where the structures become increasingly globular, the P* value increases due to a rise in the distance between the constituent particles which is a subsequent factor of globular structures. Therefore the dendritic nature of the MC-DC-P2 grains suggests a relatively uniform growth rate across the billet radius. When this is compared to the grain structures of the MC-DC-P2 billet at 6400 rpm, there is an evidently less uniform trend across the billet radius. This result is comparable to the grain structures shown in the previous section. At 6400 rpm the structure becomes increasingly globular and rosette like towards the centre of the billet, with a P* value of 81 ± 15 µm at the core. Both 4500 and 6400 rpm billets have similar P* values around the mid radius point where the dendritic structure of the CGC is

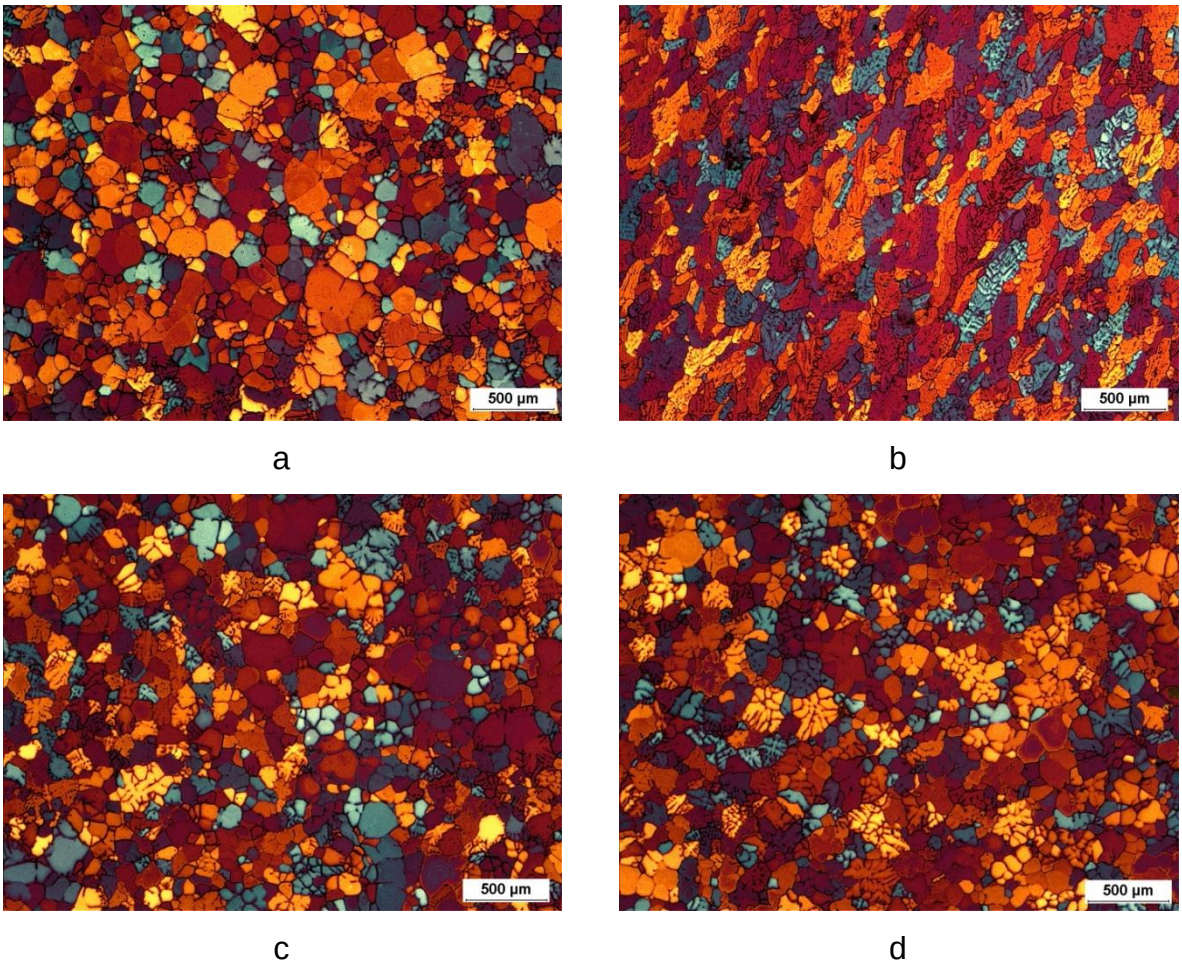

a b

c d

Figure 4.29 Micrographs obtained from the MC-DC-P2 billet sheared at 4500 rpm. (a) Surface region of the billet, (b) CGC of angled grains, (c) Mid radius region of billet after the CGC, (d) grain structure in the billet centre.

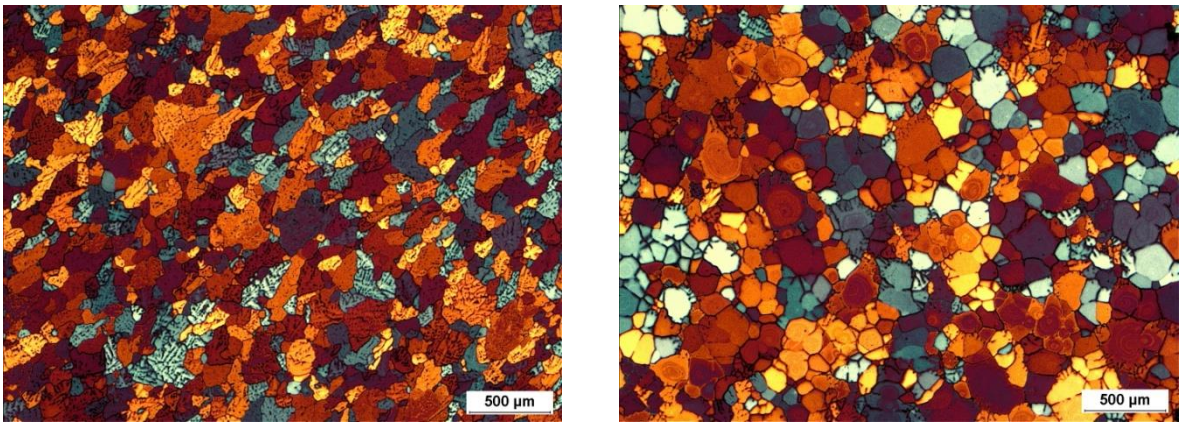

a b

Figure 4.30 Micrographs obtained from the MC-DC-GR-P2 billet sheared at 6400 rpm. (a) CGC of angled grains, (b) grain structure in the billet centre.

dominant. 30 mm from the surface the average P* value for 4500 rpm is 57 ± 5μm whilst at 6400 rpm the P* value is 55 ± 3 μm denoting a uniform dendritic structure.

These close values continue until 60 mm where 4500 rpm values remain low at 68 ± 6 μm whilst the P* value at 6400 increases to 80 ± 15 μm. The increase in standard deviation is an indication of the non-uniformity of the structure that dominates at 6400 rpm from now on. The dendritic structures have a much lower P* value than the globular rosette sections of the billet, implying a faster growth rate compared with those with a cellular morphology. This difference in morphology clarifies the increase in standard deviation between the measurements made at the centre.

Figure 4.32b presents the P* values across MC-DC-P3 at 4500 and 6400 rpm. The P* values for both 4500 rpm and 6400 rpm follow similar trends with a peak value at 40 mm and sharp drop between 45 and 60 mm. This peak is the equiaxed grain structure before the dendritic CGC which begins at 45 mm from the surface. The P* values at 40 mm for the MC-DC-P3 billet sheared at 4500 and 6400 rpm is 114 ± 13 μm and 134 ± 21 μm, respectively. These values are at the size of the grains within this region, but the high standard deviation alludes to the non-uniformity of the structure as coarse grains flow into the CGC, as a result of the layers generated during MC-DC processing. The MC-DC-P3 P* values follow the same trend as that of the MC-DC-P2 material between 45 and 60 mm from the surface. Both 4500 and 6400 rpm have low P* values and critically, between 45 and 60 mm from the surface, standard deviations denoting a uniform structure.

From 70 mm onwards, the P* values of both MC-DC-P3 billets rise, with 6400 rpm increasing the most indicating that the growth rate at the centre was slower at this speed. It is in the centre where the intensity of shearing is at its highest especially at 6400 rpm as discussed previously. This increased convection is close to the solidification front so is directly influencing the mushy zone, enhancing the heterogeneous nucleation. At 4500 rpm the intensity is less and such the number of nuclei is lower indicated by the larger grain size, a symptom of reduced nucleation.

The microstructure relative to the peak in the P* values is predominantly globular/ rosette devoid of particles within the grain body. Thus the P* values become large on the scale of the grain size. It can be argued that until 60 mm from the billet, the P* values of the billet sheared at 6400 rpm are lower than at 4500 rpm but as the

structures evolve to contain more globular grains, the growth rate reduces along with the grain size. The average grain size of billet sheared at 4500 rpm is larger in this region of the billet than 6400 rpm and more dendritic.

The P* values for the MC-DC-GR-P2 billet shows that the growth rate was fastest for this billet compared with that of the other sheared billets. The trends follow those that have been seen before in Figures 4.32a-b. Shear rotation speed 4500 rpm produces a steady growth rate and larger grains interspersed with dendritic grains, whilst 6400 rpm produces finer grains with a rosette/ globular structure.

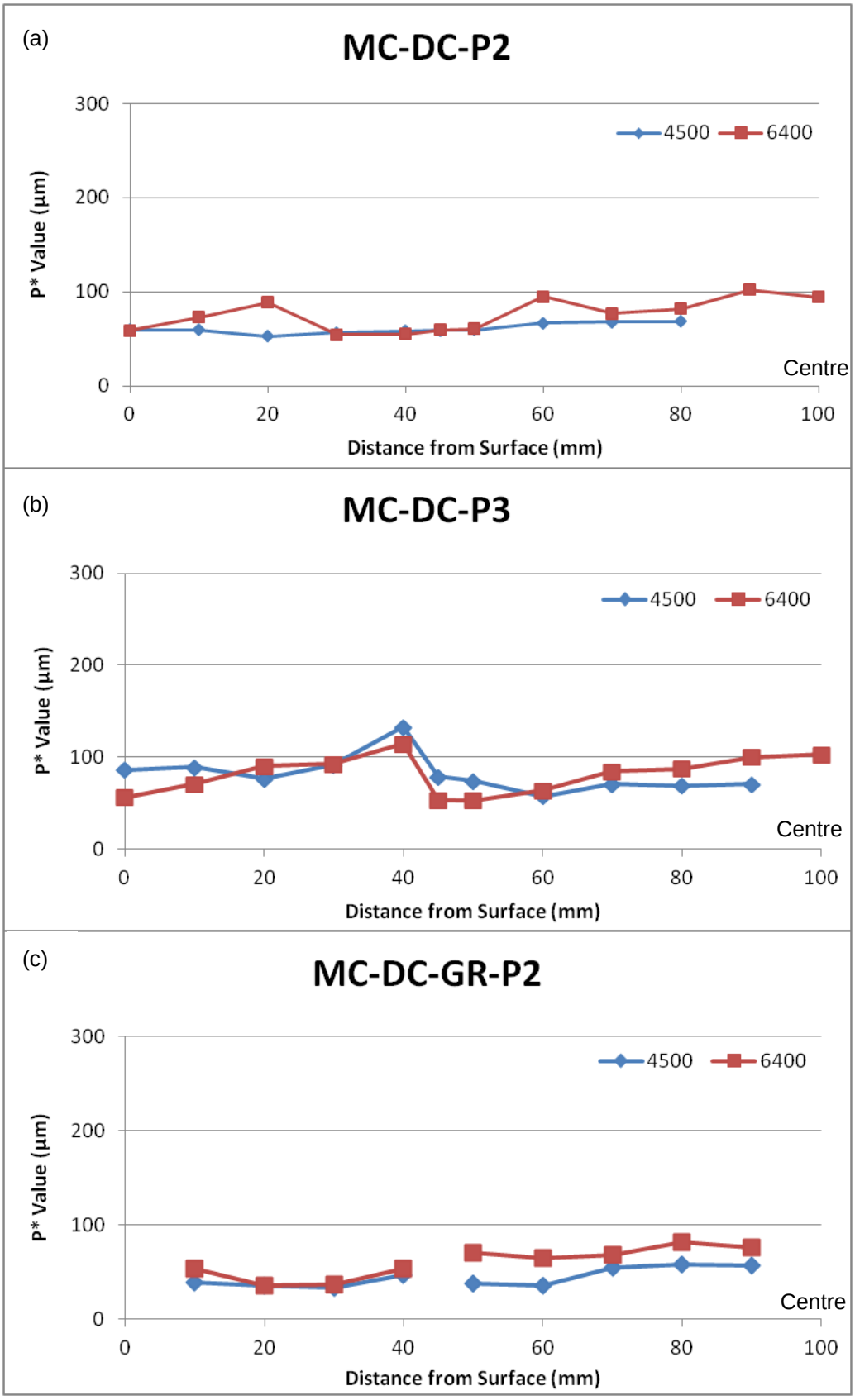

Figure 4.31 P* measurement values of the MC-DC 8" billets from the surface to the billet centre.

4.3 RESULTS-FORMATION OF FE-BEARING INTERMETALLICS

6000 series Al alloys are commonly used in extruded form. The main alloying elements in 6000 series Al alloys are Si and Mg. These alloying elements are partly dissolved in solid solution in the primary α-Al matrix, and partly present in the form of intermetallic phases. The intermetallics formed in this 6000 series alloy are Mg_2Si and Fe-bearing intermetallics. Fe is an impurity present within aluminium alloys and the amount contained in a melt is tightly controlled. Fe combines with silicon (Si) and aluminium (Al) as well as additions of manganese (Mn) to form AlFeSi and AlFeMnSi intermetallics between the Al dendrites and around grain boundaries. The type of phase that forms depends upon the local cooling rate and the local chemical composition such as, Fe to Si ratio and Mn content, etc. of the material (Liu, Thorvaldsson, & Dunlop, 1986) (Liang & Jones, 1992) (Allen, Kumar, Carroll, O'Reilly, & Cama, 2001) (Kral, 2005) (Dinnis, Taylor, & Dahle, 2005) (Sweet, Zhu, Gao, Taylor, & Easton, 2011) (Verma, Kumar, P.S. Grant, & O'Reilly, 2013). Critical to the performance of the material during downstream processing such as extrusion are the size, shape and amount of the intermetallics, with the β-AlFeSi phase being the most detrimental (Zajac, Hutchingson, Johanssons, & Gullman, 1994). This phase is planar in morphology and can initiate micro-cracks during processing as well as pick-up form the die during extrusion. Spherodised particles up to 15 μm in length are tolerated, anything larger and homogenization is required to transform the β-phase to the cubic α-Al(FeMn)Si phase. In this phase the Mn atoms are interchangeable for Fe atoms.

According to the Al-Mg-Fe-Si phase diagram, the following intermetallic compounds form during solidification; $Al_{13}Fe_4$, α-Al_8Fe_2Si, β-Al_5FeSi or $Al_9Fe_2Si_2$, Mg_2Si, π-$Al_8FeMg_3Si_6$, δ-Al_3FeSi_2 (Kral, 2005) (Kral, Nakashima, & Mitchell, 2006), and α-$Al_{15}(FeMn)_3Si_2$ as Mn is added to the melt to stabilize the α-cubic phase whilst casting and aid the beta to alpha transformation during homogenization. Note that in the 6000 series alloys investigated in the present study, Mg has very little influence on the Fe-bearing intermetallic phases or transformation rates as Mg is only added to form the age hardenable Mg_2Si precipitate.

Typically optical microscopy would determine the elongated particles present at the grain boundaries to be detrimental β - Fe bearing phase, whilst the rounded particles are considered as α - Fe bearing phase. However, it is known - and indeed shown in the following sections, that the morphology of the intermetallic is not a definitive method to determine the type of constituent phases (Dinnis, Taylor, & Dahle, 2005) (Kuijpers, Kool, Koenis, Nilsen, Todd, & van der Zwaag, 2002). As a result, Energy Dispersive Spectroscopy (EDS) was used to measure the stoichiometry of the particles to accurately determine the chemical compositions and then to identify the constituent intermetallic phases (Kuijpers, Kool, Koenis, Nilsen, Todd, & van der Zwaag, 2002). EDS produces a quantitative analysis of the element concentration of the particles selected by measuring the intensities of each element present against calibration standards of known composition.

This chapter presents the microstructure of the material cast by static mould, lab scale DC and industrial scale DC experiments to systematically investigate the type, morphology and distribution of the Fe-bearing intermetallic particles. Further examination of the intermetallic particles by SEM follow these microstructures to accurately identify the phases present with relation to alpha and beta constituents and their positions within the bulk, size and morphology in particular aspect ratio and lengths.

4.3.1 INTERMETALLICS FORMED IN STATIC MOULD SAMPLE

4.3.1.1 Intermetallic Morphology in Static Mould Samples

Figure 4.33 shows micrographs of the static mould billet from zone 1-4 (Figure 4.11). Images (a, c, e, g) were taken at 100x magnification and provide an overview of the matrix and the particle content within the bulk structure whilst images (b, d, f, h) were obtained at a higher magnification (500x) providing a closer look at the morphology of the intermetallics. Light optical microscopy (LOM) on a polished sample was used to acquire these micrographs.

Variations between the microstructures of the different zones are clear. Zones 1 and 4 solidified without direct influence by shearing with cooling rates that greatly differed due to the method of heat extraction attributed to these zones. Zone 1 was in direct contact with the chill face provided by the copper block for solidification against, whilst the heat of zone 4 escaped to the atmosphere as the top of the mould was not covered like the sides. This allowed two distinct structures to develop. Zone 4 consists of large equiaxed dendritic grains, whilst zone 1 consists of fast growing columnar grains that extend vertically from the base into the billet.

If we focus now on each zone separately for clarity of understanding, we shall start with zone 1 as this is where solidification began. The particles of zone 1 (images g and h) form as elongated needles at the grain boundaries for the majority, mirroring the elongated nature of the columnar grains. Very few large intermetallic particles of plate type morphology developed within this zone as the rapid growth of the dendrite tips into the liquid, leaves very little in the way of space for significant volumes of liquid to remain between the grains, resulting in elongated particles that are thin and have limited connectivity due to the size of the grains and lack of grain junctions. The dendritic nature of the grains leads to the well dispersed particles that can be seen within the body of the grains. However, many of the particles formed as rods and this type of morphology will certainly require transformation to a more spherical type of particle for better performance down-stream.

The microstructure of zone 2 is shown in Figures 4.33e-f. This zone was directly influenced by the conditioning action of the shear device. Subsequently the structure of this zone developed randomly with angled coarse grains at the periphery of the zone and coarse equiaxed grains directly below the shear device. Morphology of the intermetallic particles was determined by the grain size and morphology where last solidified liquid were trapped between the coherent grains. It is also clear from the images that small particles of AlFeSi are well distributed within the body of the grains due to the predominantly dendritic morphology of the structure in this zone.

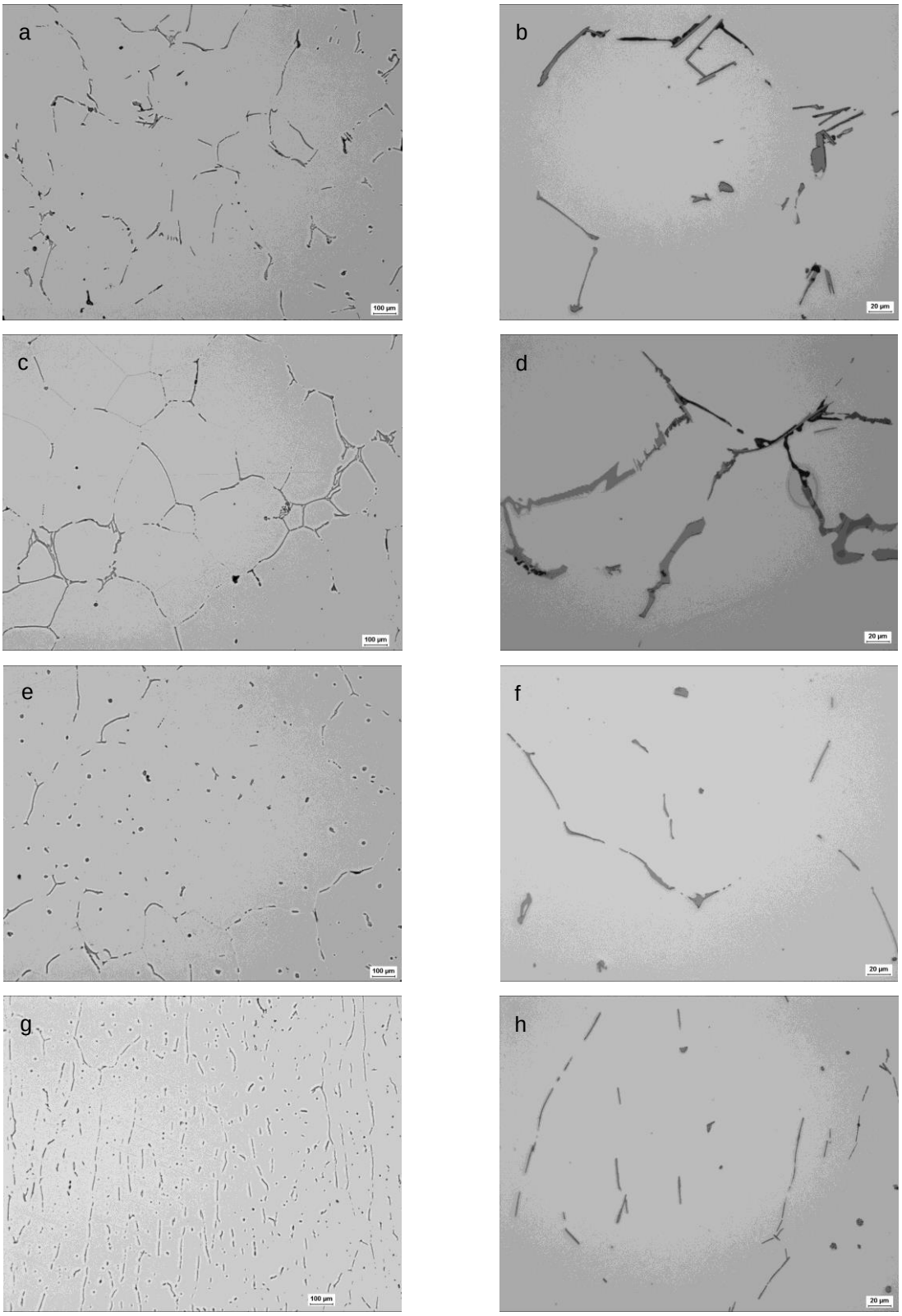

Figure 4.32 Micrographs of the intermetallics formed in the static mould within the four different zones. Each set of images was obtained by LOM at 100x and 500 x magnification respectively. (a – b) Zone 4, (c-d) Zone 3, (e-f) Zone 2, (g-h) Zone 1

Needles of AlFeSi can be seen between the dendrites but smaller block and spherical particles developed also. There is a general coarsening of the intermetallics compared to those of zone 1 (Fig. 4.33g-h) and zone 2 (Fig 4.33e-f) and a tendency of the smaller particles in the grain bulk to develop with a block morphology. There are still the needles of intermetallic at the boundaries that are arguably longer than those in zone 1, but they are well separated and distributed around the boundaries which is indicative of large dendritic grain structures.

Zone 3 was directly influenced by the shear device and as a result, the grains that formed here were the most refined of the 4 zones. The intermetallic structures are shown in Figures 4.33c-d. The images show that the intermetallics that formed are very complex and coarse. “Chinese script” morphology and complex particle formations can be seen at the grain junctions and around the smaller grains, an example of which is presented in Figure 4.33d. The intermetallics shown in Figure 4.33d are substantial plates with needles of beta phase connecting the intermetallics at the grain junctions. The variance in grey scale of the particles denotes compositions changes which could be an indication of different phases; most probably some Mg_2Si phases are present in the darker phases. Chinese script is typically associated with the preferred α-AlFeSi phase that industry strives to achieve, but the coarseness of these particles will only cause problems down-stream, especially as α-phase does not transform as readily as β- during homogenization. In Figure 4.33d, black particles of Mg_2Si have precipitated upon the grey intermetallic particles of the constituent AlFeSi phase and will need to be dissolved into solid solution during homogenization, to stop the Mg_2Si particles becoming low temperature melting points during processing.

Shrinkage porosity is evident in Figure 4.33d also. From the location of the pores in relation to the intermetallics, it would suggest that they are a result of restricted melt flow into the regions of shrinkage between the grains due to the complex nature of the intermetallics, preventing melt reaching the voids in the mushy zone.

Coarse intermetallic particles are typical of globular/ cellular grain structures as the solute segregates out of the small fine grains enriching the liquid that solidifies between the grains at the end of solidification. An example of a cellular grain encompassed by intermetallic can be seen in Figure 4.33c. Apart from the plate type

particles there is little to distinguish between the phases in terms of morphology, but it could be argued that the darker grey particles have a tendency towards a block morphology typically regarded as beta phase intermetallics. The curvier lighter grey particles could be alpha-AlFeSi.

The intermetallic structure of zone 4 is shown in Figure 4.33a-b. The intermetallics in this zone are coarse, connected rods of facetted particles that formed with definite block-like morphology. Plates of intermetallic are clearly visible within the images but these are in the minority. Mg_2Si has visibly precipitated onto the AlFeSi phases, shown in detail in Figure 4.33b as black particles on the edges of the grey rods. It should be remembered at this point that Zone 4 was not directly conditioned by the shearing device, as the head of the stator where the jets of melt exit was below this zone (zone 3) and, the device was not spinning when it was extracted from the melt. Thus the melt in zone 4 solidified after shearing had stopped with heat extraction happening through the solidified structure below and to the environment via the open top of the mould. Large equiaxed dendritic grains dominate the microstructure where the bodies of the grains are devoid of particles. The slower growth rates of zone 4 allowed the solute elements to segregate more severely from the body of the grains to the boundaries and grain junctions, where they developed into larger, coarser intermetallics.

Image analysis software INCAFeature was used to measure the size of the particles across the four zones of the billet. The results are shown in Figure 4.34. Average particle length, width and area were measured for each zone by SEM with a shape factor included to quantify the morphology of the particles. Spherical particles would have a value closer to unity with longer particles and those with block morphology having a value closer to 10.

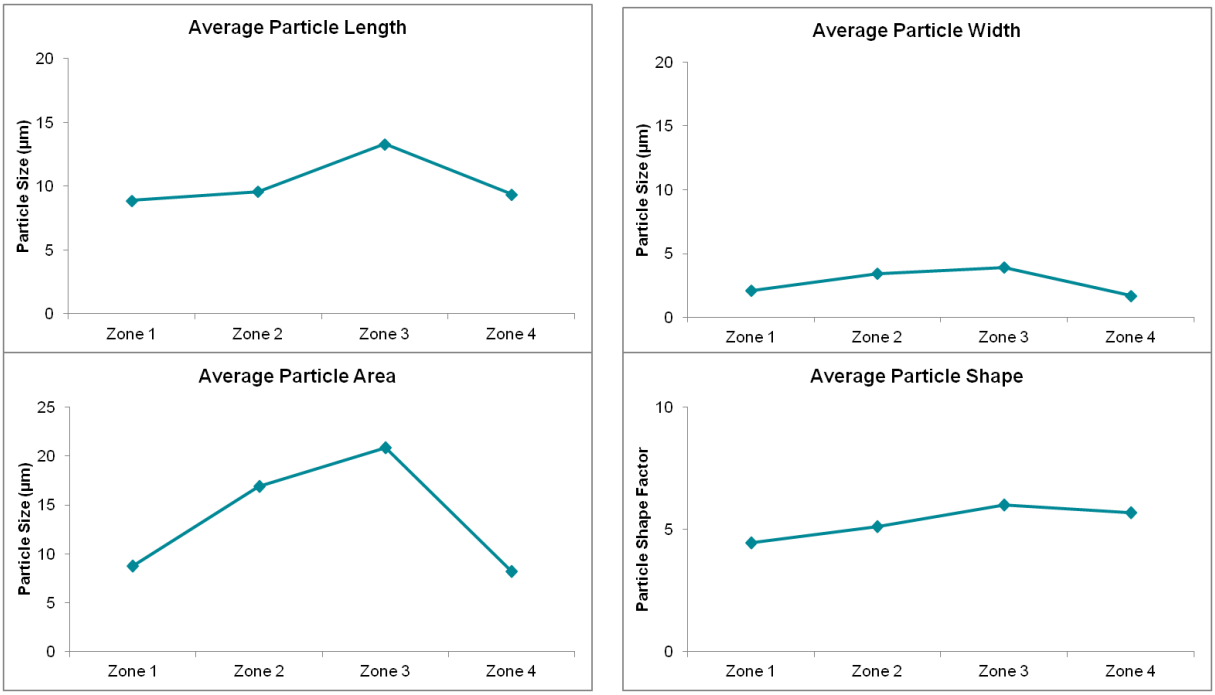

Figure 4.33 Graphs showing the average particle lengths, width, area and shape factor of the four static mould zones. The graphs show a decrease over all parameters from the sheared regions to the columnar zone at the base of the billet. Here the cooling rate was highest with zone 1 having the slowest.

The trend of the results in Figure 4.34 describe an increase in the size of the particles from zone 1, reaching a peak in all parameters at zone 3, before reducing in size in zone 4. It is clear that the particles in zone 3 stand out as being larger on average to those measured in the billet. Melt conditioning was most intense within this zone of the billet, compared with the results of zone 1 which was unaffected by shearing, leading us to consider the effect of cooling rate or more specifically, solidification rate upon the formation of the intermetallics.

The trends indicated in Figure 4.34, suggest that the particles from zones 1 and 4 are very similar in size. However, the images of Figure 4.33 present intermetallics that appear very different with those of zone 4 arguably more complex and connected. They are however predominantly rod like in morphology which is supported by the similarity in results between zone 1 and 4. The shape factor value suggests that the particles in zone 1 are more spherical than those measured in all the other three zones (Figure 4.34d). Particles within the interdendritic regions are more rounded plus the boundary intermetallics are less interconnected and facetted compared with those of the other shearing effected zones.

As we move upwards through the billet away from zone 1, the microstructure of the billet reflects the change in grain morphology and resulting difference in the intermetallics. Figure 4.34 describes an increase in the average length, width and area of the intermetallics measured within zone 2. However, the increase in the length, width and shape factor is not considerable, but it is for the particle area. The intermetallics form more complex shapes due to the variation of grains compared with the relative regularity of the zone 1 structure. The software also measures those intermetallics that are interconnected as one particle, therefore resulting in an increase in the area of the particles.

Zone 3 shows the largest increase across all 4 zones in Figure 4.34. It is the zone with the smallest granular grains and the most complex intermetallics that are highly interconnected. Therefore the lengths and area of the particles increases sharply compared with the other zones. In contrast to this is zone 4 which also has an equiaxed grain structure with a grain size double that of zone 3, the size of the intermetallics decreases dramatically to similar values of those measured in zone 1. It is therefore provisionally summarized that it is the grain structure that is critical for achieving finer and well distributed Fe-bearing intermetallics rather than the grain size.

4.3.1.2 EDX Analysis of Intermetallic Particles in Zone 1

Figure 4.35 shows SEM images of the intermetallics in zone 1. The majority of the particles are elongated along the grain boundaries (Figure 4.35a) whilst more spherical particles are found within the grains (Figure 4.35b-d). Figure 4.35b shows that the elongated particles at the grain boundaries are delta (δ) phase which is the lowest Fe ratio phase when comparing against alpha (α) and beta (β) phases. The inter-dendritic particles that are found within the body of the grains have been identified as a mix of α- and β-AlFeSi intermetallic phases. The morphology and size of the particles are very similar for the two constituent phases as shown in Figure 4.35c-d which is a good indicator of how morphology alone is not enough to accurately determine the phases present. Therefore EDX statistical analysis obtained

by scanning electron microscopy (SEM) was used to distinguish between the phases and determine if there was a dominant phase present within the zones.

Figure 4.36a contains measured data plotted against three separators designated to the alpha, beta and delta-AlFeSi phases. For greater accuracy the Mn content of the particles is added to the Fe content when calculating the Fe:Si ratio, due to Mn being present and substitutional to Fe in α-Al(FeMn)Si. The calculation is defined as Fe:Si = $(I_{Fe}+I_{Mn)}/I_{Si}$ where I is the intensity of each measured element. This ratio determines the phase based on where the value falls between set limits which are; α-, β-, δ- Fe-bearing intermetallics. The results are displayed in Figure 4.36b accompanying the phase separation diagram in determining a dominant phase(s).

Figure 4.36a shows the delta phase is the most dominant phase in zone 1 supported by the mean Fe:Si ratio of 0.88 at%. The delta phase was the most dominant phase in zone 1 due to its more common occurrence at the grain boundaries compared to the more distributed and less common intermetallics within the bulk of the grains. The inter-dendritic particles are a mix of alpha and beta AlFeSi intermetallics with higher Fe content, due to solute enrichment of the liquid between the dendrite arms. At the boundaries, Si segregates quicker than Fe and as a consequence of the rapid growth rate in zone 1, the ratio of Fe:Si is lower at the boundaries thus delta forms preferentially.

4.3.1.3 EDX Analysis of Intermetallic Particles in Zone 2

SEM images of the intermetallic particles that formed in zone 2 are shown in Figure 4.37 with the AlFeSi phase shown for a number of the particles in the images. The morphologies of intermetallic particles are varied like in zones 1 but it is clear there are more particles within the grain bulk as the structure in this zone is dendritic. The particles in the grains are a mix of spheres and plates as shown in Figures 4.37c and d, whilst at the grain boundaries the AlFeSi intermetallic phases are elongated, see Figure 4.37e. A large plate or collection of complex intermetallics is identified in Figure 4.37f at the junction of multiple grains. Here a relatively large volume of liquid

became enriched as the grains grew together, trapping the liquid and forming a large plate of beta Fe-bearing intermetallic phase.

It is clear from the images in Figure 4.37 that the intermetallics are a mix of alpha, beta and delta phases with the morphology and location of the particles an insufficient parameter for distinguishing between them. Figure 4.37c shows that the alpha and beta phases have a very similar morphology and can be found at the grain boundaries and in the body of the grains. The delta phase is less common in this sample even at the grain boundaries where this phase was most prevalent before. Particles of beta still appear as shown in Figure 4.37f with a large “Chinese script” particle at a grain junction which would be detrimental to the extrudability of the billet as well as potentially deleterious to the performance of the product further downstream

The majority of the particles identified in the images tend towards the α-phase, something that is supported by Figures 4.38a and b. It is clear that the majority of the data points from the EDX measurement are above the alpha phase separator at lower Si levels. The Fe:Si ratio diagram shows a large spread in the Fe+Mn/Si statistics with the trend line at the top of the diagram where the alpha phase is dominant. The average Fe:Si ratio value was 1.41 at% due to a high Fe concentration in the particles resulting in the dominance of the alpha phase.

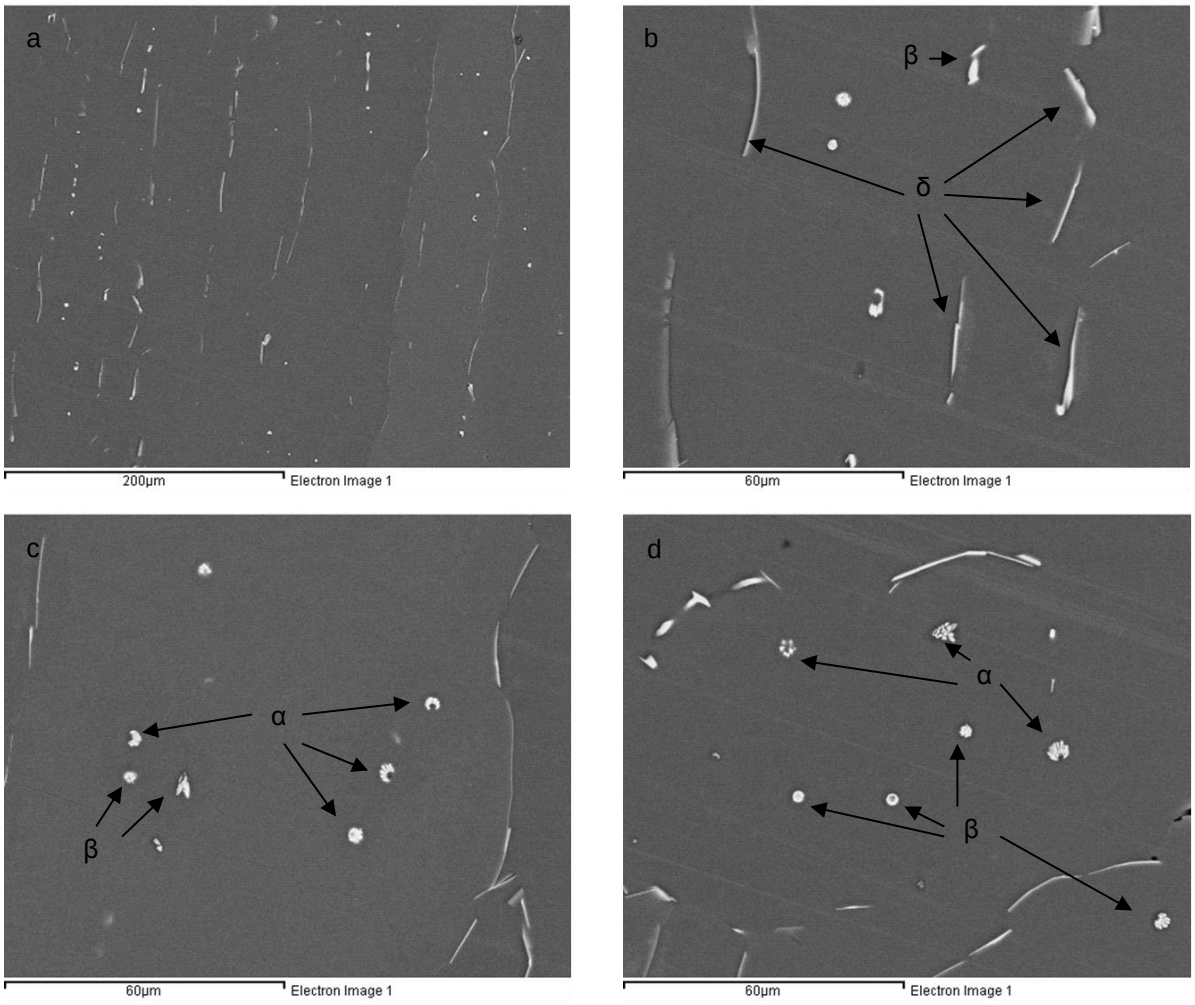

Figure 4.34 SEM (BSE) images of intermetallics found in zone 1 around the columnar grain boundaries.

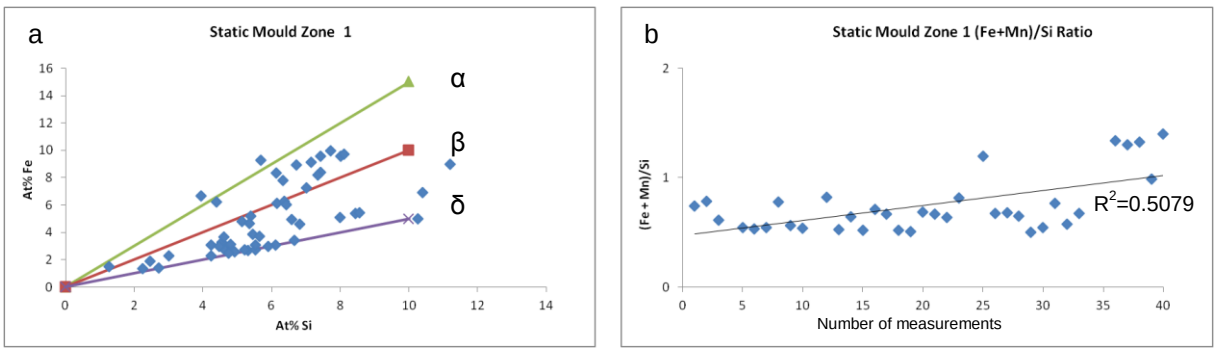

Figure 4.35 (a) (Fe+Mn)/Si ratio from intermetallics measured from zone 1 in the static mould sample, plotted against α- and β-AlFeSi separators, (b) (Fe+Mn)/Si ratio.

4.3.1.4 EDX Analysis of Intermetallic Particles in Zone 3

The grain structure in Zone 3 is very different from that of zone 2; the grains are smaller and cellular compared to coarse dendritic with the resulting intermetallics shown in Figure 4.39. Coarse intermetallics consisting of large plates and Chinese script are clearly visible (Figures 4.39b-d) at the boundaries and grain junctions. These intermetallics become coarser where smaller grains meet larger grains and they trap liquid instead of growing into the liquid as the dendritic grains do. It follows that a decrease in cell size is related to an increase in intermetallic particle size due to solute segregation to the grain boundaries, rather than dispersing inter-dendritically and at the boundaries as in zone 2.

Pure grain boundaries are indicative of this type of grain structure where cells have grown together with no trapped liquid and thus intermetallics between them at the boundaries. The final solidifying liquid that the intermetallics form from is trapped between the cells as the structure becomes more coherent and connected. There is no indication that the quantity of intermetallics increased compared with the other zones, rather the agglomeration of trapped liquid is higher in cellular structures creating coarse intermetallics that enrich in solute elements due to the increased segregating nature of the globular grains.

The majority of the intermetallics were α-AlFeSi phase especially the particles with Chinese script morphology at the grain junctions, indicated in the images. Figure 4.39d interestingly shows a plate of β-AlFeSi phase surrounded by coarse alpha phase that appears to encapsulate two small grain fragments. There is a suggestion here that the beta phase may form first, transforming into alpha as the Fe concentration increases as segregation proceeds further. The plate of beta however is isolated by the surrounding alpha phase thus remains as β-AlFeSi.

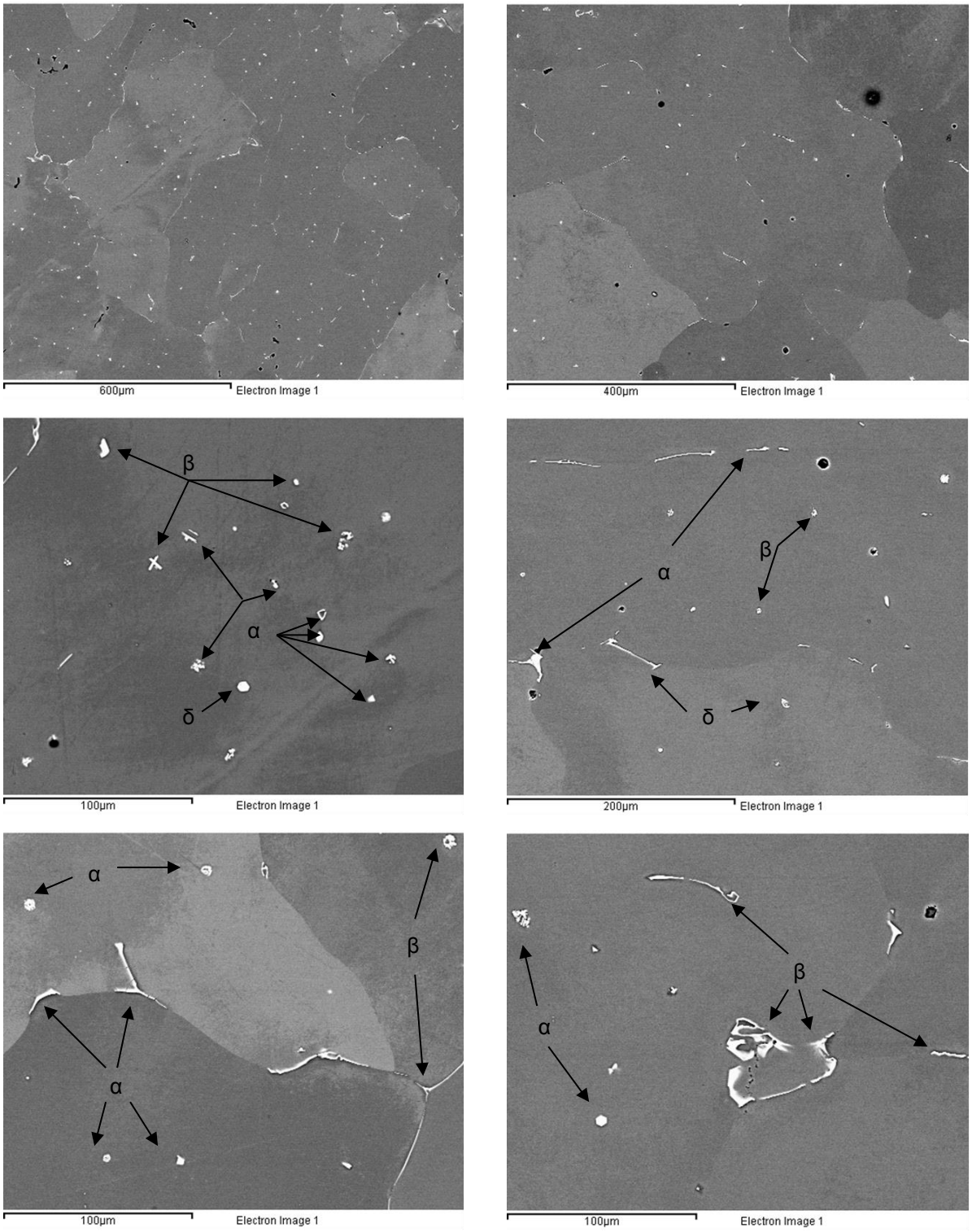

Figure 4.36 SEM (BSE) images of intermetallics found in Zone 2 of the static mould sample.

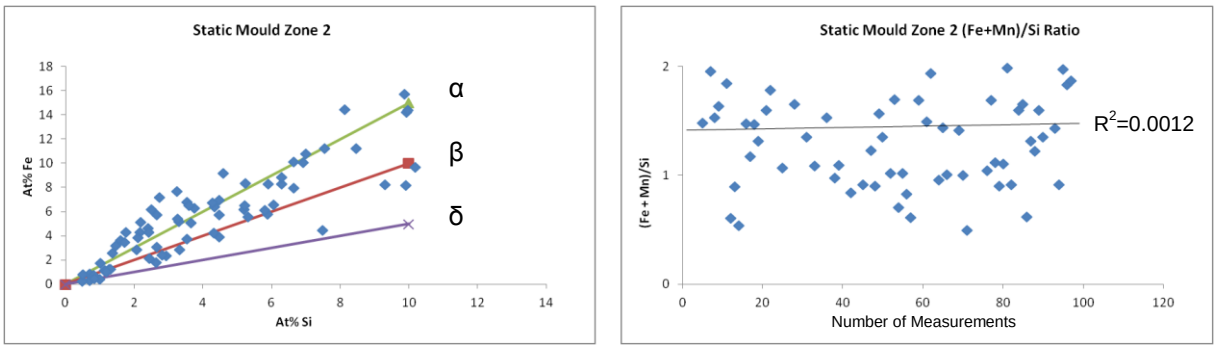

Figure 4.37 (a) Si/(Fe+Mn) ratio from intermetallics measured in Zone 2 from the static mould sample, plotted against α- and β-AlFeSi separators, (b) Si/(Fe+Mn) ratio

Alpha and beta AlFeSi are the dominant phases here with Delta being absent from all the particles measured by EDS. This is very typical of the situation experienced by industry; Alpha and beta are the two phases concerned with the 6xxx series alloys apart from the dissolvable compound Mg_2Si which is dissolved during homogenisation treatment. Figure 4.40a confirms that the dominant constituent phase of zone 3 is α-AlFeSi with the large majority of data collected above the alpha separator in the diagram. No Delta-phase intermetallics were detected out of the particles measured which is indicative of the enrichment of the intermetallics during solidification, resulting in higher Fe:Si ratios that lead to α-AlFeSi being dominant. Figure 4.40b displays the Fe:Si ratio distribution of zones 3 with an average value of 1.45 at%. The trend of the data is very flat about the 1.5 at% value, thus there is no low Fe concentration intermetallics measured confirming that delta phase is not present in this zone and that beta will be less.

4.3.1.5 EDX Analysis of Intermetallic Particles in Zone 4

The intermetallics formed in zone 4 are presented in Figure 4.41. The intermetallics have a plate morphology forming rods of intermetallic at the boundaries which are coarse and will have a noticeable effect on the performance of the material down-stream. Chinese script is evident again, an example of which is identified in Figure 4.41b at the edge of a large grain where a smaller grain appears enclosed by α-AlFeSi.

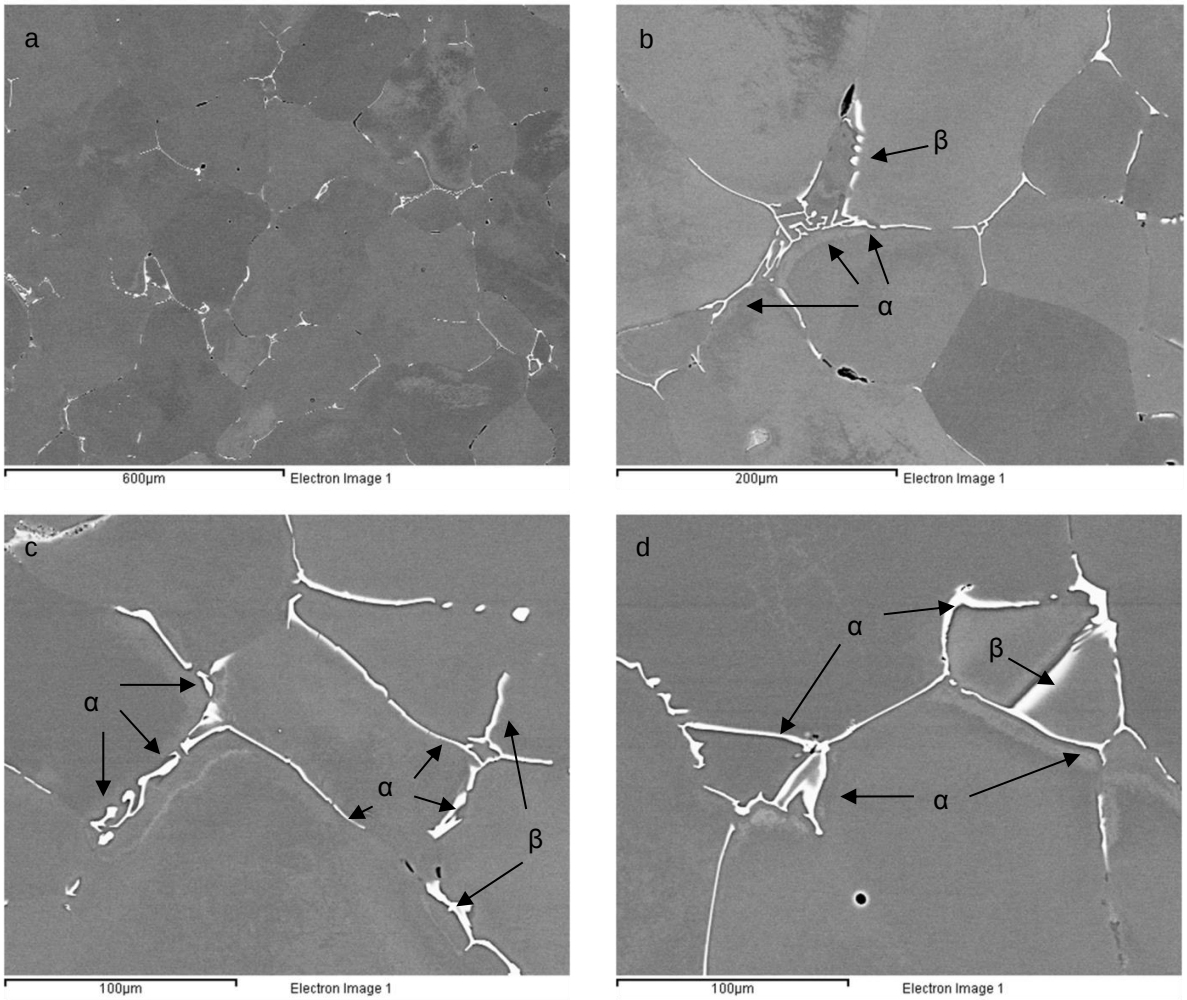

Figure 4.38 SEM (BSE) images of intermetallics found in the Zone 3 of the static mould sample.

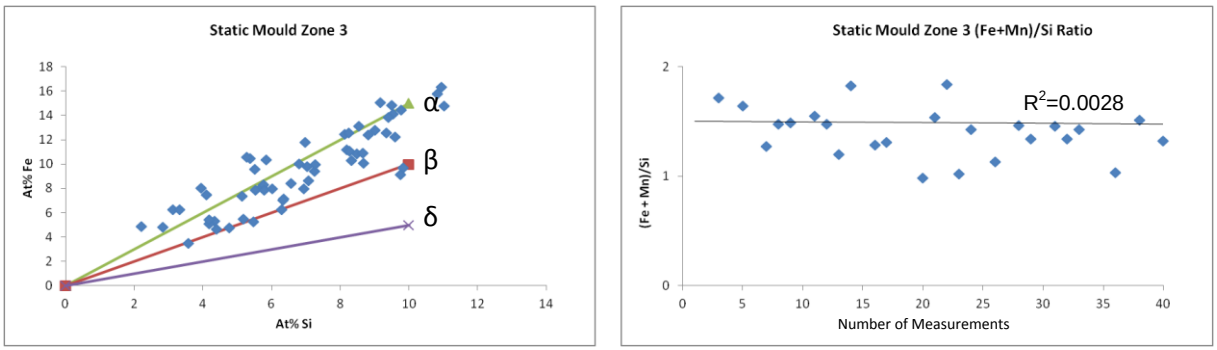

Figure 4.39 (a) (Fe+Mn)/Si ratio from intermetallics measured in Zone 3 from the static mould sample, plotted against α- and β-AlFeSi separators, (b) Si/(Fe+Mn) ratio.

Here, liquid is trapped as the grains move and grow together resulting in larger pockets of final solidifying liquid. The remaining intermetallics formed as rods that are elongated without any evidence of breaking up thus require refinement through homogenisation before processing. The majority of the intermetallics in Figure 4.41b have been identified as having a beta phase constitution with the rest being alpha phase.

In Figure 4.41c there is evidence of intermetallics that have broken-up and become smaller individual particles separated from the elongated rods around the grain boundaries. Beta-AlFeSi is the dominant phase in this image and the particles morphology is consistent with its typical blocky nature of plates and rods.

In Figure 4.42a, the diagram clearly shows that α-AlFeSi is not the dominant phase within this zone of the ingot. The alpha phase is present as expected at the grain boundaries and the particles thicken at the grain intersections. There is also a noticeable lack of particles within the bulk of the grains that would become enriched alpha phase, thus the dominant phase is β-AlFeSi which formed as rods at the boundaries. This is supported by the (Fe+Mn)/Si ratio that is presented in Figure 4.42b. The diagram shows a trend through the particles decreasing towards the low Fe levels of the delta phase with an average ratio of 0.84 which indicates beta dominance.

In summary, based on SEM-EDX analysis results, the Fe-bearing intermetallic phase formed in zone 1 is predominantly δ-phase; whist it is β- phase in zone 4; in both cases, the effect of shearing is is very weak. However, in zones 2 and 3, α- Fe-bearing intermetallics dominated, where the effect of intensive shearing was significant.

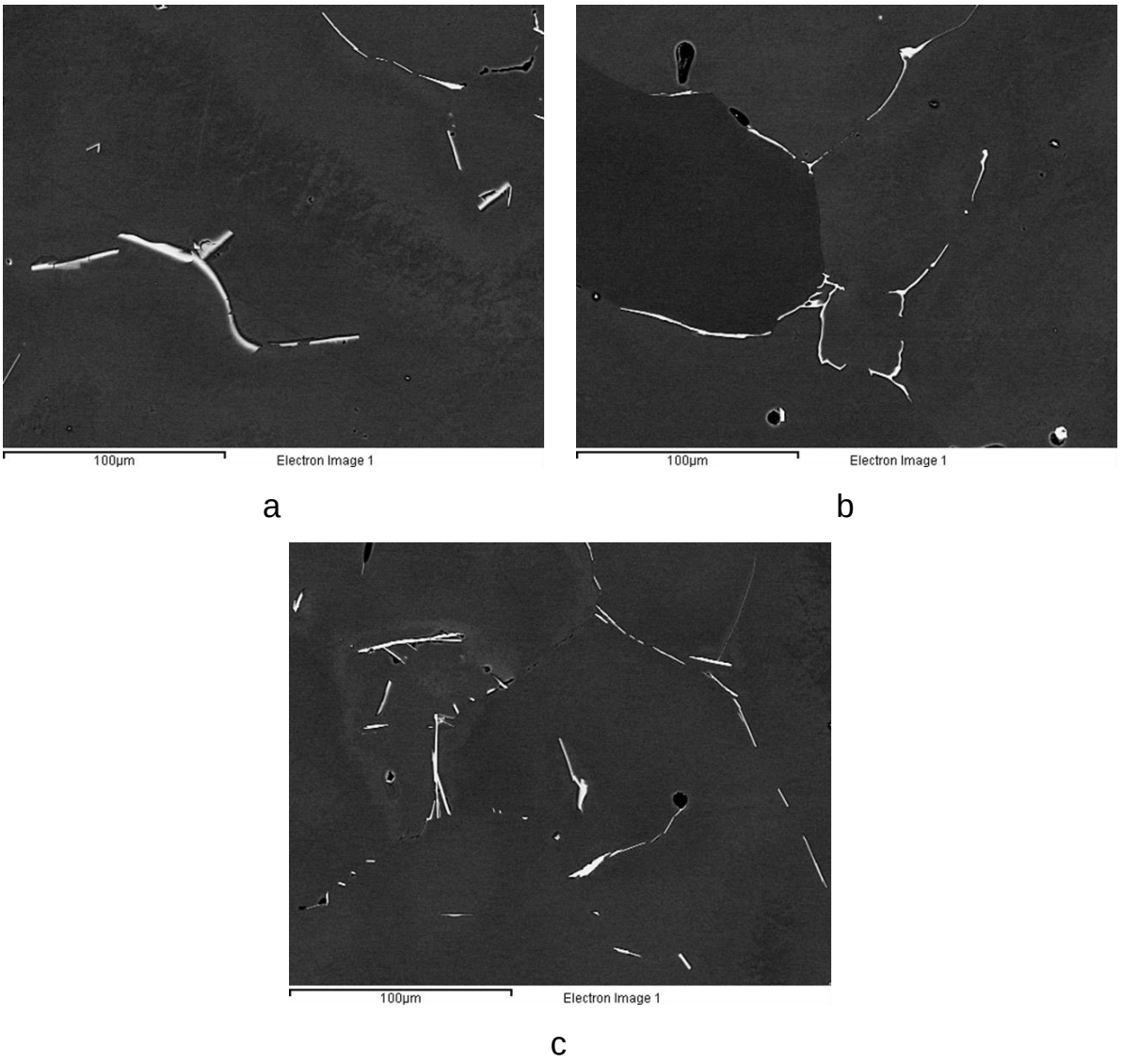

Figure 4.40 SEM (BSE) images of intermetallics found in Zone 4 of the static mould sample.

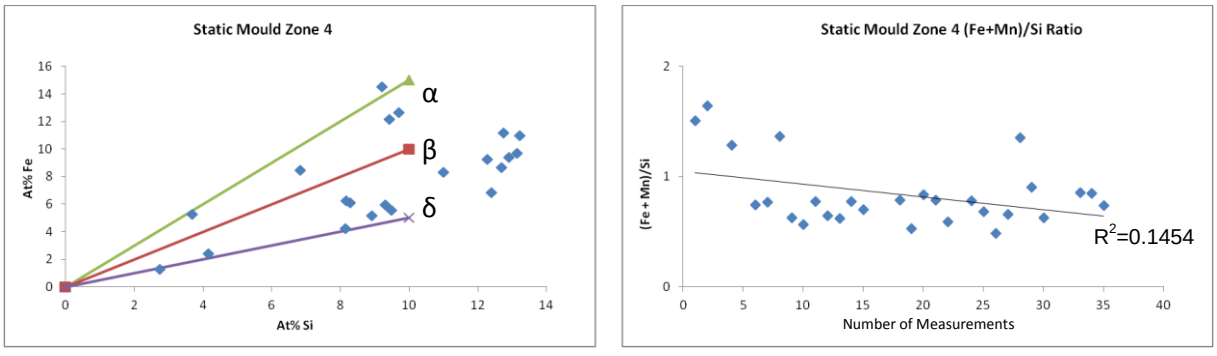

Figure 4.41 (a) (Fe+Mn)/Si ratio from intermetallics measured in Zone 4 from the static mould sample, plotted against α- and β-AlFeSi separators, (b) (Fe+Mn)/Si ratio.

4.3.2 INTERMETALLICS FORMED IN DC CAST BILLET AT OXFORD

The intermetallics of the 206 mm diameter billet cast by direct chill casting unit on the Oxford Begbroke Science Park are presented here. We start with the grain-refined material DC-GR and the grain-refined material with shearing MC-DC-GR. The DC-GR material is the comparative material in this study due to its additions of grain-refiner creating a similar billet microstructure to what is achieved in industry today. MC-DC-GR follows on from this material to determine the effect of shearing in combination with TiB_2 additions. Both billets were cast with identical parameters to those of the melt conditioned billets, but with additions of TiB_2 made to the ratio of 1.0 kg/tonne.

Melt conditioned billet with the shear device positioned at different heights MC-DC-P2 and MC-DC-P3 follows with analysis at 4500 and 6400 rpm for both shear device positions.

4.3.2.1 Morphology of Intermetallics - Oxford DC-GR

Figure 4.43 shows the microstructure of the billet of DC-GR. The microstructure is dendritic in nature with uniform size through the cross-section of the billet. As a result the intermetallics are distributed at the grain boundaries and inter-dendritic regions as shown in Figure 4.43a and c. At the surface the grains are slightly smaller than those of the centre and as such there is a coarsening of the particles at the grain junctions, Figures 4.43a-b. At the higher magnification (Fig. 4.43b) this is more evident where plates of intermetallic can be seen in groups with a connected structure. Also evident at this higher magnification (500x) is the occurrence of the needles becoming necklace like in morphology, where the particles have broken-up into arrangements of smaller particles.

At the centre (Figures 4.43c-d), the grains are larger with slightly less connected particles at the grain junctions where they have been seen at the surface but intermetallic plates of AlFeSi are still present (Fig.4.43d). What is noticeable is that there are fewer particles within the bulk of the larger grains at the billet centre, which

also have a much more needle-like morphology compared with the smaller and more spherodised particles in the bulk of the grains at the billet surface.

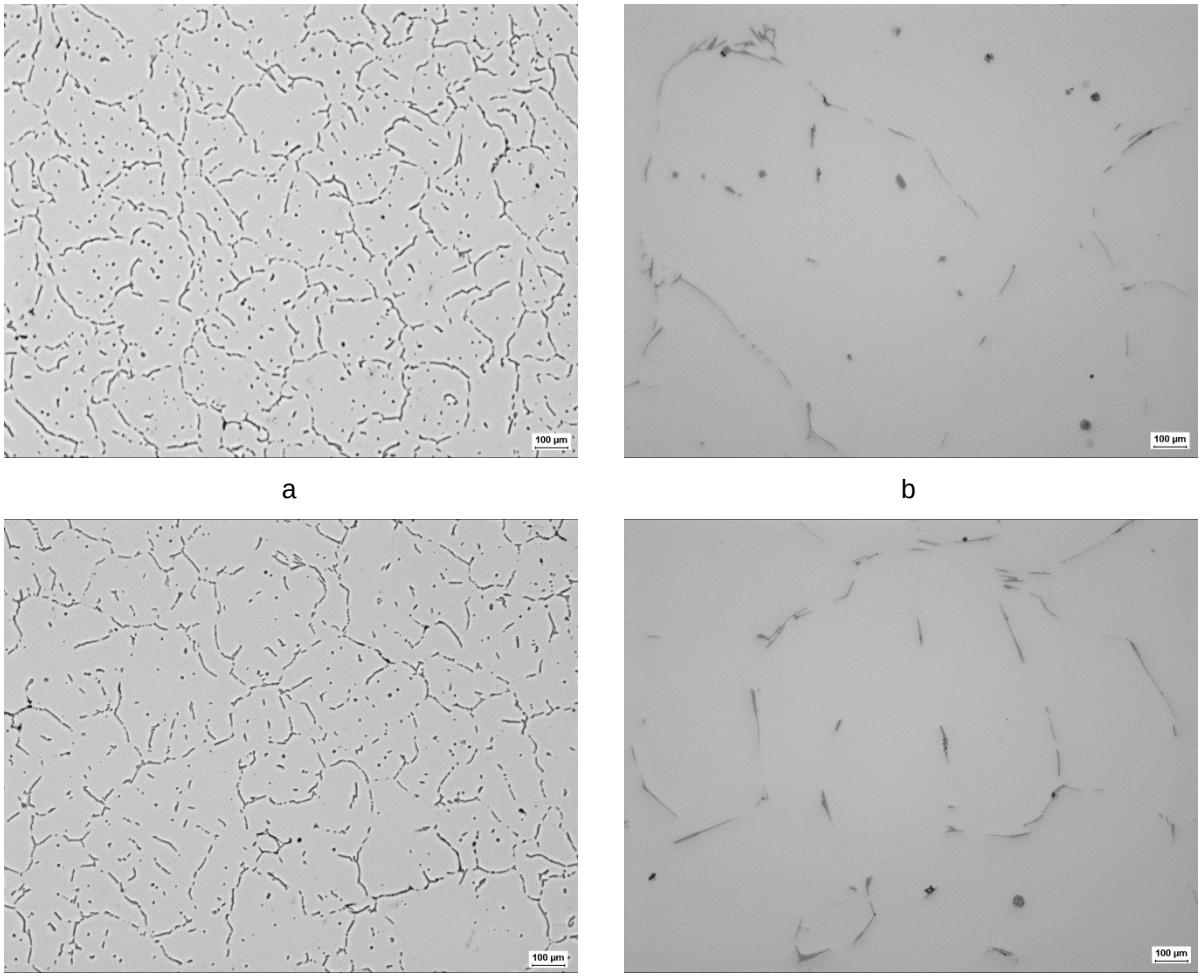

Figure 4.42 As-cast microstructure of DC-GR billet (a) Surface region at 100x magnification. (b) Surface region at 500x magnification (c) Central region at 100x magnification. (d) Central region 500x magnification. Microstructures and intermetallics look very uniform across the billet as expected form inoculated melts.

The diagrams presented in Figure 4.44 show the average particle lengths, width and area of the Fe-bearing intermetallic particles measured by INCAFeature analysis on images obtained by SEM. It can be argued that the particles at the surface are smaller than those at the centre especially the area of the particles. This is not surprising as the particles widths are the same but shorter at the surface region with the measurements taking into account the necklaces of smaller particles described above.

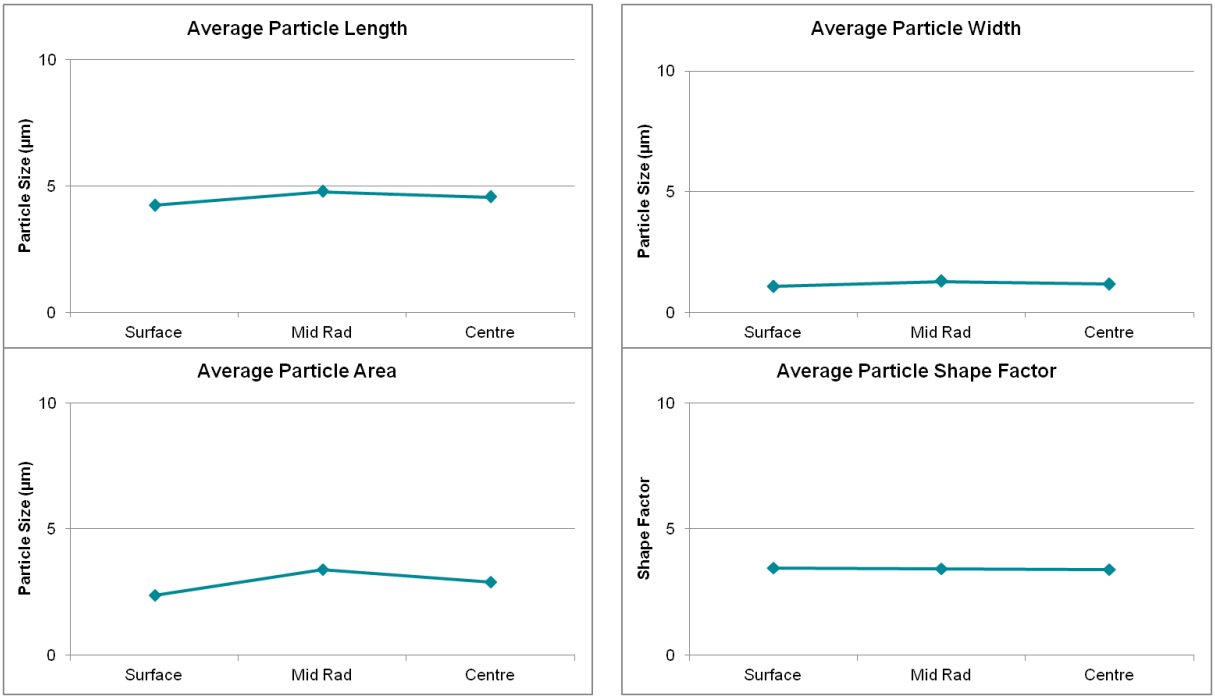

Figure 4.43 INCAFeature SEM analysis software produced results of average particle measurements. As-cast DC-GR billet produced on the DC unit at Oxford.

In general, the grain size affects the size of the intermetallic particles hence the uniform nature of the grains leads to the uniform intermetallic structure also, due to the fact that most intermetallics form in the late stage of solidification and are located in interdendritic areas or on grain boundaries in a hypoeutectic alloy system. As the grains develop, they press together as they grow becoming more interconnected pressing trapping liquid and squeezing it between the solidifying grains, thus determining the form it takes.

The shape factor presented in Figure 4.44d shows that there is nominal variation in the shape of the particles across the billet radius, with needle-like particles being the dominant morphology. This fits well with the theory that uniformity in the grain structure leads to uniformity in the intermetallic structure also.

4.3.2.2 EDX Analysis of Intermetallics –Oxford DC–DC-GR

Morphologies of the intermetallics of the DC-GR are shown in Figure 4.45. The results of the EDX analysis are presented in the high magnification images in Figure 4.45b and d. In Figure 4.45b there is a mix of beta and delta phase present with both showing similar morphologies: needles and plates. A similar situation is found in Figure 4.45d in the central region of the billet. Here beta and delta AlFeSi exist together but beta is arguably more plate-like in morphology compared to the thin needles of the delta phase.

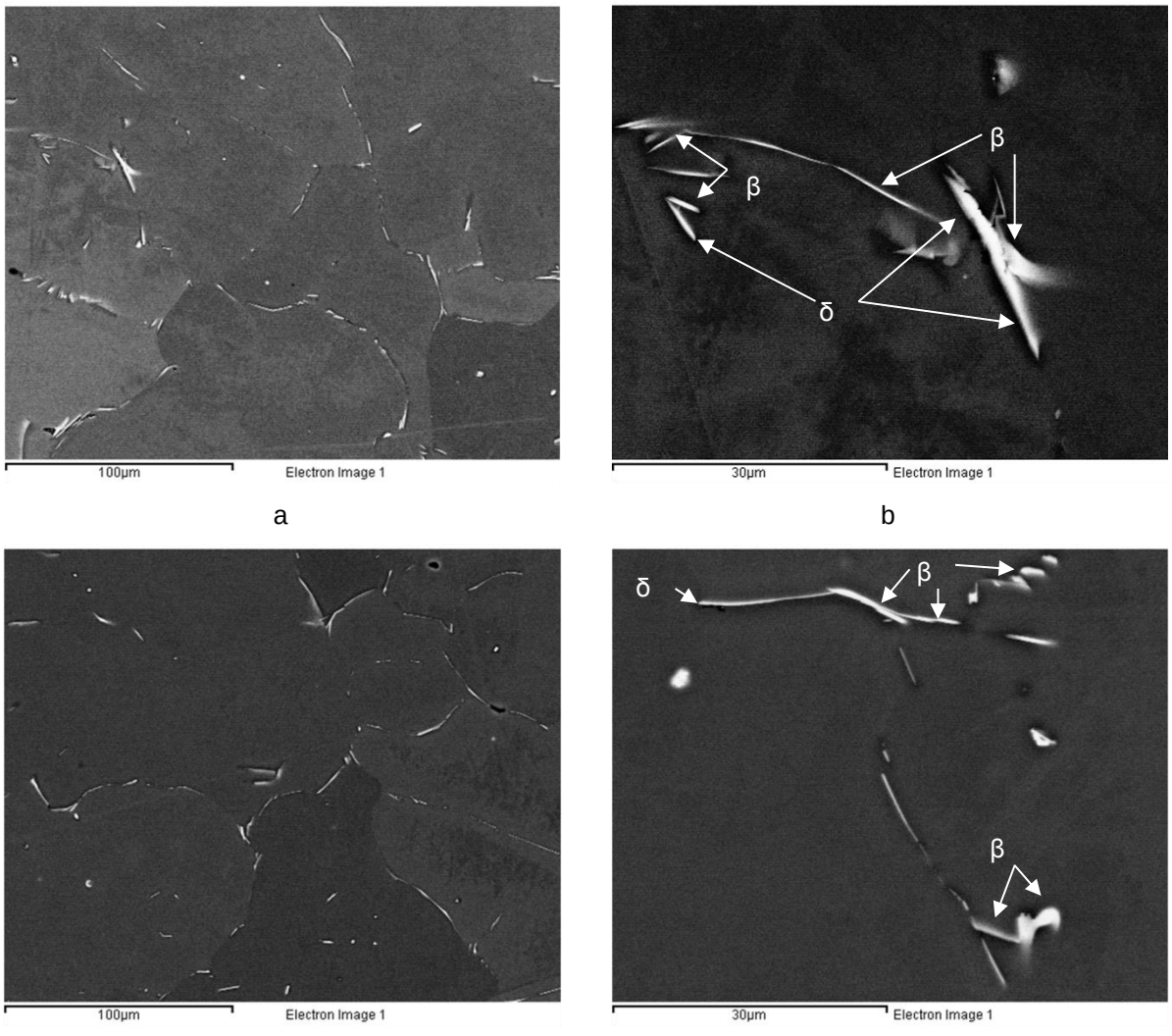

Figure 4.44 SEM (BSE) images of intermetallic particles from the DC-GR as-cast billet. (a-b) Surface region (c-d) Central region. Phase identification by EDX analysis. Note some of the phases are identified in the images.

This is supported by the diagrams presented in Figure 4.46. In Figures 4.46a and c the data collects between the beta and delta separators with an increase in the amount of beta phase particles at the centre, Figure4.46 c, whereas the amount of delta to beta is evenly split. The respective S-ratio diagrams show that there is an increase in the (Fe+Mn)/Si ratio at the centre, resulting in the equivalent increase in the beta phase particles.

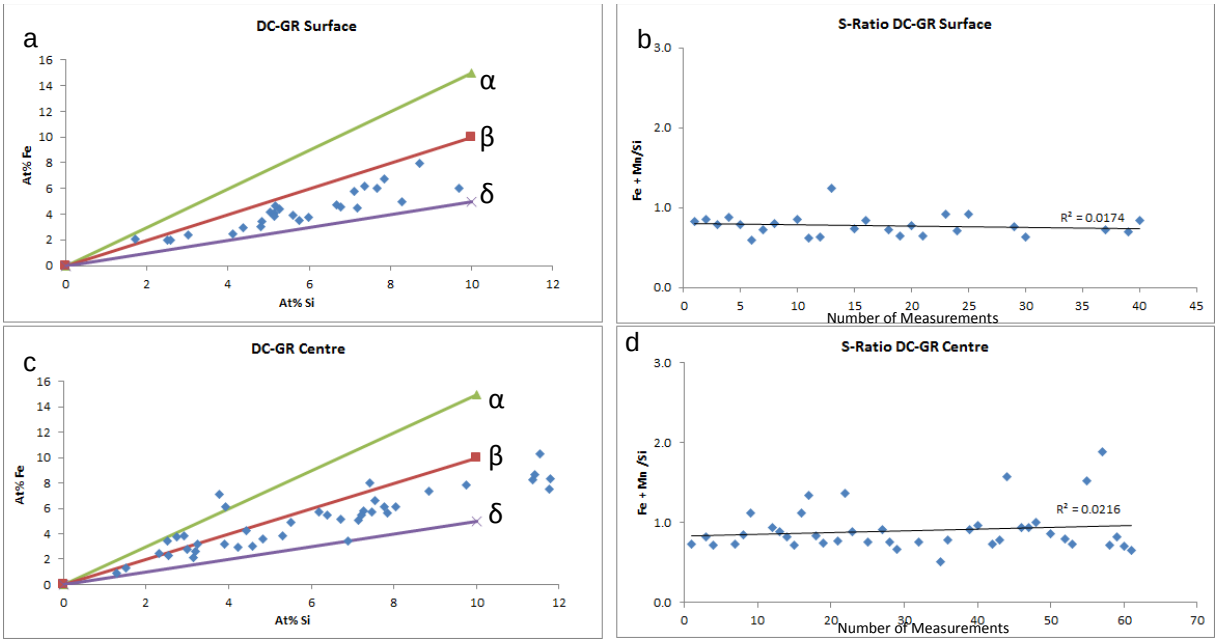

Figure 4.45 (a) and (c) (Fe+Mn)/Si ratio from the surface and central regions DC-GR billet plotted against separators for alpha-, beta-, and delta AlFeSi phases. (b) and (d) accompanying (Fe+Mn):Si ratio values.

4.3.2.3 Intermetallic Morphology–Oxford DC, MC-DC-GR-P2 Sheared at 4500 RPM

Shearing was applied to the billet in combination with grain-refiner additions during casting. Figure 4.47a shows the microstructure of the billet surface region at 100x magnification, with Figure 4.47b obtained from the same region of billet but at 500x magnification. Comparing these two images with their equivalents from the central region, Figures 4.47c-d respectively, there is a clear difference in the microstructure and grain morphologies.

If we compare the images of the surface (Fig. 4.47a) with those of the billet centre (Fig. 4.47c) the grains changes from dendritic to cellular morphology respectively.

This is similar to what has been seen in the previous sections considering sheared material as is the arrangement of intermetallics. The distribution of the intermetallics through the microstructure at the surface is in stark contrast to the cellular grain structure at the centre, Figure 4.47b and d respectively. In Figure 4.47b the intermetallics are coarse plates and needles that are connected especially at the grain junctions. The distribution of the intermetallics at the grain boundaries is good with divorced needles and smaller blocky, spherodised particles in the body of the grains. There is evidence of particle necklaces as well as Chinese script but the majority of the particles are needle-like in morphology.

Figure 4.47d shows that the body of the cellular grains are completely devoid of particles as there are no dendrite arms for liquid to become trapped between. This also denotes that the cooling rate was different from that of the surface region as the grains were able to coarsen and as a result, the solute elements were able to segregate out to the boundaries forming an intricate network of particles made up of plates and needles. Needles make up the majority of the particles at the grain boundaries but with many of the particles well broken-up and distributed.

A consequence of the cellular grain structure is the coarseness of the particles with long grain boundary particles and plates of AlFeSi distributed through the region. This is most apparent in the lower magnification images of Figures 4.47a and c. The particles at the surface are shorter and more separated around the boundaries than the central region intermetallics.

Figure 4.48 contains diagrams that look to quantify the difference in the intermetallics by displaying the average size of the particles across the billet radius in terms of length, width, area and particle shape factor. The radius of the billet was cut into three equal sized samples, surface, mid radius and centre, which were measured in three different sites on each sample, the average of which was taken and then plotted. The results trend towards an increase in particle size across the billet from the surface to the centre. However the average value presented here takes into account the small intermetallic particles at the grain boundaries of all the particles measured, 62% of them were 4 μm and below. At the centre, 2% of the measured particles were above 20 μm in length compared to 0% at the surface. In fact at the surface, only 3% of the measured particles were over 10 μm in length with 10% of

the particles measured at the centre over 10 µm. This quantifies the impression from the microstructure images that the intermetallic length increases on the grain boundaries at the billet centre (Figure 4.47).

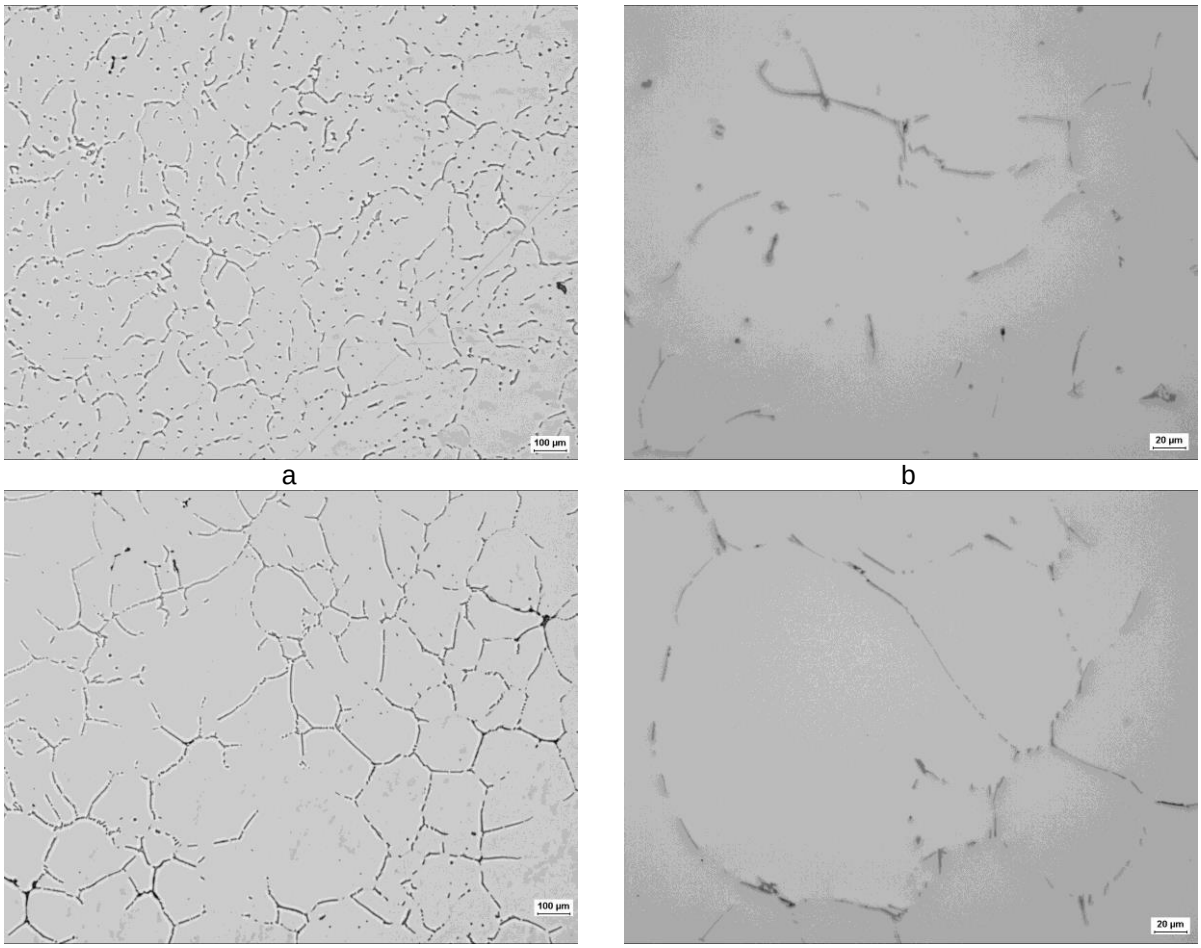

Figure 4.46 As-cast microstructure of MC-DC-GR-P2 billet sheared at 4500 rpm. (a) Surface region at 100x magnification; (b) Surface region at 500x magnification; (c) Central region at 100x magnification; and (d) Central region 500x magnification.

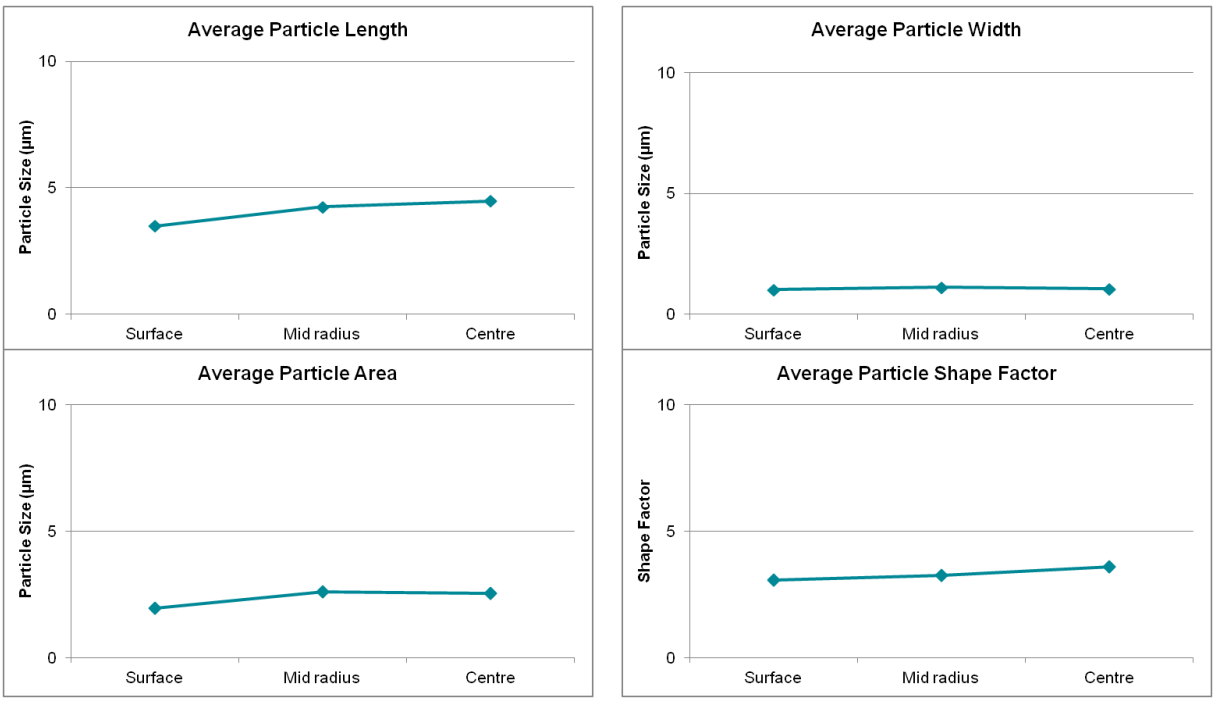

Figure 4.47 INCAFeature SEM analysis software produced results of average particle measurements. MC-DC-GR-P2 As-cast billet sheared at 4500 rpm and produced on the DC unit at Oxford.

In terms of area, 63% of measured particles had an area of 2 µm and less for both billet surface and central regions but the percentage of particles measured above 10 µm was higher again at the centre at 4% compared to 2%, which equated to nearly double the amount of particles above 10 µm in size.

The average shape factor increases very gently in Figure 4.48d suggesting that the roundness of the particles diminishes across the billet. Looking at the images in Figure 4.48c, there is an arguable dominance in elongated particles at the grain boundaries with no particles trapped within the inter-dendritic regions that may take on a more spherodised morphology, as in the grains at the billet surface (Figure 4.47a). Analysis of the measured particles shows that 33% of the particles at the centre are above a shape factor of 4, whilst only 19% that value at the surface, supporting the suggestion that the spherodised nature of the particles does indeed reduce at the centre. This is most likely a consequence of the grain morphology as stated previously, that is, the cellular structure does not allow for particles to form interdendritically and thus distributed within the bulk of the grains, resulting in

segregation only to the grain boundaries where coarser elongated needle particles developed.

4.3.2.4 EDX Analysis of Intermetallic Particles –Oxford DC, MC-DC-GR-P2 Sheared at 4500 RPM

Figure 4.49 shows SEM images of the intermetallic particles at the billet surface (Figure 4.49a-b) and centre (Figure 4.49c-d) with some of the constituent phases identified by SEM-EDX analysis and indicated in the images. It is clear from Figure 4.49d that the intermetallics are coarser in the billet centre with highly connected plates of block morphology and needles being the dominant morphology around the grain boundaries, becoming coarser at the junctions. According to the EDX analysis, the prevailing phase is delta even though the morphology of the intermetallics shares a lot with typical beta phase; block-like plates and coarse needles. Beta phase particles are still present but limited to smaller particles at the boundaries between the delta phases.

This is contrast to the intermetallics found at the surface where alpha-, beta-, delta-phases are present. The phases appear to have set morphologies and positions about the grains where each phases dominates. Alpha-AlFeSi is found predominantly in the bodies of the grain thus the interdendritic regions where they form with a spherical morphology. In these regions the particles form as alpha but instead of transforming to beta, they remain alpha as particles become more enriched and the temperatures are homogenised at the liquidus. The beta phase is identified at the grain junctions and boundaries where a coarser particle forms. These particles are plates or needles but can be distinguished from the other phases as they are coarser and display a block morphology.

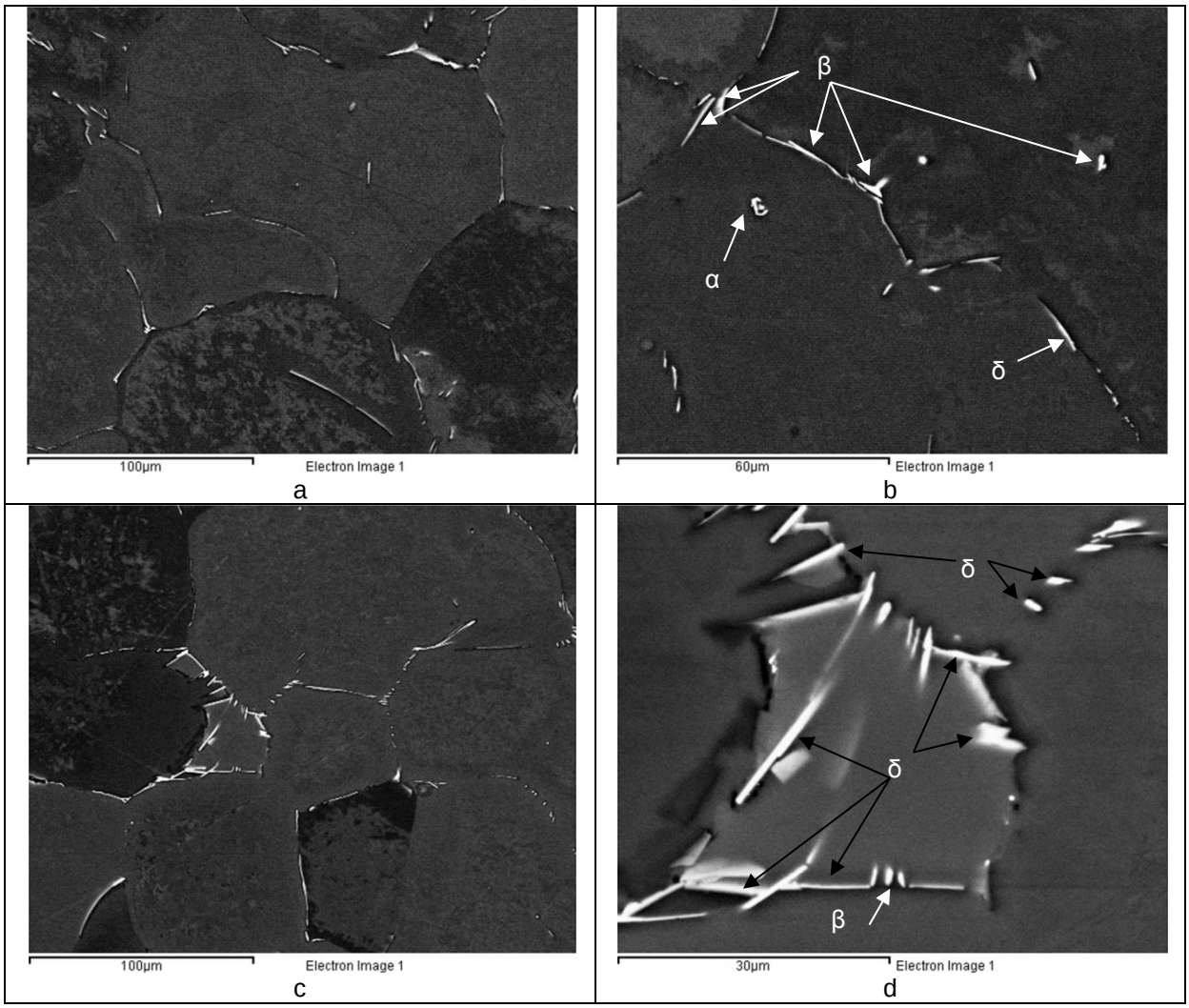

Figure 4.48 SEM images of intermetallic particles formed in the MC-DC-GR-P2 as-cast billet sheared at 4500 rpm. (a-b) Surface region (c-d) Central region. Phase identified by SEM-EDX analysis. Images are BSE.

Beta is found within the grains as small particles of intermetallic also but these are blocks compared with the spherodised α-AlFeSi. Intermetallics of delta-AlFeSi are found at the grain boundaries as needles within this region of the billet, typically away from the junctions where the final solidifying liquid was pressed between the growing grains and, as such is more broken-up and distributed than the beta phase which can have a similar morphology.

The statistical results of the EDX analysis are presented in Figure 4.50 a-d where they are plotted against separators allotted to each phase, see Figs 4.50a and c. The S-Ratio displays the concentrations of Fe, Mn and Si for each measured particle.

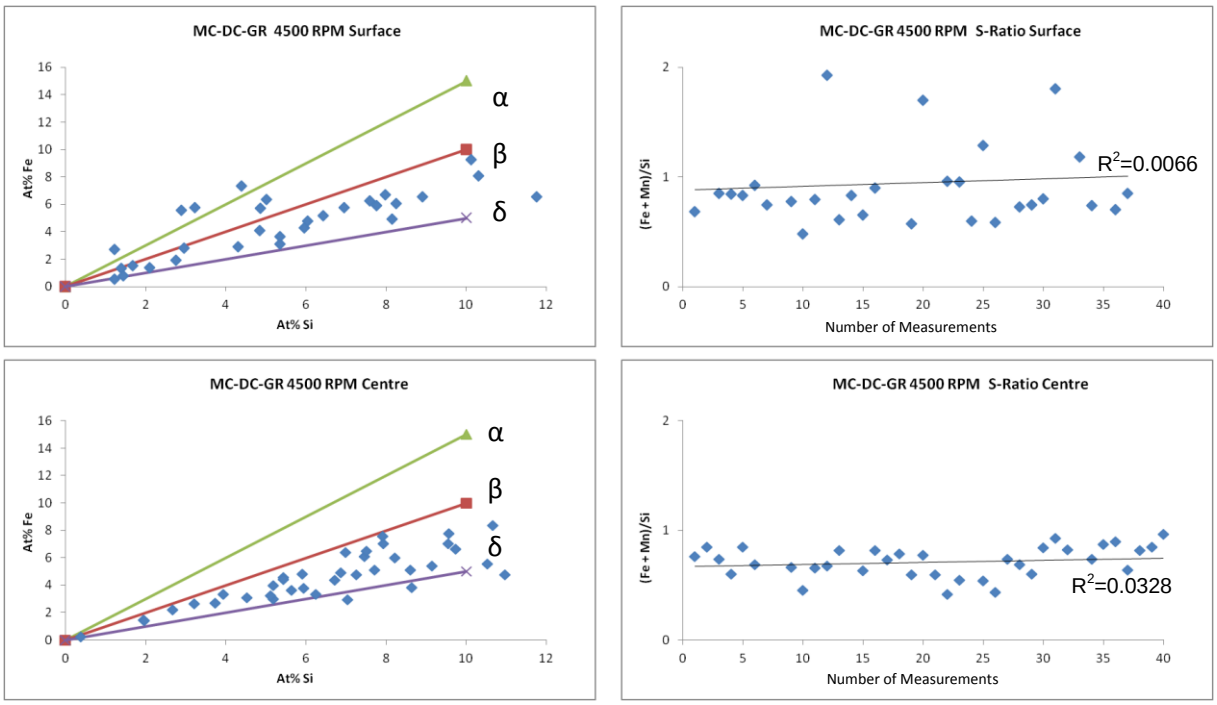

Figure 4.49 (a) and (c) (Fe+Mn)/Si ratio from the surface to central regions in the MC-DC-GR-P2 billet sheared at 4500 rpm. Measurements plotted against separators for alpha-beta-delta AlFeSi phases. (b) and (d) accompanying (Mn+Fe):Si ratio values.

At the billet surface, Figure 4.50a shows that there is a spread in the phases present but it can be argued that the beta phase is the most dominant, with few alpha phase present.

At the billet centre, Figure 4.50c shows that there has been a change in the Fe and Si ratios of the particles with lower Fe to Si ratio particles being dominant, thus beta and delta are the prevailing AlFeSi phase This is further supported by Figure 4.50d which plots the majority of the S values which are below 0.75 with an average of 0.70 which denotes a dominance of the delta phase, but explains the spread between the beta and delta phase separators in figure c. As low Fe particles are dominant, no alpha phase particles were found at the centre in the particles measured.

4.3.2.5 Intermetallic Morphology –Oxford DC, MC-DC-GR-P2 Sheared at 6400 RPM

The intermetallic structures of the billet surface and centre are presented in Figure 4.51a-d. There doesn't appear to be large differences between the microstructures or the intermetallics from the images taken at 100x magnification, Figures 4.51a and c. The morphology of the grains has the same cellular structure with the intermetallic particles found around the boundaries, with very few particles in the bulk of the grains. The intermetallics coarsen where the grains are smallest where more liquid is trapped between grains absorbing the segregated solute from the solidifying grains. This is shown clearly in Figure 4.51b, which contains a complex collection of intermetallics that are highly connected, consisting of multiple phases and particle morphologies.

Around the grain boundaries away from the grain junctions the particles are needles but long and complete, as in there is no sign of them breaking up forming a necklace type morphology that industry strives for due to its better performance under downstream processing. Then, at the grain junction of the large grains, Chinese script can be seen with the particles that extend along the grain boundary broken-up. This morphology typically suggests alpha phase which has a rounded nature to the constituents it forms.

Where the grains are smaller, in the image of the centre, the intermetallics formed coarse interconnected plates which typically would be considered beta-AlFeSi under LOM investigation and it would be safe to assume is the case here. Upon the beta intermetallics, particles of low temperature melting Mg_2Si eutectic (black particles) have preciptated that will require homogenisation to dissolve back into solid solution.

Areas of coarse intermetallic are also seen at the centre of the billet but less frequently than the surface. Typical appearance of the intermetallics are shown in Figure 4.51d. The needles of intermetallic are still present that connect with the Chinese script at the junctions with the larger grains. The difference here is that the needles appear elongated around the larger grains with coarser Mg_2Si particles connected to them.

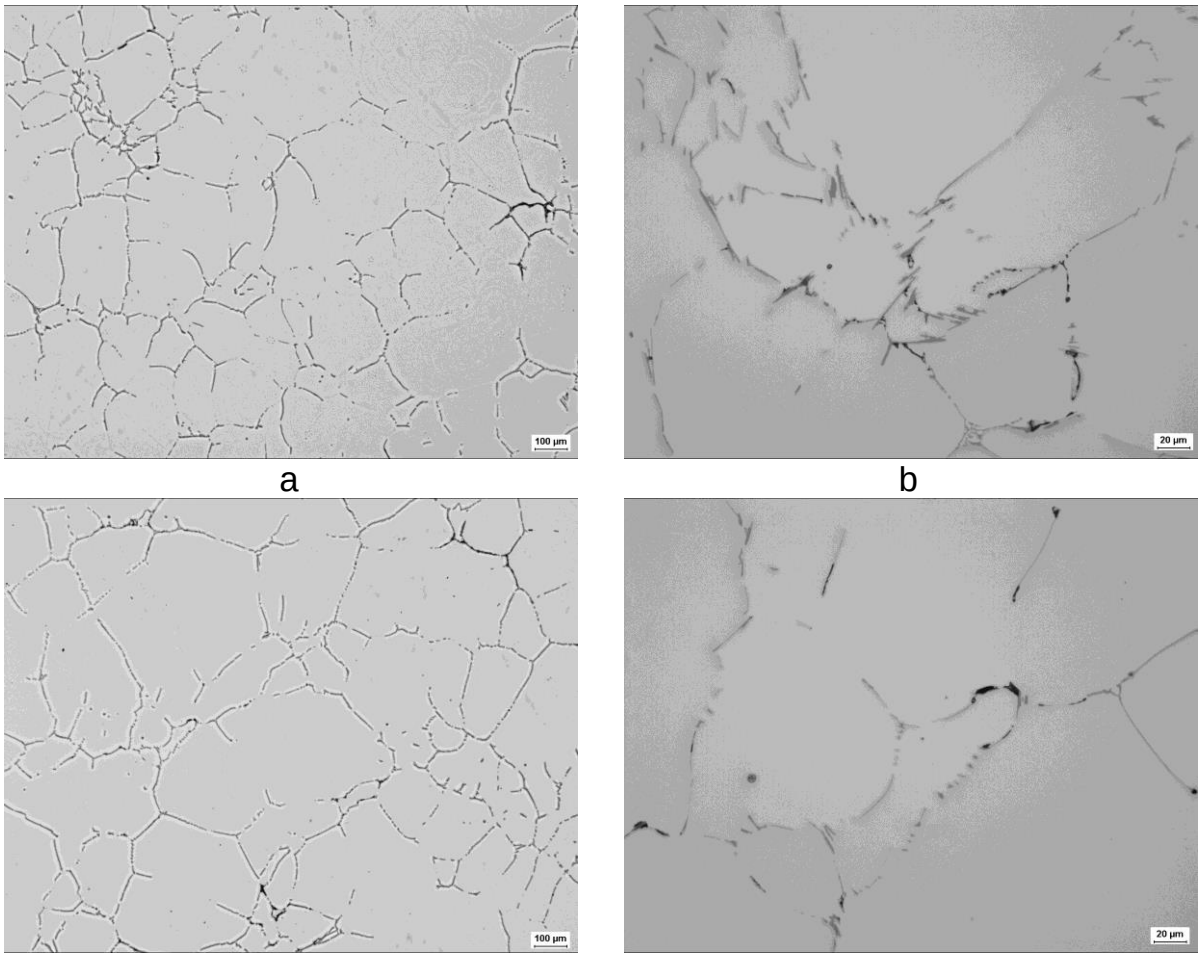

Figure 4.50 As-cast microstructure of MC-DC-GR-P2 billet sheared at 6400 rpm. (a) Surface region at 100x magnification. (b) Surface region at 500x magnification (c) Central region at 100x magnification.(d) Central region 500x magnification.

Around the smaller grains the particles are much more broken-up and distributed as plates with less connectivity than at the surface yet, coarse particles still agglomerate at the junctions with large particles of Mg_2Si precipitated onto them. Pores are present where the liquid has been unable to flow through to the gaps in the coherent grain strcutures. Large plate intermetallics have also been linked with flow restriction of the liquid during the final stages of solidification.

Figure 4.52a displays the average particle length from the billet surface to the centre, rises slightly collaberating the appearance of elongated particles at the boundaries of the grains at the centre. The core of the billet had a higher percentage of particles over a length of 10 µm than the surface; 11% to 9% respectively.

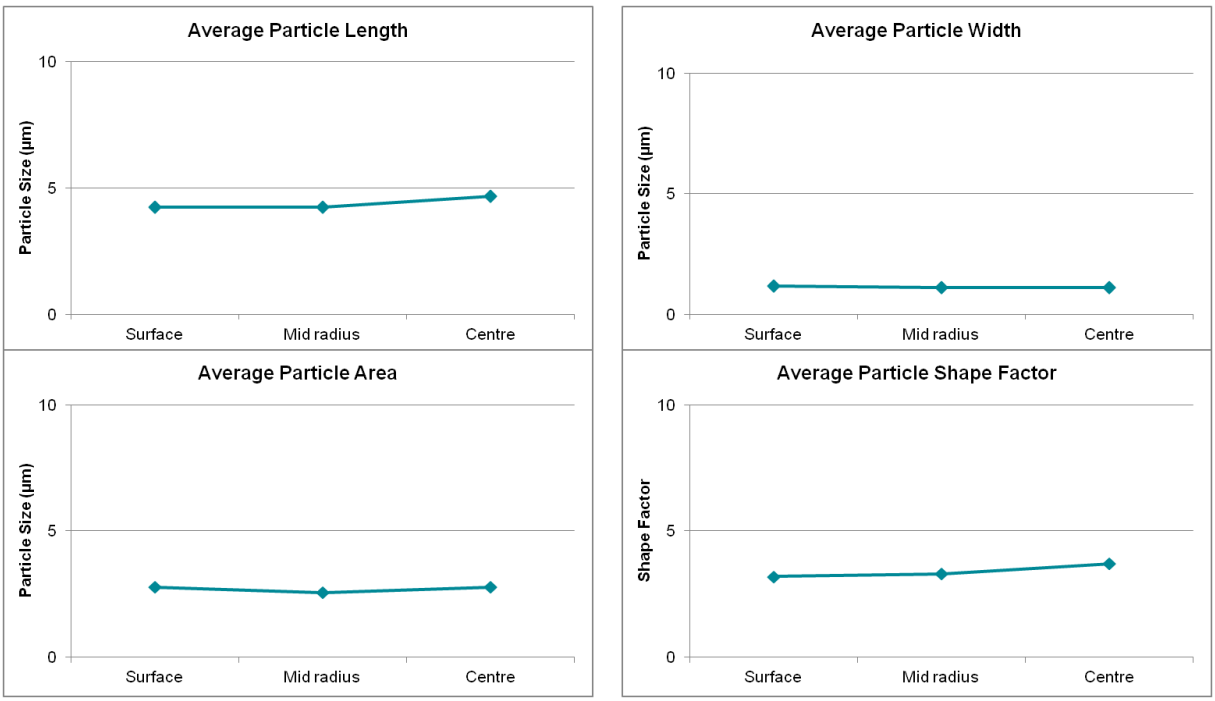

Figure 4.51 INCAFeature SEM analysis software quantified results of average particle measurements. MC-DC-GR-P2 as-cast billet sheared at 6400 rpm and produced on the DC unit at Oxford.

The average width of the intermetallics across the billet radius does not change implying that the particles do not coarsen into thick plates. However, as we have seen in the accompanying images, coarse plates are present within the structure but the average across the billet does not vary appreciablby, suggesting that the coarse structures are not common. At the billet centre, the maximum width of the particles was measured at 28.77 µm, over three times larger than the thickest particle at the surface measured at 8.03 µm. There would naturally be a coarsening of the particles at the centre due to the reduction in growth rates and higher volume of liquid flowing. However, they can be regarded as uncommon if we consider the averages. Due to the decrease in spherodised particles at the billet core, the shape factor in Figure 4.52d also increases towards the centre.

4.3.2.6 EDX Analysis of Intermetallic Particles –Oxford DC, MC-DC-GR-P2 Sheared at 6400 RPM

Figure 4.53 shows the SEM images of the intermetallics at the surface and central regions of the billet DC-GR-P2. Figures 4.53a and c show the surface and centre at the same magnification but there is a clear difference in the grain structures and the morphology of the intermetallics. At the surface (Fig. 4.53a) the intermetallics around the tips of the small grains resemble plates. The grain boundary particles are also coarser around the smaller grains compared with the relatively pure boundaries of the larger grains. This suggests the presence of fragments that have been transported to this area causing the liquid around the solidifying grains to become trapped as they are enveloped by larger grains. The majority of these particles at the tips of the smaller grains are delta phase AlFeSi whilst the particles inside the larger grains are smaller blocks of β-AlFeSi.

In the centre, segregation of solute elements from the larger grains to the edges creates plates of intermetallics that are shown in Figure 4.53d. These plates are typically beta phase and formed with the plate morphology. At the edge of the grains a clear segregation area can be seen by the change in contrast between the bulk of the grain and the edge region.

What can also be seen is intermetallics that are highly broken-up thus resemble a necklace of particles. These necklaces formed at the extent of the intermetallic particles from the grain junctions, along the grain boundaries. Delta–AlFeSi dominates the constituent phases of these particles. Although the particles at the junctions are interconnected, no alpha phase particles were identified in the intermetallics measured. Therefore the intermetallics of the billet core were found to consist of beta plates and needles at the grain junctions, with small delta phase particles forming along the grain boundaries. Alpha-AlFeSi was not present in this region.

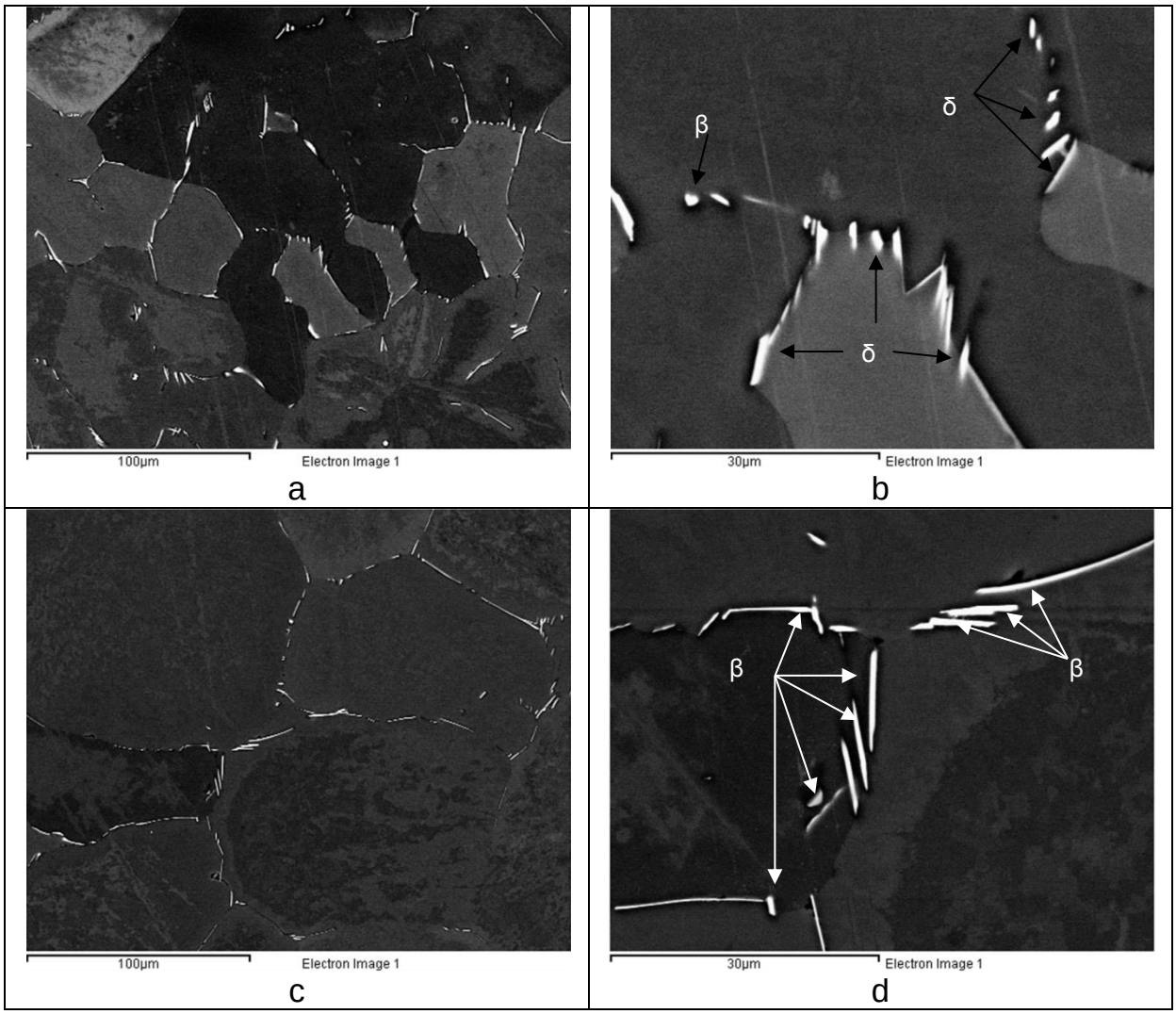

Figure 4.52 SEM images of intermetallic particles from the MC-DC-GR-P2 as-cast billet sheared at 6400 rpm. (a-b) Surface region (c-d) Central region. Phase identification by EDX analysis. Note some of the phases are identified in the images. Images are BSE.

Figure 4.54 shows the distribution of phases at the surface and central regions against designated separators. As seen in the previous section, the surface contains alpha, beta and delta phase intermetallics, Fig. 4.54a, but alpha was not identified in the particles measured at the core, Fig. 4.54c.

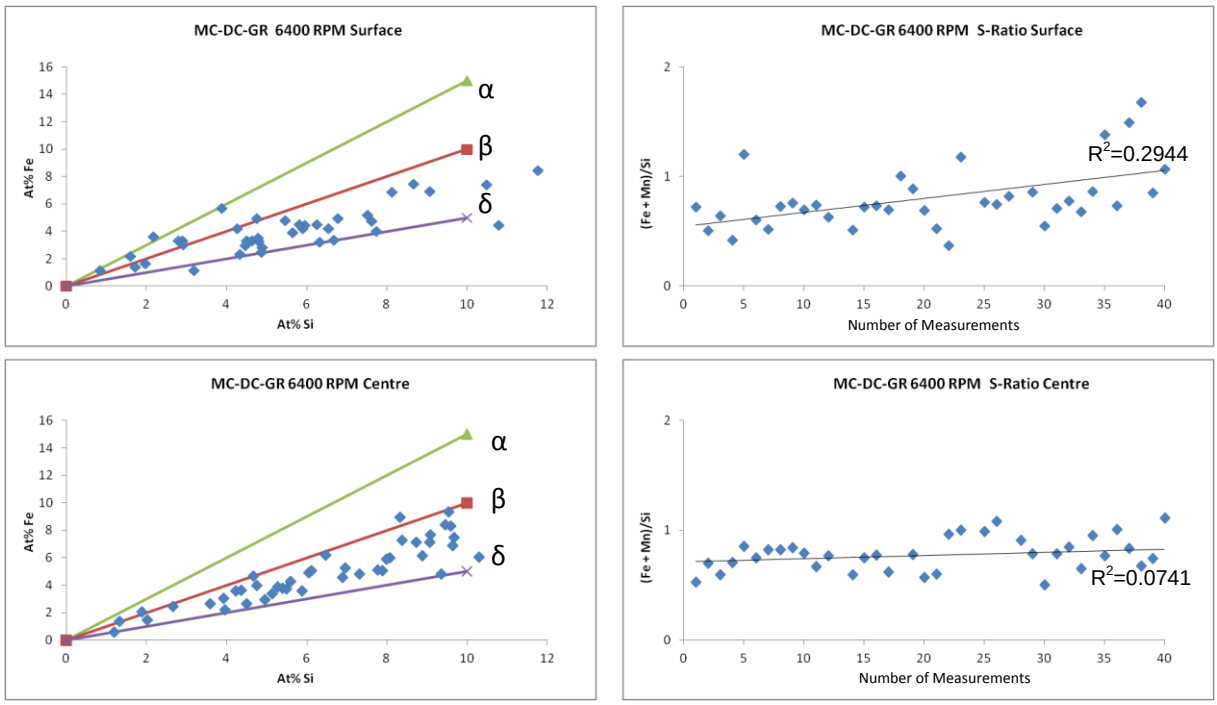

Figure 4.53 (a) and (c) (Fe+Mn)/Si ratio from the surface and central regions MC-DC-GR-P2 billet sheared at 6400 rpm. Measurements plotted against separators for alpha-beta-delta AlFeSi phases. (b) and (d) accompanying (Mn+Fe):Si Ratio values.

As indicated in Figure 4.54a, the (Fe+Mn)/Si ratio for the surface region of the billet, the dominant phase in the surface region is β-AlFeSi. At the centre, the (Fe+Mn)/Si ratio value is lower at 0.75 but still beta dominant. The constituent phase data is spread between the low Fe beta and delta separators.

In summary, beta/delta Fe-bearing intermetallic phases dominated in DC-GR or DC-GR-MC castings. This means the formation of Fe-bearing intermetallics is more dependent on grain refiner additions, in the current study, with AlTiB master alloy used, than melt conditioning whether it was high shear speed or low shear speed, if both grain refiner added and melt conditioning are carried out.

4.3.2.7 Intermetallic Morphology–Oxford DC, MC-DC-P2 Sheared at 4500 and 6400 RPM

The microstructure of this billet was refined by melt conditioning only; no grain-refiner additions were made. Analysis of the intermetallics by OM images and phase identification by EDX measured on a SEM are presented here. The billet was

sheared with the device at position P2 and rotation speeds of 4500 and 6400 rpm. Across the billet radius, the structure of the MC-DC billet is not completely uniform. It also varies from section sheared at 4500 rpm and 6400 rpm. It is interesting to compare the intermetallics that formed between the different grain structures in terms of size, type and morphology.

The intermetallic structures of the billet surfaces are shown in Figure 4.55. Images Figure 4.55a-b were obtained by OM from the billet sheared at 4500 rpm at 100x and 500x magnification respectively; Figures 4.55c-d were obtained from the surface region of the billet sheared at 6400 rpm at the same magnifications. The grain structure of the billet sheared at 4500 rpm is slightly coarser dendritic throughout until the mid-radius of the billet. The grain structure in Figure 4.55d sheared at 6400 rpm is clearly different from that in Figure 4.55b sheared at 4500 rpm. The globular grains are devoid of particles within the bulk with elongated rods of intermetallic along the grain boundaries (Figure 4.55d). This is typical of globular grain morphology. In the dendritic region, the particles are well distributed within the bulk of the grains. Liquid trapped interdendritically solidified as eutectic within the grain bulk resulting in well dispersed particles which are small and highly independent at the grain boundaries (Figure 4.55b).

In the dendritic regions of both shear speeds, the intermetallics formed as spherical particles within the bulk and small plates/rods at the boundaries. The interdendritic regions usually had a higher Fe to Si ratio due to Fe segregation from the dendrite arms into the trapped liquid there, resulting in α-AlFeSi dominating the particles found inside the grains. However the dispersion and size would suggest that this will not be deleterious to extrusion performance. The morphology of the grain boundary particles is dictated by its position within the matrix and composition. If they are part of the interface between globular and dendritic, needles formed from the liquid trapped between the different morphologies due to growth rate variations. The Fe to Si ratio is either 1:1 so beta forms or the Fe level is lower than the Si, in which case delta forms. It is the crystallographic nature of these phases to form blocks which leads to the plates that are seen where increased liquid content occurs, typically at grain junctions or around smaller grains with cellular morphologies. Chinese script is a product of the increased liquid content typically found at the junction of multiple

grains, the stoichiometry of which can develop either α- or β- AlFeSi depending on the Fe:Si ratio of the liquid at the late stages of solidification.

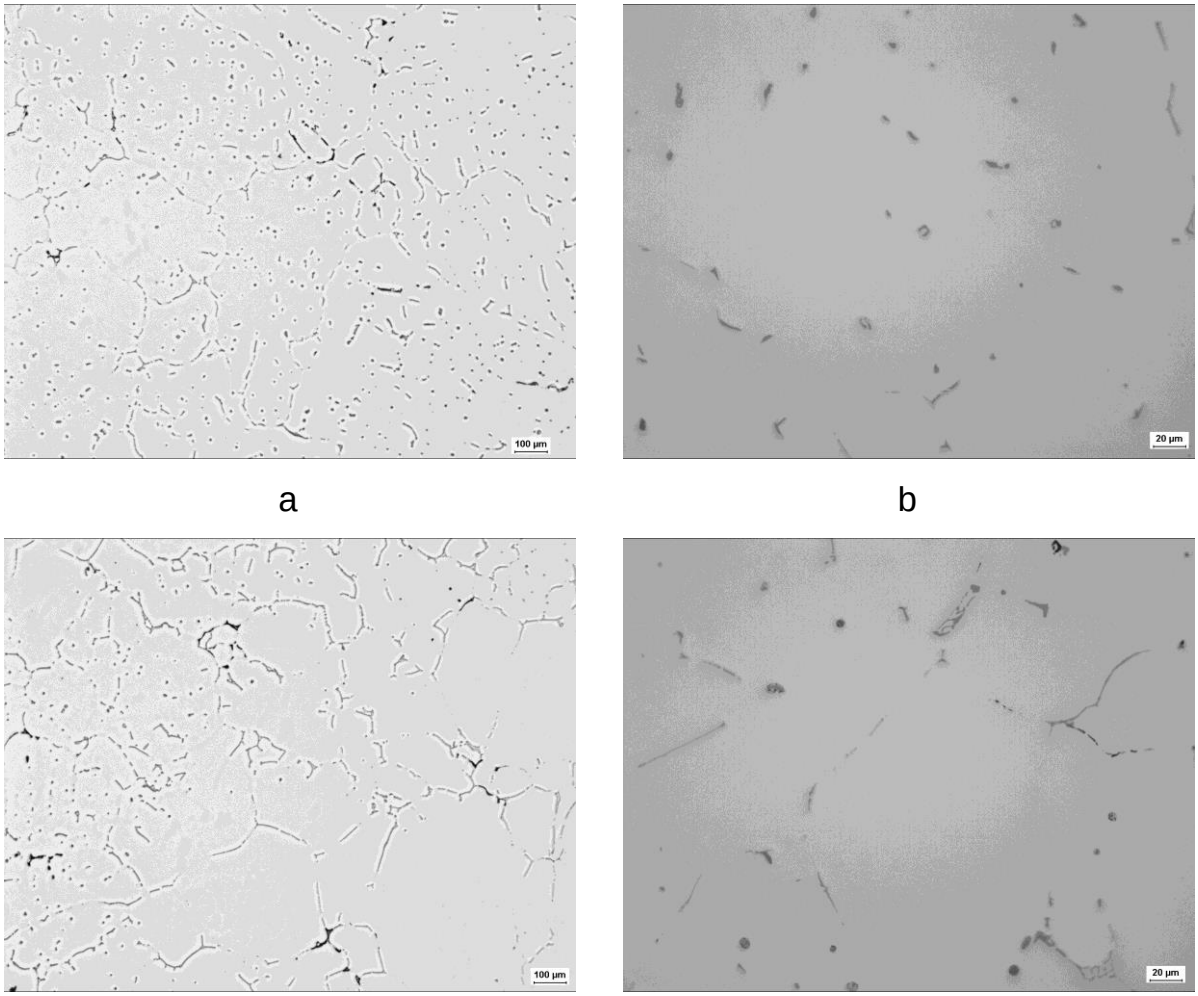

Figure 4.54 As-cast microstructure of MC-DC-P2 billet sheared at 4500 and 6400 rpm. (a) Surface region at 100x magnification 4500 rpm. (b) Surface region at 500x magnification 4500 rpm (c) Surface region at 100x magnification 6400 rpm. (d) Surface region 500x magnification 6400 rpm.

Figure 4.56 was obtained from the coarse grain columns (CGC) in the MC-DC-P2 billet sheared at 6400 rpm. The coarse grain columns have a dendritic grain structure but the intermetallic morphology is different from those seen before due to the angled and elongated nature of the grains. The angled nature of the grains and the intermetallics are shown in the OM image of Figure 4.56a taken at 100x magnification. Here, the needles at the grain boundaries are elongated as the grain

grows into the liquid, with coarser particles forming as Chinese script at the tips of the grains. This is reminiscent of the particles that formed within Zone 1 of the static mould.

Figure 4.56b shows the elongated intermetallics at the grain boundaries obtained by OM at 500 x magnification. The particles are thin elongated needles interspersed by smaller particles of a spherical morphology. Within the grains, many well dispersed particles are present which is consistent with dendritic grains. The majority of the particles inside the grain interdendritic regions are fine and spherical in nature, most probably of α-AlFeSi stoichiometry.

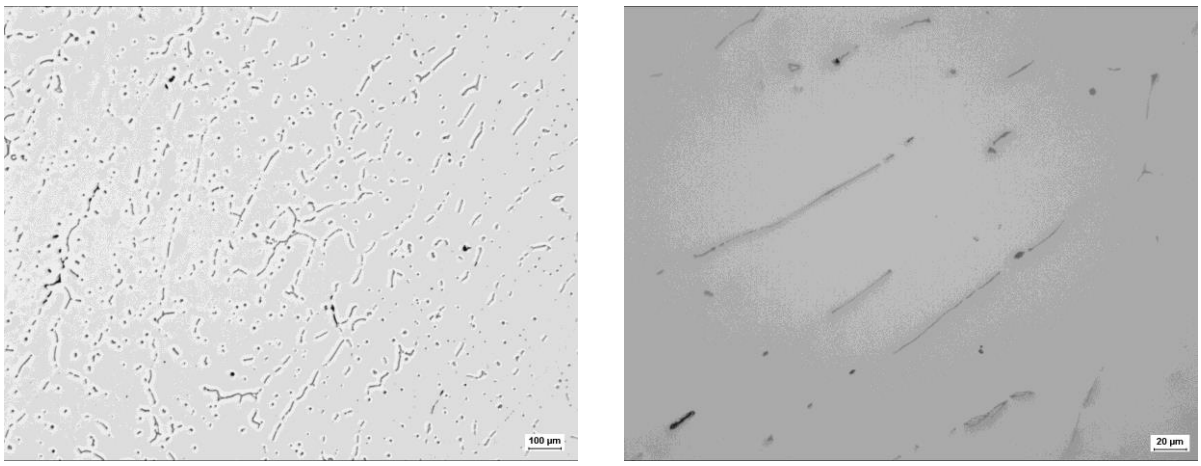

a b

Figure 4.55 As-cast microstructure of the coarse grain columns (CGC) within the MC-DC-P2 billet sheared at 6400 rpm. (a) CGC region at 100x magnification 6400 rpm. (b) CGC region at 100x magnification 6400 rpm.

After the coarse grain structures, a finer equiaxed grain structure developed in both billet sections sheared at 4500 and 6400 rpm. It extended into the centre and the microstructure is shown in Figure 4.57. The section sheared at 4500 rpm is presented in Figure 4.57a-b at 100 and 500 x magnification respectively; the section sheared at 6400 rpm is shown in Figure 4.57c-d and follows the same magnification format.

The grain structure between the two pairs of images could be considered similar. What could be argued though is that there appears more Chinese script present at 6400 rpm than at 4500 rpm. It may well be that alpha phase formed first, but the slow

growth rates enabled transformation of the phase into beta with excess Si segregating to the liquid at the final stages of solidification.

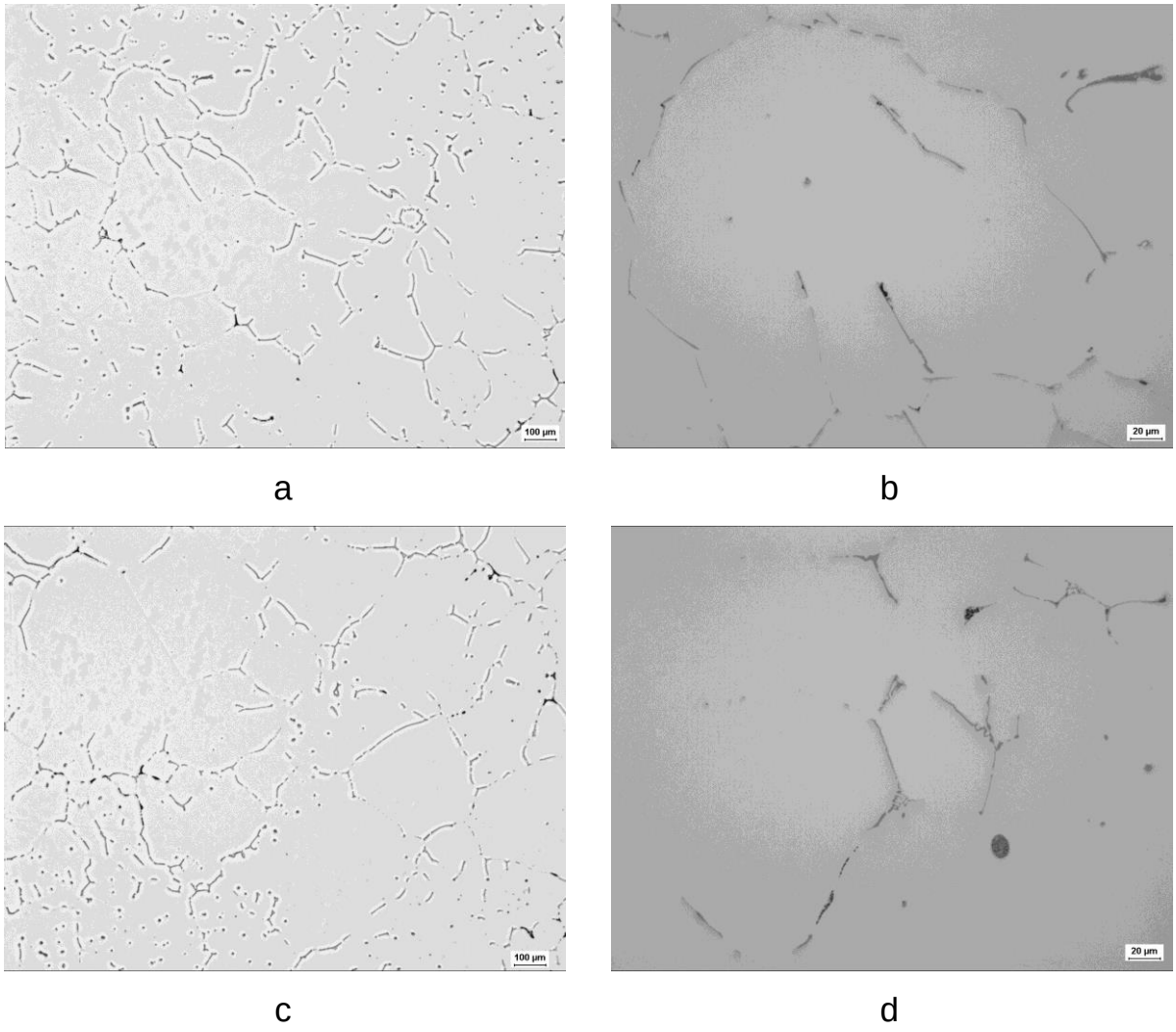

Figure 4.56 As-cast microstructure of MC-DC-P2 billet sheared at 4500 and 6400 rpm. (a) Billet centre at 100x magnification sheared at 4500 rpm. (b) Billet centre at 500x magnification sheared at 4500 rpm (c) Billet centre at 100x magnification sheared at 6400 rpm. (d) Billet centre 500x magnification sheared at 6400 rpm.

The globular/rosettes are encompassed by long rods of intermetallics whilst devoid of particles within the grain bulk at both rotation speeds. The intermetallic particles around/inside the dendritic structures are shorter and less coarse, with particles present within the grain bulk. The globular rosettes formed at slower growth rates than the dendritic grains, resulting in more segregation and coarser SDAS, which caused larger volumes of liquid to be located at the boundaries. The increased

segregation will most likely lead to a variance in the intermetallic phases which formed as well.

Figures 4.58 and 4.59 represent the particle measurements from the billet sheared at 4500 rpm and 6400 rpm respectively, confirming that there is little difference in the average particles length, width and area. However, at 6400 rpm, there is an increase in particle length and area at the mid radius point of the billet, due to the elongated nature of the intermetallics around the boundaries of the grains in the coarse grain columns. At 4500 rpm the average particle length at the mid radius and centre are essentially equal as the same dendritic structure continues across the billet that contributes to the homogenity of the particles across the billet. The growth rates in the billet sheared at 4500 rpm are the most uniform especially through the mid radius, after which a slight decrease is experienced towards the centre, thus the change in microstructure is seen with cellular grains developing.

The shape factor value increases towards the centre as elongated and blocky particles are more common than at the centre with an arguably higher value at 4500 rpm, signifying less spherical particles measured and tendency towards blocky particles at the centre as seen in the microstructure images. At 6400 rpm the shape factor value is uniform from the mid radius through to the centre suggesting that the intermetallic particles are similar with block morphology being dominant.

4.3.2.8 EDX Analysis of Intermetallic Particles –Oxford DC, MC-DC-P2 Sheared at 4500 and 6400 RPM

Back scatter electron SEM images of the billet intermetallic structures are presented in Figures 4.60, 4.61 and 4.62 in the same format as before; Surface zone of the billet sheared at 4500 and 6400 rpm in Figure 4.60 a-b and c-d respectively; coarse grain mid radius section of the billet sheared at 6400 rpm Figure 4.61a-b; central region of the billet sheared at 4500 and 6400 rpm in Figure 4.62a-b and c-d respectively.

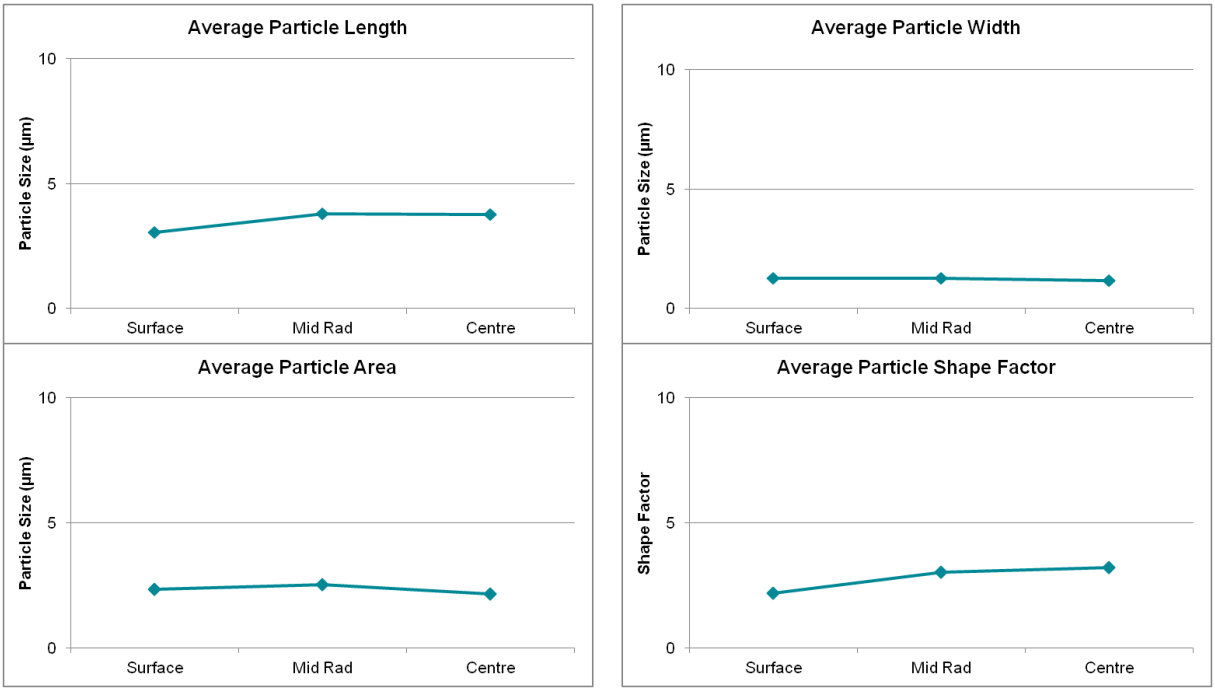

Figure 4.57 SEM INCAFeature software analysis of average particle measurements from as-cast MC-DC-P2 billet sheared at 4500 rpm.

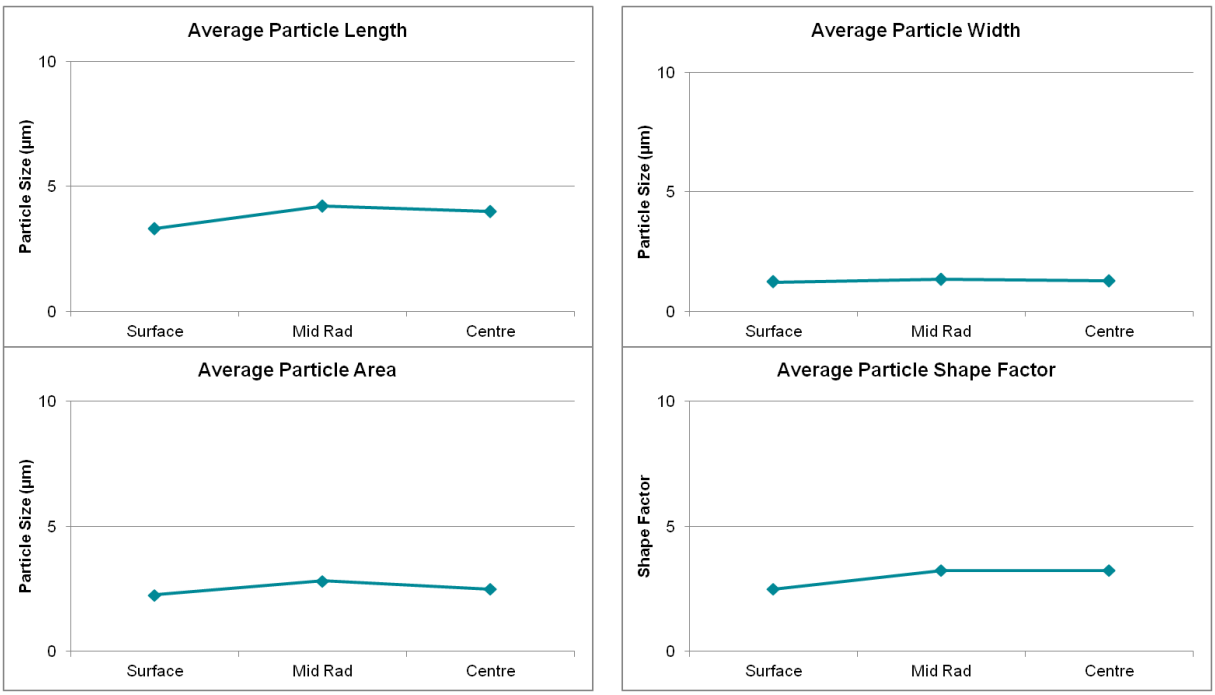

Figure 4.58 SEM INCAFeature software analysis of average particle measurements from as-cast MC-DC-P2 billet sheared at 6400 rpm.

The SEM images in Figure 4.60a and c show clearly the differing intermetallic structures at the surface regions of the billet sheared at 4500 and 6400 rpm. The particles are more distributed within the grains at 4500 rpm with needle like rods of intermetallic interspersed with spherical particles. Figure 4.60b shows particles that have had the phases identified by EDX analysis. Three phases of AlFeSi are represented throughout the region, alpha, beta and delta. The particles identified as α and β have morphologies typical to their phase, i.e. spherodised particles of α-AlFeSi, plates and blocky intermetallics of β-AlFeSi, whilst delta has a morphology similar to that of spherodised alpha. Past analysis has shown that the morphology of the particles changes throughout the material under different solidification conditions.

This is evident in Figure 4.60d where the high magnification SEM image shows a large crystal of α-AlFeSi intermetallic at the junction of multiple grains, particularly at the boundary of what appears to be a rosette like grain in Figure 4.60c. Alpha-AlFeSi has also been identified as a rod at the grain boundary, whilst the smaller spherical particles are delta-AlFeSi and beta-AlFeSi. The beta particles are more readily transformed compared to the alpha and delta phase. An alpha phase plate such as this will then become a problem in downstream processing as homogenisation practices will not be able to refine it. Thus at 6400 rpm, it is α-AlFeSi that becomes the coarse intermetallic at the surface.

Figure 4.61a is an SEM image of the coarse grain column of the MC-DC-P2 billet sheared at 6400 rpm. It shows that there are coarse intermetallics at the grain boundaries and less particles in the grain bulk when compared with the grains at the surface. It can be argued that the particles are at their most coarse at the edge of the grains around the tips, where more liquid becomes trapped in the grain junctions. Along the grain boundaries the intermetallics are elongated rods consisting of beta and delta phase constituents with the beta phase also prone to forming plates as seen in other studies.

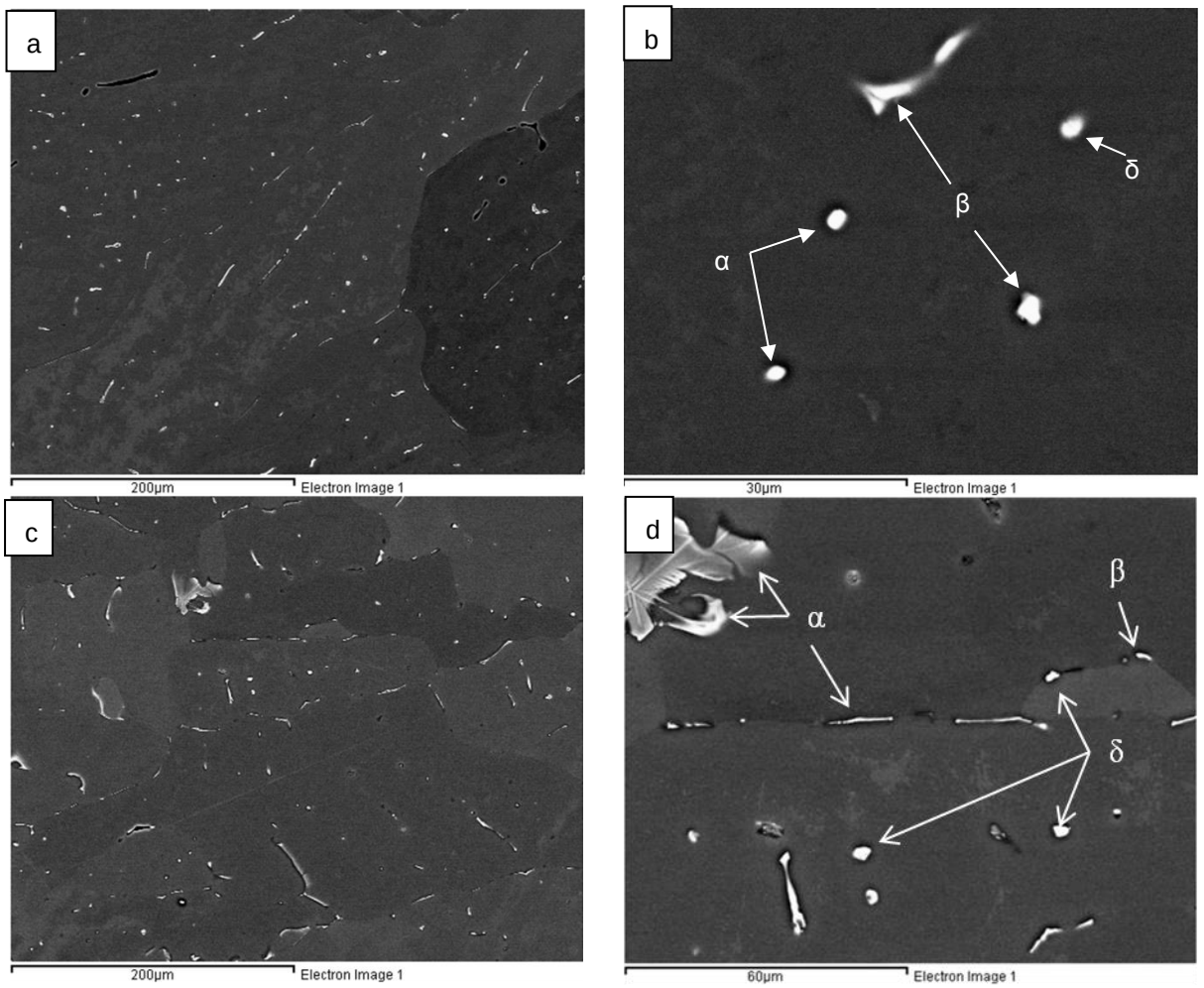

Figure 4.59 SEM images of intermetallic particles from the MC-DC-P2 as-cast billet sheared at 4500 and 6400 rpm. (a-b) Surface region (c-d) Central region. Phase identification by EDX analysis. Note some of the phases are identified in the images.

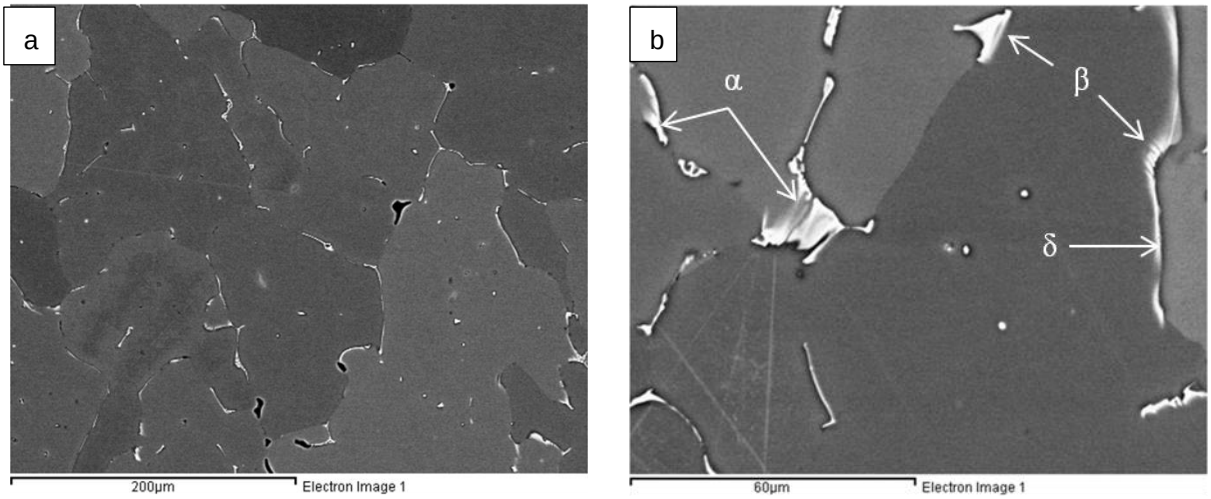

Figure 4.60 SEM images of intermetallic particles from the MC-DC-P2 as-cast billet sheared at 6400 rpm. (a-b) coarse grain columns of the MC-DC-P2 billet sheared at 6400 rpm. Phase identification by EDX analysis. Note some of the phases are identified in the images.

The elongation of the rods of intermetallics at the boundaries is supported by the increase in average particle length seen at the mid radius in Figure 4.59a. There is certainly a coarsening of particles moving through the billet towards the centre, affected by the grain morphology and growth rate during solidification.

At the centre, the grain structures of both rotation speeds are similar with cellular grains interspersed within the dendritic grains that make up the bulk of the microstructure. The difference is, at 4500 rpm, it is mainly equiaxed dendritic, however, it is mainly rosette like. The intermetallics are also very similar as a result with similar average lengths etc as shown in Figures 4.58 and 4.59. The composition of the phases is also similar between the sections of billet sheared at 4500 and 6400 rpm with complex beta phase structures resembling Chinese script at grain junctions becoming plates and rods as they extend along the grain boundaries. An example is shown in Figure 4.62b, note the magnification is higher in this image to highlight the Chinese script structures observed.

At both rotation speeds, smaller particles are found within the bulk of the grains which are predominantly alpha phase intermetallics with a spherical morphology. Alpha phase is also found in its common form for this alloy system, as Chinese script at the boundary junctions. Rods of alpha phase were also identified but these tended to have a more spherodised nature than those formed as beta-AlFeSi.

The morphology of the grains as stated above is crucial for the distribution of particles as can be seen in comparison of the images through this section, especially those in Figure 4.62 where the more dendritic grain structures developed less coarse intermetallics that are well distributed through the matrix. At the centre the intermetallics are still dispersed about the grains and the majority of grain boundaries do not contain large needles or rods of intermetallic, a result of the grain size above 100 µm. Chinese script intermetallic is present at the centre but the coarse plates seen at the surface and mid radius of the billet sheared at 6400 rpm have been refined

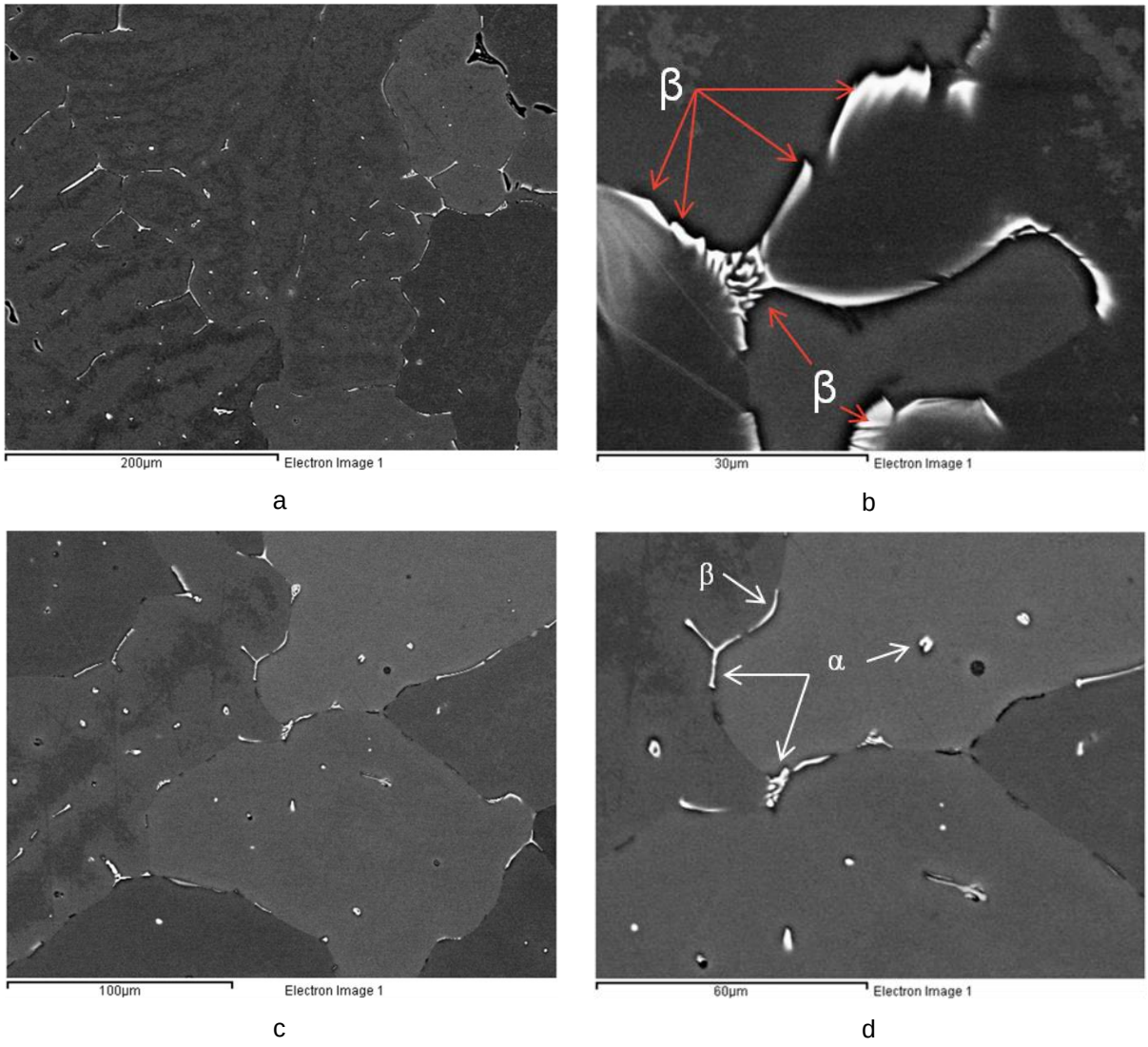

Figure 4.61 SEM images of intermetallic particles from the MC-DC-P2 as-cast billet sheared at 4500 and 6400 rpm. (a-b) Billet centre at 4500 rpm; (c-d) Billet centre sheared at 6400 rpm. Phase identification by EDX analysis. Note some of the phases are identified in the images.

Composition of constituent particles and the dominance of a certain phase or phases at either 4500 rpm or 6400 rpm are determined from Figures 4.63 and 4.64, respectively. The diagrams present data taken from the surface and central regions of the billet and plot the results against separators of each phase.

The constituent phases at the surface of the billet sheared at 4500 rpm are well spread between the alpha-beta-delta separators mirroring the observations made previously of the multiple phase types present within the grains and the boundaries. The (Fe+Mn)/Si ratio average is just above unity at 1.17 for this region of billet, which determines β-AlFeSi as the dominant phase. Distribution of Fe to Si in beta is at a

ratio of 1:1, so as the value is slightly above this, that would suggest that there is bias towards the alpha phase rather than the lower Fe level delta phase.

At the centre, the dominant phase has shifted to α-AlFeSi according to the diagram in Figure 4.63c where the data points have collected between the alpha and beta separators.

A similar pattern follows in the material sheared at 6400 rpm as seen in Figures 4.64a-d. The surface region of the billet sees a mixture of phases. What is different from the material at 4500 rpm is the trend of the Fe:Si data which at the surface decreases, suggesting low Fe level intermetallics factor heavily in this region, such as delta phase AlFeSi. Looking at the data against the separators in Figure 4.64c, the data points are spread between the phases but not beta. Comparing this data and the particles measured in the SEM images, β-AlFeSi can be argued as the least common phase within this region of the billet.

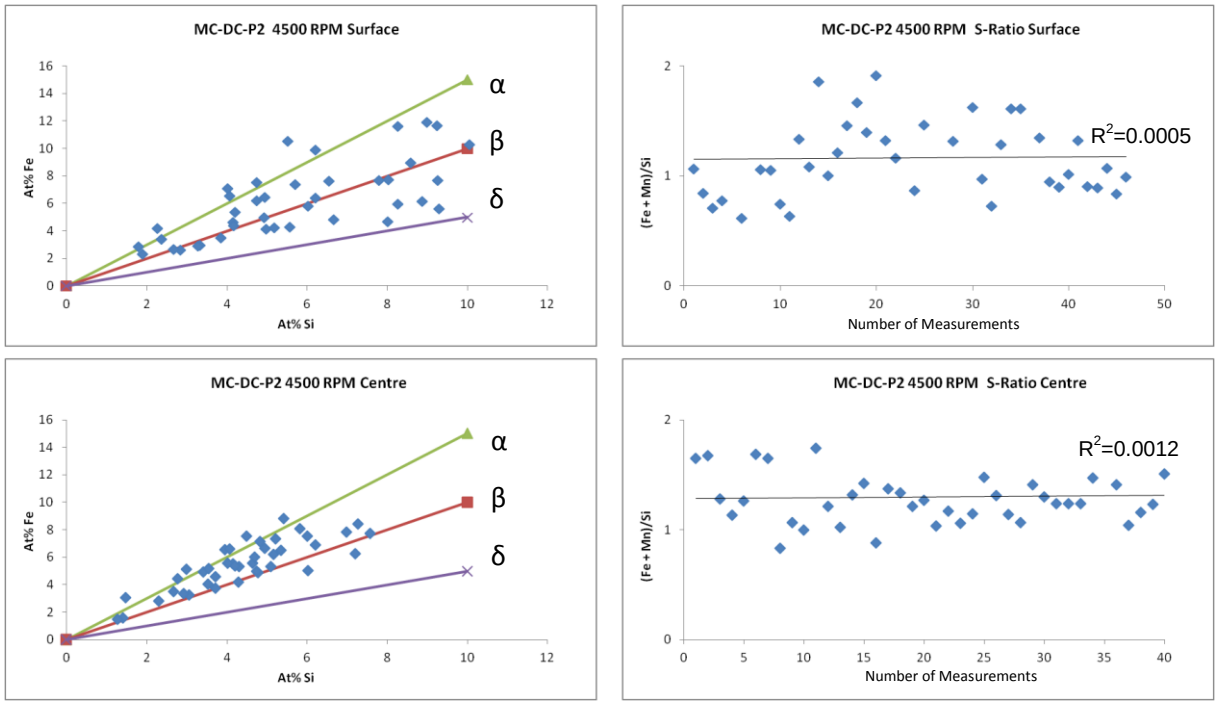

Figure 4.62 (a) and (c) Si/(Fe+Mn) ratio from the surface and central regions MC-DC-P2 billet sheared at 4500 rpm. Measurements plotted against separators for alpha-beta-delta AlFeSi phases. (b) and (d) accompanying Fe:Si-Ratio values

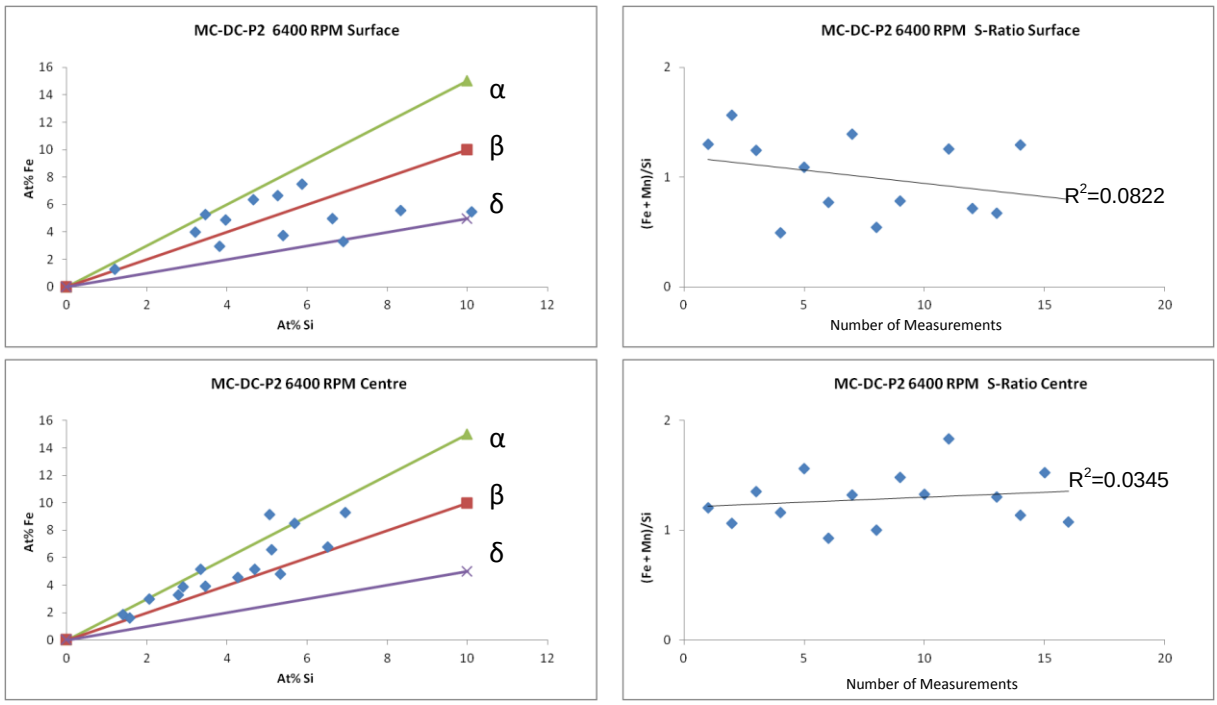

Figure 4.63 (a) and (c) (Fe+Mn)/Si ratio from the surface and central regions MC-DC-P2 billet sheared at 6400 rpm. Measurements plotted against separators for alpha-beta-delta AlFeSi phases. (b) and (d) accompanying Fe:Si-Ratio values

4.3.2.9 Intermetallic Morphology –Oxford DC, MC-DC-P3 Sheared at 4500 and 6400 RPM

The intermetallic structures of the MC-DC-P3 billets sheared at 4500 and 6400 rpm are presented in this section in Figures 4.65 and 4.66, respectively. For each set of figures, images a, c, e, were obtained by OM at 100x magnification, images b, d, f was obtained at 500x magnification. Images from the surface region, figures a-b; mid-radius of the billet, figures c-d; and the core of the billet, figures e-f, are presented for both rotation speeds.

If we compare the sets of images presented in Figures 4.65 and 4.66, there are clear similarities in the microstructures that formed despite the two different rotation speeds. The surface and central regions of the billet formed a mixed structure comprising dendritic and cellular grains, whilst at the mid-radius, coarse grain columns developed. The mixed grain structure produced unsurprisingly varied intermetallic structures. Coarse particles were found around the smaller cellular

grains with Chinese script and intermetallics plates at the boundaries between the dendritic and cellular grains.

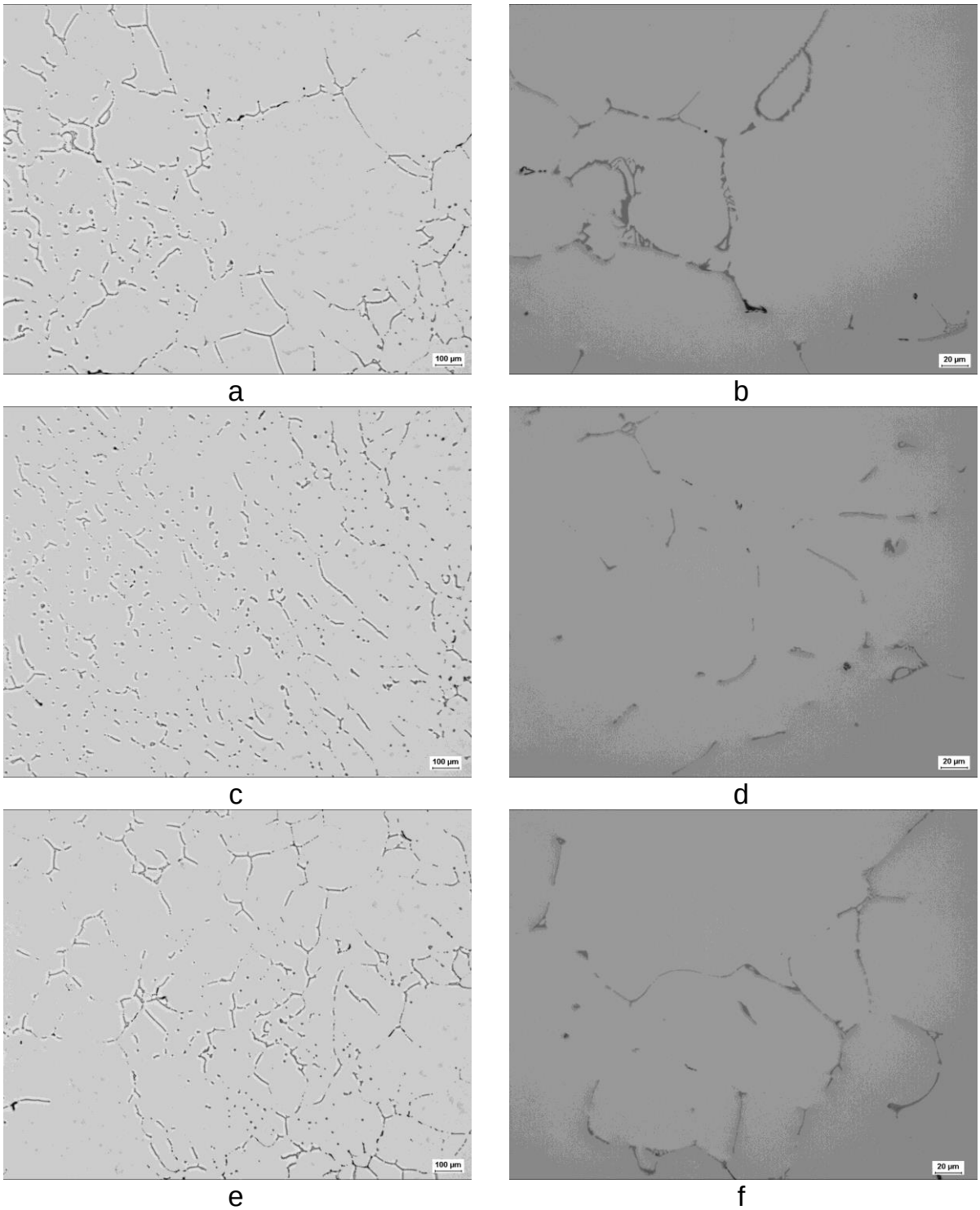

Figure 4.64 As-cast microstructure of MC-DC-P3 billet sheared at 4500 rpm. (a) Billet surface at 100x magnification. (b) Billet surface at 500x magnification (c) Mid-radius at 100x magnification (d) Mid-radius 500x magnification (e) Billet centre at 100x magnification (f) Billet centre 500x magnification.

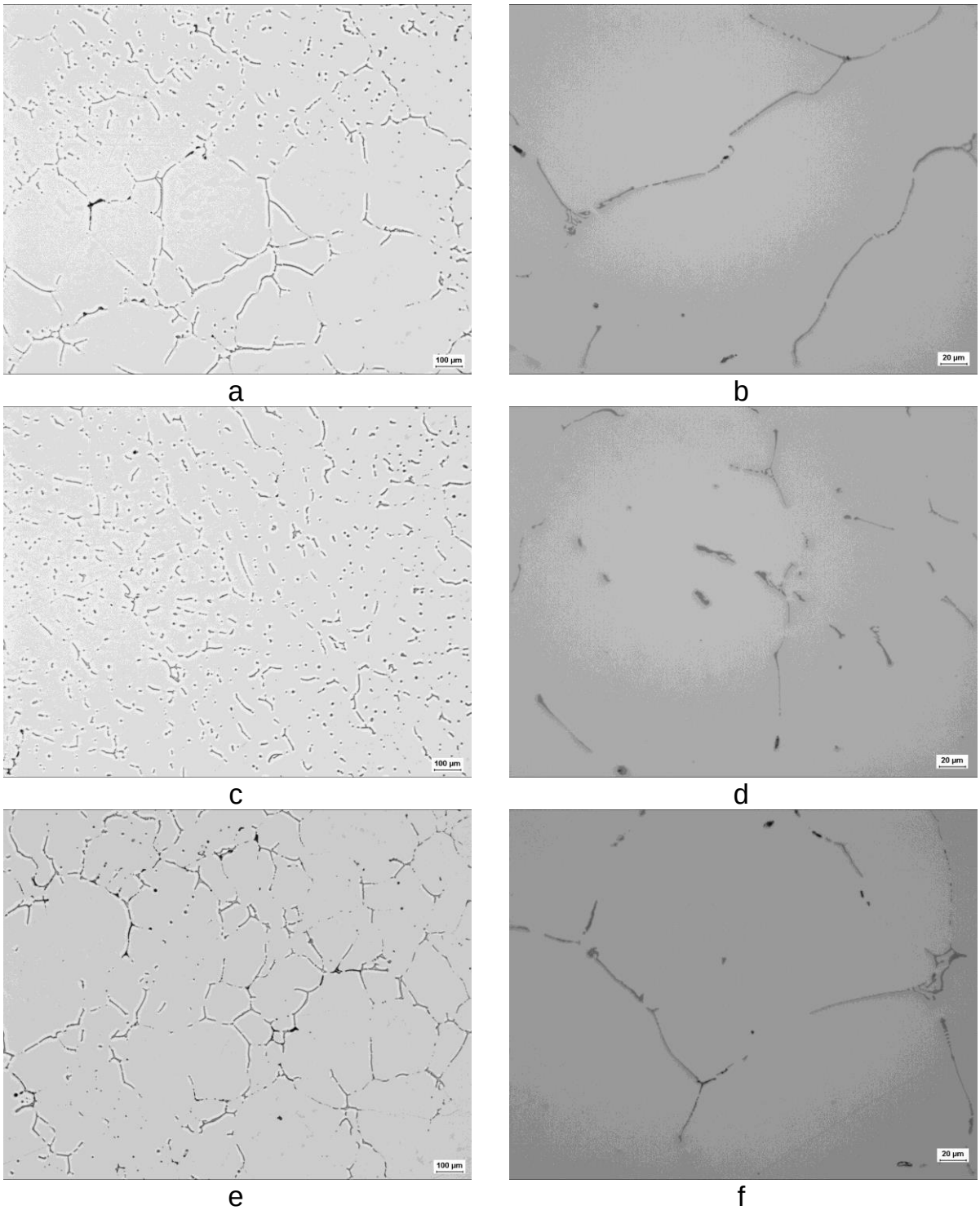

Figure 4.65 As-cast microstructure of MC-DC-P3 billet sheared at 6400 rpm. (a) Billet surface at 100x magnification. (b) Billet surface at 500x magnification (c) Mid-radius at 100x magnification (d) Mid-radius 500x magnification (e) Billet centre at 100x magnification (f) Billet centre 500x magnification

Comparing the same images taken from the billet sheared at 6400 rpm in Figure 4.66b and f, Chinese script is present at the grain junctions with rods of intermetallic around the boundaries of cellular grains. However, at the surface, the rods of intermetallics around the grains developed as necklaces effectively breaking-up into smaller particles. At the centre, the rods remain intact forming longer more complete particles.

If we consider the diagrams shown in Figures 4.67 and 4.68, this observation is supported by the clear difference shown between the particle lengths at the central region of the billet, when sheared at different rotation speeds. At 4500 rpm, the average particle length stays below 5 µm from the surface to the centre, Figure 4.67a, but at 6400 rpm the same diagram shows a sharp increase in the average length above 5 µm as a result of the intermetallic rods remaining intact. It should be noted that the cellular grain structure dominates the microstructure at the billet centre when sheared at 6400 rpm.

At 4500 rpm, the diagrams in Figure 4.67 show that the particles at the surface of the billet are similar in size to those of the centre. What has been seen in previous melt conditioned billets is an increase in particle size from the billet surface to the centre. As the cast and melt conditions have been the same during each cast, shear depth within the mould is the variable that affects the formation of the intermetallic particles through manipulation of the cast structure during solidification.

The average particle area and width does not deviate significantly across the billet at a shear speed of 4500 rpm as shown in Figure 4.67, with the average values of both measurements consistently below 5 µm. 85 % of the particles measured had an area of 5 µm or less for each position across the billet and only 5 % of particles reached a size above 10 µm.

When we consider the particle length and shape factor measurements, these two criterion are closely linked with the shape factor determined by the perimeter of the particles. Hence their trends are similar here with a dip in the average values corresponding to the measured particles within the coarse grain columns at the mid radius of the billet. Comparing this result to Figures 4.65c-d it matches the shorter particles that are well distributed throughout the bulk of the material. The rods are well broken-up and separated into short needles of intermetallic AlFeSi with

occasional Chinese script forming. Inside the grains, smaller and more spherodised particles are present resulting in the reduction in shape factor value seen in Figure 4.67. The fact that the average shape factor values on a whole are under 5 implies that the particles are spherical in nature. This is also typical of alpha phase intermetallics that commonly forms Chinese script and rounded particles, with beta usually being the rod and plates at the grain boundaries.

At 6400 rpm Figure 4.68 shows that there is an increase in the average particle size across the measured criterion with the increases being most significant at the centre of the billet. Particle length and shape factor are lowest at the surface. The necklace of particles is more spherical as a result with rounded alpha phase particles. This particle structure also reduces the average length due to the increased number of smaller particles present (Figure 4.68a).

In the central region of the billet the average particle length has risen dramatically and the shape factor naturally follows. Intermetallics at the grain boundaries are considerably longer around cellular grains of which there is a higher volume in the centre. These grains are devoid of particles within their bulk so none of the final solidifying liquid is held inside the grain, but concentrates at the boundaries around the grains resulting in coarse intermetallics. Comparing the particle length data across the billet, the percentage of particles below 5 µm and 10 µm (smaller particles) decreases significantly across the billet from surface to the centre; 75% and 95% at the surface respectively compared to 50% and 79% at the centre, thus a higher percentage of the particles measured at the billet centre are above 10 µm with 4% being above 20 µm when the shear device rotation speed was increased to 6400 rpm. The effect of shearing was also very acute at depth P3 within the core of the sump and this was magnified by the rotation speed increase.

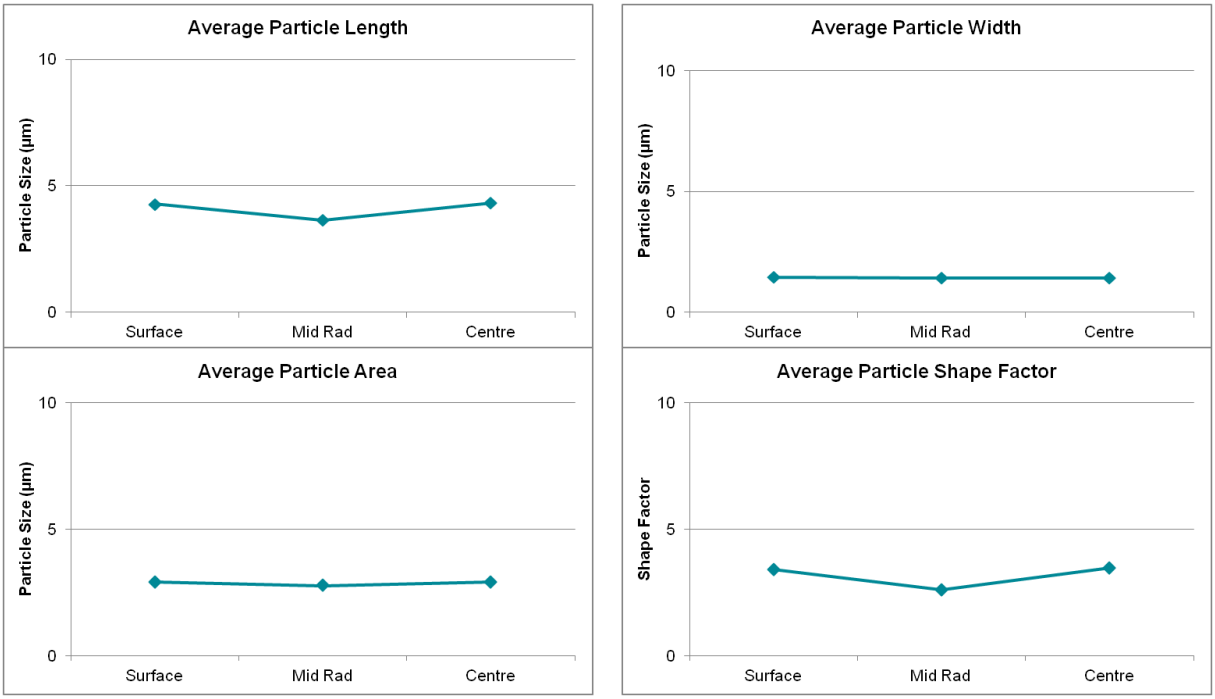

Figure 4.66 SEM INCAFeature software analysis of average particle measurements from as-cast MC-DC-P3 billet sheared at 4500 rpm.

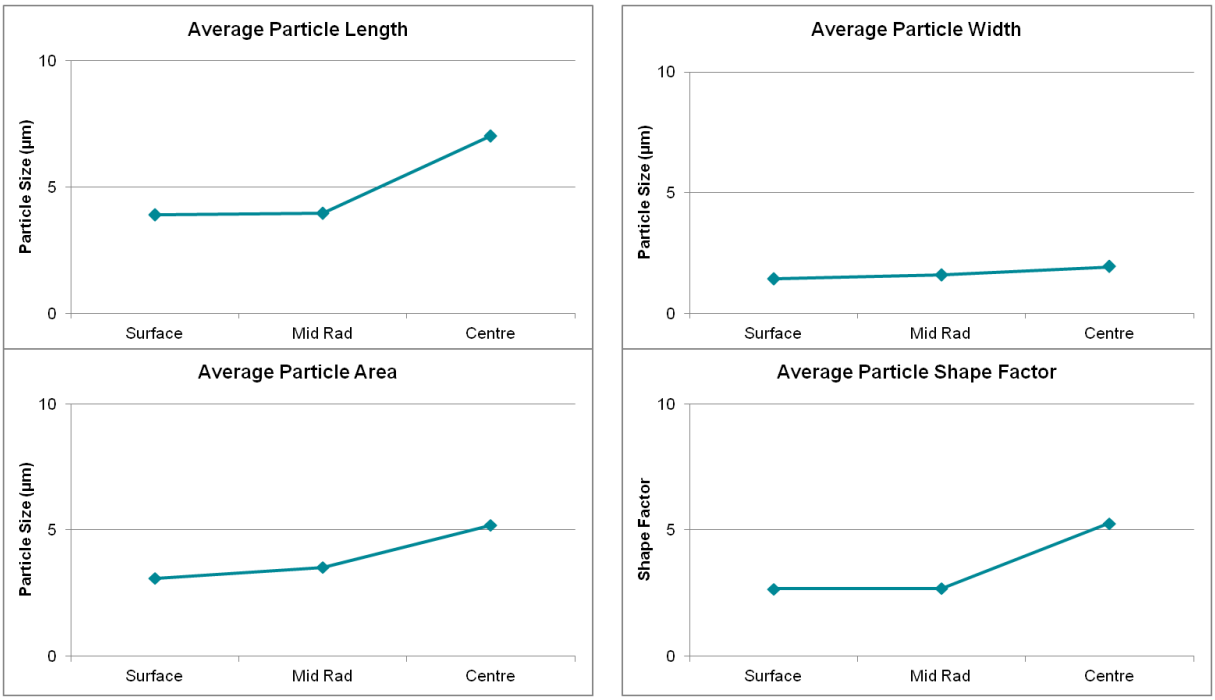

Figure 4.67 SEM INCAFeature software analysis of average particle measurements from as-cast MC-DC-P3 billet sheared at 6400 rpm.

The rise of the average shape factor value at the billet centre would imply that the intermetallics have transformed from a more spherical morphology typical of alpha phase AlFeSi to the block morphology associated with the beta phase. The length of the particles has certainly increased due to the cellular nature of the grains and plates of intermetallic are present as a result also. At the mid radius of the billet within the coarse grain columns, the intermetallic particles shown in Figure 4.66c-d are similar to those of the surface region as well as those at the coarse grain columns of the billet that was sheared at 4500 rpm. The grain structure at both rotation speeds is dendritic with the bulk of the grains dominated by well distributed intermetallics Figures 4.66c-d and 4.67c-d, including well broken-up rods of intermetallic at the boundaries.

4.3.2.10 EDX Analysis of Intermetallic Particles –Oxford DC, MC-DC-P3 Sheared at 4500 and 6400 RPM

SEM images of the intermetallic structures obtained from the surface, mid radius (coarse grain) and central regions of the billet sheared at 4500 rpm and 6400 rpm are presented in Figures 4.69a-f and 4.70a-f, respectively. EDX was used to identify the intermetallic phase in relation to its stoichiometry.

If we consider the images taken from the billet sheared at 4500 rpm first, Figure 4.69a-f, and start at the surface, moving through to the billet centre comparing the types of intermetallics present and their morphologies. Unsurprisingly, at the surface there are both alpha and beta AlFeSi phases present as shown in Figure 4.69b. Both the alpha and beta phase particles are found at the boundaries and inside the grains. It could be argued that the alpha phase particles have a more spherical morphology compared to the beta phase, which is certainly true of those particles found in the inter-dendritic regions of the grains. In the cellular grain areas, the intermetallics are more complex especially at the boundaries and junctions where Chinese script is prevalent. Here, beta plates form with alpha script, as the particles form with different concentrations of solute elements. The needles of intermetallic appear broken-up forming necklaces of particles which are good for downstream processing as they will flow with the material without acting as crack initiation sites that plate intermetallics

are prone to do. The beta is also small and well distributed and should require short homogenisation times to transform into small spherical particles of alpha phase AlFeSi.

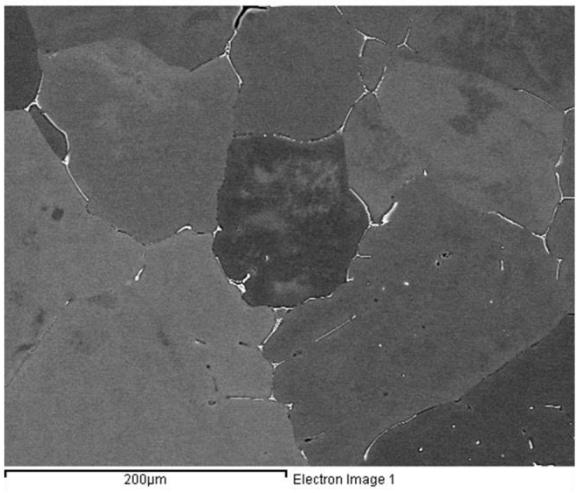

a

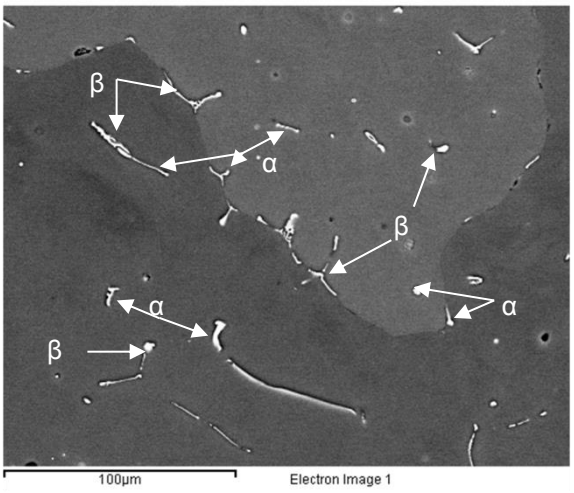

b

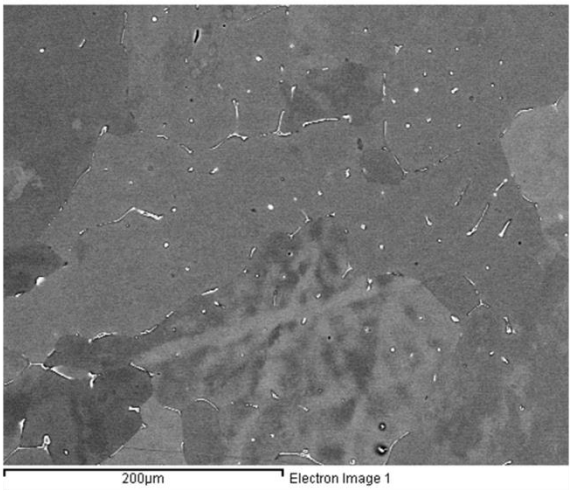

c

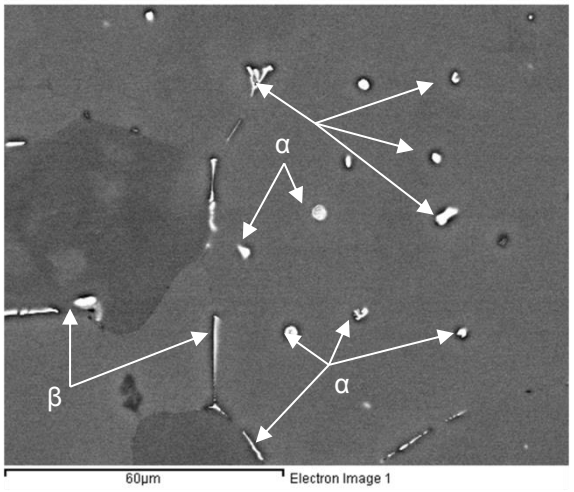

d

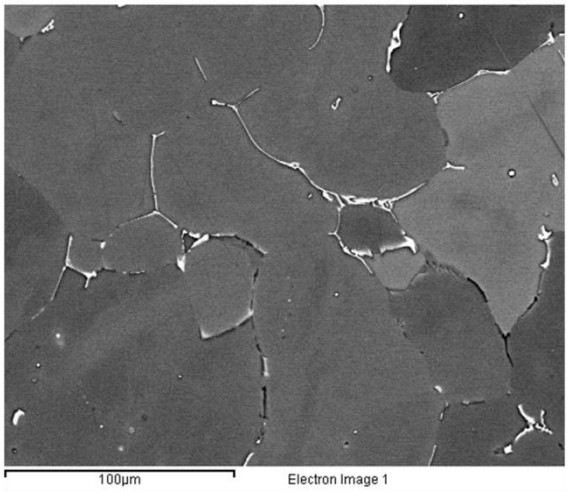

e

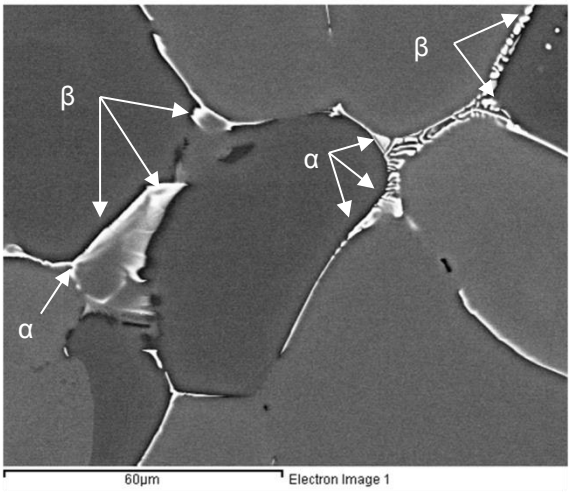

f

Figure 4.68 SEM images of intermetallic particles from the MC-DC-P3 as-cast billet sheared at 4500 rpm. (a-b) Billet surface (c-d) Mid radius. (e-f) Billet centre. Phase identification by EDX analysis. Note some of the phases are identified in the images

It could be argued that there is a trend towards the alpha phase becoming dominant which is supported by the diagrams in Figure 4.70 that display the statistical data of the measured intermetallics against phase separators. The data is spread between the alpha and beta separators but it could be argued that there is dominance of the alpha phase which is supported by the (Fe+Mn)/Si ratio of 1.41. The trend of the data is rising indicating that the ratio is climbing towards the alpha phase being dominant.

The dendritic grains of the coarse grain columns contain well distributed particles of predominantly alpha phase intermetallics that have become enriched due to being trapped within the inter-dendritic regions of the grains. This is shown in Figure 4.69c-d along with beta phase that typically found at the boundaries in this region of the billet. There is a clear difference in the morphologies of the intermetallics depending on where they formed; alpha phase is spherical within the bulk of the grains whilst it becomes rods or Chinese script at the boundaries and junctions respectively. Beta phase particles form plates at the junctions and rods of AlFeSi at the grain boundaries. This is due to the trapping of liquid between the grains during solidification that spreads along the grain boundaries and collects in the junctions where pockets of eutectic liquid solidify at the end of the solidification process. EDX analysis of the intermetallics measured the average (Fe+Mn)/Si ratio to be 1.29 which still suggests the dominant phase is α-AlFeSi.

At the billet centre, the intermetallics did form some very coarse particles as shown in Figure 4.69e-f, with plates of beta and alpha phase Chinese script at the junctions of small grains, whilst smaller, finer intermetallics formed around the boundaries of larger grains and dendritic regions. Figure 4.69e shows this well with the small cellular grains surrounded by larger grains having coarse intermetallics enveloping it, whilst the intermetallics around the larger grains are much more spread out along the boundaries with a finer structure. The higher magnification image of Figure 4.69f shows an example of the plate and Chinese script morphologies that formed around these cellular grains. It also shows how the alpha phase particles extend along the boundaries after the Chinese script, as rods of intermetallic but still broken-up with a

spherical morphology. The beta phase has its typical block morphology and is arguably coarser than the alpha phase.

Figure 4.70b shows phase analysis data plotted against separators for the central region of the billet sheared at 4500 rpm. Similar to the surface area of the billet, there is a mix of phases present in the central region of the billet. There is also an increase in the amount of delta phase intermetallic in the centre of the billet which denotes a tendency for an excess of Si to occur more often than at the surface. However, alpha-AlFeSi is still the dominant phase in the centre of the billet.

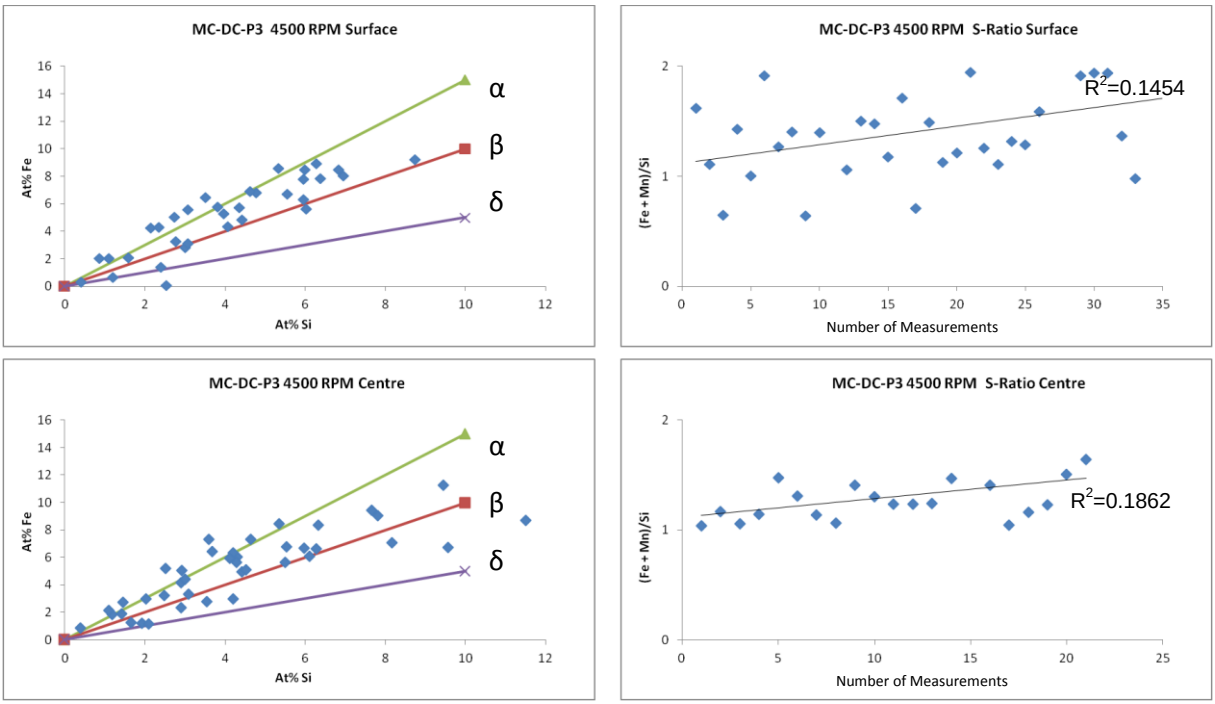

Figure 4.69 (a) and (c) (Fe+Mn)/Si ratio from the surface and central regions MC-DC-P3 billet sheared at 4500 rpm. Measurements plotted against separators for alpha-beta-delta AlFeSi phases. (b) and (d) accompanying (Mn+Fe):Si ratio values.

The SEM images of the material sheared at 6400 rpm are shown in Figure 4.71a-f. In Figures 4.71a and b, the grain structure is dendritic but as has been mentioned previously, the microstructure consists of cellular and dendritic grain morphologies. Noticeably there are shrinkage pores present at some of the inter-dendritic regions of the grains, shown in greater detail in Figure 4.71b. The pores do not seem to be related to any of the intermetallics even though the particles are of a coarse alpha

Chinese script, rather they will be due to a restriction in a flow of liquid feeding the shrinkage during the final stages of solidification. The intermetallic particles identified are predominantly alpha phase as shown in Figure 4.71b which is confirmed by the diagrams presented in Figure 4.72a-b.

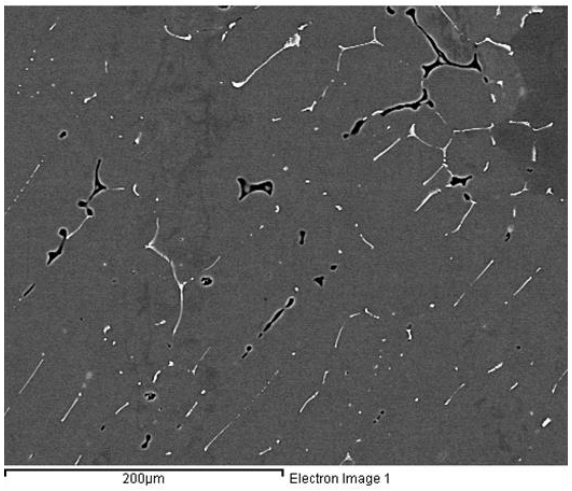

a

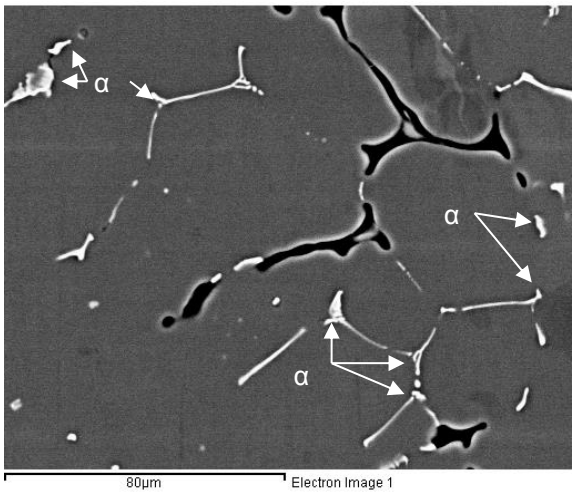

b

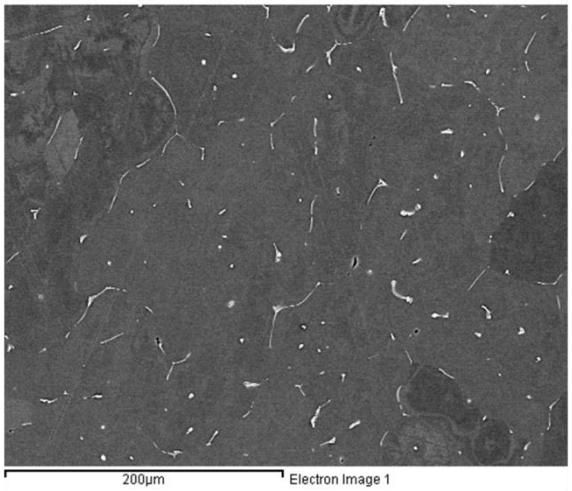

c

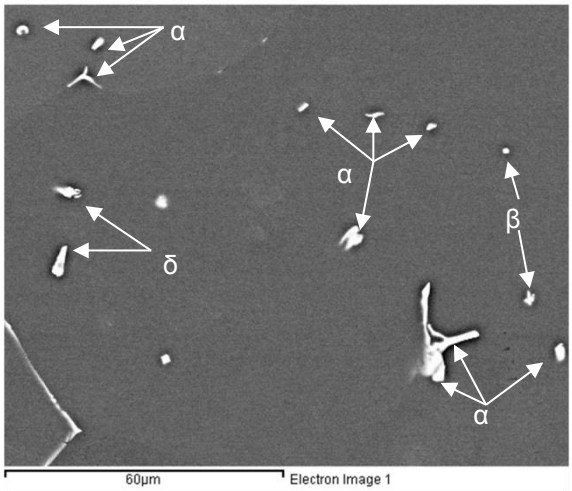

d

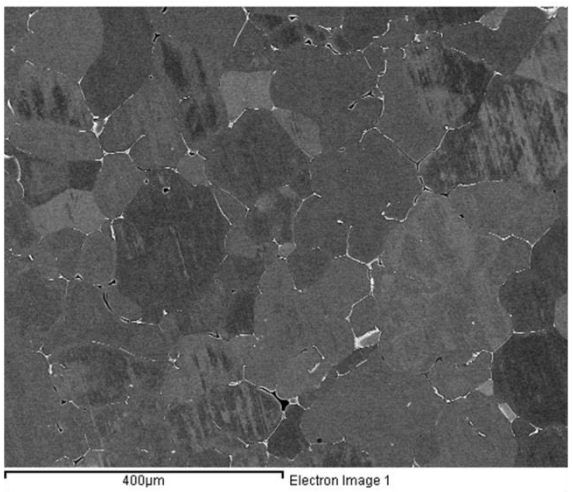

e

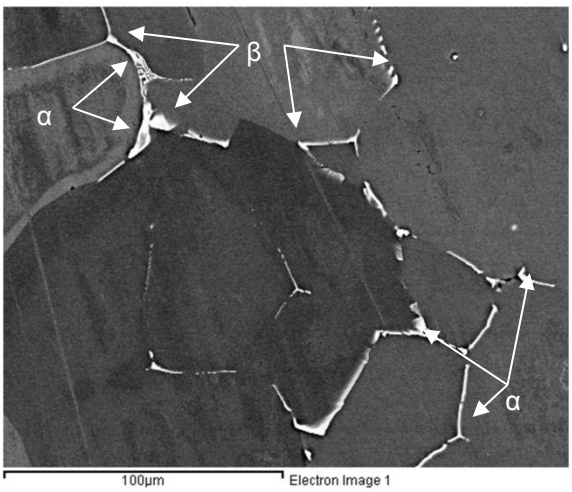

f

Figure 4.70 SEM images of intermetallic particles from the MC-DC-P3 as-cast billet sheared at 6400 rpm. (a-b) Billet surface (c-d) Mid radius. (e-f) Billet centre. Phase identification by EDX analysis. Note some of the phases are identified in the images

In Figure 4.72a, the majority of the data is found about the separator for the alpha phase with an average (Fe+Mn)/Si ratio of 1.27, supporting the argument that the alpha phase is the dominant intermetallic at the surface.

The dendritic grain morphology of the coarse grain columns is shown in Figures 4.71c-d. Fine well dispersed particles formed within the bulk of the grains at the inter-dendritic spaces. All three phases; alpha-beta-delta are present as shown in Figure 4.71d. Each phase has a mixed particle morphology with the alpha phase being the most coarse. All three phases are found within the bulk of the grains with the alpha phase being the dominant phase overall, with an average (Fe+Mn)/Si ratio of 1.36 from the measured particles.

The grain structure at the billet centre developed a more cellular structure, Figure 4.71e, which is devoid of particles within the grain and thus they are more concentrated at the boundaries. As a result these intermetallics can become coarser than seen previously at the surface and mid radius of the billet, examples of which are shown in Figure 4.71f. Beta phase particles are also more common at the centre forming plates at grain junctions and rods of intermetallic at the boundaries.

The alpha phase particles that formed did so with its characteristic Chinese script morphology at concentration points such as grain junctions and needles of intermetallic at the boundaries. However, plates of alpha-AlFeSi are shown in figure f also, especially around the edge of smaller grains where the concentration of final solidifying liquid is greatest. The average Fe+Mn/Si ratio of the measured particles is 1.27, which is arguably above the threshold for the beta phase to be dominant of 1.25 but this is extremely close. Analysis of the data spread against the phase separators in diagram c suggests an even spread between the two phases, thus a single dominant phase is likely not determinable, but is a mix of alpha- and beta-AlFeSi similar to what is experienced in industry today.

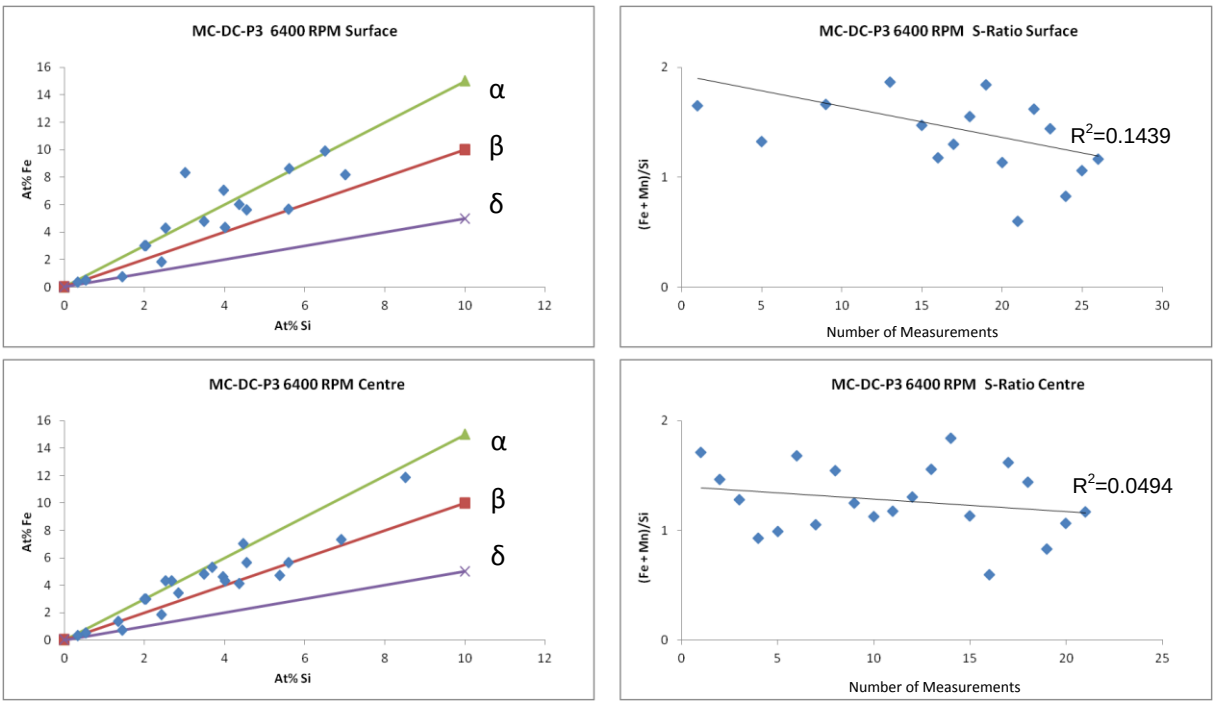

Figure 4.71 (a) and (c) (Fe+Mn)/Si ratio from the surface and central regions MC-DC-P3 billet sheared at 6400 rpm. Measurements plotted against separators for alpha-beta-delta AlFeSi phases. (b) and (d) accompanying (Mn+Fe):Si-Ratio values

CHAPTER 5 - DISCUSSION

A new liquid metal treatment technology has been investigated in this work by integrating it with an older or more established technology, Direct Chill (DC) casting. This integration became the MC-DC casting process; Melt Conditioned Direct Chill casting. This chapter examines the effect of melt conditioning upon the billet microstructure, macrosegregation and intermetallic structures based on the results of quantitative image analysis, spectroscopy and characterisation of intermetallic particles. Discussions into the mechanisms that contribute to the MC-DC process will be included.

5.1 MICROSTRUCTURES OF DC CASTING WITH AND WITHOUT GRAIN REFINER

Industry strives for a well refined equiaxed grain microstructure during the semi-continuous production of commercial extrusion billet. Direct chill casting is the technique most commonly employed to reach this goal combined with established grain refinement practices. Additions of TiB_2 containing aluminium rod at a typical ratio of TiB=5:1 is fed into the melt during casting, before it enters the mould. This enriches the melt with nucleant particles promoting heterogeneous nucleation and ensuring crack free logs of fine equiaxed grains. An average grain size of 60–100 µm is routinely achieved using this technique with appropriate control of casting parameters. A result such as this would suggest that another method of grain refinement is redundant. But, this is not the whole story to producing a billet of suitable quality for down-stream processing. Billet that is destined for use in the production of multiple end products: automotive, marine, building systems and aeronautical to name a few.

Literature, although stating that a fine and equiaxed grain size is beneficial, refuses to ascertain the actual size required to achieve the best combination of mechanical properties, surface appearance and production rates. Jones and Pearson considered a grain refiner to be effective if the grain size of aluminium falls below an acceptance

level (220 μm) (Jones & Pearson, 1976). There is also the energy and time expensive homogenisation step that follows casting, to get the alloying elements dissolved into the matrix and further refine the intermetallic precipitates in the refined billet, in order for the billet to achieve downstream processing (production) and mechanical performance of the end product targets.

Therefore, investigations of new technologies to refine the microstructure do so with the amplified aim of refining the billet as a whole; on the micro level as well as the macro, with the expressed goal to reduce inoculants usage and homogenisation processing.

The alternative to not grain refine or melt conditioning is shown in Figure 4.22a. Feather grains dominate the structure and as striking and beautiful as the image may be, the large centreline crack and strong anisotropic nature of the grains make this microstructure highly unattractive to industry. These feather grains formed naturally within the billet, cast with the parameters used for the grain refined DC billet (DC-GR), grain refined and melt conditioned billet (MC-DC-GR) and solely melt conditioned billets (MC-DC). Initial solidification will have followed the process proposed by Flemings (schematic) which features equiaxed grain growth at contact with the mould wall, followed by columnar growth into the mould which precedes equiaxed grain growth in the core of the ingot. In this case, high thermal gradients and melt flow due to melt entering the mould and metalostatic pressure of the metal head creating convection, has led to the development of feather grains. Turchin *et al* found that feathery grain growth was as an intermediate growth phase between equiaxed and columnar grains (Turchin, Zuijderuiyk, Pool, Eskin, & Katgerman, 2007). Feather grains form similarly to regular dendrites but with a <110> growth direction compared with <100>. Both morphologies form from a competitive growth mechanism, but the inflow of melt into the mould and high thermal gradients typical of DC casting, contributed to the feather grains dominating growth. Stacking faults and the build-up of stresses due to increased flow are believed to initiate the switch from the dendritic growth direction <100>, to the <110> growth direction of feather grains. When the thermal gradient is close to the <110> direction, feathery grain growth dominates over equiaxed and columnar. The distinctive “fan” shape to the left of Figure 4.22a is due to the distances between the main trunks of the dendrites increasing as solidification continues into the core of the billet.

On the right of the centreline crack in Figure 4.22a, the structure although regarded as feather grained, is different from that of the left. The grains are much less “fan like” as on the right, being more twinned lamellae with random grains spread through the structure. These grains appear as fragments that would have been caused by remelting of dendrite arms as the hot inflow of melt washed over the solidification front, carrying them off towards the core. The twinned grains have pushed these fragments to the centreline similar to the columnar grains described above would do, where the equiaxed transition would take place as they block the growth of the columnar grains. The reason why the morphologies of the grains vary from one side of the sample to the next is not immediately clear. Speculation would lead to an increase in the solidification rate due to increased cooling. Perhaps the water flow rate was biased to the point where the water entered the mould and was perhaps cooler. There certainly appears to be increased nucleation on the right side and fragmentation due to the higher number of fragments and floating crystals. Secondary cooling of DC cast billet is a critical parameter to restricting the onset of feather grains as it contributes 80% of the heat extraction during solidification. Reducing the water flows will reduce the cooling rate thus the thermal gradients which contribute to feathery grain growth.

Another method is grain refinement and stirring of the melt.

Figure 4.19 shows the microstructure of the billet which has been grain refined by Ti:B=5:1 ratio TiB_2 rod at a rate of 1.0 kg per tonne. The grain structure is fine and equiaxed with an average size of 90 µm, well on par with industrial standards. The centreline crack that was a part of the un-grain-refined billet was controlled by the widespread heterogeneous nucleation which dominated solidification. The grain size is uniform along the billet cross-section implying that nucleation happens throughout the sump and the casting parameters are suitable for the alloy and mould assembly. Nucleation and growth depends on the constitutional undercooling ahead of the solidification front where the rejected solute acts as growth restrictors.

The centreline crack in the DC billet (Fig 4.22a) formed as a consequence of the large grain boundaries and high stresses generated by solidification shrinkage. Melt is unable to flow into the void that the shrinkage creates and thus the crack propagates the full length of the log. A centreline crack did not materialise in the grain

refined billet as experienced by industry, hence why grain refinement through inoculation is the most common method.

The DC and DC-GR samples were cast, a means of providing comparative material for the MC-DC billet using the same DC unit and casting parameters, therefore ensuring that melt conditioning is the only variable to the process refining the microstructure. In each of the three experiment series where only shearing has been applied as the only method of melt treatment; static mould experiments, lab scale DC castings and industrial scale DC casting, the structure has been refined. The discussion will now attempt to explain the mechanisms that contributed to the refinement of the material by melt conditioning and compare the results against the material cast with and without grain refiner.

5.2 MICROSTRUCTURAL EVOLUTION THROUGH MELT CONDITIONING

5.2.1 MICROSTRUCTURAL EVOLUTION IN STATIC MOULD EXPERIMENT SAMPLES

Although the comparative material above was cast at the industrial scale, it is still equivalent to the other material cast. Each casting can be seen to follow a similar trend where melt conditioning or grain refiner has either not begun or been used. Therefore, the discussion on the mechanisms of grain refinement by melt conditioning starts here from the results of static mould experiments (Figure 4.11). Zone 1 of the static mould experiments (Figure 4.11) has a coarse columnar structure that grew rapidly from the chill face of the copper block. In the lab scale DC billets, before melt conditioning began, the structure followed the model devised by Chalmers; equiaxed grains at contact with the mould wall; columnar grains that grew into the melt towards the centre; coarse equiaxed grain structure in the core and centreline cracking. In the MC-DC billet at Oxford, the sump shows a coarse columnar structure and centreline cracking until melt conditioning refines the material.

Solidification in the static mould experiments began with zone 1 as the melt contacted the chill face of the copper block. The columnar grains grew rapidly into the

melt as an essentially planar front due to the reduced cooling from the mould walls. This growth continued until physically blocked by the coarse grain structure of zone 2. The growth rate of zone 1 will be the fastest of the billet as it is in direct contact with the copper block providing the undercooling for the initial growth, similar to that of the mould wall in DC casting. Large temperature gradients are present here from the chill zone to the hotter melt above. These gradients are essentially equal across the planer front as there is negligible effect from the side walls, due to them being at equal temperature with the melt. Columnar grains dominate growth here, rejecting solute ahead of them into the region that will become zone 2.

At the transition from zone 1 to zone 2 fine equiaxed grains form a kind of boundary to the columnar grain growth. The transition between the zones is very definite with the columnar grains of zone 1 assumed completely solid at the point that shearing begins. Considering the vortex that is created by shearing it is not hard to imagine the effect this must have on the material when confined to such a tight vessel. When shearing was started and the rotating speed reached 5000 rpm the vortex created instantaneously spins the melt ahead of zone 1, stalling the columnar growth and facilitating the fragmentation of dendrite arms. Fragmentation occurred due to the shock of the forced flows against the solidified front which would be followed by remelting of arms from the thermal-solutal flows. The forced flow of the melt carried the grains to regions where they would not have otherwise been under normal convection, in this case zone 3. These fragments are the nuclei for grain growth which blocks the columnar grains and this is clearly seen by the fine equiaxed grains at the boundary between zones 1 and 2.

Zone 2 is a mixture of semi-solid and liquid in the space between the shear device and solid front; thus a transition region similar to the mushy and slurry zones in a DC cast billet sump. This columnar – equiaxed – columnar transition has been seen before under forced flow condition. Forced flow actually decreases the solidification rate whilst the superheat increases the thermal gradient, leading to a change in grain morphology. Grain morphology certainly changes with temperature gradient and cellular microstructures are only stable for short range temperature gradients, whilst columnar grains are considered to grow in the direction of the thermal gradients. The close proximity of the shear device and mould walls could have restricted the flow of hotter melt from flowing down across the solidification front. Instead, as described

above, zone 2 is a semi-solid that is spinning with the spiral vortex that forms below the shear device, resulting in the angled nature of the grains as they grow with the thermal gradients. These gradients are rotating against the hot wall of the mould and the cooler melt is being drawn along the centre line into the device and out into zone 3.

Fine and equiaxed grain structure in zone 3 produced during steady state solidification with intensive melt shearing will be easily understood following the above analysis of static mould experiments:

- Grain refinement: Intensive melt shearing in the sump disperses the naturally occurring oxides films into fine and well distributed individual oxide particles. The number density increase can be as high as three orders of magnitude (Men, Jiang, & Fan, 2010). Therefore, grain refinement in DC casting with intensive melt shearing can be attributed to enhanced heterogeneous nucleation in the sump (Jones, Prasada Rao, & Fan, 2013). Considering the equiaxed microstructure in Zone 3 above the columnar of Zone 2, this nucleation on oxide particles can be understood. Zone 2 would have started to form before the shear device was inserted and operational due to operational difficulties. Thus transition from Zone 1 to Zone 2 with coarse columnar dendrites is expected. In Zone 3 which is fully liquid around the shear device, oxide particles and fragmented grains can fully disperse through this Zone. Here an equiaxed grain structure would be expected as a result.
- Equiaxed growth: Intensive melt shearing in the sump leads to a uniform temperature field and enhanced mass transport therefore uniform compositional filed. Temperature measurement during steady DC casting with intensive melt shearing has confirmed that the melt temperature in the sump is a few K below the alloy liquidus (Zuo, Jiang, & Fan, 2011). This was also confirmed in the present study by industrial trials at Oxford. This provides a unique condition for growth with low temperature gradient and high growth velocity. This is a condition which favours equiaxed growth according to Hunt's theory for CET (columnar to equiaxed transition) (Hunt, 1984).

In zone 4 shown in Figure 4.11, the structure is coarse however due to the reduced number of nucleant particles and slow cooling rate. This zone shows a coarse

equiaxed grain structure and is formed after the withdrawal of the high shear device from the melt. If melt conditioning had been able to proceed for longer, it is conceivable that the grains of zone 4 would have become finer. The vortex generated by melt conditioning, travel past the shear device so convective melt flows are created above the head of the tool. This coarse grain structure can be mainly attributed to the reduced number density of nucleation sites due to less shearing. Other factors, such as growth without melt shearing and increased temperature gradient, may also contribute to the coarse grain structure.

In summary, the microstructural evolution in the static mould sample clearly demonstrates the effect of intensive melt shearing on grain refinement. It is the enhanced heterogeneous nucleation by dispersed oxide particles that contribute mainly to the grain refining effect. The uniform temperature and compositional fields in the sump achieved by intensive melt shearing also favours the CET (Hunt, 1984).

5.2.2 MICROSTRUCTURAL EVOLUTION IN MC-DC AT OXFORD-IMPORTANCE OF PROCESSING PARAMETER OPTIMISATION FOR INDUSTRIAL TRIAL

Comparing the four zones of the static mould to that of the MC-DC billet cast at Oxford, similarities can be drawn with the stages of development in the MC-DC billet structure (Figure 4.22). Referring to the Figures of the MC-DC-P2 billet cross-sections presented in section 4.2.3.2 a break down of the parallels follow:

1. Zone 1 represents the columnar growth at the base of the billet in Figure 4.22a. Both zones experience high cooling rates and large temperature gradients; zone 1 of the static mould due to the copper block and low melt volume; MC-DC sump due to cooling effect of starting head and water quenching.
2. Zone 2 represents Figure 4.22b and c as the intermediate zone after shearing has begun and melt conditioning is starting to take effect. The billet structure here is definitely beginning to change with steeper gradients developing and an increase in the number of grains along the centerline of the billet, before and equiaxed structure formed in Figure 4.22c.

3. Zone 3 is the fully equiaxed section of billet in Figure 4.22d. Here the melt reservoir inside the mould is treated fully by the shear device. The homogeneous temperature and solute fields were created, promoting CET and the enhanced heterogeneous nucleation by dispersed oxide particles, contributing to grain refinement.
4. Zone 4 is not represented here as it is effectively what happens within the hot-top above the intensive melt shearing region. It has been shown by the simulated flow patterns that forced melt flows were also present above the jets of the device in the hot-top. It then effectively disappears within the melt conditioned region due to the continuous flow of melt in MC-DC casting.

The macro-structure at the base of the MC-DC-P2 billet (Figure 4.22a) formed prior to melt conditioning beginning. The shear device was inserted but was not rotating until 250 mm of the billet had been cast. This point is at the top of this sample. The activation of the shear device has had an immediate effect on the mushy zone of the sump, indicated by the appearance of layers at the top of the image. These layers give a good approximation of the sump shape at this point. Within this region fragmentation of the dendrites is enhanced by melt conditioning at the forced flows move across the columnar front. The diagrams produced by SolidWorks give us an indication of the flow patterns that the shear device potentially generated at 4500 rpm, which is the rotation speed at this point in the cast. There certainly is not the restriction that was experienced in the static mould or at position P1 for that matter. At MC-DC-P2, the forced flows make good use of the mould geometry, moving down the transition plate (T-plate) at the thimble exit into the sump. At the point where these flows come into contact with the mushy zone, they move towards the billet core driving warmer melt through and along the solid front. This transports solid particles and solute towards the centre where it is drawn up powerfully through the shear device where it is re-circulated into the melt within the mould reservoir. This reservoir of liquid is spinning inside the mould as shown in Figure 4.2 creating a vortex that moves the melt below and above the head of the tool where the jets exit through the holes.

This means that hotter melt is mixing with colder semi-solid homogenizing the temperature field within the mould reservoir, whilst enriching it with solute and potent

nucleating particles. These particles have similar lattice parameters to that of the α-Al matrix, resulting in perfect matching and lower activation energy requirements for nucleation. As the forced flows generated by the shear device sweep across the mushy zone in the sump, solute is removed from the region ahead of the columnar grains. This allows the growth rate to increase as the restricting factor of the solute is removed. The growth rate then increases and slows depending on the solute concentration ahead of the interface. The melt temperature fluctuates in the same manner as it travels across the interface. Hotter melt is drawn down and across the front towards the centre where it is sucked into the shear device and cooling down distributed by the jets. Cooler melt then replaces the hotter melt in a cyclic pattern. The melt does not have to be above the melting point of the alloy to assist remelting, it is the fluctuation in solute and melt temperature that promotes remelting.

As the discussion above made mention of fragmentation and solute/thermal gradient changes resulting in remelting, it would be prudent at this point to mention the mechanisms of grain fragmentation or grain multiplication and the role of melt conditioning. One of the mechanisms causing fragmentation or grain multiplication is the accumulation of solute at the root of the dendrite branches, causing remelting and eventual detachment from the parent branch (Eskin, D. G., 2008). These branches are transported by convective/forced flows within the sump to an area of constitutional undercooling, created by solute rejection at the solid-liquid interface. This area creates favorable conditions for growth and heterogeneous nucleation some distance ahead of the solidification front. These detached grains start to grow, rejecting solute and generating latent heat influencing fragmentation further. Conditioning of the melt at the point of solidification is another mechanism that can cause fragmentation. Conditioning of the melt refers to stirring either by electromagnetic or mechanical means or ultrasonic cavitation. In this study mechanical stirring increases penetration of liquid flow into the mushy zone, partially remelting dendrite arms resulting in fragmentation, whilst lowering the thermal gradient in the liquid extending the undercooled region favoring a columnar-to-equiaxed transition (Campanella, Charbon, Rappaz, 2004). The mechanical stirring of the rotor-stator device happens at high velocities. It is suggested that oxide films are broken-up as they pass through the device and dispersed through the melt (Li, Wang, & Fan, 2012; Li, Xia, Jarry Scamans, G. M., & Fan, 2011). They too travel to

the constitutionally undercooled zone where it is suggested these oxide particles act as highly potent nucleation sites for α-Al phase, contributing to grain refinement.

The equiaxed grain structure in the MC-DC cast billet takes approximately 150 mm after shearing has begun and reached 4500 rpm before it dominates the columnar grain structure. This suggests that there is a considerable delay between the steady state running of the shear device and the emergence of the equiaxed grain structure. Jackson et al state that for an equiaxed zone to develop, crystals have to form, travel to the centre of the ingot and survive. In order for the crystals to survive the central region of the casting must be undercooled. In the static mould experiments, the closeness of the tool to the solid front and the resulting intensity resulted in fracturing at the initial stage, hence the definite zone boundaries. After this initial “shock” of the shearing action, dispersion of oxide films/particles and thus significantly increased number density of the oxide particles by intensive shearing would have been the mechanism that generated the nucleating particles, especially in zone 3. Therefore, the forced convective flows will have swept across the entire front with the same intensity in the static mould. In the DC casting billet, the strengths of the flows would have varied across the sump (e.g., Figures 4.2). The most intense would be at the point where the downward flows contact the sump and the core of the billet.

Whilst it is difficult to provide evidence of oxides nucleating α-Al phase during MC-DC casting, previous investigations provide evidence to suggest that naturally occurring oxides present in aluminium alloys act as highly potent sites for nucleation. Interesting conclusions on the potency of some oxides as nucleating sites of α-Al can be drawn from the results shown in Table. Here the crystal lattice disregistry is calculated not between the crystallographic planes but between the interatomic distances in the most close-packed directions, with the data extrapolated to 660°C using the thermal expansion coefficient (Wang, Li, Fan, 2012). In practice, activation of oxides as nucleation sites during solidification is enhanced by action upon the melt such as in MC-DC or ultrasonic cavitation (Gradfield, Eskin, Bainbridge, 2013).

The potency of oxides as nucleation sites has been evidenced in previous investigations (Li, Wang, Fan, 2012) (Li, Xia, Jarry, Scamans, Fan, 2011) as well as experimentally using ultrasonic cavitation aided grain refinement of pure aluminium containing oxide particles (Atamanenko, Eskin, Zhang, Katgerman, 2012). Whilst

nucleation potency may be fixed for a given nucleating system, the efficiency can be increased through modification of the nucleating particles and/or solidification conditions. With intensive melt shearing, oxides are dispersed as individual particles uniformly distributed throughout the melt. In this study, intensive melt shearing works to break-down and disperse oxide films, facilitating activation of fine oxide particles as nucleation sites for α-Al. In the meantime, the number density of the fine oxide particles is increased significantly due to the breakaway of oxide films into dispersed particles. In a previous study, the mechanisms of grain refinement by intensive melt shearing were investigated through a combination modeling and experimentation (Men, Jiang, Fan, 2010). Theoretical modelling using the free growth model revealed quantitatively that intensive melt shearing can effectively disperse oxide particles densely populated in the oxide films, into more individual particles in the melt. This increased the oxide particle density by three orders of magnitude and the density of active oxide particles by a factor of 20 compared with those of non-sheared melt. Therefore, the grain refining effect of intensive melt shearing was confidently attributed to the significant potency of naturally occurring oxide particles in the melt.

Table 5.1 Calculated lattice misfit between Al and substrates at 660°C. (Wang, Li, Fan 2012).

Interface of Al/S	Crystal structure & lattice parameters, nm	OR: (hkl)[uvw]Al//(h'k'l')[u'v'w']S	d[uvw]Al, nm	d [u' v'w']S, nm	Disregistry, f (%)
Al/MgAl2O4	Al: fcc, a = 0.41212, S: fcc, a = 0.81263	(111)[110]//(111)[110]	2x0.29141	0.57462	1.41
Al/□-Al2O3	Al: fcc, a = 0.41212, S: Rhomb. a = 0.47823; c = 1.30575	(100)[001]//(0001)[10-10]	2x 0.41212	0.82818	-0.48
Al/□-Al2O3	Al:fcc, a = 0.41212, S: fcc, a = 0.79634	(111)[110]//(111)[110]	2 x0.29141	0.56310	3.38
A/MgO	-	(111)[110]//(111)[110]	0.29141	0.30036	3.07
Al/Al3Ti	Al: fcc a = 0.42112, S: Tetragonal, a = 0.3883, c = 0.8679	(111)[110]//(112)[20-1]	0.29141	0.29116	0.09
Al/TiB2	Al: fcc, a = 0.42112, S: hcp, a = 0.30372, c =	(111)[110]//(0001)[11-20]	0.29141	0.30372	-4.22

	0.32368				

In Figure 4.22b we can see that at the structure has refined somewhat from the original structure in Figure 4.22a. The columnar grains have become finer and more numerous whilst along the centerline, coarser grains that could arguably be the beginning of the equiaxed grain structure. Regarding the flow patterns mentioned above and the structures that formed at this stage of the billet, there is the surface region, the steeply angled columnar zone, the mixed coarse and columnar grained region either side of the centerline and the centerline itself. The surface region can be considered as independent of shearing to some degree at this stage. Equiaxed grains form as the shell, followed by a short columnar grain zone that developed along the temperature gradients towards the centre as described in classic solidification theory. These columnar grains sharply angle upwards at approximately 10 mm from the surface. The reason for this sharp change in angle is most probably down to the grains growing towards the hotter melt flows. Turchin et al found that increased flow changed the initial angle of growth in columnar dendrites as they grew away from the chill faces. Grain morphology and flow rates were also found to affect grain orientation, with an increase in the flow producing an increase in the deflection angle.

Although a change in the angle of growth within the same region is evident in Figure 22a before shearing begins, it could be argued that the change is consistently more severe at the surface region of Figure 4.22b. The grains of the coarse second stage columnar region certainly formed at a steeper angle than before melt conditioning began. It is accepted that columnar growth occurs in the direction of thermal gradients. The exaggerated angle of growth here would suggest that the forced flows amplified the gradients at this point, as hotter melt is pushed downward towards the cooler solid front. The dendritic columnar grains grew upwards against the flow paths within the boundaries of the primary columnar zone at the surface and spiralling melt along the centreline.

It has been seen from previous experiments using the shear device in water, that a vortex is created directly under the shear device. This vortex spins the melt as it draws it into the tool from the base. It then passes through the tool, exiting via the holes as jets into the melt. The sucking force of this vortex is high and drives the melt

across the interface. This helps extract fragments that become trapped in the forming solid as well as those that remelt due to growth fluctuations. Solute content here could potentially be higher facilitating the remelting of grains further, resulting in the fragmented structure that developed.

It comes as no surprise then, when the equiaxed grain structure materialises in the central region of the billet, as shown in Figure 4.22c. The constitutional factor in the core will be increasing due to the drawing of solute into the area whilst the temperature is held at approximately the liquidus temperature of the melt. Thus the growth restricting factor increased at the core of the billet, eventually facilitating the equiaxed zone sufficient to block the columnar growth. As melt conditioning and solidification continued, the size of the equiaxed region increased with the number of grains as more and more fragments are carried to this area. It is clear however that there was a delay before the equiaxed structure becomes fully dominant. Once it had formed at the core, it progressed under the shear device restricting all other growth. It can be argued that at the point where the equiaxed structure dominates at the centre of the sump, that domination permeates from this point to the surface along the sump profile. But in the areas where the columnar growth is near vertical, approximately 20 mm from the surface, these grains still dominate as they succeed in the growth competition.

Within the 20 mm of billet between the shell and columnar region, the structure is coarse equiaxed and pseudo-columnar. The flow streams do not yet deposit enough grain fragments in this area and the constitutional zone is still developing at this stage. Cellular growth is occurring in the surface region as a result of the thermal gradients reducing during melt conditioning and the increasing number of nuclei that settle in this region. Grain fragments can be seen within the columnar grain structures between the surface and the billet core. These fragments were not able to be extracted from between the columnar front and became trapped. As the front continues to grow however, the fragments that occur enter the equiaxed zone as the columnar grains come into contact with the interface. These fragments contribute to the eventual dominance of the equiaxed zone across the solidification front as a whole.

A reason for the lack of extraction and the continued columnar growth are eddies that formed between flow streams at this specific point. Figure 4.2a shows the flow patterns and the eddies that relate to this position along the radius. They are voids within the forced flow streams where the melt is isolated from the flows. Thermal gradients may still be relevant within these voids and the grains that formed are angled steeply upwards away from the chill face into the hotter liquid above. The jets of flow out of the shear device drive melt to the edge of the mould where it contacts the slope walls at the exit of the thimble. This drives the flows downwards, then pulled across towards the core by the spinning vortex under the device. The eddies are generated as a result of this, a void encircled by the downward streams and central vortex of the shear device. At the point where the flow streams curve and head towards the core, fragments that are being transported in these streams will deposit here. They then grow with the thermal gradient into coarse or pseudo-columnar grains. The melt temperature of the eddies is probably higher than the melt around them and the flow streams, causing the thermal gradients that the coarse dendrites grow along.

At 4500 rpm the eddies described above are larger than at 6400 rpm, noticeably when we compare the two SolidWork images in Figure 4.2. That is a consequence of the rotation speed increase which intensified the turbulence and flow streams, including the vortex under the device. This is crucial to the shortening of these eddies. The effect on the structure will be discussed later in the chapter, but it is sensible to mention it here when discussing the microstructural evolution of the MC-DC billet as the rotation speed increased during the experiment. These eddies are a crucial component in the structures that formed across the billet as will be shown later.

In zone 3 of the static mould, the grain structure achieved was fine and uniform equiaxed. An equiaxed structure similar to this was achieved in the MC-DC billets as shown in Figure 4.22d. The macrostructure in the image appears very uniform at a size comparable to that of the DC-GR. Figure 4.23a is a high magnification (50x) mosaic of the MC-DC-P2 billet radius microstructure from the uniform section treated at 4500 rpm. It shows that the microstructure actually contains a significant region of course grains, arguably half the radius. The coarse grains grew in the eddies between the flow streams from the jets and the spiraling vortex below the device.

There are two regions of coarse grains if it is examined; a column of coarse grains at an angle away from the vertical 20 mm from the surface; and the coarse pseudo-columnar grains that grew vertically at 40 mm from the surface until approximately 60 mm from the surface. The first column formed in the eddies of the flow streams and is repeated in each of the MC-DC billets in similar forms, including the MC-DC-GR-P2 billet.

The angled coarse grain columns (CGC) grew towards the flows as described above. The coarse grains that followed grew vertically when they settled at the interface, specifically the solid where they were cooled and grew along the thermal gradient towards the liquid. What must be mentioned at this point is that not all nucleant particles (in this case crystal fragments) will be the same size across the billet. This is simply not the case. Crystals (floating) and crystal fragments will be transported in the melt flows, arriving at the solid front to take their place in the forming layer from different heights and at different speeds. Larger grains “fall” to the solid front having had time to grow and therefore dominate growth. Those that originate near their settlement point or did not have the same amount of time to grow as the “fallen” grains, will be smaller and much more susceptible to columnar growth. They also travel at slower speeds to the larger crystals so either form a layer on top of the coarse grains or a section of the newly forming layer themselves. Both of these scenarios are seen in the MC-DC material and will be discussed further on in the chapter.

Larger crystals or grain fragments settled in this region of the billet in the semi-solid region of the sump below the high intensity field of the central vortex. Here they will have grown vertically upwards becoming more dendritic as they did so due to the undercooling of the liquid bulk within the mould by melt conditioning. The temperature profiles presented in section 4.1.3 show that the temperatures around the shear device did reduce dramatically to around the liquidus temperature of the alloys. We do not know however, what the spread of the temperature was across the billet towards the surface. We assume that the temperatures are undercooled to the same degree but further investigation into this aspect of the process is required.

There is however data relating to the growth rates across the billet radius in the form of the P* analysis values. Measurements for the P* values were comprehensively

taken across the billet radius and plotted as shown in Figures 4.32. At 4500 rpm the growth rates appear relatively uniform including those of the coarse grain regions. This region begins at 20 mm from the surface until approximately 60 mm. It has the lowest P* values and standard deviation compared with the remaining billet sections, indicating the highest growth rates and uniform structure. The standard deviation of the fine equiaxed zones were double those of the equiaxed coarse grains, with larger P* values, indicating a more random structure developed.

Either side of the coarse grain region a fine equiaxed microstructure developed. The anodized images of the grain structures in Figure 4.28 shows that dendritic grains dominate the grain morphology in the MC-DC-P2 billet sheared at 4500 rpm. It is not until the core of the billet at the centreline that globular rosettes appear within the dendritic structure. Growth rate is at its lowest in the centre and the standard deviation at its largest, showing the variation in grain morphology compared with the rest of this section of billet.

5.3 COLUMNAR TO EQUIAXED TRANSITION (CET) IN MC-DC CASTING

Intensive melt shearing in the sump leads to a uniform temperature and enhanced mass transport. Temperature measurement during steady DC casting with intensive melt shearing has confirmed that the melt temperature in the sump is a few K below/above the alloy liquidus (Zuo, Jiang, & Fan, 2011). The temperature measurement in the current study also confirmed the uniform temperature in the sump. This is also reflected by the fact that the sump had a flatter bottom and a much reduced sump depth.

The respective roles of thermal gradient and nuclei density on the columnar to equiaxed transition (CET) have been well established since Hunt's pioneering work published in 1984 (Hunt, 1984). The role of a grain refining additive/nucleating particle is, in essence, to promote the CET (McCartney, 1989). At higher thermal gradients, a higher nuclei density is necessary in order to obtain the CET. So in consideration of the significantly increased number density of oxide particles with high nucleation potency for the α-Al phase in the investigated alloys (Li, Xia, Jarry, Scamans, & Fan, 2011) (Men, Jiang, & Fan, 2010), melt conditioning in the sump

during DC casting provides a unique condition for CET with low temperature gradient and high growth velocity (Hunt, 1984).

5.4 REFINEMENT OF GRAIN STRUCTURE AND INTERMETALLICS IN MC-DC CASTING

In DC casting process, to achieve high quality (less casting defects, such as hot tearing, cold cracking, etc.) and high productivity, chemical grain refiner additions are the standard practice in industry. Extensive efforts have been devoted to the investigations on grain refinement by either chemical inoculant additions or imposition of physical fields. However, very little information has been reported in the literature on the correlation between grain refinement, which focuses on the refining of grain size, and the grain structural parameters, such as secondary dendritic arm spacings (SDAS), which is, in effect, more important for the distribution of intermetallic particles, which are formed in the late stages of solidification (Easton, Davidson, & StJohn, 2011). Both the grain size and the SDAS are affected by alloy composition and cooling rate through constitutional undercooling (CU) parameters. The major difference is that the grain size is affected by the constitutional conditions as solidification begins, whilst the SDAS is more affected by the CU generated by the liquid remaining near the end of solidification (Easton, Davidson, & StJohn, 2011).

In the present study, due to the different grain refining mechanisms compared to the usual chemical grain refiner additions, the grain structural development by melt conditioning is also different. On the one hand, in the case with chemical grain refiner additions, the grain structure is more or less similar to rosette grain structure, whilst it is more like fine equiaxed dendritic grains in the case of melt conditioned DC castings. On the other hand, quantitatively, one can see the significant refinement of SDAS by melt conditioning. Under conventional DC casting with grain refiner additions, due to coarse SDAS, with the formation of primary α-Al phase, solute elements would be rejected and concentrated on the grain boundaries of α-Al phase rather than being well distributed on either interdendritic regions or grain boundaries, which is the case of MC-DC with finer SDAS. The latter enables more evenly distribution of the solute elements. Theoretically, the fine dendritic grain structure provides more sites for intermetallic particles to form whist the rosette grain provides less. According to the solidification sequence, Fe-bearing intermetallics formed in the late stage after the formation of the α-Al phase. As a result, in MC-DC casting, Fe-bearing intermetallics formed either along grain boundaries or interdendritic regions inside grains, which

means more evenly distribution of Fe-bearing intermetallics. This results in refined intermetallic particles. This is the reason why melt conditioned DC castings have refined and uniformly distributed intermetallic particles.

5.5 POTENTIAL TO REDUCE HOMOGENISATION TREATMENT DUE TO REFINED INTERMETALLICS

Dissolution of Mg_2Si and break-up and transformation of β- to α-Fe-bearing intermetallics (monoclinic β-Al_5FeSi into cubic α-$Al_{15}(FeMn)_3Si_2$) are the major objectives of homogenisation treatment, while the latter is the controlling factor to determine the homogenisation treatment parameters (temperature, time and cooling mode, etc.) due to the fact that Mg_2Si particles dissolve rather quickly during homogenisation. It was found that α-Fe-bearing intermetallics were nucleated on the top or the rim of the β-plate (Zajac, Hutchingson, Johanssons, & Gullman, 1994). It was observed that the interface between the β- and α-Fe-bearing intermetallics does not move. Hence there is no mass transport across the interface between the β- and α-Fe-bearing intermetallics. Since the α-Fe-bearing intermetallics grow by adsorption of Si, Mn and/or Fe, these elements must have been transported through the α-Al matrix (Zajac, Hutchingson, Johanssons, & Gullman, 1994). It has been concluded that the transformation from β- to α-Fe-bearing intermetallics kinetics is diffusion controlled (Zajac, Hutchingson, Johanssons, & Gullman, 1994). In the present study, alpha Fe-bearing intermetallic phase AlFeSi was found to be the dominant phase in the melt conditioned material. This facilitates a shortening of homogenisation treatment. In addition, the morphology and sizes of the intermetallics has an important effect on the transformation rate and therefore influences the homogenisation time as a whole. Thin β-plates will transform faster than the thick ones (Zajac, Hutchingson, Johanssons, & Gullman, 1994). In the current study, the refined and uniformly distributed Fe-bearing intermetallic particles offer the potential to reducing homogenisation process. In the MC-DC castings, α-Fe-bearing intermetallics dominated which is desirable to a reduced homogenisation processing.

5.6 ALLEVIATED MACROSEGREGATION IN MC-DC CASTING

As an irreversible defect, which is essentially unaffected by subsequent heat treatment, macrosegregation in DC casting has long been one of the hot topics. This surface to surface chemical non-uniformity is mainly due to the nature of DC casting in terms of the high thermal gradients and relative movement of liquid and solid phases during solidification in the sump. Negative segregation at the center of the billets develops as solute-depleted dendrites are affected along the interface of the rigid, mushy zone and settle near the centerline to form a uniformly packed region at the bottom of the sump.

It is well established that the driving force for relative movement of liquid and solid phases during solidification in the sump is mainly due to thermal-solute flow which is resulted from the large thermal gradient in the sump and density difference. In the current study, in MC-DC casting, when intensive melt shearing was applied, the sump had a flatter bottom and a much reduced sump depth. The melt temperature in the sump during the MC-DC process is uniform and just slightly below/above the alloy liquidus. This ensures uniform nucleation and growth of the equiaxed grains. It has also been established that solidification in the MC-DC casting process proceeds by sedimentation of rosettes/equiaxed dendrites which nucleate and predominately grow in the sump with an almost isothermal temperature under the severe convective melt flow (Xia, Prasada Rao, & Fan, 2013). It is therefore ruled out for the solute–depleted, free floating grains to settle and build-up near the centerline of the sump, which is the main reason accounting for the negative centreline macrosegregation.

It has also been pointed out that grain morphology is an important factor to be considered to understand the mechanisms of macrosegregation (Lesoult, et al., 2001) (Joly, Grun, Daloz, & Lesoult, 2000). Lesoult et al. reported that grain refining caused more severe centreline segregation in a DC cast Al-4.75wt%Mg-0.35wt%Mn alloy sheet ingot. In their case, it was more dendritic in non-grain-refined ingot with less severe segregation; whist the grain was more globular in the grain refined ingot, with more severe centreline segregation (Lesoult, et al., 2001) (Joly, Grun, Daloz, & Lesoult, 2000). In the present study, the P* value analysis shown in Figure 4.32 compares the difference in grain structures formed at different rotation speed of the high shear device. At 4500 rpm and P2 position, the grain structure developed as

mainly equiaxed dendrites; whist at 6400 rpm, it developed mainly as rosette. Quantitatively, the P* value at 4500 rpm was almost consistent across the section, ranging from 57 ± 5 µm to 68 ± 9 µm whist at 6400 rpm, it varied between 55 ± 3 µm and 81 ± 15 µm. This demonstrates that the uniformity of grain structure at 4500 rpm is much better than those formed at 6400 rpm. This high uniformity of grain structure at 4500 rpm, in addition to its equiaxed dendritic structures, explains the alleviated macrosegregation of the MC-DC cast billet sheared at this speed, as evidenced in the compositional analysis results across the billet section shown in Figure 4.8.

In contrast to the above observation, there is a study, which shows that grain refining results in positive centreline segregation (Finn, Chu, & Bennon, 1992) (Nadella, Eskin, Du, & Katgerman, 2008). Finn et al. showed that grain refining with Al5Ti0.2B produced positive centreline segregation in 530-mm billets of an Al-4,5% Cu alloy; whilst the non-grain-refined counterpart exhibited the usual pattern of negative centreline segregation. It was proposed that the high permeability in the mushy zone with the addition of grain refiners, allowed advection of solute-rich liquid toward the centreline, thus changed the centreline segregation pattern (Finn, Chu, & Bennon, 1992). Therefore, it remains open for the mechanisms of macrosegregation in terms of the effect of grain structure/morphology, size and permeability in the mushy zone on the mechanisms of macrosegregation.

In the current study, it has also been demonstrated that properly chosen melt conditioning parameters, such as shear position and shear speed, the surface quality of the MC-DC castings can be improved (Figure 4.26). In the present study, at 6400 rpm and P2 position or P3 position, the meniscus depths were the smallest, around 1000 µm (Table 4.1).

5.6 TOOL PERFOMRANCE DURING MC-DC CASTING

A fair and honest discussion about the performance of the shear device tooling and its performance over repeated experiments should be included at this point. Detailed explanations of the performance of the tool in terms of results when combined with DC casting has been given above, but nothing about the tool itself and its susceptibility to clogging or other failures.

The device used at BCAST in the lab scale DC experiments was the same tool that went on to be used at Oxford in the up-scale experiments. It should be stated here also that the shear device was shared between personal at BCAST on multiple studies. Whilst the performance of the shear device and how it was used by others cannot be written upon here, the reader could probably understand when one's own experience that not everyone may be as conscientious when it comes to equipment. Furthermore, the medium in which these devices are used is hostile to most materials, with other metals being dissolved within molten aluminium in short order whilst ceramics are susceptible to thermal shock and impact damage. The tolerances of the shear device are extremely tight to ensure proper operation so wear, clogging of the holes and freezing of metal within the stator and around the rotor are concerns. To claim that experiments always went smoothly would be hard to believe at the best of times but when operating a device with tight tolerances in liquid aluminium, another dimension is added.

Great care was taken so as not to introduce excessive thermal shock to the tool before and after it interacts with the melt. This prolongs the life of the tooling significantly. To reduce this shock, the rotor-stator assembly is heated slowly to the temperature of the melt before being inserted. This is a safety consideration as well as a way to protect the device and not reduce melt temperatures by inserting either a cold or damp tool. After operation, the device was wrapped in FibreFrax thermal blanket and allowed to cool down to room temperature slowly before cleaning in caustic solution. As much metal should be removed from the device when lifted from the melt to reduce cleaning time and potential for damage.

When operated incorrectly, the shear device can be fragile. It should only be run, i.e. the rotor should spin, when fully submerged in liquid, thus lubricating the shear surfaces as the rotor spins. "Dry" spinning of the rotor in the stator has been known to shatter a device.

Clogging of the stator holes and freezing of the melt to the stator is a constant threat, but was not experienced during casting at Oxford. At this point in the experiments, good practices with the device had been established as outlined above. A point to mention here is that before use, the rotor is spun by hand (heat resistance gloves worn) to ensure that it spins freely. It must be stressed that this was done by hand

and not using the motor! The rotor-stator assembly is kept hot between casts and excess material removed to keep the device from freezing up between drops. If this happened, then caustic is the preferred method of removing the aluminium build-up. Heating the shear device whilst frozen with aluminium results fracturing of the stator as the aluminium expands. In the lab experiments, clogging did occur due to freezing melts. When build up was large enough the rotor would not spin. On less than a handful of occasions whilst operating the device at Oxford in the 200mm mould, the device appeared to be operating normally only to stop during the cast. Explanation for this unplanned stoppage was oxide build up between stator and rotor, must likely plugging a hole or a number. This was sufficient to stop the tool, but was more of an issue with the motor being unpowered than the device. Indeed, when a more powerful motor was used, no un-planned stoppages such as described above occurred again.

Great care is required to operate the shear device continuously, casting drop to casting drop, but with careful consideration the lifetime of the tooling can be extended through a high number of casts. It has proved itself to be resilient in the face of harsh working environments and multiple operators. How this translates to industry would speculation at this point but at the end of this work, the same device and motor that was used at Oxford was used in the on the casting table to condition logs cast in a full production facility, at Sapa casthouse Belgium with no incidents to report. Although out of the scope of this report due to time it was nevertheless an encouraging beginning to the future planned for this study.

CHAPTER 6 - CONCLUSIONS

Based on the 6xxx series aluminum billet cast using the MC-DC system at the lab and industrial scale and the micro-structural analysis, chemical analysis and characterization of the constituent phases, the following conclusions were drawn;

1. Shearing Technology was successful in reducing the grain size across the billets without the aid of grain refinement. This was clear when the MC-DC material was compared with the un-grain-refined and un-conditioned material at a macro level. The technology was used in 85 mm lab scale casting and a 206 mm industrial scale unit with success.

2. The MC-DC process was shown to heal centerline cracks that propagate at the start of casting due to the omission of grain-refiner additions. Centreline cracks are a common un-reversible defect in castings that are typically un-healable during the cast, even when using grain refiner. Ti levels are maintained at 0.014 wt.% for this alloy to aid refinement and reduce cracking, with addition of TiB_2 in the form of rod, fed into the melt before the mould during casting. This creates plentiful nuclei within the melt for multiple grain growth events to occur and a fine crack free structure to form. The MC-DC process was able to replicate this effect without Ti and TiB_2 additions, by enhanced heterogeneous nucleation by dispersed oxide particles and grain fragmentation/multiplication. The achieved grain refinement and CET improves the permeability in the mushy zone of the sump and eliminates the shrinkage induced centerline cracking defects.

3. The temperature and solute fields within the sump and across the billet were homogenized by the MC-DC process. The melt temperature during casting was maintained at slightly above/below the liquidus temperature within the mould and hot-top, creating a

suitable temperature field for nuclei survival and equiaxed grain growth. Uniformity of the temperature happens rapidly after shearing begins, especially within close proximity of the shear device. Homogenisation of the solute was shown to occur after the surface zone of the billet and proceed to the centre at 4500 rpm and shear device position P2. At the maximum rotation speed of 6400 rpm, the inverse segregation increased at the surface region, but reduced below the material average composition from the mid radius of the billet to the centre.

4. Alpha Fe-bearing intermetallic phase AlFeSi was found to be the dominant phase in the melt conditioned material.

5. In the melt conditioned material, the intermetallic particles were found to be smaller than those in the material that was cast without shearing and with grain refiner.

6. Fine equiaxed dendritic structure is characteristic of the grain structures that form as a result of the MC-DC process. This is a benefit to industry as interdendritic liquid creates structures with well dispersed fine intermetallic particles within the body of the grains. At the grain boundaries, the particles are more fragmented and well distributed also, due to the increased size of the grains but the reduced final solidified liquid pools, evidenced by finer secondary dendritic arm spacings (SDAS).

7. Microsegregation reduction. Linescans showed that the solute is better distributed throughout the dendritic grains compared with the industrially more common cellular structures in grain refined DC casting billets. This creates a more uniform distribution of solute cross the individual grains thus helps to reduce macrosegregation by eliminating the occurrence of solute-deleted free floating grains.

8. Solidification in the MC-DC casting process proceeds by sedimentation of rosettes/equiaxed dendrites which nucleate and

predominately grow in the sump with an almost isothermal temperature under the severe convective melt flow. It therefore rules out that solute–depleted free floating grains settle and build up near the centerline of the sump, eliminating negative centreline macrosegregation.

9. In terms of the effect of grain structure/morphology on macrosegregation, in the present study, it demonstrated that slightly coarser equiaxed dendrites are better than the finer granular/rosette grains to achieve alleviated macrosegregation.

10. The MC-DC process did not disrupt the surface of the melt during casting when inserted into the melt, integrating with the DC casting process very well. Even at 6400 rpm, the rotation effects of the shear device were contained within the mould and hot-top, without causing a vortex from the surface down into the mould. This could have been a source of oxide inclusion and porosity if a vortex occurred. However, during operation, there was no indication of shearing taking place, with only the natural ebb and flow seen on a casting table. No evidence of increased porosity was found even at 6400 rpm.

FUTURE WORK

The MC-DC process has been established over the course of this work from pilot scale through to an industrial size billet. There is some real potential for this process and this work has sparked much interest in the technology. But, as is common with this type of investigation, a really good base has been laid but future work is needed to take it further.

1. Optimization of the process is required. MC-DC-P2 at 4500 rpm appears to be the closest to optimum in terms of overall quality. However, the structure still requires refining fully to become uniform. Further work is required to find an optimum tool depth and rotation speed for efficient refinement.
2. Further understanding of the mechanisms of formation of Fe-bearing intermetallic phases by MC-DC casting technology in combination with varying cooling rates. This was suggested by the different results obtained when the samples made at BCAST lab were analysed, where different DC casting parameters were employed from the ones used at Oxford. The related results are presented in the Appendix.
3. Extrusion trials of the MC-DC billet. This will add some much needed quantitative analysis to the quality of the billet but also whether certain structures do indeed require no homogenisation or a reduced amount when compared to a standard billet.
4. Mechanical testing of the extruded sections will complete the analysis into the viability of the MC-DC process.
5. Testing of the MC-DC process within an industrial facility under current DC casting practices to evaluate its acceptability to industry.

BIBLIOGRAPHY

Allen, C. M., Kumar, S., Carroll, L., O'Reilly, K. A., & Cama, H. (2001). *Mater. Sci. Eng. A*, 304, 604.

Arnberg, L., Ba¨ckerud, L., & Chai, G. (1996). . *Solidification characteristics of aluminum alloys. Dendrite coherency, vol.3. Des Plaines [IL].* American Foundrymen's Society.

Backerud, L., Gustafson, P., & Johnsson, M. (1991). *Aluminum*, 67, 910.

Brown, S. G., & Spittle, J. A. (1989). *Mater. Sci. Tech.*, 5, 362.

Campanella, T., Charbon, C., & Rappaz, M. (2004). *Met. Mater. Trans. A*, 35, 3201.

Chalmers, B. (1963). *J.Australian Inst. Met.*, pp. 8,255.

Chalmers, B. (1964). *Principles of Solidification.* John Wiley & Sons Inc.

Charles, V. (1989). *Metall. Trans. B*, 20,623-629.

Charles, V. (1989). *Metall. Trans. B*, 20, 631.

Charles, V. (1993). *Mater. Sci. Eng. A*, 173, 169.

Chu, M. G. (2002). In: Schneider W, editor. . *Light metals 2002* (pp. 899-907). Warrendale [PA]: TMS.

Cibula, A. (1949). *J.Inst.Met.*, pp. 76,321.

Cibula, A. (1951). *J.Int.Met.*, pp. 80,1.

Coangelo, V. J., & Heiser, F. A. (1987). *Analysis of Metallurgical Failures, second ed.* New York: John Wiley and Sons.

Crossley, F. A., & Mondolfo, L. F. (1951). *AIME Trans*, 191, 1143.

Das, A., Ji, S., & Fan, Z. (2002). *Acta Mater.*, pp. 50,4571.

Davies, I. G., Dennis, J. M., & Hellawell, A. (1970). *Metall Mater Trans B*, 1, 275.

Dinnis, C. M., Taylor, J. A., & Dahle, A. K. (2005). *Script Mater.*, 53, 955.

Doherty, R. D., Lee, H.-I., & Feest, E. A. (1984). *Mater. Sci. Eng.*, pp. 65,181.

Donnelly, S. E., Birtcher, R. C., Allen, C. W., Morrison, I., Furuya, K., Song, M., et al. (2002). *Science*, 296, 507.

Du, Q., & Li, Y. (2014). *Acta Meter.*, 71,380.

Du, Q., Eskin, D. G., & Katgerman, L. (2005). *Mater. Sci. Eng. A*, 413, 144.

Easton, M. A., & StJohn, D. H. (1999). *Metall Mater Trans A*, 30, 1613.

Easton, M. A., & StJohn, D. H. (2001). *Acta Mater*, 49, 1867.

Easton, M. A., & StJohn, D. H. (2005). *Metall Mater Trans A*, 36, 1911.

Easton, M., Davidson, C., & StJohn, D. (2011). *Mater. Trans.*, 52, 842.

Emley, E. F. (1976). Continuous casting of aluminium. *Int. Mater. Rev.*, 206, 75.

Eskin, D. G. (2008). *Physical Metallurgy of Direct Chill Casting of Aluminium Alloys.* CRC Press.

Eskin, D. G., Nadella, R., & Katgerman, L. (2008b). *Acta Mater.*, pp. 56,1358.

Eskin, D. G., Savran, V. I., & Katgerman, L. (2005). *Metall. Mater. Trans. A.*, 36, 1965.

Eskin, D. G., Zuidema Jr, J., Savran, V. I., & Katgerman, L. (2004). *Mat. Sci. & Eng. A*, 384, 232.

Eskin, G. I. (1994). *Ultrason. Sonochem*, 1, 59.

Fan, Z., & Liu, G. (2005). *Acta Mater.*, 53, 4345.

Fan, Z., Bevis, S. J., & Ji, S. (1999). *Patent No. WO 01/21343 A1.* PCT Patent,.

Fan, Z., Jiang, B., & Zuo, Y. (2012). *Patent No. WO2012035357 A1.*

Fan, Z., Liu, G., & Hitchcock, M. (2005). *Mater.Sci. Eng. A*, 413,229.

Fan, Z., Wang, Y., Xia, M., & Arumuganathar, S. (2009). *Acta Mater.*, 57, 4891.

Fan, Z., Wang, Y., Zhang, Y., Qin, T., Zhou, X. R., Thompson, G. E., et al. (2015). *Acta Mater.*, 84, 292.

Finn, T. L., Chu, M. G., & Bennon, W. D. (1992). In C. Beckermann, *Micro/Macro scale phenomena in solidification* (pp. 17-26). New York: ASME.

Flemings, M. C. (1974). *Solidification Processing.* McGraw-Hill, Inc.

Flemings, M. C. (1991). *Metall. Trans.A*, pp. 22, 957.

Flemings, M. C. (2000). *ISIJ International*, pp. 40,833.

Getselev, Z. N., Kvasov, F. I., Cherepok, G. V., Varga, I. I., & Martynov, G. I. (1983). In *Continuous casting in electromagnetic mould.* Moscow: Metallurgiya.

Grandfield, J. F., Eskin, D. G., & Bainbridge, I. F. (2013). *Direct-Chill Casting of Light Alloys Science and Technology.* Hoboken, New Jersey: John Wiley & Sons, Inc.

Grandfield, J., & McGlade, P. (1996). *Materials Forum*, 20, 29.

Greer, A. L. (2003). In B. Cantor, & K. O'Reilly, *Solidification and Casting* (pp. 199-214). Bristol and Philadelphia: Institute of Physics Publishing.

Hellwell, A., Liu, S., & Lu, S. Z. (1997). *JOM*, 18.

Henry, S., Gruen, G. U., & Rappaz, M. (2004). *Metall. Mater. Trans. A*, 35, 2495.

Henry, S., Jarry, P., & Rappaz, M. (1998). *Metall. Mater. Trans. A*, 29, 2807.

Henry, S., Minghetti, T., & Rappaz, M. (1998). *Acta. Mater.*, 46, 6431.

Hunt, J. D. (1984). *Mater. Sci. Eng. A*, 65, 75.

Jackson, K. A., Hunt, J. D., Uhlmann, D. R., & Seward III, T. P. (1966). *Trans. Met. Soci. AIME*, pp. 236,149.

Ji, S., & Fan, Z. (2002). *Metall. Mater. Trans. A*, pp. 33, 3519.

Johnsson, M. (1993). A critical survey of the grain refining mechanisms of Al. *PhD thesis*. Stockholm University.

Johnsson, M., Backrud, L., & Sigworth, G. K. (1993). *Metall. Trans. A*, 24, 481.

Joly, A., Grun, G. U., Daloz, D. C., & Lesoult, G. (2000). *Mater.Sci.Forum*, pp. 329, 111.

Jones, G. (1987). In: Beech J, Jones H, editors. *Solidification Processing* (p. 496). Sheffield: University of Sheffield.

Jones, G. P., & Pearson, J. (1976). *Metall. Mater. Trans. B*, 7,223.

Jones, S., Prasada Rao, A. K., & Fan, Z. (2013). *Trans. Indian Inst. Met.*, 66, 117.

Kral, M. V. (2005). *Materials Letters*, 59, 2271.

Kral, M. V., Nakashima, P. N., & Mitchell, D. R. (2006). *Metall. Mater. Trans. A*, 37, 1987.

Kuijpers, N. C., Kool, W. H., Koenis, P. T., Nilsen, K. E., Todd, I., & van der Zwaag, S. (2002). *Materials Characterization*, 49, 409.

Kumar, G. S., Murty, B. S., & Chakraborty, M. (2010). *J Mater Sci*, 45, 2921.

Lesoult, G., Albert, V., Appolaire, B., Combeau, H., Daloz, D., Joly, A., et al. (2001). *Sci. Tech. Adv. Mater.*, pp. 2, 285.

Li, H. T., Wang, Y., & Fan, Z. (2012). *Acta Mater.*, 60,1528.

Li, H. T., Xia, M., Jarry, P., Scamans, G. M., & Fan, Z. (2011). *J. Cryst. Growth*, 314, 285.

Liang, D., & Jones, H. (1992). *Z. Metallk.*, 83, 224-226.

Liu, P., Thorvaldsson, T., & Dunlop, G. L. (1986). *Mater. Sci. Technol.*, 2, 1009-1028.

Marcantonio, J. A., & Mondolfo, L. F. (1970). *J Inst Met*, 98, 23.

Marcantonio, J. A., & Mondolfo, L. F. (1971). *Metall Mater Trans B*, 2, 465.

Maxwell, I., & Hellawell, A. (1975). *Acta Metar.*, 23, 229.

McCartney, D. G. (1989). Grain refining of aluminium and its al'loys. *Int. Mat. Rev.*, 34, 247.

Men, H., & Fan, Z. (2011). *Acta Mater.*, 59, 2704.

Men, H., & Fan, Z. (2014). *Comp. Mater. Sci.*, 85, 1.

Men, H., Jiang, B., & Fan, Z. (2010). *Acta. Mat.*, 58, 6526.

Mo, A. (1993). *Int. J. Heat Transfer*, 36, 4335.

Mohanty, P. S., & Gruzleski, J. E. (1995). *Acta Mater.*, 43, 2001.

Mulazimoglu, M. H., Zaluska, A., Guzleski, J. E., & Paray, F. (1996). *Metall. Mater. Trans. A*, 27,929.

Mullis, A. M. (1999). *Acta Mater.*, pp. 47,1783.

Murty, B. S., Kori, S. A., & Chackraborty, M. (2002). *Int. Mater. Rev.*, pp. 47,3.

Nadella, R., Eskin, D. G., Du, Q., & Katgerman, L. (2008). *Prog. Mat. Sci.*, 53, 421.

Oh, S., Kauffmann, Y., Scheu, C., Kaplan, W. D., & Rühle, M. (2005). *Science*, 310, 661.

Paradies, C. J., Smith, R. N., & Glicksman, M. E. (1997). *Metall. Mater. Trans. A*, 28, 875.

Patel, J. B., Li, H. T., Xia, M., Jones, S., Kumar, S., O'Reilly, K., et al. (2014). pp. 794, 149.

Qian, M., Cao, P., Easton, M. A., McDonald, S. D., & StJohn, D. H. (2010). *Acta Mater.*, 58, 3262.

Quested, T. E. (2004). *Mater. Sci. Tech.*, pp. 20,1357.

Reddy, A. V., & Beckermann, C. (1995). *Materials Processing in the Computer Age II* (p. 89). Warrendale,PA,USA: TMS.

Schumacher, P., & Greer, A. L. (1994). *Mater Sci Eng A*, 181,1335.

Schumacher, P., Greer, A. L., Worth, J., Evans, P. V., Kearns, M. A., Fisher, P., et al. (1998). *Mater. Sci. Tech.*, 14, 394.

Sigworth, G. K. (1984). *Metall. Mater. Trans. A*, 15, 277.

Sigworth, G. K. (1996). *Scripta Mater.*, 34, 919.

Sigworth, G. K. (2008). In *ASM Handbook, Casting* (p. 255). OH: ASM, Metal Park.

StJohn, D. H., Qian, M., Easton, M. A., & Cao, P. (2011). *Acta Mater.*, 59, 4907.

Sweet, L., Zhu, S. M., Gao, S. X., Taylor, J. A., & Easton, M. A. (2011). *Metall. Mater. Trans. A*, 42, 1737.

Tang, M. O., Xu, J., Zhang, Z. F., & Bai, Y. L. (2010). *Transactions of Nonferrous Metals Society of China*, 20,1591-1596,.

Turchin, A. N., Zuijderuiyk, M., Pool, J., Eskin, D. G., & Katgerman, L. (2007). *Acta Mater.*, 55,3795.

Vader, M., Noordegraaf, J., & van Wiggen, P. C. (1991). Rooy, E L. *Light Metals* (pp. 1123–1130). Warrendale, PA: TMS.

Verma, A., Kumar, S., Grant, P. S., & O'Reilly, K. A. (2013). *Journal of Alloys and Compounds*, 555, 274.

Vogel, A., & Cantor, B. (1977). *J.Cryst.Growth*, pp. 37,309.

Vreeman, C. J., & Incropera, F. P. (2000). *Int. J. Heat Mass Transf.*, pp. 43,687.

Vreeman, C. J., Krane, M. J., & Incropera, F. P. (2000). *Int. J. Heat Mass Transf.*, pp. 43,677.

Vreeman, C. J., Schloz, J. D., & Krane, M. J. (2002). *J. Heat Transfer*, 124, 947.

Wagner, R., & Kampmann, R. (1991). Homogeneous second phase precipitation. In R. W. Cahn, *Materials science and technology: a comprehensive treatment.* Weinheim: John Wiley.

Wang, C. Y., & Beckermann, C. (1994). *Metall. Mater. Trans. A*, 25, 1081.

Wang, Y., Fan, Z., Zhou, X., & Thompson, G. E. (2011). *Philosophical Magazine Letters*, pp. 91, 516-529.

Winegard, W. C., & Chalmers, B. (1954). *Trans. ASM*, pp. 46,1214.

Xia, M., Prasada Rao, A. K., & Fan, Z. (2013). *Mater. Sci. Forum*, 765, 291.

Yu, H., & Granger, D. A. (1986). *Aluminium Alloys-Their Physical and Mechanical Properties* (pp. 17-29). United Kingdom: EMAS.

Zajac, S., Hutchingson, B., Johanssons, A., & Gullman, L. O. (1994). *Mater. Sci. Techn.*, 10, 323.

Zaloznik, M., Kumar, A., Combeau, H., Bedel, M., Jarry, P., & Waz, E. (2011). *Advanced Engineering Materials*, pp. 13,570.

Zhang, B., Cui, J., & Lu, G. (2003). *Mater. Sci. Eng. A*, 355, 325.

Zhang, L., Eskin, D. G., & Katgerman, L. (2011). *J. Mater. Sci.*, 46, 5252.

Zhang, Z. Q., Le, Q. C., & Cui, J. Z. (2010). *Trans. Nonferrous Met. Soc. China*, s376−s381.

Zuo, Y., Jiang, B., & Fan, Z. (2011). *IOP Conf. Series: Mat. Sci. Eng.*, pp. 27,012043.

Zuo, Y., Li, H., Xia, M., Jiang, B., Scamans, G. M., & Fan, Z. (2011). *Scripta Mater.*, 64, 209.

APPDENDIX 1 - INTERMETALLICS FORMED IN DC CASTINGS AT BCAST PILOT

The following section of the results deals with the material cast in the BCAST laboratory DC unit. This unit effectively up-scaled the static mould results in term of melt volume whilst changing the shape of the solidification front from planar to the characteristic sump of DC casting. The cooling effect of the water impingement also creates a different cooling profile across the billet compared to the static billet which was only cooled from the copper block and the heat extracted unidirectionally through the solidified melt at base.

4.4.2.1. BCAST DC – INTERMETALLIC MORPHOLOGY – NO SHEAR

Figure 4.4.11a-d shows the intermetallics present at the surface and central regions of the DC billet cast at BCAST laboratory. Figures 4.4.11a-b are images of the microstructure at the surface region at 100 x magnifications and 500 x magnification respectively. Figures 4.4.11c-d are arranged similarly but are images of the microstructure at the centre of the billet. All the images were obtained by LOM.

There is a clear change in the structure between the surface zone of the billet and the centre even though it was un-sheared and un-grain-refined. The microstructural variance is attributed then to the cooling effect of the mould and water impingement onto the surface without modification from other sources. In Figure 4.4.11a, needles of intermetallic can be seen at the boundaries with well distributed particles within the grain bulk. The needles of intermetallic are elongated along the boundaries of the angled grains. These particles would require refinement via homogenisation to achieve extrusion performance.

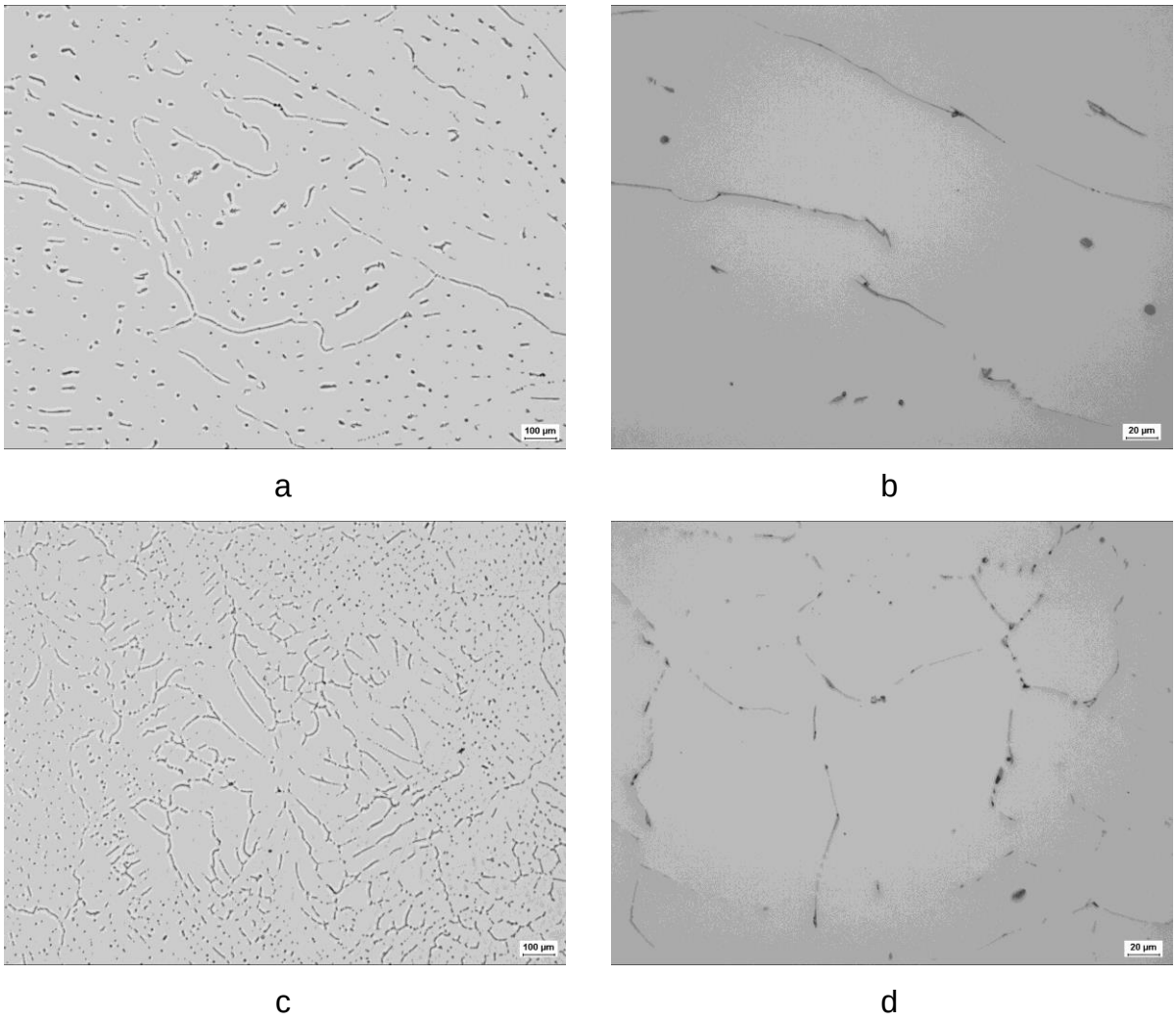

Figure 4.4.0-1 **As-cast microstructure of the lab scale cast without shearing or grain refiner. (a)Surface region at 100x magnification. (b) Surface region at 500x magnification. (c) central region at 100x magnification. Note the large floating grain present in the dendritic structure. (d) central region 500x magnification.**

Within the body of the grains, well distributed but large particles of mixed morphology precipitated out of the residual liquid. In figure 4.4.11b, the higher magnification shows clear examples of the intermetallics found in this region of the billet. Spherical particles can be seen as can needles or rods within the grain bulk, but encompassed by the long needles of intermetallic at the boundaries. These long particles have what appears to be Mg_2Si (black particles) attached to the phase which would have precipitated onto the AlFeSi phase during the final stages of solidification. These are low temperature melting sites and will require dissolving back into solid solution to avoid problems during extrusion.

At the centre, in Figure 4.4.11c, a floating crystal appears to be surrounded by a dendritic structure that is distinguishable by the distribution of particles throughout the bulk of the material, whereas the floating grain is devoid of particles within its bulk but each dendritic arm is enclosed by intermetallic rods. Images a and c are taken at the same magnification but the intermetallics in image c and thus the centre, are shorter at the boundaries and arguably finer within the body of the grains, especially away from the floating grain. In the higher magnification image of figure 11d, the particles are revealed to be a mix of needles and blocks with Mg_2Si particles distributed about the grey coloured AlFeSi phases. The intermetallic needles would most typically be considered beta Al_5FeSi phase with the thinner and lighter grey particles and needles being alpha Al_8Fe_2Si phase. The intermetallics are certainly shorter around the grain boundaries and as a result are broken up into short rods and blocks of particles encircling the grains.

The intermetallics at the surface appear more interconnected then those at the centre forming coarse alpha and beta intermetallic particles at the grain boundaries. P* analysis earlier found that the growth rate at the surface was lower than that of the centre, meaning that the grains in the centre had a finer dendritic structure than those at the surface. This has contributed to the finer inter-dendritic particles due to the reduced volume of liquid trapped in the space between the dendrite arms. Due to the rapid growth rates at the centre the intermetallics at the grain boundaries are smaller and less interconnected around the dendritic grains. However, particles at the boundaries of the large floating crystals are coarser and highly connected.

INCA feature measurement software was used again to quantify the particle size and evolution across the billet radius from the surface region to the centre, the results of which are displayed in Figure 4.4.12 as average particle length, area, width and shape factor. Overall the results support what has been described in the images; that the intermetallics refine towards the centre of the billet. Their average length and area decrease from peak size at the surface to centre, figures 12a and c respectively, a factor of the distribution of the particles around the coarse grain structure and inter-dendritic regions. Figure 4.4.12 also suggest that the morphology of the particles becomes more spherical at the centre which is most likely a result of the increased particle count within the inter-dendritic spaces that ensure small particles due to low volume of liquid trapped between the arms. The shape factor is determined by? The

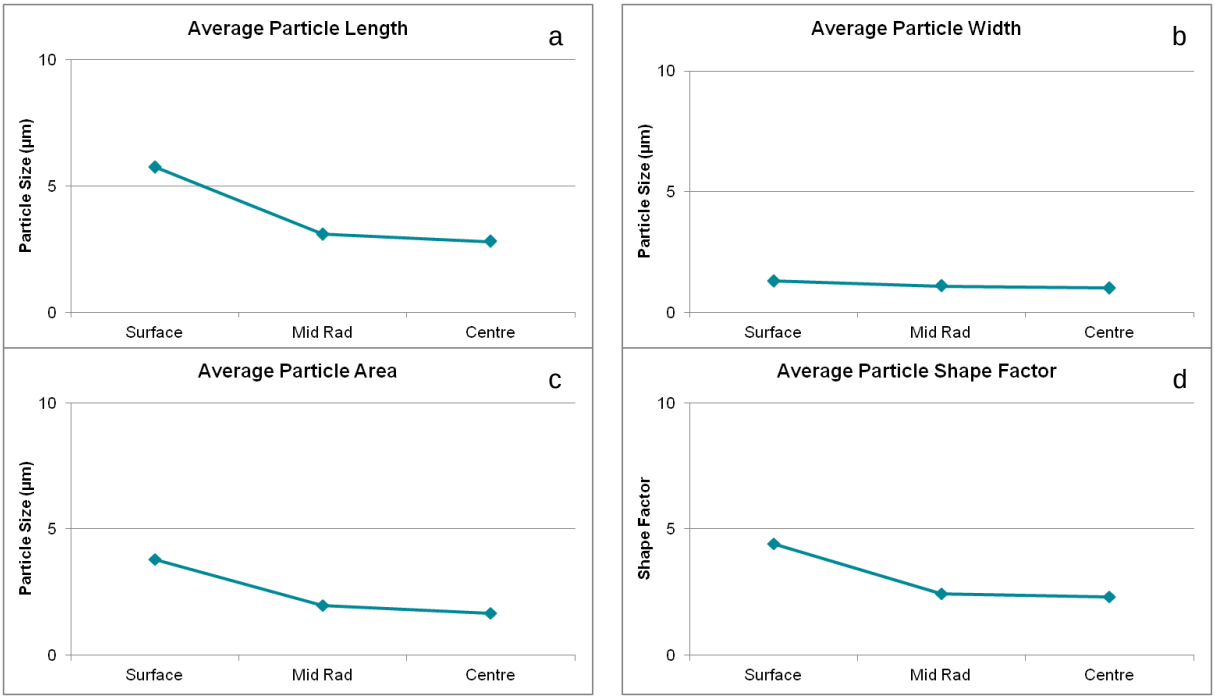

Figure 4.4.0-2 **INCAFeature produced results of particle measurements from un-sheared billet cast on the DC unit at BCAST. Particle length, width, area and shape factor are plotted showing that the particles refined towards the central region of the billet.**

average width of the particles did not change significantly across the billet as the particles did not become coarser developing plates of intermetallics from surface to central regions.

What is interesting about the results is that the mid radius point of the billet and the central regions do not differ significantly in average across each of the measured categories, suggesting that the surface region formed independently to the remaining billet. This will clearly be down to the surface having contact with the wall of the mould and the intensive cooling associated with this contact.

4.4.2.2 BCAST DC –EDX ANALYSIS OF INTERMETALLIC PARTICLES - NO SHEAR

Secondary electron images of the surface and billet centre microstructures have been obtained with EDX analysis used to determine the phases present. Some of

these phases have been identified in the images presented and the data used to identify if there was indeed a phase that was favoured above the others.

Figures 4.4.13a-b reveals the intermetallic particles at the surface region via SEM imaging. Image a shows the larger intermetallic particles at the grain boundaries are a mix of alpha and beta AlFeSi plates and needles, without a dominant phase immediately apparent. It can be argued that where the intermetallics are thicker and contain more segregated solute, the alpha phase forms. The α-phase plates at the boundaries and junctions are enriched with Fe above that of the β-phase having a stoichiometry of Al_8Fe_2Si to Al_5FeSi. However, it would be very difficult to differentiate between the two phases without the help of EDX analysis by morphology alone.

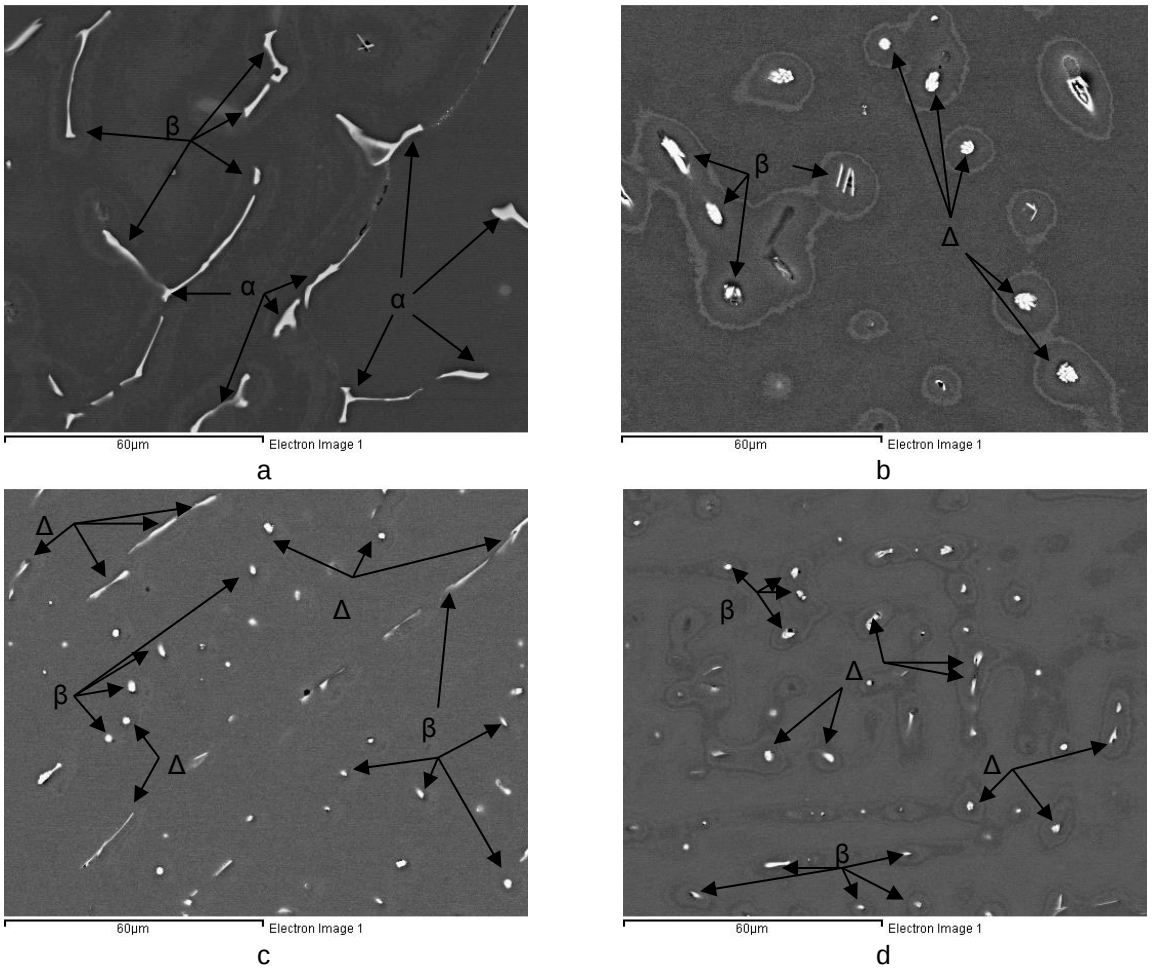

Figure 4.4.13 **Intermetallic particles from the surface (a-b) and central (c-d) region of the BCAST DC billet. This cast was un-sheared or grain refined. Phase identification by EDX analysis. Note some of the phases are identified in the images.**

Within the bulk of the grains at the surface, Figure 4.4.13b, the intermetallic particles are smaller with complex dendritic shapes developing rather than the elongated rods in figure a. These interdendritic particles were identified by EDX to most commonly be either delta or beta phase as indicated. Both β- and δ- AlFeSi are low Fe phases suggesting that in the surface region the segregating Si enriches the interdendritic particles with Fe segregating further to the boundaries driving the transformation to α-AlFeSi. Beta phase has a ratio of Fe and Si closer to 1:1 thus it can be a more readily forming phase that is thus easily transformed by post solidification thermal treatments.

The morphology of the phases in Figure 4.4.13b offer up some distinguishing features also. The beta phase it can be argued has a facetted morphology compared with the spherical nature of the delta phase. Examples of the complex dendritic particles or rosettes are shown in Figure 4.4.14a-d. Figure 4.4.14a shows a “Petal” -like particle, the body of which has beta phase stoichiometry but with excess Si at the periphery, identified by the black blocky particle under the “petal” of the beta rosette. The excess Si present here can give false readings if the sample area is small enough that it could be included in the sampling field. An example of this is given in Figure 4.4.14b. Here the particle consists of fragments of multiple phases held in a matrix of high Si. The dominant light grey bulk of the particle is measured as delta phase, but beneath the particle are darker grey and black areas that are high in Si. These darker grey and black areas may be included in the sampling array which increases the Si readings, thus the particles may in fact be beta phase intermetallics but the calculations determine them to be delta because the Fe/Si ratio is lower.

Figures 4.4.14c-d are further examples of the particle rosettes that formed, identified by EDX as delta phase. In Figure 4.4.14c, the rosette appears embedded within a facetted block of high Si whist the particle in figure d has a row of black Si particles ahead of the petals, appearing to in fact block the growth of the rosette. The bright white particles that can be seen around the particles are impurities such as lead that have entered the melt most probably through additions of hardeners during the alloying process.

Figure 4.4.15a shows the distribution of the particle stoichiometry measurements in relation to the Fe and Si levels against separators for the alpha-beta-delta phases at

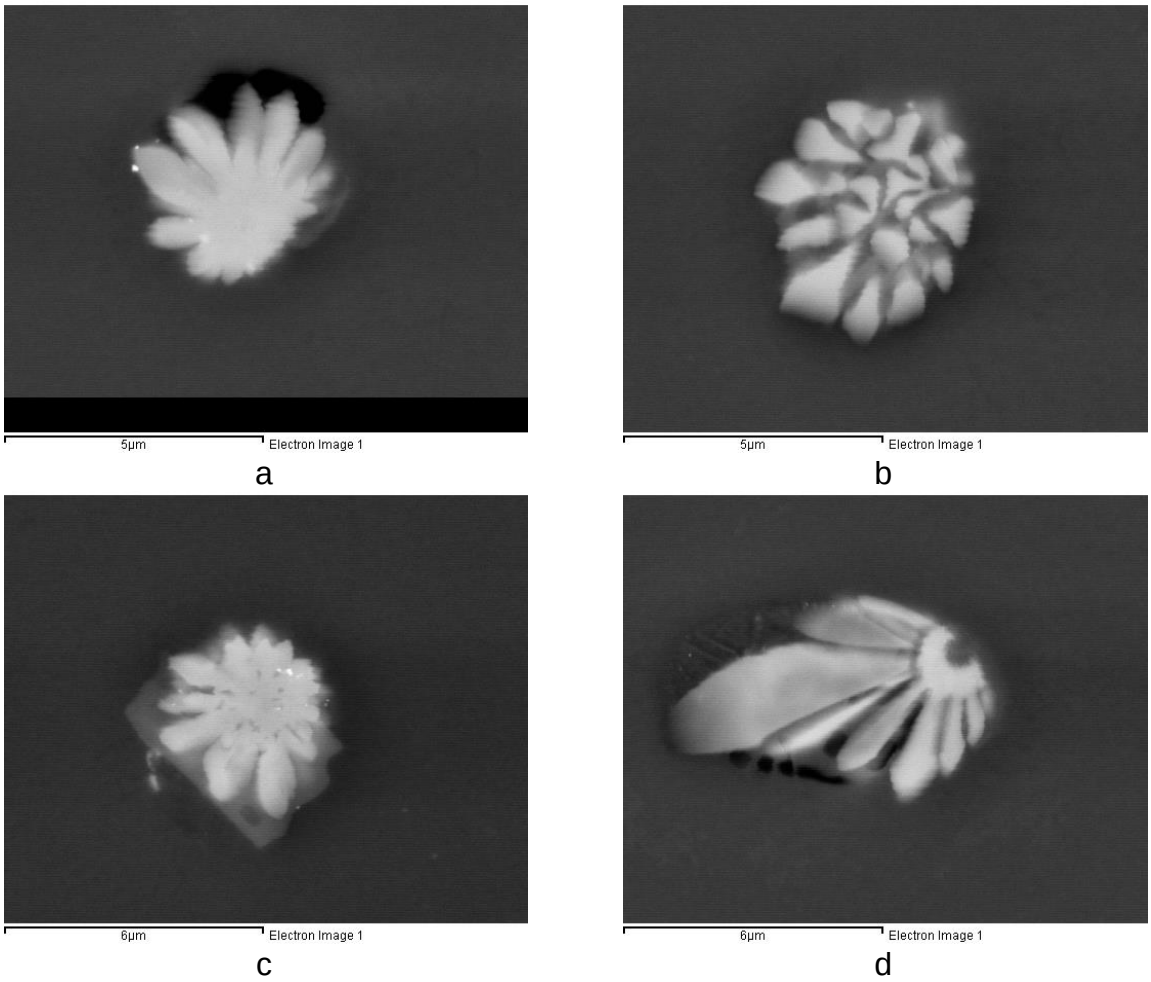

Figure 4.4.14 **Intermetallic particles that formed in the un-sheared billet cast on the pilot scale DC unit at BCAST.**

the surface region of the billet. To determine a single dominant phase within this region from the diagram is not straight forward due to the high variance in the spread. However, Figure 4.4.15b offers a value for the Fe to Si ratio as an average of the particles measured at the surface which falls between the ratios associated with the three phases considered. The average at the surface is 1.1 which suggests that the most common phase present at the surface region of the billet is the beta phase.

The SEM images taken from the central region of the billet, Figure 4.4.15c-d, show smaller particles of intermetallic formed at the boundaries and in the grain bulk than at the surface. The majority of these particles formed as beta phase especially in the bulk whilst the majority of boundaries particles are low Fe delta phase. That is not to say that these phases are specific to interdendritic particles or boundary particles; it is clear from the images that that is not the case. Determining the phases by

morphology is not possible from these images as the particle size and shape is very similar with rods of intermetallic at the boundaries and fine distributed particles in the bulk. Intermetallic plates and Chinese script are not present in large quantities in this region of the billet unless floating crystals are present. In-fact, the intermetallics here would require less time to homogenise before processing than at the surface and the structure in Figure 4.4.15c-d would not require treatment at all.

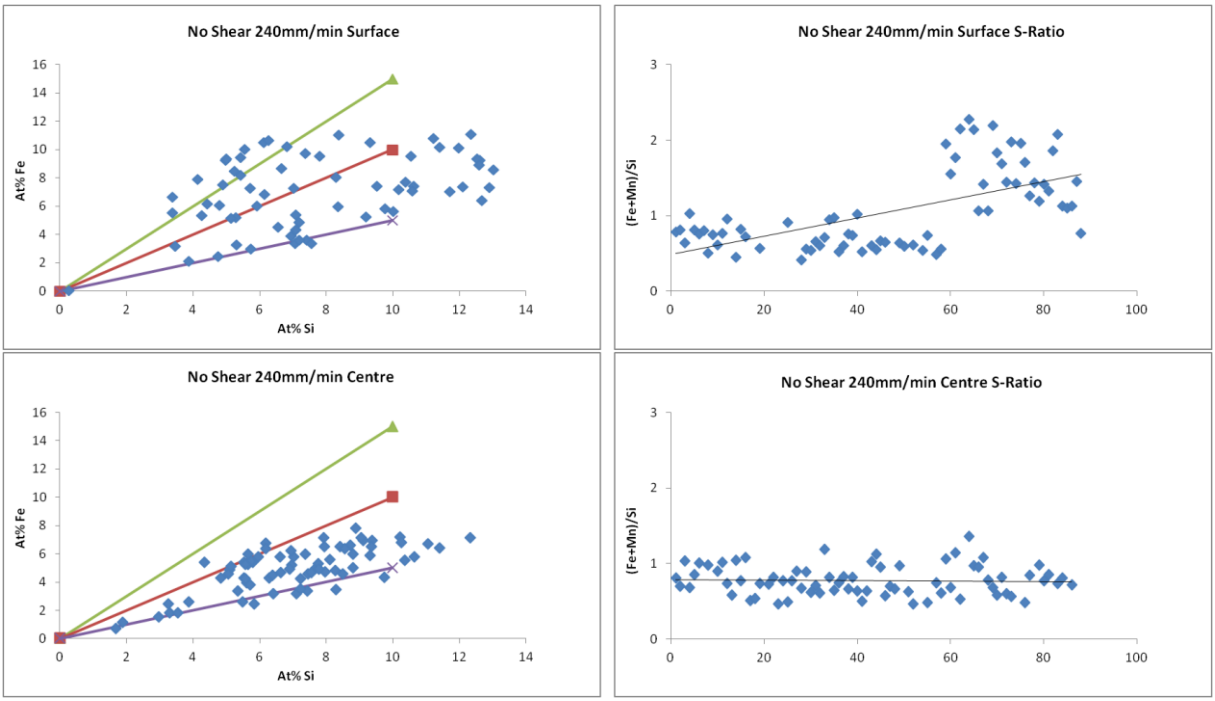

Figure 4.4.15 **(Fe+Mn)/Si ratio from the surface and central regions of the un-sheared BCAST lab scale DC billet plotted against separators for alpha-beta-delta AlFeSi phases and the accompanying Fe:Si-Ratio values. This material was not sheared and no grain refiner or titanium additions were made.**

At the centre, the diagrams in Figure 4.4.15c shows that the alpha phase is not common in the intermetallic particles measured here, to the point of being absent almost entirely leaving beta and delta AlFeSi to dominate. The majority of the data points fall between the beta and delta separators though it can be argued that there is a slight preference towards the beta phase. This is supported by the Fe to Si value of diagram Figure 4.4.15d, that shows the tight correlation of data points below a

value of 1. The average is 0.8 which does suggest that β-AlFeSi is the dominant phase but the value is very close to the 0.75 cut off between beta and delta, thus it might be more accurate to consider both beta and delta phase particles to be the common phases in this region.

There is a clear difference between the intermetallics that formed at the surface and the centre, both in morphology, size and phase dominance. Billets that have been produced using the same unit and processes will now be compared over the coming sections, however shearing has been applied and the effects of this conditioning will be analysed.

4.4.2.3 BCAST DC – INTERMETALLIC MORPHOLOGY – SHEARED AT THE EDGE OF THE GRAPHITE RING, CAST SPEED 220 MM/MIN

Figure 4.4.16a-b show the intermetallic structures at the surface of the billet at 100x magnification and 500 x magnifications, respectively. The structure is cellular in appearance with connected intermetallic needles around the grain boundaries that agglomerate at the grain junctions, forming what is known as “Chinese script” which is commonly associated with alpha phase intermetallics, shown clearly in Figure 4.4.16b.

At the centre of the billet, Figure 4.4.16c-d, the structure changes from a cellular structure at the surface to that of a semi-solid material; dendritic grains with particles inside the grain bulk and large floating crystals/ rosettes devoid of particles but with intermetallic at the boundaries. Figure 4.4.16d shows coarsening of intermetallic at the junctions where larger pockets of liquid become trapped between the grains and became enriched by the elements segregating out to the liquid during solidification. The Chinese script morphology appears to have disappeared within this region of the billet also.

Both regions of the billet have needles of intermetallic that Mg_2Si particles have precipitated onto, identified as the black specs on the grey AlFeSi intermetallics in Figure 4.416b-d. Needles or rods of intermetallic are commonly considered to be

beta phase when viewed under microscope, as are the plates that are present in the billet centre (Fig 4.4.16d).

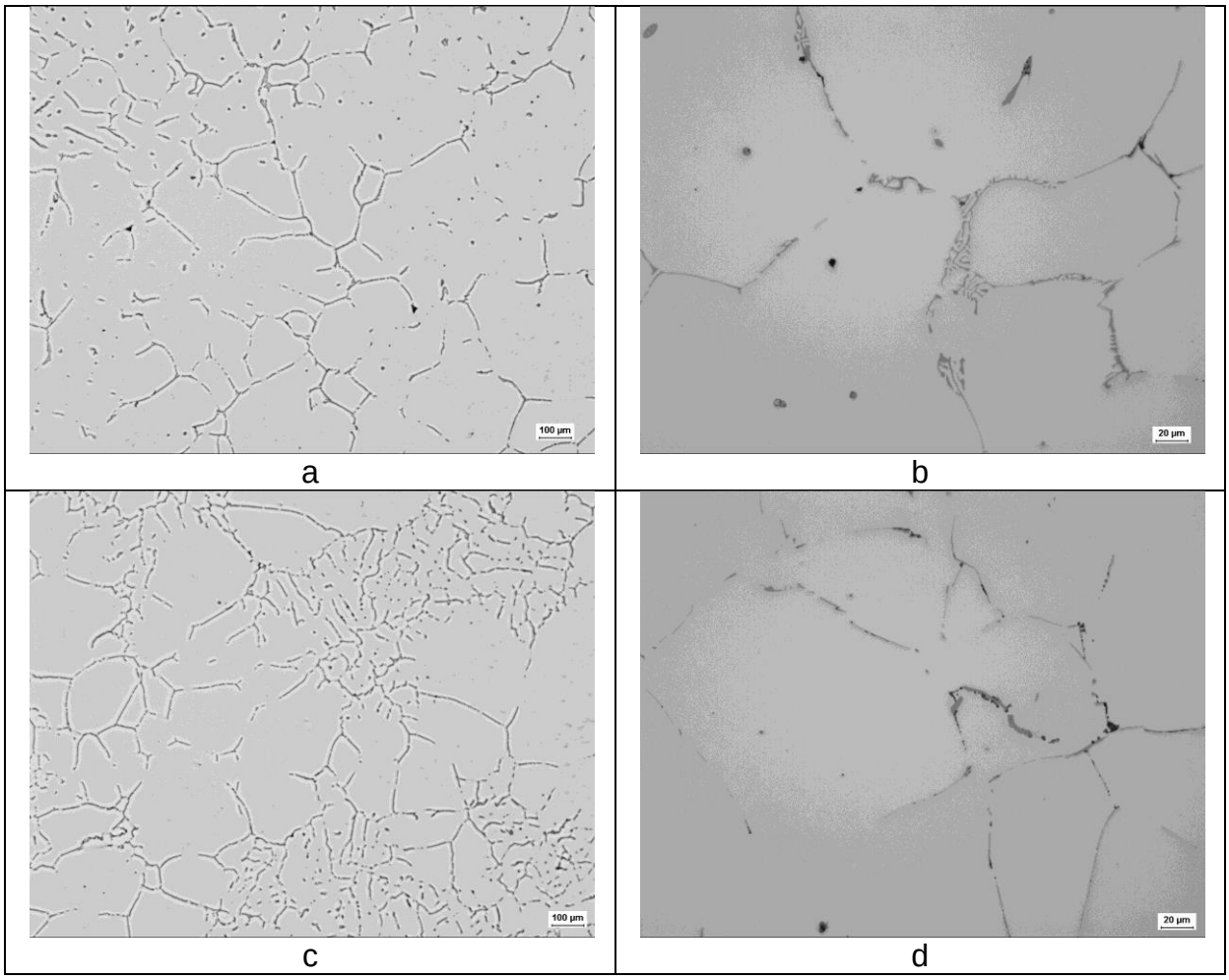

Figure 4.4.16 **As-cast microstructure of the lab scale cast with shearing. Shear unit was positioned at the edge of the graphite ring. Cast speed was 220 mm/min. (a) Surface region at 100x magnification. (b) Surface region at 500x magnification. (c) Central region at 100x magnification. (d) Central region 500x magnification.**

It is clear then just be analysis of the two structures under LOM that the intermetallics change over the radius of the billet from surface to centre. From the images it can be argued that the intermetallics are coarser at the surface due to the highly connected nature of the intermetallics and the Chinese script that is present. The cellular nature of the grains leads to this type of intermetallic structure so it not a surprise to see coarse structures mixed with well distributed and broken up strings of particles at the centre, where we see both cellular and dendritic structures. Indeed, the coarser

particles occur at the interface between the two types of grain structures as they form at different speeds and cooling rates.

Figure 4.4.17 presents the average particle lengths, width, area, and shape factor across the billet radius from the surface to the centre. The average particle length at the centre of the billet was found to be shorter than that of the surface, Figure 4.4.17a. This result is mirrored by the other categories measured; width, area and shape factor all show a reduction in values from the surface to the centre. The average area of the particles follows this trend which is not surprising considering the reduction in length, but obviously taking into consideration the higher number of smaller particles attributable to the “broken-up” nature of the particles at the centre, creates a much more considerable reduction in the value compared the average particle length. There is a large difference in the area of the particles (fig 18c) which is may be as a consequence of the measuring as the software distinguishes between grey particles and white of the matrix. If there are white pixels between the grey particles then just that particle area is measured, but where the Chinese script is concerned there could be occasions where the intermetallics are connected and as such, are measured as one particle resulting in a larger area.

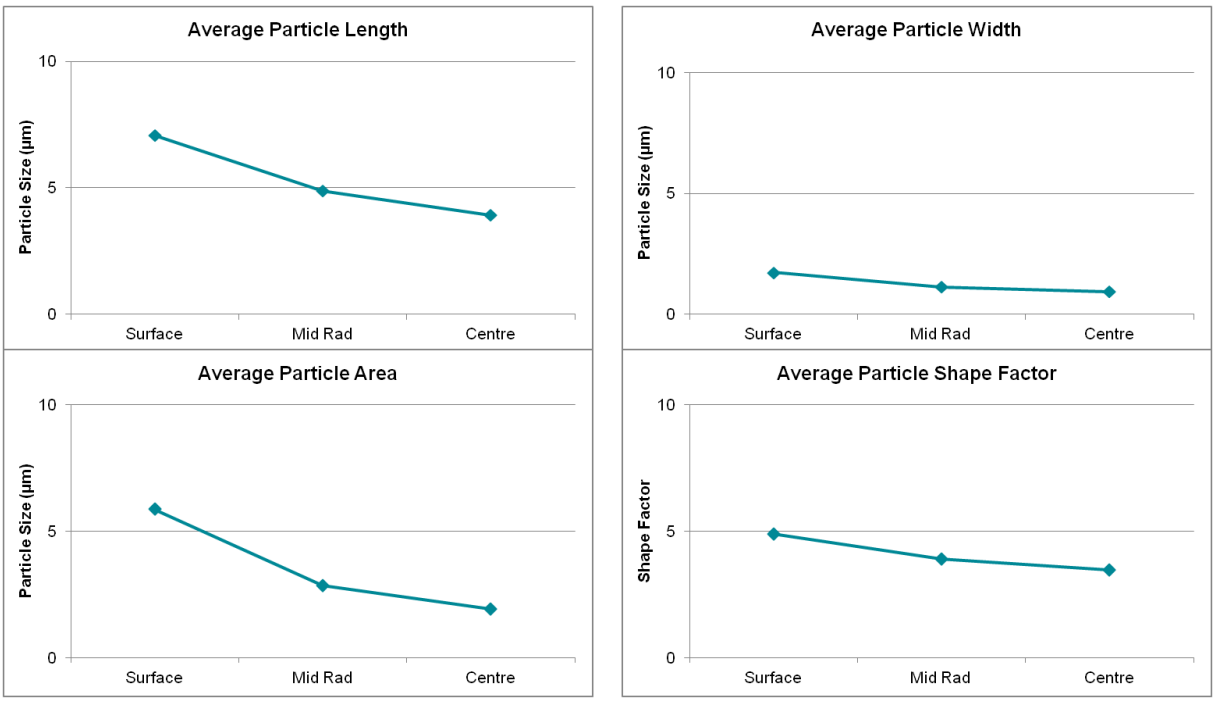

Figure 4.4.17 **INCA Feature produced results of particle measurements from sheared billet cast on the DC unit at BCAST. Shear unit was positioned at the edge of the graphite ring. Cast speed was 220 mm/min**

Interestingly, the average widths of the particles are very similar with almost nominal variation in the thickness form the surface through to the centre. This suggests that there is in fact little coarsening of the particles into large plates and certainly no significant increase across the billet.

In Figure 4.4.17d, the shape factor does decrease across the billet towards the centre from a value of 5 to 3 respectively. The particle morphology at the surface and the centre certainly does change in the images and the broken nature of the intermetallic rods at the grain boundaries at the centre helps reduce the shape factor value further. The shape factor is determined by equation 1, which takes into calculated by the perimeter and area of the particles. Certainly, comparing the two images, there is clear difference between the morphologies of the particles with the block type plates of intermetallic normally being associated with higher shape factor values. However, the widths of the particle from the surface to the centre are nearly uniform, if slightly smaller at the centre, so the shorter particles of the centre will have smaller perimeters as the needles around the boundaries are that much shorter and more broken up, resulting in lower shape factors thus may not reflect the true complexity of the particles between the two regions.

However, the central region of the billet has been sheared with a high intensity and the particles of the sheared region are arguably more refined at the grain boundaries and distributed through the bulk than those of the surface. At the junctions where the final solidifying liquid collected becoming enriched by the solute segregating form the grains, plates of β-AlFeSi developed in the centre compared with rounder Chinese script of the α-AlFeSi phase.

4.4.2.4 BCAST DC –EDX ANALYSIS OF INTERMETALLIC PARTICLES – SHEARED AT THE EDGE OF THE GRAPHITE RING, CAST SPEED 220 MM/MIN

Figure 4.4.18 shows the SEM images of the intermetallic particles from the surface and centre regions of the billet. Images a-b are from the surface region, images c-d the centre. It is clear that the dominate morphology of the particles are needles; long

thin particles with the longest particles found naturally at the grain boundaries. Figure 4.4.18b shows that spherodised particles are present as well with Chinese script and a nice example of rosette particle identified in the previous section. The spherodised particles are alpha phase as indicated whilst particles that have a more plate type morphology can be associated with beta phase constituents. The needle like particles which are longer and thinner than the plates, are predominantly delta phase.

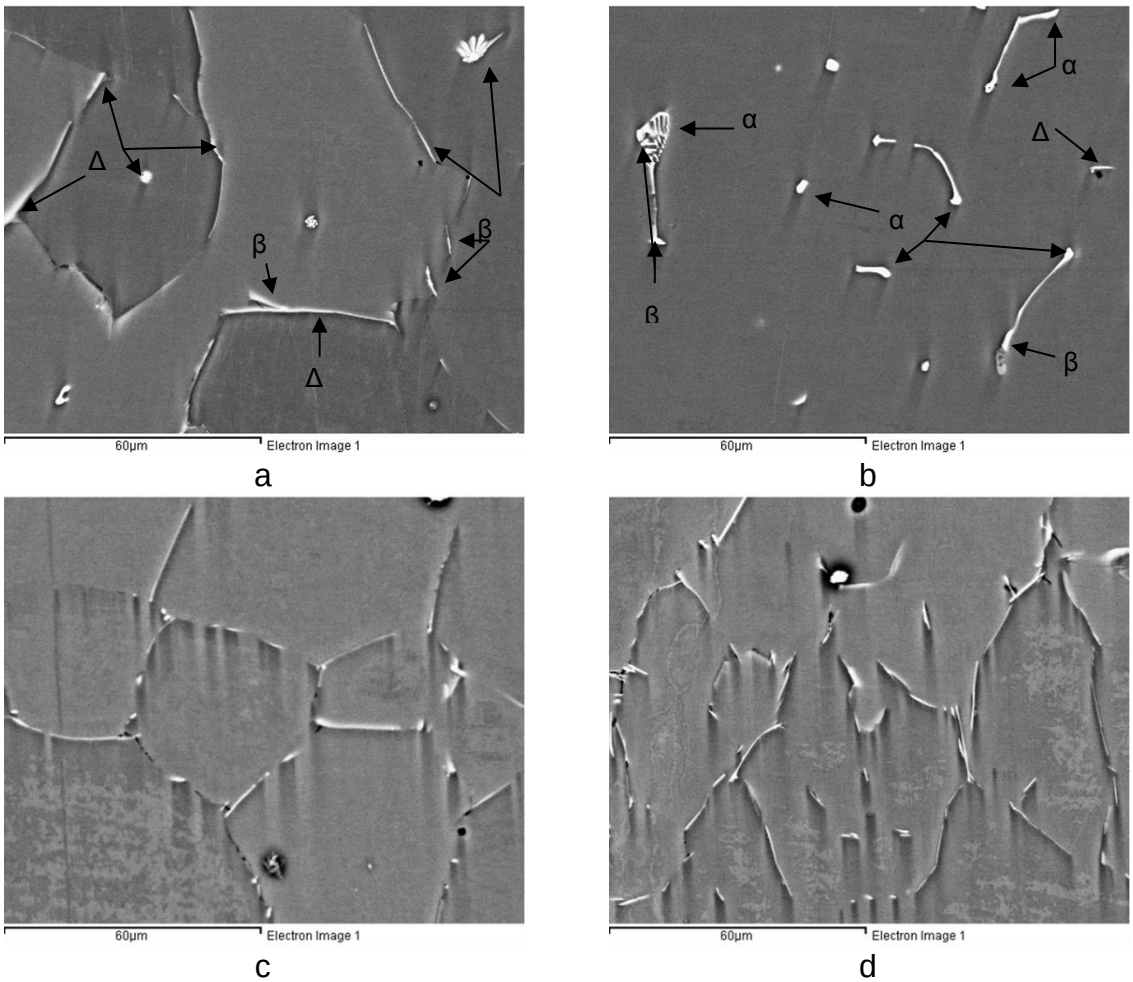

Figure 4.4.18 **Intermetallic particles from the surface (a-b) and central (c-d) region of the BCAST DC billet. This cast was sheared at the edge of the graphite ring Cast speed was 220 mm/min. Phase identification by EDX analysis. Note some of the phases are identified in the images.**

The surface region has a mixture of phases and particle morphologies compared to that of the centre which has predominantly needle based particle morphology. Both regions show boundaries separated by needles of intermetallics but these appear

shorter and more broken up in the central region, Figures 4.4.18c-d. There is noticeably fewer particles in the bulk of the cellular grains at the centre of the billet which are dominated by the alpha phase at the surface. A typical Chinese script particle developed as alpha-AlFeSi indicated in Figure 4.4.18b. These particles are formed in the inter dendritic spaces becoming enriched in Fe and Si with those having a higher Fe content forming α-AlFeSi and becoming more rounded in morphology. In contrast, lower Fe constituents formed δ-AlFeSi needles at the boundary of the grains with plates of intermetallic identified as β-AlFeSi forming as part of the network of intermetallics, connected with other phases or separate particles at the grain boundaries.

Figure 4.4.18c-d shows the intermetallics at the centre of the billet. The cellular grains in figure c are devoid of particles in their bulk but surrounded by particles at the boundaries. These particles are needles of delta phase interspersed with Mg_2Si eutectic on the particles or at the boundaries. The intermetallics are broken up and not inter connected even at the grain junctions and no particles of Chinese script morphology were found. Particles that could be described as plates were rare and the dominant phase is delta.

The same morphology of the particles continues in the dendritic regions of the microstructure, shown in Figure 4.4.18d. Here the bulk of the grains contain many needles of intermetallics that are divorced from each other whilst at the grain boundaries the intermetallics are broken up similar to the cellular grains, although at the grain junctions' plates of eutectic are present where the trapped liquid volume increases. Mg_2Si is also present here precipitated onto the needles of the δ-phase at the boundaries.

Figure 4.4.19a shows that there is a wide spread in the particles measured with the data points distributed between the alpha – beta – delta separators. There is clearly a mix of phases present at the surface of the billet so the ratio of Fe to Si is measured and displayed in Figure 4.4.19b. The average value determines the most common phase in this region of the billet and, the average value was 1.20 determining that β-AlFeSi is the dominant phase at the surface.

At the billet centre the low Fe delta phase intermetallic is undoubtedly dominant with the measured values distributed along the delta phase separator, clearly seen in

figure 19c. The Fe to Si-ratio displayed in figure 19d is low with the values below 1 with an average of 0.6 and a flat trend line suggesting that the Fe to Si ratio remained low and the delta phase was certainly the dominate intermetallic at the billet centre.

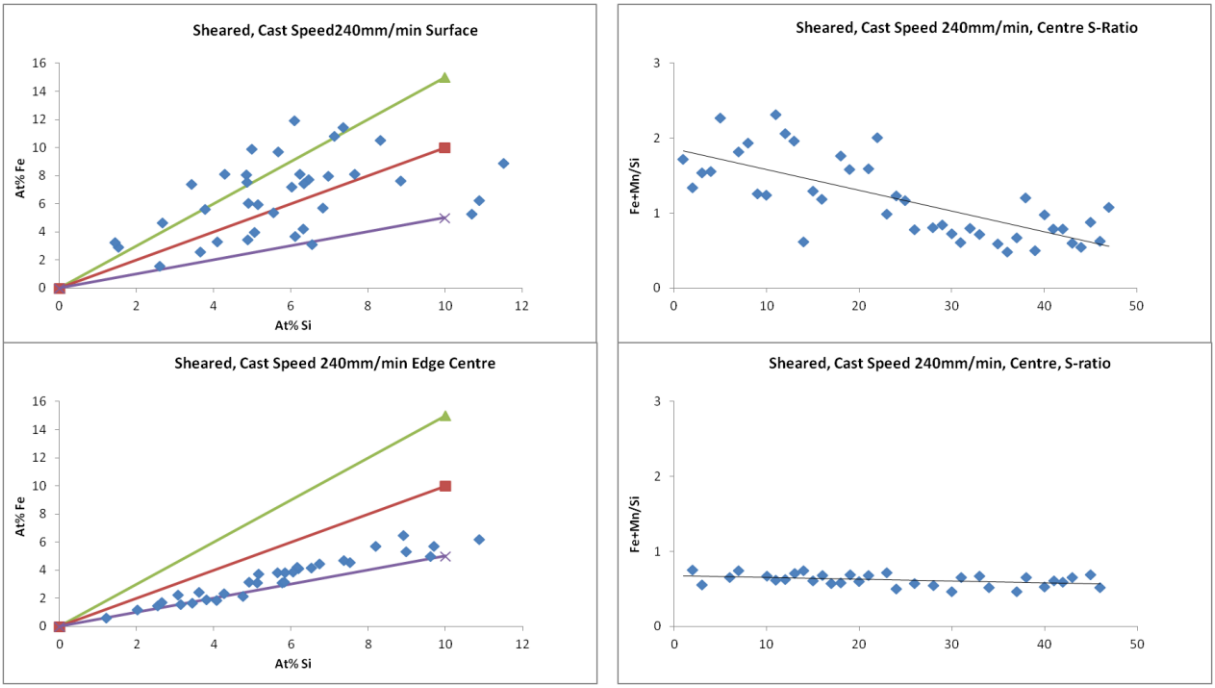

Figure 4.4.19 **(Fe+Mn)/Si ratio from the surface and central regions of sheared BCAST pilot scale DC billet plotted against separators for alpha-beta-delta AlFeSi phases and the accompanying Fe:Si-Ratio values. This material was sheared at the edge of the graphite ring and no grain refiner or titanium additions were made.**

4.4.2.5 BCAST DC – INTERMETALLIC MORPHOLOGY – SHEARED AT THE EDGE OF THE GRAPHITE RING, CAST SPEED 240 MM/MIN

A billet was produced on the BCAST lab facility with shearing applied with the device level to the edge of the graphite ring and the cast speed increased to 240 mm/min. The intention being to examine the effect that cast speed increase may have upon the influence of shearing when applied to an un-grain-refined melt, compared with a similar cast and conditioned billet but at a slower draw speed. The surface zone in the billet produced at BCAST is susceptible to prolonged contact with the mould wall due to the length of the graphite ring which extends over the lengths typically seen in industrial units. Thus increasing the casting speeds helps to overcome this influence

somewhat and the resulting structure should be different to that of the billets cast at slower speeds. Cast speed increase has been known to enhance macrosegregation across the billet, cooling rates at the billet core during casting and defects such as centreline cracking. The previous sections have examined these concerns, the following work sets to outline the intermetallic structures and phases.

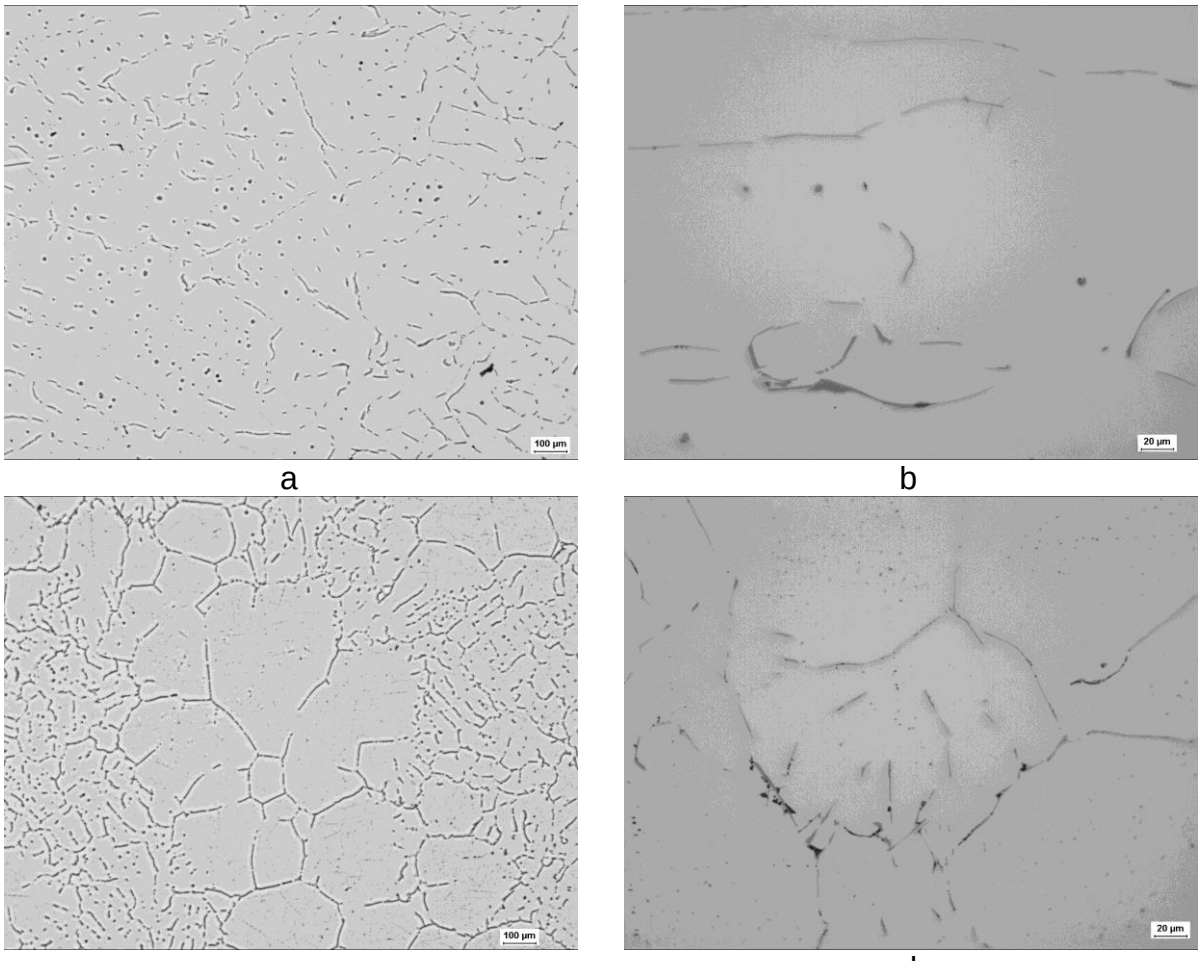

Figure 4.4.20 **As-cast microstructure of the lab scale cast with shearing. Shear unit was positioned at the edge of the graphite ring. Cast speed was 240 mm/min. (a) Surface region at 100x magnification. (b) Surface region at 500x magnification. (c) Central region at 100x magnification. Note that a mixed structure of rosettes and dendritic grains are present here (d) Central region 500x magnification.**

The intermetallics at the billet surface are shown in Figure 4.4.20a-b. Needles and plates of intermetallic can be seen at the boundaries with no Chinese script visible. The particles are well dispersed and plentiful with a good dispersion of particles within the grain bulk that appear spherical and fine. Figure 4.4.20b shows the

intermetallics at a higher magnification. Elongated rods of intermetallic at the boundaries are clearly visible with spherical particles in the bulk of the grains. At the junction of grains, larger coarse plates formed that are interconnected and require treatment before processing.

At the centre, the cellular and dendritic structures that have been seen previously are present as shown in Figure 4.4.20c. The cellular structures are devoid of particles with the solute elements segregating to the boundaries, whilst the dendritic areas have plates and needles at the boundaries and small well distributed particles in the bulk of the grain, although these have a needle like morphology. The particles are much more interconnected especially at the junctions where the different grain morphologies meet. There is also a noticeable increase in Mg_2Si that has precipitated onto the AlFeSi intermetallics at the billet centre, especially at the junctions where the cellular and dendritic morphologies meet and the solute concentration increases. Mg_2Si is present in the surface region of the billet but not to the extent of the core where it has had time to precipitate out and form as the finally solidified eutectic possibly due to the reduced solidification rate during shearing. The increase of Mg_2Si at the centre could be a result of the grain morphology. As the line-scans showed, the amount of segregation from the cellular grains is larger than that of the dendritic structures, resulting in enrichment at the boundaries of the cellular grains. This enrichment and the different growth rates of the grain structures allow coarsening of the particles.

Figure 4.4.21a-d shows that the average size and shape of the intermetallic particles is reasonably consistent across the billet. There is a slight reduction in particle length and area from the billet surface to the centre but then the grain size across the billet varies with the larger average size grains found at the centre, which could contribute to the reduction in particle lengths. The reduction is nominal and could also be considered equal to the error in measurement. The plates of AlFeSi phase present at the junctions of the grains in the surface region being the cause of the slightly raised average area size. It is interesting that the width of the particles does not vary over the billet, suggesting that there isn’t a coarsening of particles rather the intermetallics are very similar in nature.

This is supported by the flat line of the average shape factor in Figure 4.4.21d. The shape of the particles is consistent across the billet at an approximate value of 4. The

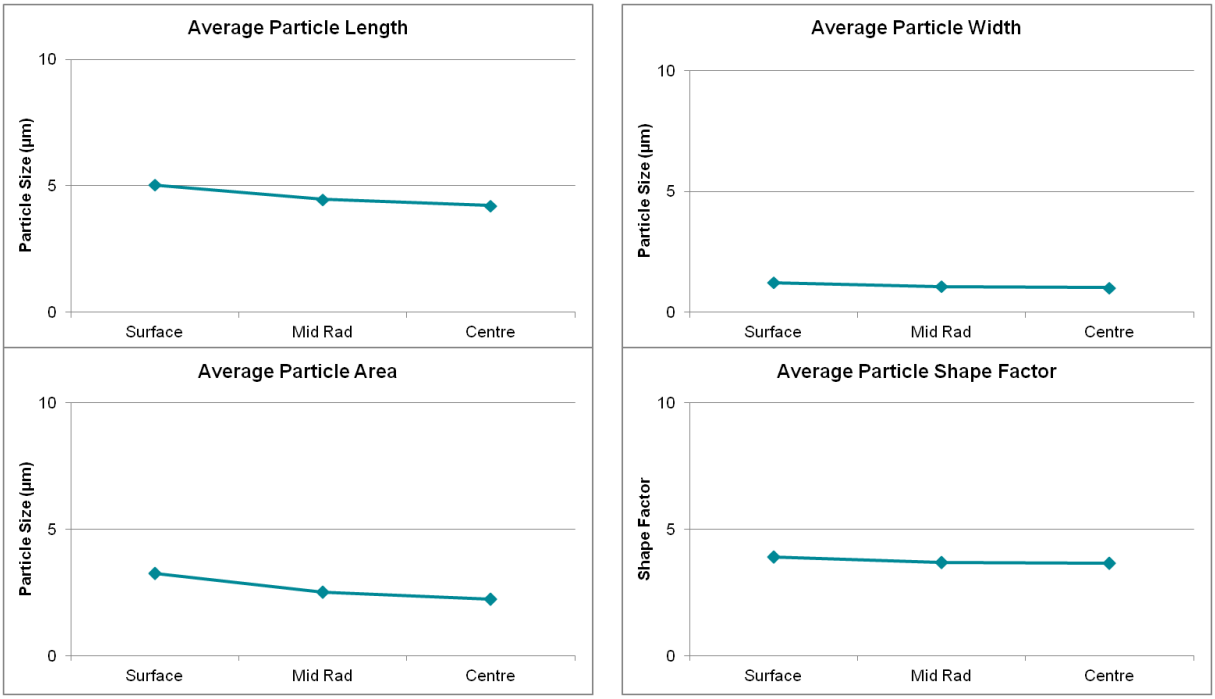

Figure 4.4.21 **INCAFeature produced results of particle measurements from sheared billet cast on the DC unit at BCAST. Shear unit was positioned at the edge of the graphite ring. Cast speed was 240 mm/min**

shape factor describes the particles as not spherical as that would require a value closer to unity, but they cannot be considered plates with a wholly block type morphology either as the value would be close to 10. The particles can be described as needles which is comparable to what is seen in Figure 4.4.20. This implies that shearing has influenced the billet microstructure and intermetallics throughout the billet cross-section including the surface zone.

4.4.2.6 BCAST DC –EDX ANALYSIS OF INTERMETALLIC PARTICLES – SHEARED AT THE EDGE OF THE GRAPHITE RING, CAST SPEED 240 MM/MIN

Figures 4.4.22a-d present SEM obtained images of the intermetallic structures at the surface and central regions of the billet. Phases that have been identified within the images by EDX analysis are shown in the images. At the surface, the intermetallics were identified predominantly as β- and δ- AlFeSi which is shown in Figure 4.4.22b.

The larger rods and coarser needles of intermetallic consist of the low Fe delta phase at the grain boundaries whilst the beta phase was found as fine needles dispersed around the grain boundaries.

At the billet centre, β- and δ- AlFeSi dominate the structures. Particles within the grain bulk have been identified as delta AlFeSi but as described earlier in this section, these particles have formed with Si present thus the high Si value compared to the Fe levels, could be a mis-reading, and this type of intermetallic could be β-AlFeSi.

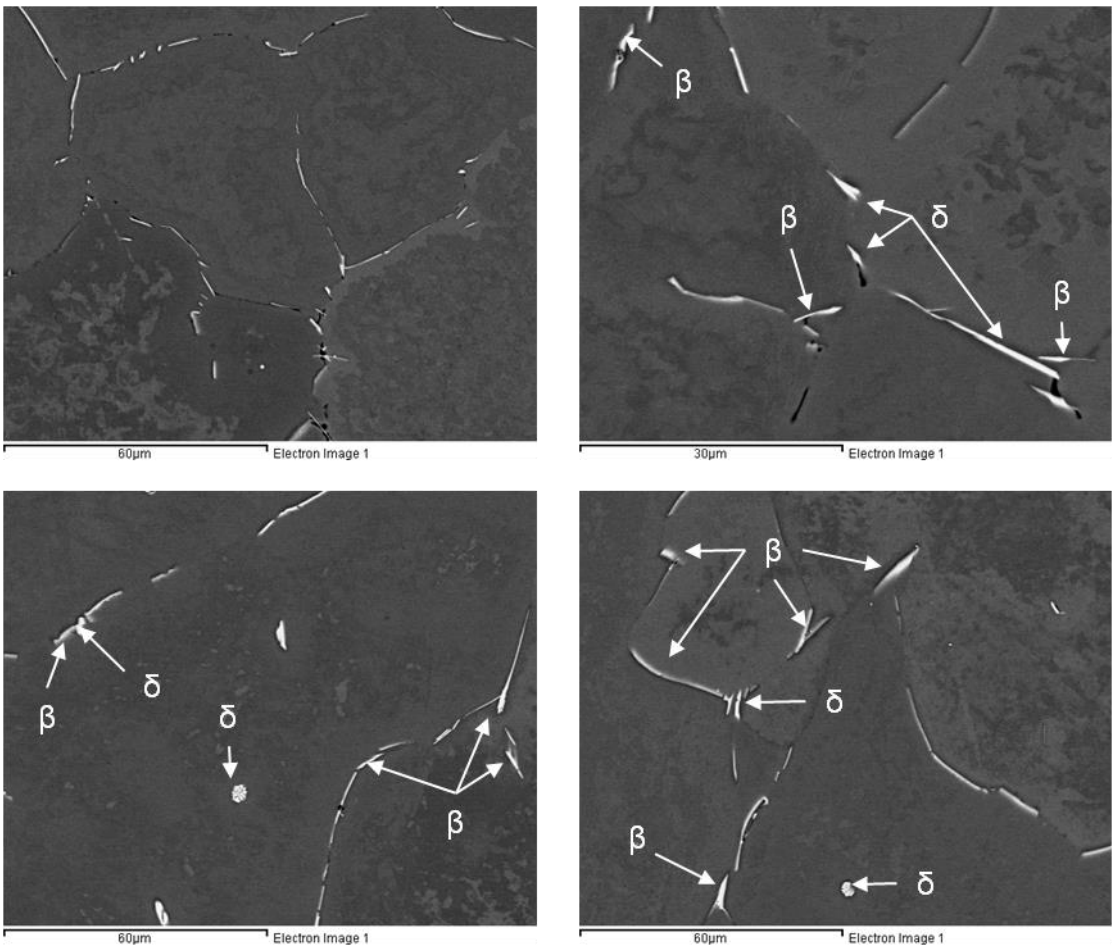

Figure 4.4.22 **SEM images of Intermetallic particles from the surface (a-b) and central (c-d) region of the BCAST DC billet. This cast was sheared at the edge of the graphite ring Cast speed was 240 mm/min. Phase identification by EDX analysis. Note some of the phases are identified in the images.**

The diagrams in Figure 4.4.23 support the findings of the SEM images relating to the dominance of the delta and beta phases in this billet. In Figure 4.4.23a (surface region) and 4.4.23c (billet centre), the diagrams show the plotted particle measurements are predominantly spread between the delta and beta phase separators, with few measurement points above the beta separator about the alpha phase separator in Figure 4.4.23a.

The Fe:Si ratio diagrams in Figure 4.4.23b (surface) and Figure 4.4.23d (centre) so that the trend of the measurements decreases and both average ratios are below 1.0 with values of 0.8 and 0.7 for the particles at the surface and centre respectively. Both of these values determine the dominant phase is delta which relates very well with the identified phases in the SEM images of Figure 4.4.22.

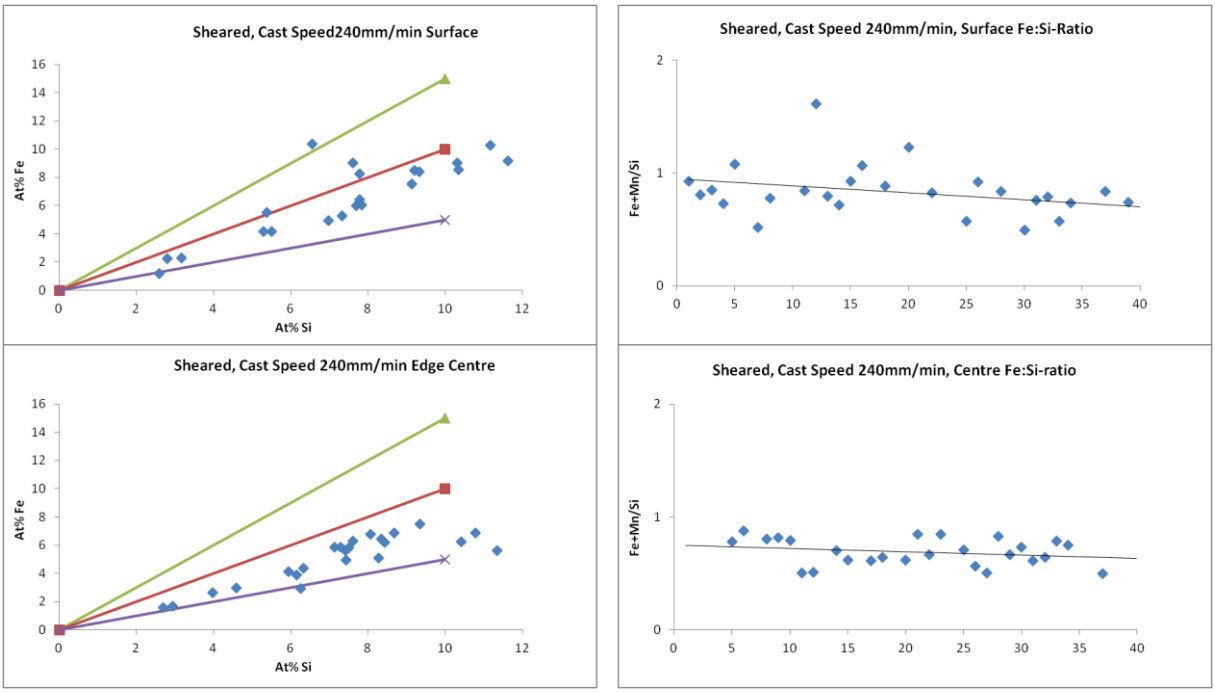

Figure 4.4.23 **(Fe+Mn)/Si ratio from the surface and central regions of sheared BCAST pilot scale DC billet plotted against separators for alpha-beta-delta AlFeSi phases and the accompanying Fe:Si-Ratio values. This material was sheared at the edge of the graphite ring and no grain refiner or titanium additions were made.**

The fact that the dominant AlFeSi phase is delta with beta in this billet may be considered a disappointing result if taken independently of the other results relating to this material. As it happens, the average particle size is small and consistent across the billet and dominated by a phase that is most likely metastable and thus can be transformed into spherical alpha phase particles after homogenisation. The delta phase is commonly found within low concentration 6xxx series alloys, it is prevalent here due to the removal of the system from equilibrium during the shearing process. Little is known about it but its assumed metastable constitution enables transformation unlike the alpha phase.

4.4.2.7 BCAST DC – INTERMETALLIC MORPHOLOGY – SHEARED 25 MM ABOVE THE GRAPHITE RING, CAST SPEED 240 MM/MIN

The rotational speed of the shear rotor was kept at 3000 RPM and the cast speed at 240 mm/min for this experiment but the depth of the shear device was reduced by raising it so the base was 25 mm above the edge of the graphite ring. The intermetallic structures obtained by LOM are shown in Figure 4.4.24 for the surface region (a-b) and the central region (c-d) of the billet.

The intermetallic particles at the surface are clearly coarser than those at the centre, figures 25b and 25d respectively. In figure 25b, particles that can be described as plates can be seen at the junctions of the grains with Chinese script present where the intermetallics become increasing complex. There is arguably a spherical nature to the particles however suggesting that α-AlFeSi is present rather than the block type of particles associated with the metastable beta phase. The rods of intermetallic become connected with the plates at the grain junctions and around smaller grain fragments where the volume of final solidified liquid concentrates between the coherent grains. However, where the rods remain isolated around the grain boundaries the intermetallics become a broken string of increasingly finer particles that includes fine particles of Mg_2Si identified as the small black particles precipitated on and close to the grain boundary AlFeSi intermetallics.

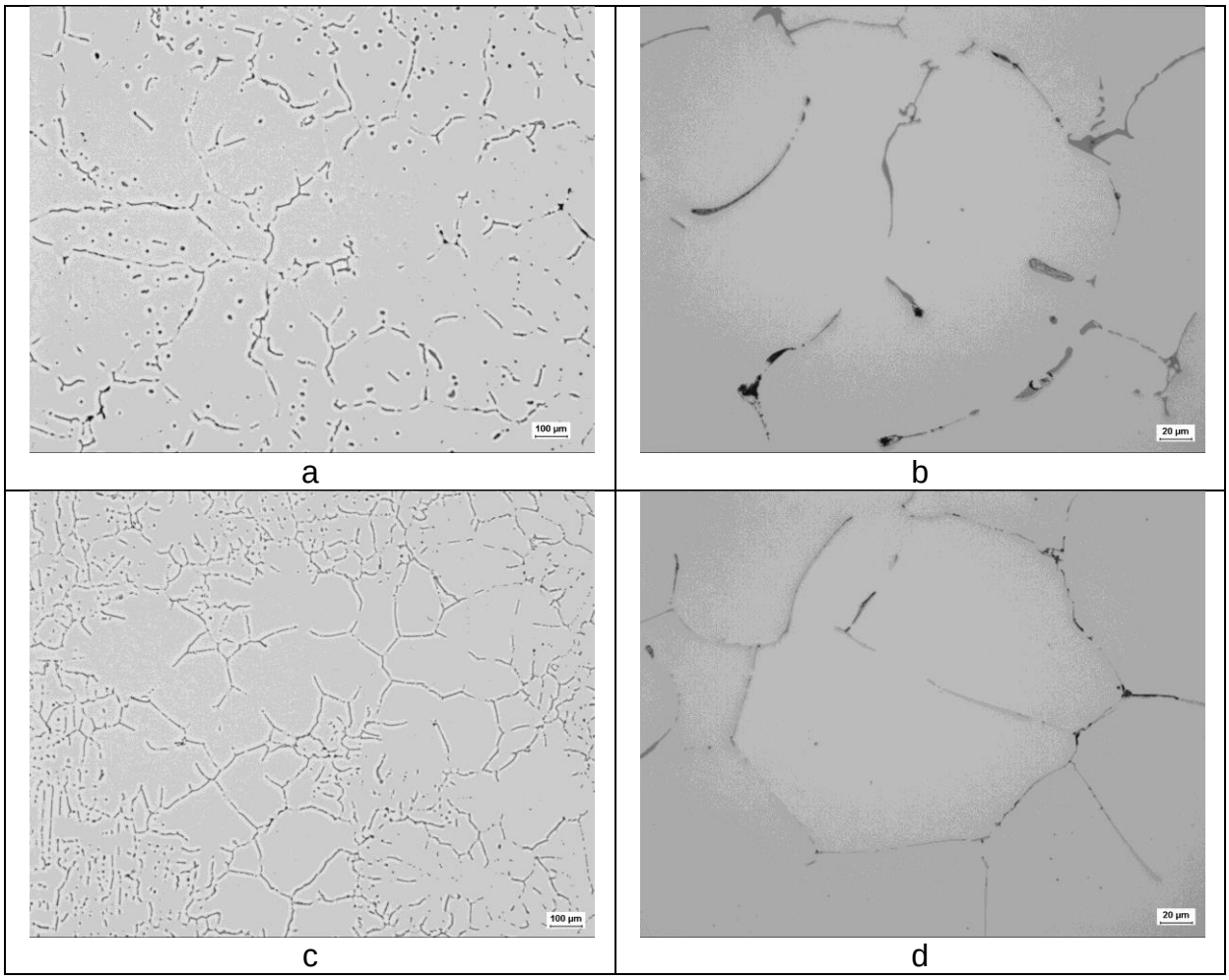

Figure 4.4.24 **As-cast microstructure of the lab scale cast with shearing. Shear unit was positioned 25 mm above the edge of the graphite ring. Cast speed was 240 mm/min. (a) Surface region at 100x magnification. (b) Surface region at 500x magnification. Heavy intermetallics and porosity are evident here as primary cooling was more intense. (c) Central region at 100x magnification. Note that a mixed structure of rosettes and dendritic grains are present here (d) Central region 500x magnification.**

Enrichment of these pockets of liquid could drive the transformation of the alpha phase form the beta phase as there a few intermetallic particles within the bulk of the grains, thus the segregating solute enriches the liquid at the boundaries as the interdendritic liquid is not available to enrich. The few particles that formed within the grains did so with a spherical morphology and are found in the more dendritic grains as rosettes are also present which are larger devoid of intermetallic particles in their bulk.

At the centre of the billet there is the mixed structure that has been seen previously in the sheared structures; dendritic structures around pockets of cellular grains/

rosettes. The intermetallics around the dendritic grains are short with intermetallic needles being the stand out morphology. Inside the grains, the intermetallics are a mix of short needles and fine spherical particles. An example of the intermetallics at the boundaries of the cellular grains is shown in Figure 4.4.24d. Intermetallics encircle the grains but they are thin could be described as a necklace of particles due to their broken up nature. Thus the intermetallics consist of rods interspersed with finer spherical particles that coarsen into thicker particles t multiple grains points. Mg_2Si can be seen on the coarser particles and on the thin rods of intermetallic at the grain boundaries.

Figures 25a-d are diagrams that illustrate the change in particle length, width, area and shape factor across the billet from the surface to the centre. In Figure 25a, the length of the particles clearly reduces from its peak at the surface, flattening off from the mid radius to the billet centre. This trend is mirrored by the average particle width and area, diagrams b and c respectively. This follows what is seen in the images of Figure 25b and d where the intermetallic structures are coarser in the surface region compared with the core. This suggests that although the billet was sheared during casting creating a refined structure, the surface region formed independently of the melt conditioning.

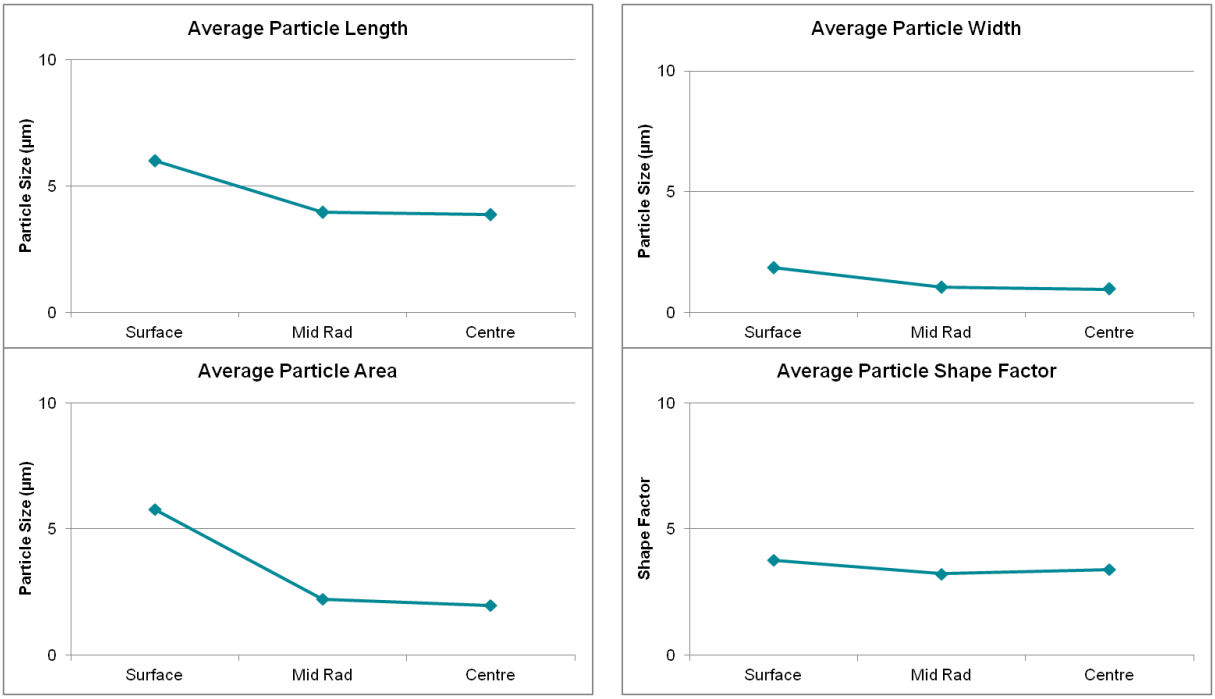

Figure 4.4.25 **INCAFeature produced results of particle measurements from sheared billet cast on the DC unit at BCAST. Shear unit was positioned 25 mm above the edge of the graphite ring. Cast speed was 240 mm/min**

4.4.2.8 BCAST DC –EDX ANALYSIS OF INTERMETALLIC PARTICLES – SHEARED 25MM ABOVE THE GRAPHITE RING, CAST SPEED 240 MM/MIN

SEM images of the intermetallic structures at the surface region of this billet are shown in Figures 4.4.26a-b. In Figure 4.4.26a the particles within the bulk of the grain are the focus whilst an example of coarse intermetallics that formed at the grain boundary are presented. In each image a selection of the identified phases are indicated.

In Figure 4.4.26a, the particles are a mixture of α- and δ-AlFeSi with the alpha phase forming coarser particles, an example of which is identified in the image. The plate like particle does have a spherical nature to it however rather than a heavily facetted plate typical of the beta phase. The delta phase particles are finer and formed with multiple morphologies, from spherical particles to those with a more facetted and rod like morphology, as indicated in Figure 4.4.26a.

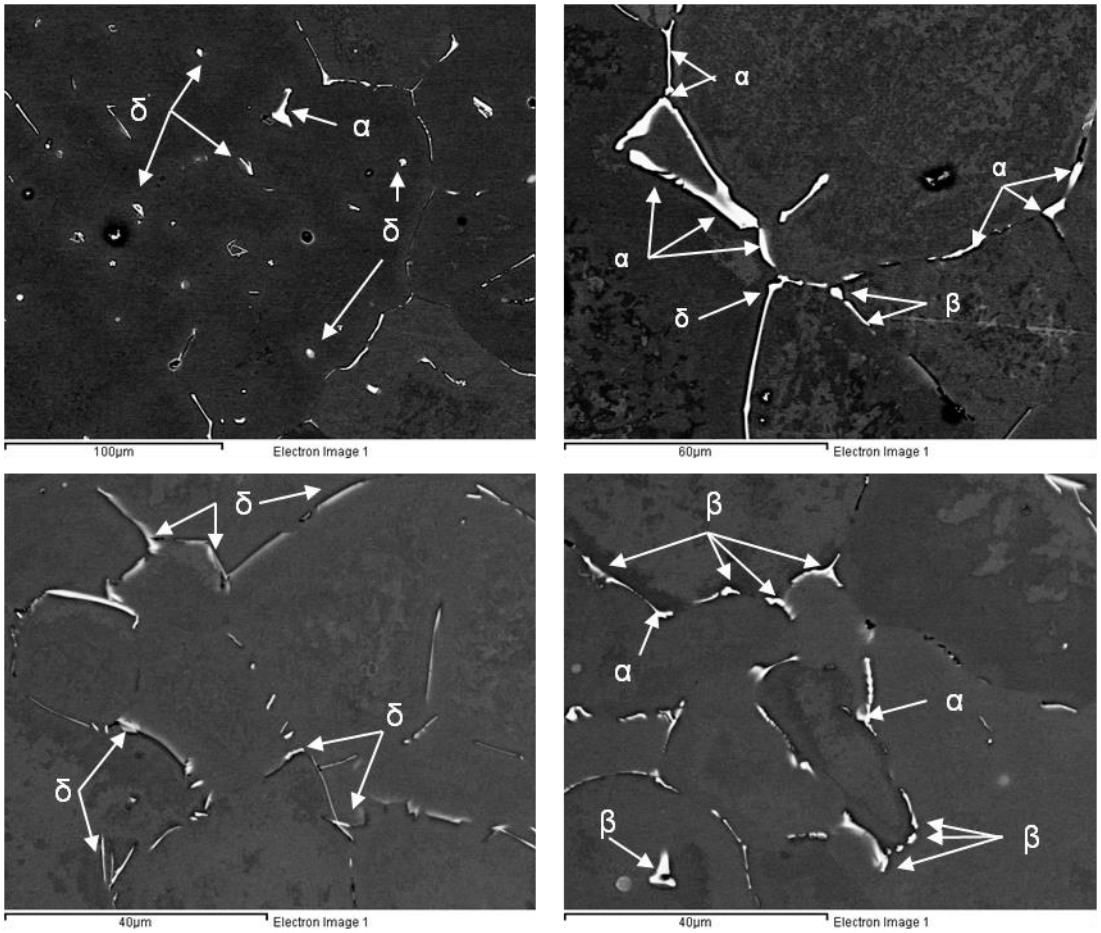

Figure 4.4.0-3 **SEM images of intermetallic particles from the surface (a-b) and central (c-d) region of the BCAST DC billet. This cast was sheared 25mm above the edge of the graphite ring Cast speed was 240 mm/min. Phase identification by EDX analysis. Note some of the phases are identified in the images.**

In Figure 4.4.26b, alpha-AlFeSi is arguably the dominant phase here. The large, coarse, intermetallic particle has been identified by EDX as being alpha, along with the majority of the particles at the grain boundaries in this image. These alpha particles range from rods to plates and coarse Chinese script. The finer alpha intermetallics will not pose a problem down-stream but the coarser rods and Chinese script will most likely reduce die life and create die lines during extrusions of certain profiles.

Beta phase intermetallics are indicated at the grain boundaries, but are not as common as those of the alpha phase. These particles resemble fine needles and spherical particles that are found away from more complex intermetallics that formed at multiple grain interfaces and will require short homogenisation times to further

refine. The delta phase is the rarest constituent within the surface region and only found at the boundaries as part of another intermetallic where it perhaps enriched in Si due to the position of other grains around it as shown in Figure 4.4.26b. Here a rod alpha becomes or begins as δ-AlFeSi at the grain junction, but away from this point extending along the boundary of the grain, the intermetallic solidified as α-AlFeSi.

In Figure 4.4.26c-d, intermetallic structures obtained by SEM from the billet centre are presented. It is clear that there has been a shift in the phase dominance from the high Fe alpha-AlFeSi to the lower Fe constituents of beta and delta AlFeSi. In Figure 4.4.26c, the intermetallics have been identified exclusively as delta phase needles and rods at the grain boundaries.

However, multiple phase zones have been discovered also as shown in Figure 4.4.26d. This is typical of the cellular structures that formed as pockets within the dendritic structures. These intermetallics are broken up spheres that resemble necklaces and are either alpha or beta AlFeSi as shown in the image. The image also formed as plates especially at the boundaries of grain fragments that appear embedded within larger grains, examples of which are presented in Figure 4.4.26d. In these zones of the billet, the delta phase was absent, restricted mostly to the dendritic regions of the billet centre.

Figures 4.4.27a-b and 4.4.27c-d present diagrams that help determine the dominant phase for at the surface and centre regions of the billet, respectively. If we compare the diagrams in Figure 4.4.27a with Figure 4.4.27c, we can see that there is a clear shift in the values about the alpha-beta-delta separators. At the surface, the dominant phase is arguably α-AlFeSi with the majority of the data values spread along the alpha separator. As seen in the SEM images of Figure 4.4.27a-b, beta phase and delta phase particles were measured by EDX and plotted in the diagram, but are few and practice present at very high Si values.

Diagram b in Figure 4.4.27 plots the Fe and Si ratio of the particles at the billet surface measured by EDX, where the average value indicates the dominant phase as measured by its position within a range associated with each AlFeSi phase. The average Fe :Si ratio for the surface region is 1.52 which actually signifies β-AlFeSi is the dominant phase rather than alpha as the limit of the beta phase value range is

1.55, which indicates how close the phases are and how α-AlFeSi could be considered dominant.

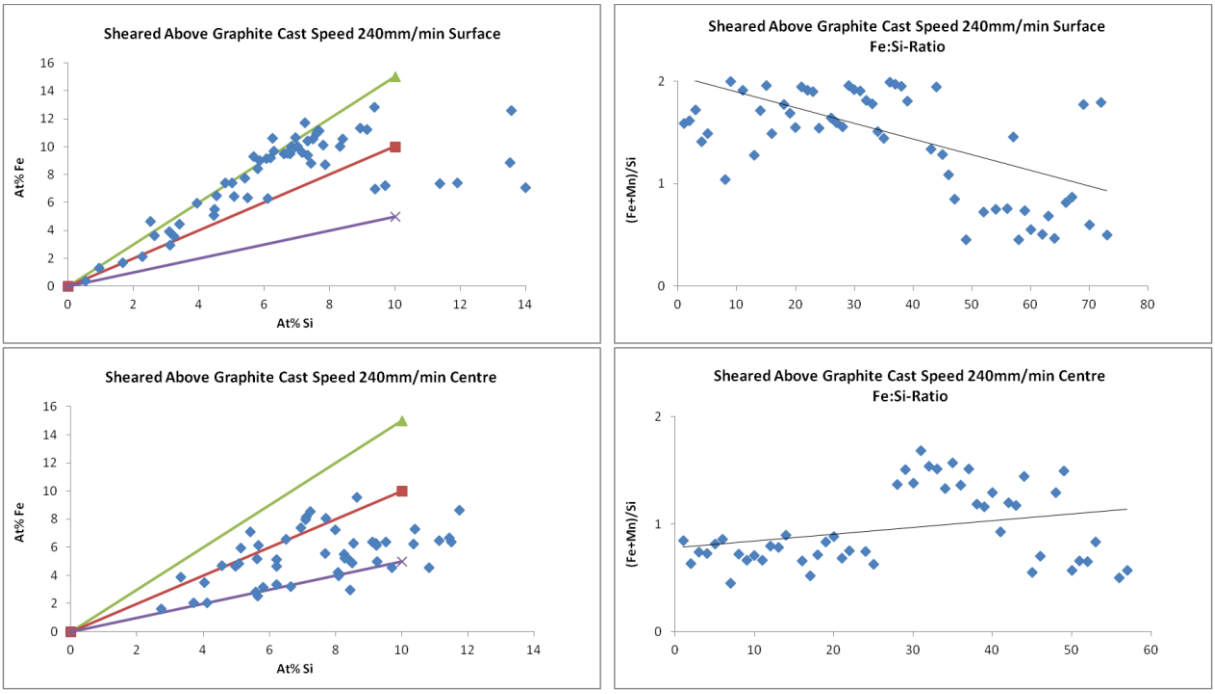

Figure 4.4.27 **Fe+Mn)/Si ratio from the surface and central regions of sheared BCAST pilot scale DC billet plotted against separators for alpha-beta-delta AlFeSi phases and the accompanying Fe:Si-Ratio values. This material was sheared at the edge of the graphite ring and no grain refiner or titanium additions were made.**

At the billet centre (Fig 4.4.27c) the spread of the particles are much more widely distributed, predominantly around the lower Fe separators of the beta and delta phases. It could be argued that the delta is the most dominant phase here but it is not clear just from this diagram alone. Figure 4.4.27d thus provides an accurate method to aid determination of the dominant phases, by providing an average Fe to Si value that is then applied to the reference values used to separate the phases. The average value is 0.96 which determines β-AlFeSi as the dominant phase at the billet centre.

APPDENDIX 2 – FLOW PATTERN ASSEMBLY DIAGRAMS

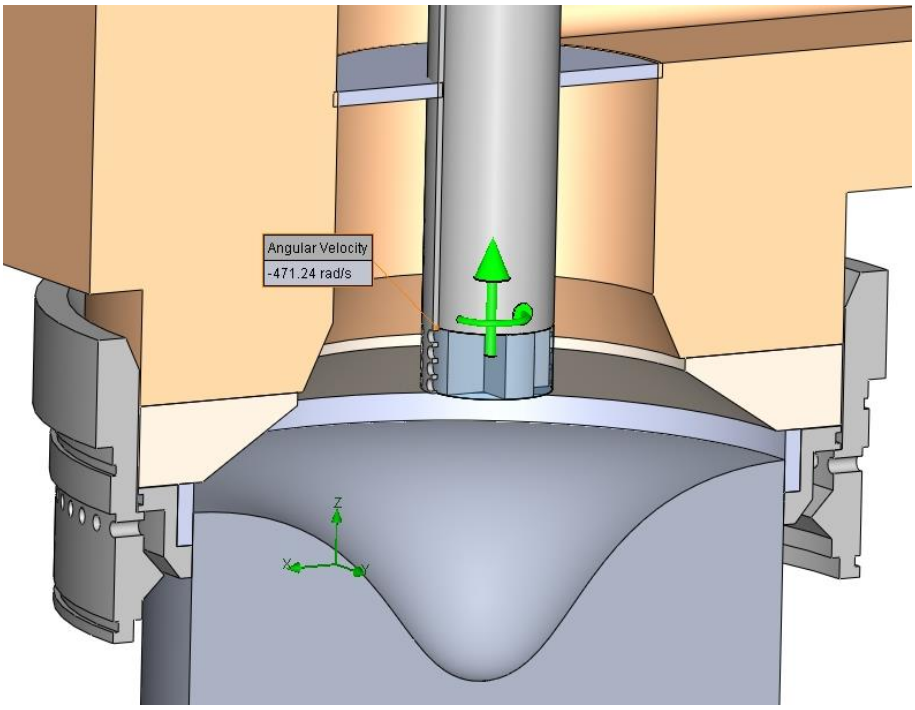

Figure 0-1 Local rotating region

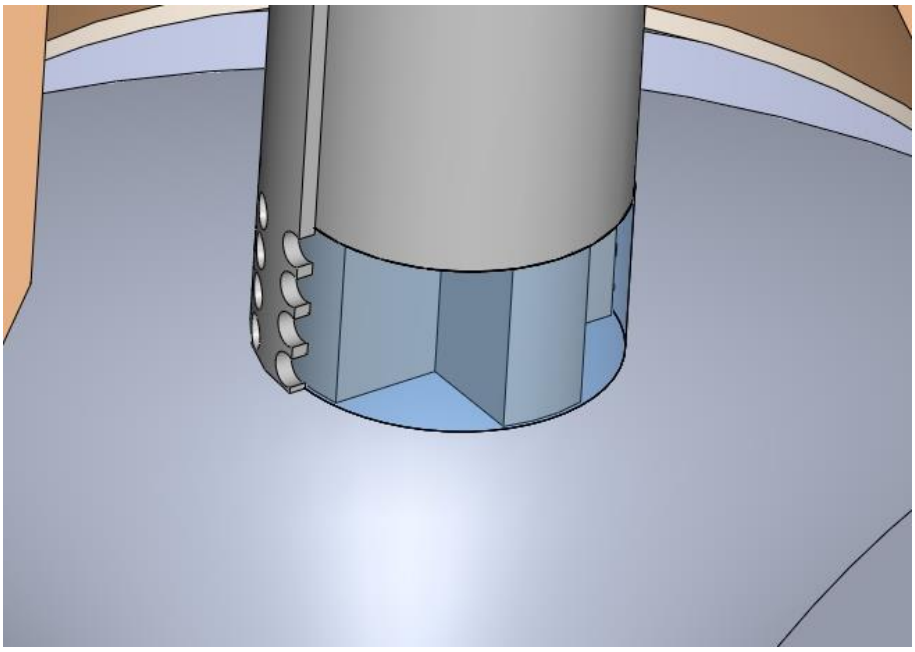

Figure 0-2 magnified view of local rotating region

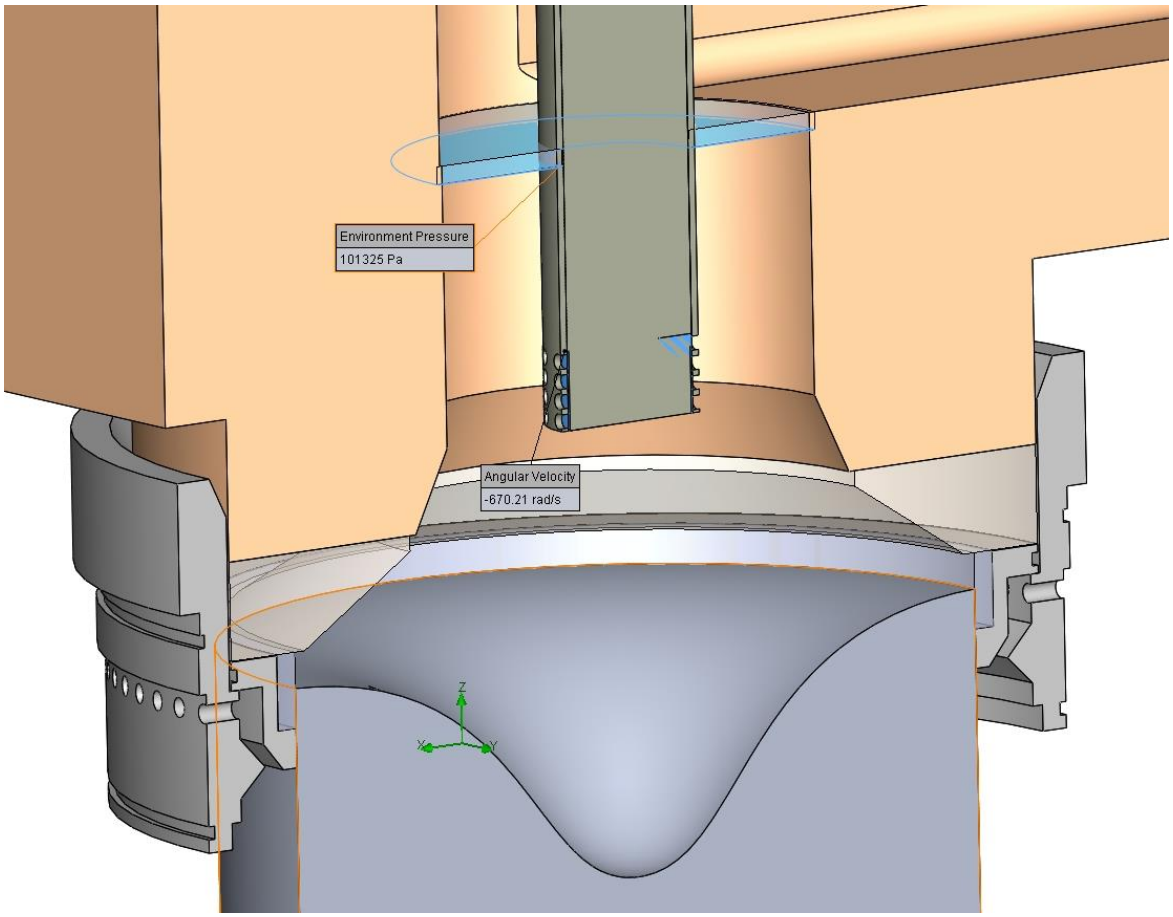

Figure 0-3 Environment pressure for top domain boundry